ELECTRICAL RESISTIVITY TOMOGRAPHY COMBINED WITH PREVIOUSLY COLLECTED SURFACE WAVE DATA IN A KARST TERRAIN: A CASE FOR COMBINING TECHNIQUES TO DETECT SUBSIDENCE FEATURES

by

Ryan Joseph Jubran

(Under the Direction of Robert B. Hawman)

ABSTRACT

Two-dimensional electrical resistivity tomography was used to image the subsurface in a karst environment in Albany, GA. Nine electrical resistivity profiles were conducted over previous seismic lines. Apparent resistivity data were inverted and compared with shear-wave velocity models. All profiles show a steep increase in resistivity values (73-123 ohm-m, Line A 156-250 ohm-m) at approximately 10 m indicating a transition from a sandy-clay overburden to limestone bedrock of the Ocala Formation, in agreement with shear-wave velocity models and borehole data. Resistivities for bedrock range from 100-250 ohm-m. A low-resistivity anomaly (56 ohm-m) along Line A and Z corresponds with a previously mapped burn pit. High resistivity anomalies (100-156 ohm-m, 0-10 m depth) correlating with low shear-wave velocity anomalies (200-300 m/s, 0-10 m depth) along three profiles correlate to subsidence features.

INDEX WORDS: Sinkholes, Electrical Resistivity Tomography, Surface-Wave Analysis, Karst

ELECTRICAL RESISTIVITY TOMOGRAPHY COMBINED WITH PREVIOUSLY COLLECTED SURFACE WAVE DATA IN A KARST TERRAIN: A CASE FOR COMBINING TECHNIQUES TO DETECT SUBSIDENCE FEATURES

by

Ryan Joseph Jubran

B.S., Georgia Southwestern State University, 2012

A Thesis Submitted to the Graduate Faculty of The University of Georgia in Partial Fulfillment of the Requirements for the Degree

MASTER OF SCIENCE

ATHENS, GEORGIA

2015

ELECTRICAL RESISTIVITY TOMOGRAPHY COMBINED WITH PREVIOUSLY COLLECTED SURFACE WAVE DATA IN A KARST TERRAIN: A CASE FOR COMBINING TECHNIQUES TO DETECT SUBSIDENCE FEATURES

by

Ryan Joseph Jubran

Major Professor: Robert B. Hawman

Committee: Paul A. Schroeder
Adam M. Milewski

Electronic Version Approved:

Julie Coffield
Interim Dean of the Graduate School
The University of Georgia

ACKNOWLEDGEMENTS

I would like to thank Rob Hawman for all the time, energy, and support that was given throughout this project. Having someone be excited to teach and support in any way possible really allows for a great learning environment.

I would also like to thank the following individuals for their support to the project: Albany Water, Gas, and Light Commission (WGL) for allowing the use of their property to conduct the project, Gary Morefield (WGL) for providing site access and support, Bill Wylie, James Thompson, and Clinton Brown for all of their support with data collection that would have been made much more tedious without them.

Financial support was provided by the Joseph W. Berg Fund (UGA) and NSF grant EAR-0844154. I would also like to thank the University of Georgia Department of Geology for the use of their vans that provided transportation to and from the study area in Albany, GA.

TABLE OF CONTENTS

Page

APPENDICES

LIST OF TABLES

Page

LIST OF FIGURES

Page

CHAPTER 1

INTRODUCTION

Objectives of the Study

Located in a karst environment, Albany, Georgia is at risk for sinkhole formation. Knowing factors such as depth to bedrock and where zones of sinkhole development within the subsurface are located is important in knowing where to build and work in the area. This thesis outlines the use of the electrical resistivity method to identify anomalous zones of resistivity for comparison with previously collected seismic surface-wave data (Parker, 2010; Parker and Hawman, 2012). Using the dipole-dipole method, nine resistivity profiles were completed over the same nine profiles completed for the seismic study. The goal of the project was to show how the electrical resistivity method and multi-channel surface-wave analysis can be used as complimentary techniques that provide a better understanding of the subsurface geology than one technique alone and to find zones of potential sinkhole development. The combination of resistivity and surface wave analysis can help resolve ambiguities in the interpretation of anomalies. Of particular interest is the detection of zones of very high electrical resistivity that suggest a void in the subsurface, that can lead to the opening of a sinkhole.

Geologic Setting

The study area is located on an active well field owned by Albany Water, Gas, and Light Commission (WGL) located in Albany, GA. It is located in the Coastal Plain geologic province of Georgia, and specifically the Dougherty Plain physiographic province (Figure 1.1). The

Dougherty Plain physiographic province is characterized by karst topography from active solution causing most of the drainage to occur in underground channels instead of the surface (Hicks *et al.,* 1987). This results in the formation of sinkholes throughout the province that are shallow and flat-bottomed or rounded and ranging in depth from a few meters to more than seven meters (Hicks *et al.,* 1987) Figure 1.2 shows a stratigraphic column of the Dougherty Plain province. Throughout this region there is approximately 30 to 60 feet (9 to 19 meters) of overburden classified as undifferentiated sand and clay overlying the Ocala Limestone which is the main unit that hosts the Upper Floridan Aquifer (Gordon, 2011).

The Upper Floridan Aquifer, a limestone aquifer, underlies parts of Georgia, Alabama, South Carolina, and all of Florida and is one of the most productive aquifers in the United States (Hicks *et al.,* 1987). Primarily consisting of the Ocala Limestone in the study area, the Upper Floridan Aquifer also includes the Clinchfield Sand and the Lisbon Formation throughout the Dougherty Plain province (Hicks *et al.,* 1987). In Albany, the Upper Floridan Aquifer is divided into upper and lower water-bearing zones with the lower zone corresponding to the lower unit of the Ocala Limestone and the upper water-bearing zone corresponding to the upper and middle units of the Ocala Limestone (Stewart *et al.*, 1999). The Upper Floridan is confined below by the Lisbon Formation and usually confined above by undifferentiated overburden and zones of low permeability (Stewart *et al.*, 1999). The thickness of the Upper Floridan can range from 15 to 145 meters; thickness increases towards the coast (Hicks *et al.,* 1987).

The Ocala Limestone is "underlain by the Lisbon formation, which consists of brownish-gray, clayey, glauconitic, dense limestone." Because of its lower water-yielding capability, the Lisbon formation is considered the base of the Upper Floridan Aquifer (Stewart *et al.*, 1999).

Three distinct lithologic units, the lower, middle, and upper units, comprise the Ocala Limestone with the middle unit representing the top of the formation in the study area (Parker and Hawman, 2012). The middle unit of the Ocala Limestone consists of "relatively impermeable white to brown, clayey, dense, chalky limestone and interlayers with non calcareous clay and silt layers that are not extensive" (Stewart *et al.*, 1999). The lower unit consists of "inter-layered gray to dark-brown, recrystallized, glauconitic, dolomitic limestone" and has "well-developed secondary permeability along solution-enlarged joints, fractures, and bedding planes" (Stewart *et al.*, 1999). The middle unit of the Ocala Limestone consists of "relatively impermeable white to brown, clayey, dense, chalky limestone and interlayers with non calcareous clay and silt layers that are not extensive" (Stewart *et al.*, 1999).

As noted earlier, the Ocala Limestone is overlain by 30 to 60 ft of undifferentiated Quaternary sand and clay (Gordon, 2011). This overburden is thought to be alluvium deposited by area streams and rivers and weathering products of the Ocala and Suwannee Limestones and generally increases in thickness towards the Flint River (Hicks *et al.,* 1987). USGS borehole logs for the study area indicate a bedrock depth of approximately 9 meters (Figure 1.3) (Parker, 2010).

Before 1987, the city of Albany used deep aquifers for its municipal and irrigation purposes but after drops in water-level of over 140 ft, Albany WGL started to pump water from the Upper Floridan Aquifer (Hicks *et al.,* 1987). The main concern regarding the Upper Floridan Aquifer was the potential for aquifer contamination from urban runoff and agricultural activities (Stewart *et al.*, 1999).

Karst Development and Significance in Albany, GA

Karst topography is defined by specific hydrology and landforms that are a result of highly soluble rock and high secondary fracture porosity (Ford and Williams, 2007). Karst features include sinkholes, caves, solution channels, and underground drainage networks (Ford and Williams, 2007). These landforms can lead to "potential hazards for land use, serve as entry points for groundwater contaminants, and promote lowering of the surface by conveying sediment underground" (Hyatt and Jacobs, 1996). Sinkholes in the Albany area have been triggered by flooding events as seen in flooding of the Flint River in 1994 (Hyatt and Jacobs, 1996), drought, and over pumping of the Upper Floridan Aquifers and deeper aquifers resulting in lowering of the water table and loss of hydrostatic support of the overburden (Gordon, 2011).

Pre-existing fractures in the bedrock and lineaments, as well as fracture planes that intersect the surface, are controlling factors in the formation of karst features and the identification of these zones can be crucial for investigating potential site collapse (Hyatt and Jacobs, 1996). Preferential weathering along these fractures allows for more erosion and high probability of sinkhole formation. Brooks and Allison (1983) have identified fracture orientations in the area of 325, 5, and 40 degrees. Orientation of sinkhole development in this area has been found to correlate with fracture trends along the Flint River (Brooks and Allison, 1983).

The majority of the hundreds of sinkholes in Albany have been classified as suffosion and collapse sinkholes formed by "piping and collapse of unconsolidated sediment into the Ocala limestone" (Hyatt and Jacobs, 1996). Figure 1.4 shows an illustration of the process of a collapse sinkhole forming in a karst area similar to Albany. "Piping creates cavities in the overburden

above joints; these cavities grow until the overlying soils can no longer maintain an arch and collapse" (Hyatt and Jacobs, 1996). Also, groundwater flow leads to erosion of the overburden and limestone units causing voids to develop which can become filled with water. When water levels drop below the roof of the void, there is no more support and the overlying material collapses (Gordon, 2011).

After the 1994 flood, 312 sinkholes opened within Albany city limits as the initial water influx into the system was lost resulting in the " (1) saturation and loss of cohesion in sediments overlying bedrock openings, (2) increased loading because of saturation of the sediment and standing surface water, and (3) liquefaction and piping of sediment downward into underlying cavities" (Hyatt and Jacobs, 1996). Between 2003, when WGL began well-field pumping, and 2010 more than 23 sinkholes developed in the well-field area (Gordon, 2011). These sinkholes were believed to have developed in response to the excavation of holding ponds and more than 30-ft fluctuations in the water level (Gordon, 2011). The locations of these more recent sinkholes along with the study area (highlighted in yellow) can be seen in Figure 1.5.

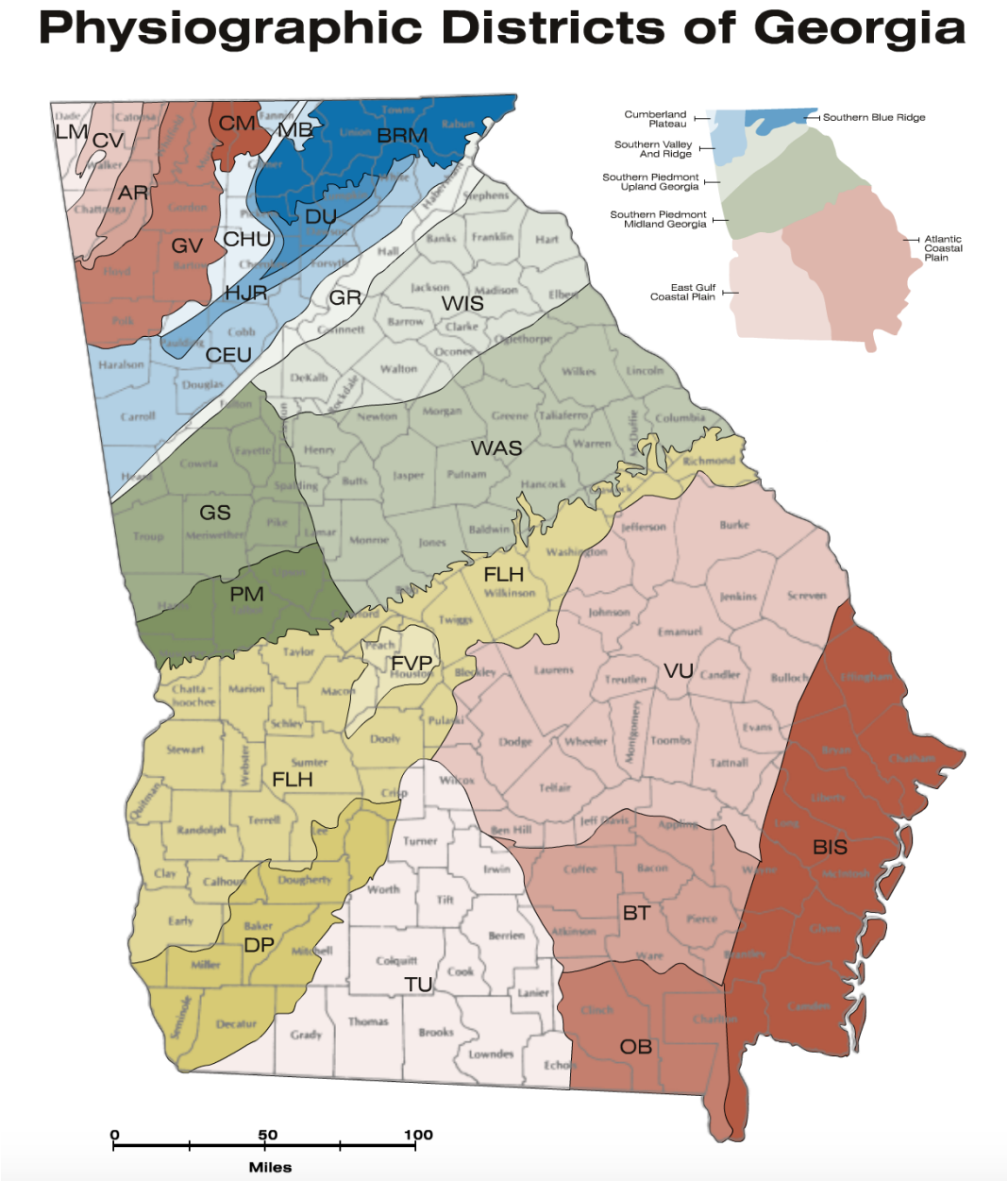

Figure 1.1 - Location of the Dougherty Plain (DP) Physiographic province (Clark Jr. and Zisa, 1976).

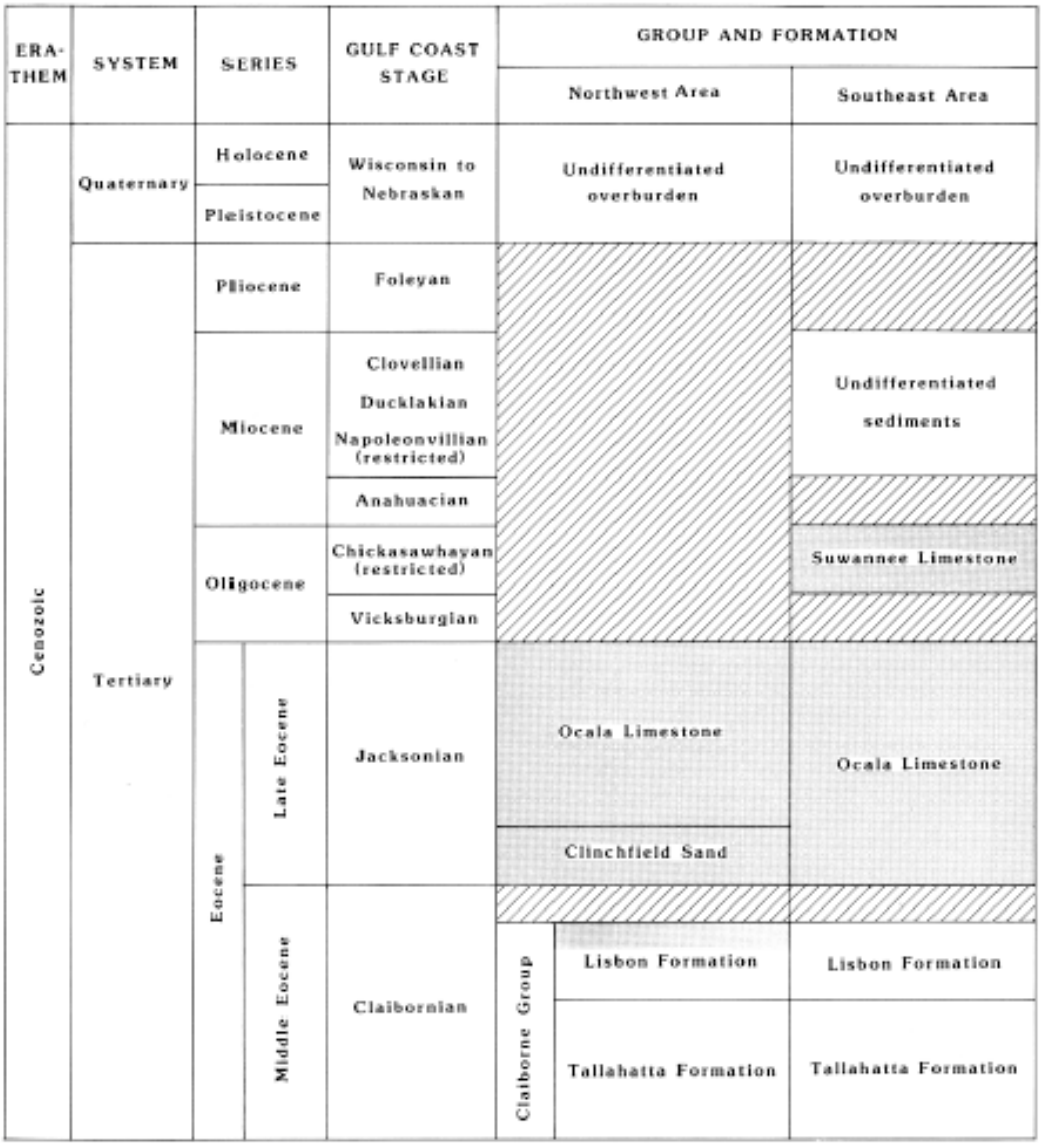

Figure 1.2 - Stratigraphic Column for the Dougherty Plain physiographic province (Hicks *et al.*, 1987).

Figure 1.3 - USGS Borehole Data for Well #44 (Figure 1.5) obtained from the USGS Water Science Center in Atlanta, GA (Parker, 2010).

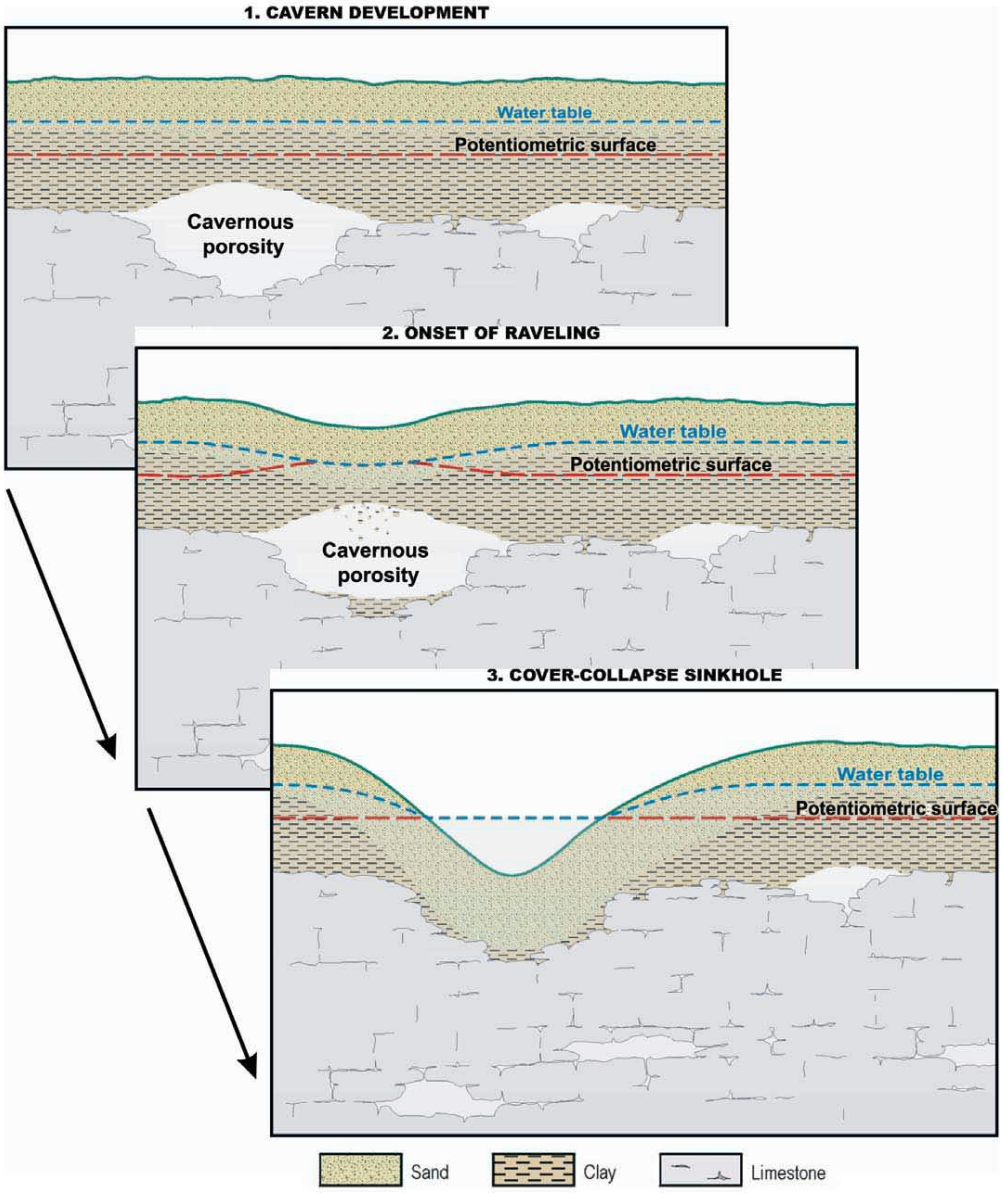

Figure 1.4 - Formation of cover-collapse sinkholes (Dobecki and Upchurch, 2006).

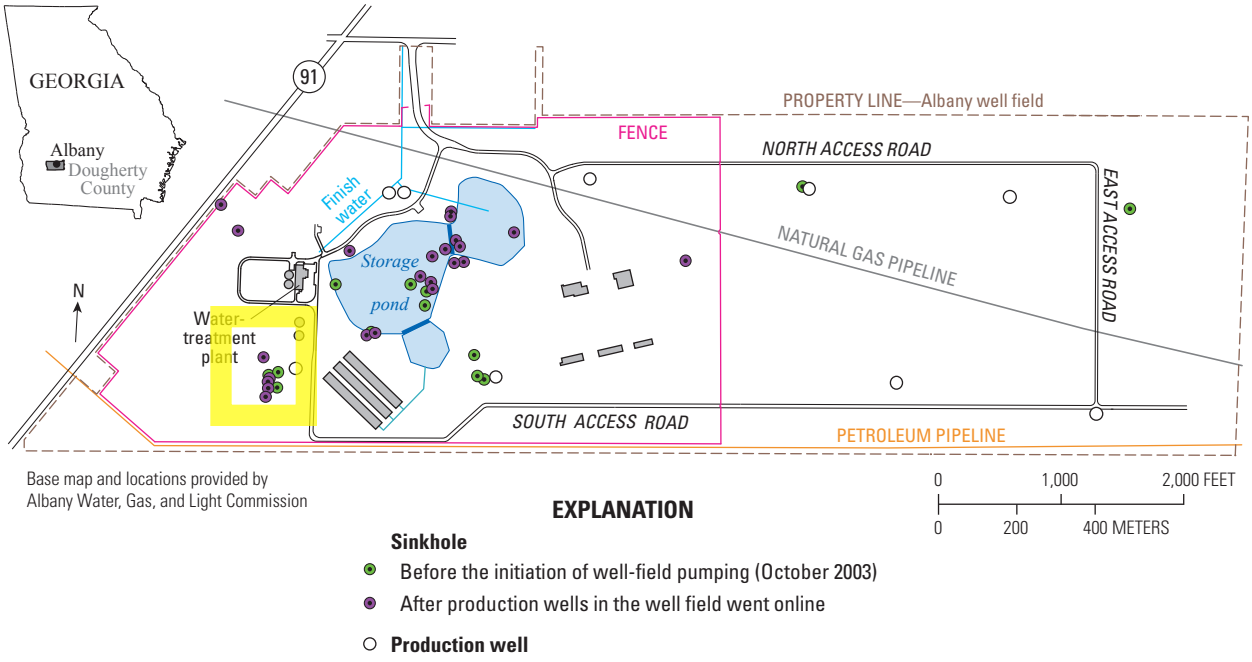

Figure 1. 5 - Location of sinkholes and production wells on Albany WGL Commissions' property in Albany, Ga (Gordon, 2011). Field location outlined in yellow.

CHAPTER 2

METHODS AND PREVIOUS KARST INVESTIGATIONS

Electrical Resistivity Method

Electrical resistivity measurements are made by introducing direct current into the ground through surface electrodes and measuring the Earth's response as a resistor (Robinson and Coruh,1988). The degree of resistance of current a substance provides is its electrical resistivity. A main goal of these measurements is to provide a way to distinguish layering and structures in the subsurface based on electrical resistance (Robinson and Coruh,1988). Measured in ohm-meters, electrical resistivity values can vary considerably between lithologically and mineralogically similar samples (Robinson and Coruh,1988). Overall, a range of resistivity values is expected for a given earth material. Typical resistivities of earth materials can be seen in Figure 2.1. The material occupying pore spaces can have a profound effect on the electrical resistivity. If a pore space is filled with water, it will have a lower resistivity than if that pore space is unsaturated, therefore making electrical resistivity surveys an effective tool for identifying boundaries between saturated and unsaturated layers. Although electrical resistivity will not yield exact geologic properties and materials, it can constrain the nature of the pore spaces and pore fluids.

Current flow in electrical resistivity surveys is three-dimensional. From one of the current electrodes, or source, the electrical current flows out in all directions through the earth and into the other current electrode, or sink (Robinson and Coruh,1988). As current moves away from the

source, it creates a hemispherical surface, the equipotential surface, over which the electrical potential related to the current flowing from the source is constant (Figure 2.2) (Robinson and Coruh,1988). Current flow lines are perpendicular to equipotential surfaces and by determining the positions of the equipotential surfaces, it is possible to draw a set of lines to represent the current flow through the ground from the source and sink (Figure 2.3) (Robinson and Coruh, 1988). Depending on the geometry of the survey, different lateral and depth variations of resistivity can be measured.

Multi-channel Analysis of Surface Waves

The multichannel analysis of surface waves (MASW) method uses dispersion of surface-waves to generate models of shear-wave velocity structure (Park *et al.,* 2007). Shear-wave velocity is directly related to the shear modulus (rigidity). Shear modulus is the ratio of shear stress to shear strain. This relationship is given by:

$$V_s = \beta = (\mu/\rho)^{1/2}, \quad (1)$$

where β is shear-wave velocity, μ is the shear modulus, and ρ is the material density. For shallow depths of investigation, MASW deals with frequencies from a few to a few tens of hertz (Hz) and is recorded by a system containing 24 or more channels with a receiver array with aperture up to a few hundred meters (Park *et al.,* 2007). Two methods to generate surface waves include the "active" method, which generates surface waves through an impact source such as a sledgehammer, and the "passive" method which uses surface waves generated passively by cultural and natural sources such as traffic or thunder (Park *et al.,* 2007).

With MASW, phase velocities are measured as a function of frequency and the phase velocities are then inverted for models of shear-wave velocity as a function of depth (Parker and

Hawman, 2012). Shear-wave velocity can be used to distinguish between various types of unconsolidated soils and bedrock (Odum *et al*., 2007). In carbonate rocks, shear-wave velocity is strongly controlled by porosity (Baechle *et al*., 2009). This means that competent bedrock will show higher shear-wave velocities than soils and fractured bedrock (Parker and Hawman, 2012).

Electrical Resistivity Studies in Karst Environments

The most commonly used geophysical surveys for the investigation of potential sinkhole activity are ground-penetrating radar (GPR), electrical resistivity, and seismic methods (refraction tomography, reflection, and surface wave inversion) (Dobecki and Upchurch, 2006). A disadvantage of GPR is that the signals generally don't penetrate deep enough to image bedrock in karst terrains, penetrating only 5-10 m, and the signals can be strongly attenuated by shallow clay or shallow, salty ground-water (Dobecki and Upchurch, 2006). Electrical resistivity and surface wave methods provide greater depth penetration.

In the electrical resistivity tomography (ERT) method, surface measurements of electrical resistance are used to generate a 2D model of subsurface resistivity. The electrical resistivity method is often used to determine the depth to bedrock, locate air-filled cavities, and also locate fracture zones in a karst environment seen in zones with high contrast in resistivity (Nyquist *et al.*, 2007). Limestone bedrock and air-filled voids have a higher resistivity compared to the conductive clay-rich soil that make up the overburden (Nyquist *et al.*, 2007). Resistivity values can vary depending on the material and conditions such as previous rainfall events (Youseff *et al.*, 2012).

The electrical resistivity method is commonly used to identify the ravel zone, a volume of soil with high porosity in which raveling, a process where water transports soil down into voids,

has occurred. With shallow limestones and large enough dissolution features, the electrical resistivity method can identify voids or cavities (Dobecki and Upchurch, 2006). For example, on the Korean Peninsula, a 2D electrical survey was completed in a karst environment where underground cavities were identified based on results from borehole investigations (Park *et al.,* 2009). The survey used a dipole-dipole array with an electrode spacing of 5 m for a maximum penetration depth of 25 m and used an automatic analysis method to calculate the apparent resistivity values and then used a non-linear least-square optimization to invert the data (Park *et al.,* 2009). The results showed that the limestone cavities were filled with weathered limestone blocks and clay which resulted in significantly lower resistivity values than the surrounding bedrock (Park *et al.,* 2009).

2D electrical resistivity surveys can be completed with several different array types. The most common array types are Wenner, Schlumberger, and dipole-dipole (Robinson and Coruh, 1988). Each array has its own advantages and disadvantages (Figure 2.4). For example, the Wenner array uses a constant spacing between electrodes but all electrodes need to be moved between measurements (Nyquist *et al.*, 2007). The Schlumberger array is “efficient for depth sounding because only the two outer current electrodes are moved between measurements" and the spacing between the potential electrodes is only increased to keep the signal above noise (Nyquist *et al.*, 2007). The dipole-dipole array can give better lateral resolution than vertical resolution while only moving two electrodes at a time (Athanasiou *et al.*, 2007).

In an effort to improve upon the dipole-dipole array, a traditional dipole-dipole array was compared to a new computer optimized array and the tradeoffs for identifying features in a karst environment in Pennsylvania were discussed (Nyquist *et al.*, 2007). As seen in Figure 2.5, the

traditional dipole-dipole array pseudodepths were compared to the optimal array pseudodepths testing the hypothesis that the optimal array would show significantly better resolution at depth (Nyquist *et al.*, 2007). This optimal array was based on the work of Stummer *et al*. (2004) who used a computer simulation to search for the optimal electrode measurement sequence that allowed for adequate resolution and less measurement time. The conclusion was that the optimal array provides resolution comparable to the traditional array, but that the optimal array is preferable when a slight improvement in resolution at depth is more important than data acquisition time. The traditional array acquisition time is approximately three times faster (Nyquist *et al.*, 2007).

Distinction between developing sinkholes and mature sinkholes is also possible as shown by a study conducted by Schoor (2002). An ERT survey in a dolomitic area was conducted using a dipole-dipole survey designed so that the topographic variation in the area was negligible (Schoor, 2002). The study was able to show differences between developing sinkholes, where the material is primarily weathered and conductive, and mature sinkholes, where the cavities can be air-filled (resistive) or water-filled (conductive) (Schoor, 2002). Water-filled cavities will be more conductive than the surrounding dolomite (Schoor, 2002).

Surface-Wave Analysis Study in a Karst Environment

The focus of this thesis was developed based on previously collected data from a MASW study in Albany, GA by Parker (2010). MASW was used to map bedrock topography, image anomalies in the subsurface, and detect variations in weathering of the limestone bedrock (Parker, 2010). The seismic lines were established near a production well with known depth to bedrock. Seven east-west profiles (lengths: 89 to 173 m) spaced 20 m apart were tied with two

north-south profiles 155 and 240 m long, also 20 m apart (Figure 2.6) (Parker and Hawman, 2012). The surface-wave data were collected using a 24-channel seismograph and 4.5 Hz geophones in a "roll-along survey" in which the source and recording channels were moved at one-station intervals along the line (Parker and Hawman, 2012).

Two types of survey were conducted. The first used a sledge-hammer with four hammer blows stacked for each record. The receiver spacing for the hammer survey was one meter with a recording aperture of 23 m for each shot record (Parker and Hawman, 2012). The shot spacing and source-receiver offset were also one meter (Parker and Hawman, 2012). The maximum depth of penetration and resolution width for this survey were 12 m. Lateral resolution was later improved to 6 m during post-processing by including only half of the traces. The passive-source array used a moving passenger van as a source to generate lower frequency energy for greater depth penetration (Parker and Hawman, 2012). The van was driven in line with the array and the geophone spacing was increased to two meters to double the recording aperture for each shot record. This increased the depth penetration and minimum resolution width to 23 m (Parker and Hawman, 2012). Table 2.1, Table 2.2, Table 2.3, and Table 2.4 outline the survey parameters and the recorder parameters.

Dispersion curves then were generated for each shot gather and were inverted for models of shear-wave velocity as a function of depth to create a "1D shear-wave velocity model of an average velocity function at the mid-point of the geophone spread" (Parker and Hawman, 2012). These 1D models were combined to make a 2D pseudo-section model of the subsurface for each line. Standard penetration tests and borehole logging were conducted at three locations along Line A (Figure 2.7). Results from these tests were incorporated into the inversions.

The results of the shear-wave velocity models show a clear boundary marked by a steep velocity gradient centered at 350 m/s at approximately 9-12 m depth indicating a transition from the sandy-clay overburden to Ocala limestone bedrock (Parker and Hawman, 2012). The limestone bedrock velocities varied from 350-700 m/s depending on the rigidity of the limestone as confirmed by standard penetration tests (Parker and Hawman, 2012). Sinkholes within the study area correlated to lower-velocity zones and lower-velocity zones in the bedrock suggest fracture zones and weathered bedrock that can be useful in determining areas of potential subsidence (Parker and Hawman, 2012). Along with the subsidence features and bedrock analysis, an anomaly associated with a burn pit at the intersection of Line Z and Line A was imaged and constrained showing a low velocity zone where the pit was filled in, correlating to a low rigidity zone.

Combined Analysis of Surface-Wave and Electrical Resistivity Data

Ambiguities in interpretation of geophysical data can often be resolved by using more than one method. For example, the burn pit along Line A and Line Z is a low velocity zone, but the surface-wave data cannot distinguish between a clay-filled or air-filled cavity. By using data from an electrical resistivity survey, this ambiguity is resolved. This was done for several other zones throughout the survey by comparing the 2D shear-wave velocity models to the 2D resistivity models.

By using electrical resistivity data and combining it with shear-wave velocity data, four outcomes are possible: low resistivity and low shear-wave velocity, low resistivity and high shear-wave velocity, high resistivity and low shear-wave velocity, and high resistivity and high shear-wave velocity (Table 2.5). A combination of low resistivity and low shear-wave velocity

would be an indication of saturated, less-rigid, more porous materials, (e.g. saturated clay-rich overburden). A combination of low resistivity and high shear-wave velocity would be indicative of saturated and more rigid material, possibly fractured bedrock below the water table. A combination of high resistivity and low shear-wave velocity is consistent with dry materials and high porosities, e.g. dry sands. A combination of very high resistivity and very low shear-wave velocity would indicate a void and therefore a possible site for sinkhole collapse. A combination of high resistivities and high shear-wave velocities is consistent with dry bedrock (Table 2.5).

Table 2.1- Parker (2010) MASW Inversion Parameters

Inversion Parameters	
Poisson's Ratio	0.4
Density	2.0 g/cc
Layers	10
Maximum Iterations	12
RMSE (in phase velocity)	5 m/s

Table 2.2- Parker (2010) MASW Active-Source Seismic Lines

Active-source Seismic Lines			
	Distance spanned by recording stations (m)	Distance spanned by mid-point of 24-channel arrays (m)	Station numbers of mid-points
Line A	173	143	13-156
Line B	101	76	13-89
Line C	120	93	13-107
Line D	92	73	13-86
Line E	89	70	13-83
Line F	89	70	13-83
Line G	89	70	13-83
Line Y	240	215	13-228
Line Z	155	130	13-153

Table 2.3- Parker (2010) MASW Passive Source Seismic Lines

Passive-source Seismic Lines			
	Distance spanned by recording stations (m)	Distance spanned by mid-point of 24-channel arrays (m)	Station numbers of mid-points
Line A	173	122	25-147
Line B	101	52	25-77
Line C	120	72	25-97
Line D	92	46	25-71
Line E	89	46	25-71
Line F	89	46	25-71
Line G	89	46	25-71
Line Y	240	190	25-215
Line Z	155	94	25-119

Table 2.4 - Parker (2010) MASW Recording Parameters

Recording Parameters		
	Active	Passive
Seismic Source	Hammer	Van
Geophones	4.5 Hz	4.5 Hz
Sampling Rate	0.002 s	0.002 s
Number of Samples	500	5000
Record Length	1.0 s	10.0 s
Geophone Spacing	1.0 m	2.0 m
Source Spacing	1.0 m	Variable
High-cut Filter	250 Hz	250 Hz
Low-cut Filter	4 Hz	4 Hz

Table 2.5- Resistivity and Shear-Wave Velocity Combinations

Combination	Conclusions	Geology
Low Resistivity / Low Shear-Wave Velocity	Saturated, less rigid, more porous material	saturated, clay-rich overburden
Low Resistivity / High Shear-Wave Velocity	Saturated, more rigid material	fractured bedrock
High Resistivity / Low Shear-Wave Velocity	Dry material, high porosities	dry sands
High Resistivity / High Shear-Wave Velocity	Dry, more rigid material	dry, competent bedrock
Extreme Case: Very High Resistivity / Very Low Shear-Wave Velocity	Very dry, high porosities, less rigid material	cavities

TABLE 13–2 Resistivities of Earth Materials

EARTH MATERIAL	RESISTIVITY, AVERAGE OR RANGE (ohm-m)
Metals	*Average R*
Copper	1.7×10^{-8}
Gold	2.4×10^{-8}
Silver	1.6×10^{-8}
Graphite	10^{-3}
Iron	10^{-7}
Lead	2.2×10^{-7}
Nickel	7.8×10^{-8}
Tin	1.1×10^{-7}
Zinc	5.8×10^{-8}
Sulfide Ore Minerals	*Average R*
Chalcocite	10^{-4}
Chalcopyrite	4×10^{-3}
Pyrite	3×10^{-1}
Pyrrhotite	10^{4}
Molybdenite	10
Galena	2×10^{-3}
Sphalerite	10^{2}
Oxide Ore Minerals	*Range of R*
Bauxite	10^{2}–10^{4}
Chromite	1–10^{6}
Cuprite	10^{-3}–300
Hematite	10^{-3}–10^{7}
Magnetite	10^{-5}–10^{4}
Ilmenite	10^{-3}–10^{2}
Rutile	10–10^{3}
Silicate Minerals	*Range of R*
Quartz	10^{10}–10^{15}
Muscovite	10^{2}–10^{14}
Biotite	10^{2}–10^{6}
Hornblende	10^{2}–10^{6}
Feldspar	10^{2}–10^{4}
Olivine	10^{3}–10^{4}

EARTH MATERIAL	RESISTIVITY, AVERAGE OR RANGE (ohm-m)
Other Minerals	*Range of R*
Calcite	10^{12}–10^{13}
Anhydrite	10^{9}–10^{10}
Halite	10–10^{13}
Coal	10–10^{11}
Crystalline Rocks	*Range of R*
Granite	10^{2}–10^{6}
Diorite	10^{4}–10^{5}
Gabbro	10^{3}–10^{6}
Andesite	10^{2}–10^{4}
Basalt	10–10^{7}
Peridotite	10^{2}–10^{3}
Schist	10–10^{4}
Gneiss	10^{4}–10^{6}
Slate	10^{2}–10^{7}
Marble	10^{2}–10^{8}
Quartzite	10–10^{8}
Sedimentary Rocks	*Range of R*
Shale	10–10^{3}
Sandstone	1–10^{8}
Limestone	50–10^{7}
Dolomite	10^{2}–10^{4}
Unconsolidated Sediment	*Range of R*
Sand	1–10^{3}
Clay	1–10^{2}
Marl	1–10^{2}
Groundwater	*Range of R*
Portable well water	0.1–10^{3}
Brackish water	0.3–1
Seawater	0.2
Supersaline brine	0.05–0.2

Modified from W. M. Telford, L. P. Geldart, R. E. Sheriff, and D. A. Keys, *Applied Geophysics*, Cambridge, England, Cambridge University Press, pp. 451–455, 1976.

Figure 2.1 - Resistivities of Common Earth Materials (Robinson and Coruh, 1988).

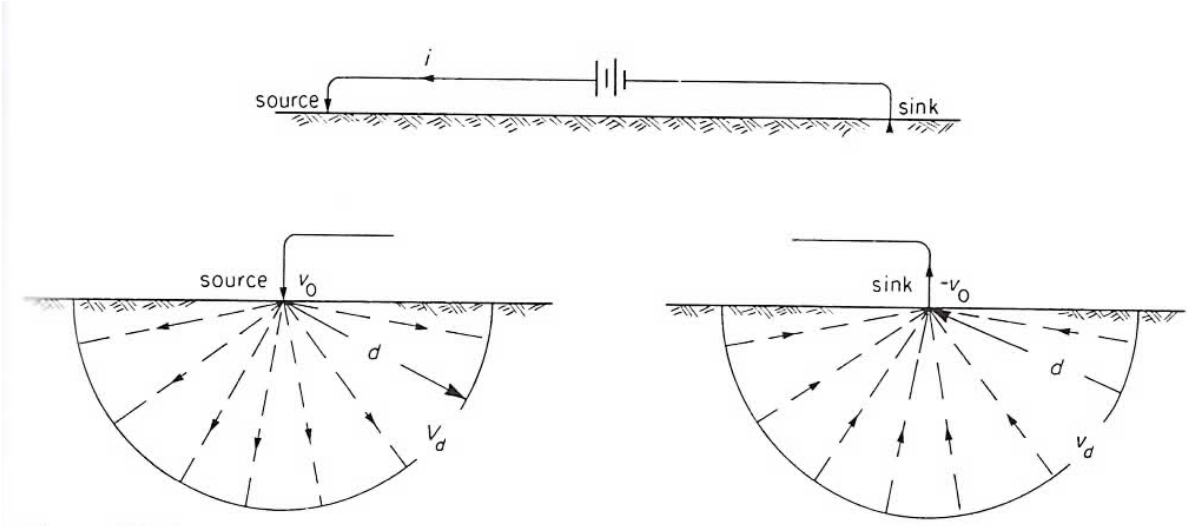

Figure 2.2 - Illustration of current flow paths out of the source and into the sink (Robinson and Coruh, 1988).

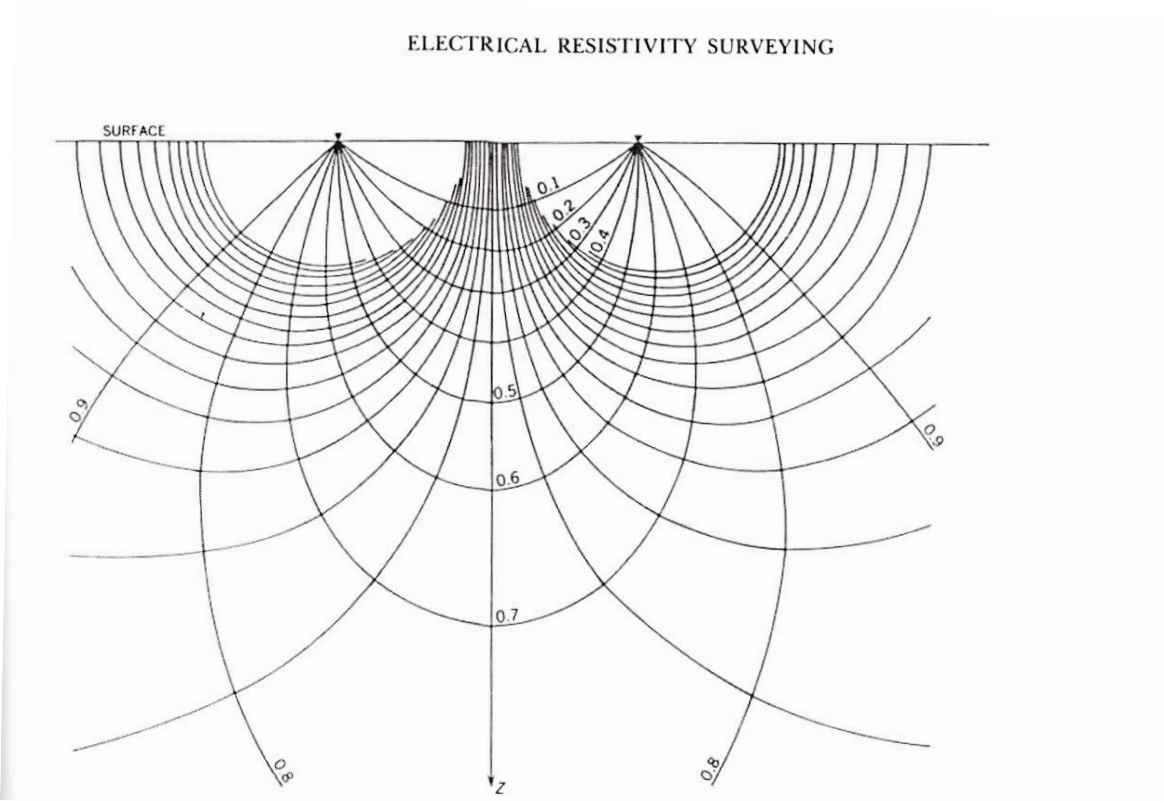

Figure 2.3 - Illustration of the current flow lines and the equipotential surfaces in the subsurface (Robinson and Coruh, 1988).

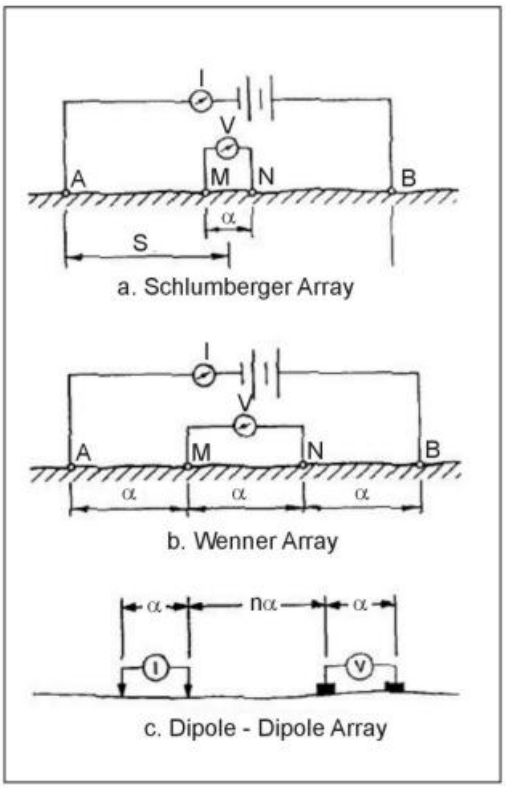

Figure 2.4 - Illustration of different array types and current and potential electrode placement (EPA, 2011).

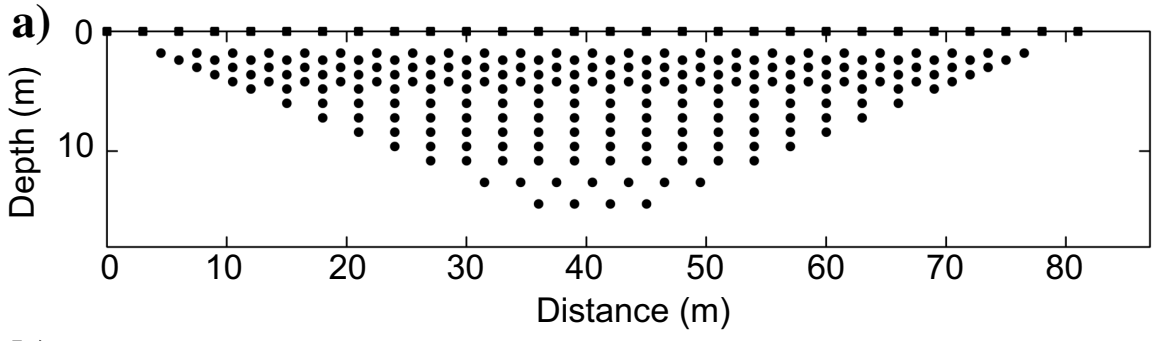

Figure 2.5 - An illustration of a dipole-dipole pseudosection showing the depths (modified from Nyquist *et al*., 2007).

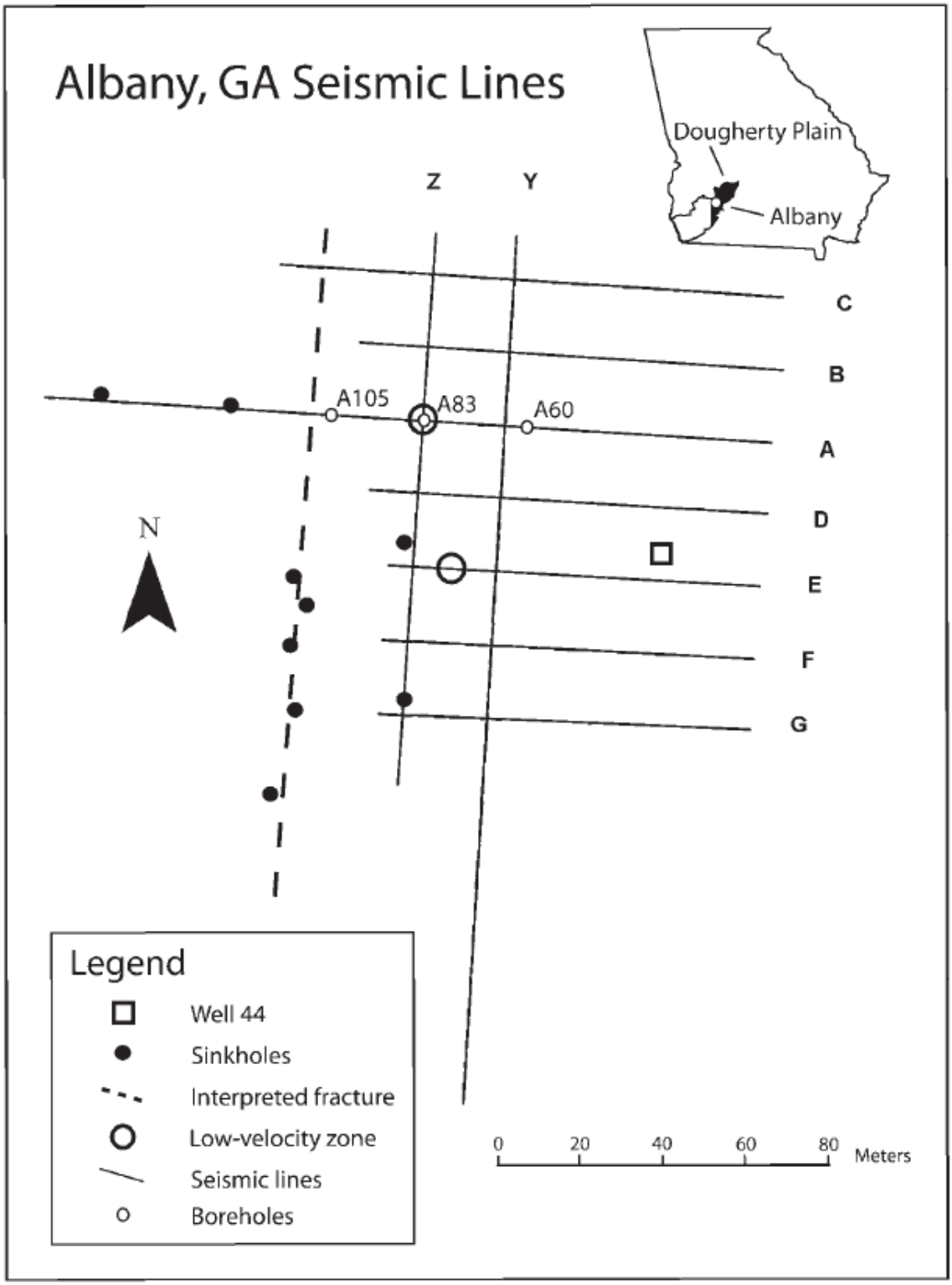

Figure 2.6 - MASW profile location map (Parker and Hawman, 2012).

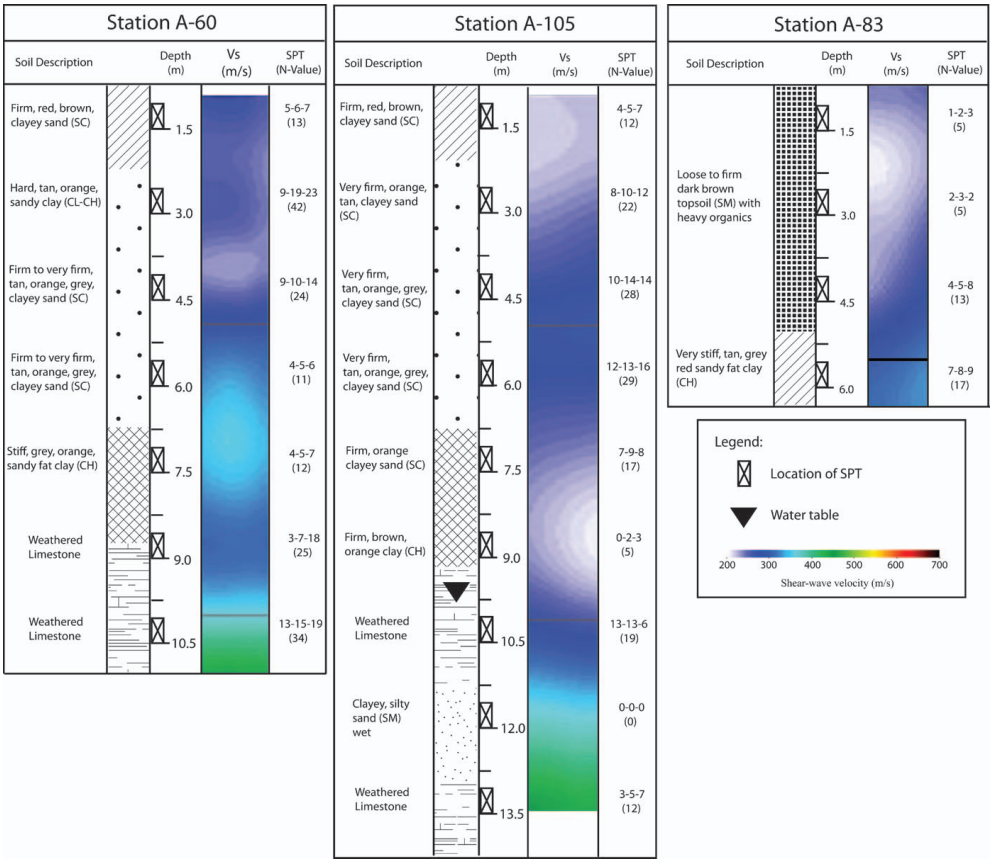

Figure 7. Borehole logs for Line A. Boreholes were drilled with a CME-45 track rig and 2-1/4 in. (inside diameter) hollow-stem auger. Standard penetration tests were performed at 1.5-m intervals, and soil samples were recovered and described for each test. In the SPT column, the blow count for each of the three 150-mm intervals of the test is shown; the N-value (total number of blows for the last two intervals) is shown below in parentheses. Extrapolation between boreholes at STA A60 (left) and A105 (middle) suggests that a more rigid, clayey-sand layer (N-values: 24–42) in the upper 2–6 m overlies a weaker clay layer (N-values: 11–17); the depth to bedrock is approximately 9 m. For STA A60, high N-values (25 and 34) for the limestone indicate more competent bedrock in this location. For STA A105, an in-filled dissolution feature (N-value: 0) was encountered below the bedrock surface, and lower N-values (12 and 19) for limestone indicate more extensive weathering of the bedrock in this location. Sections from the updated full-spread, hammer-source velocity models (Fig. 10) are shown for comparison with borehole logs to indicate the strong correlation between Vs and N-value at the soil-bedrock interface. The image of the clayey-sand layer in the uppermost 6 m is less distinct. For STA A83 (right), the high organic content in the upper 5 m is derived from a "burn pit" at the site. A 3-m wide section (STA 80–83) from the updated full-spread, hammer-source velocity model (Fig. 10) is shown for comparison with the borehole log. Note that the position and lateral extent of the LVZ associated with the burn pit is shown more accurately in the velocity model for the half-spread hammer data (Fig. 6(a), top).

Figure 2.7 - Borehole data and description of the units seen in the standard penetration tests by Parker and Hawman (2012).

CHAPTER 3

METHODOLOGY

Electrical Resistivity Survey

Electrical resistivity profiles were collected over the previous seismic lines (Parker, 2010), as described before, to directly compare results and determine if the results would be complimentary and help constrain the subsurface more accurately. Resistivity measurements were collected using an Advanced RM85 four-channel resistance meter, advanced model, made by Geoscan Research. This resistivity unit provided a digital readout of the resistance in ohms. Settings on the RM85 allowed for choosing of a pre-programmed array type along with editing specific settings like current, gain, and frequency so the highest possible signal-to-noise ratio could be achieved. Data for this thesis were collected using a dipole-dipole roll-along array with a current of 1mA, 35 Hz frequency, and a gain factor of 10x.

In a dipole-dipole array, the current electrodes (C2 and C1) are spaced at a constant distance apart and are held fixed while the potential electrodes (P1 and P2), also spaced a constant distance apart, are gradually moved away from the current electrodes (Figure 3.1).

The equation for converting resistance to apparent resistivity is:

$$\rho_a = (\Delta V/i)\pi n(n+1)(n+2)a \qquad (2)$$

where ρ_a is the apparent resistivity, V/i is the resistance reading, "n" equals a geometric factor, and "a" is the electrode spacing. Figure 3.1 is a diagram of the geometry from the dipole-dipole survey showing the "n" and "*a"* values for each deployment of current and potential electrodes. With the "*a"* spacing fixed (5 m in this survey), the "n" factor was increased from 1 to 6 to

increase the depth of penetration. This "n" factor is multiplied by "*a*" to denote the distance between the current and potential electrodes. Increasing the "n" factor increases the depth of penetration of current flow (Figure 3.2). The "n" factor wasn't increased past six because the larger values of "n" start to have very small signal strength. "The voltage is inversely proportional to the cube of the 'n' factor" and by using the same current, the voltage drops by approximately 200 times when n is six compared to when n is one (Loke, 1999). A way to compensate for this problem is to make the *a* spacing larger. With a fixed *a* spacing of 5 m and a max "n" factor of six, meaning the spacing between current electrodes and potential electrodes was 30 m, the maximum depth of penetration was approximately 15 m (Loke, 1999). This is important to remember because the resistivity inversion models that were created show depths to 20 m, meaning the models are not well constrained below 15 m.

To extend the horizontal coverage of each profile, the roll-along technique was used which involves shifting the electrodes after a sequence of measurements to extend the line (Figure 3.1) (Wylie *et at.,* 2014). In this survey, after the "n" factor was increased to 6 (corresponding to a distance between current and potential electrodes of 30 m), the current electrodes were moved down the line by 5 m and the process was repeated until the end of the line was reached and distance between each current and potential electrode was 5 m and the distance from C1 to P1 was also 5 m (i.e., rolling the array off the line). C1 and P1 refer to the current and potential probes in the array. There were two current probes, C1 and C2, and two potential probes, P1 and P2, as seen in Figure 3.1.

Data Collection

The first step in data collection was to first secure the field area and to reoccupy the nine survey lines (A-G and Y, Z) established by Parker (2010). To do this, a GPS hand-held unit was used to find the endpoints of each line within +/- 5 m. As the endpoints were established, it was observed that the wooden stakes that were used as endpoints for the seismic lines were still in the ground, so these wooden stakes previously used were also used for this thesis. Once the endpoints were marked, a 50-m tape measure and rod and transit were used to ensure straight lines. Labeled flags with the location within the line were placed at each 5 m interval with flags starting at 0 m to the end of the line. Table 3.1 shows the lengths of each line.

Three separate trips to the field area in Albany, GA were required to collect all the data. Two trips were made in December, 2013 and one in January, 2014 to ensure that data wouldn't be collected during or right after a rainfall event so as to avoid standing water. If rain occurred, at least a day passed before data was collected again. This waiting period was enacted because it has been shown that rainwater infiltration can affect resistivity results. This was based on the work of Mojica *et al*. (2013), in which variations in rainwater infiltration during the dry, transitional, and rainy season were studied using ERT. When comparing the dry season data to data collected after the rainy season, resistivity values were decreased by 100% showing that rainfall and water infiltration can have an effect on the data.

Before starting each line, several things were noted such as the time, date, days after the last rainfall, the GPS coordinates for each endpoint of the line, and the current weather. At least two people were needed to made data collection efficient. One person was in control of the RM85 resistivity unit recording data and the other person was in charge of moving the current

and potential electrodes to the corresponding positions in the dipole-dipole array as outlined in the previous section. The readout on the resistivity meter was a number on the screen, constantly updating so the values were always changing within a certain range. The goal here was to let the numbers stabilize so the most reproducible numbers were displayed, which only took approximately five seconds, and then the high and low values out of the series of numbers was recorded. The scatter in numbers is attributed to noise in the area such as the well or any electrical lines or electrical generators in the area. Most of the data showed little scatter except for line D and E which were on each side of the production well which had an electrical generator next to it. Figure 3.3 shows an example of 5-m common-offset data with error bars showing high and low values of resistance that were collected from Line A. Appendix A contains all offset plots from all nine profiles.

Although MASW, borehole, and elevation data was previously collected by Parker (2010), data that were not previously collected was mineralogical sampling in the area. Resistivity readings are controlled in part by mineralogy of the overburden; resistivities generally decrease with increasing clay content. One of the most important factors controlling resistivity is porosity and the nature of the pore fluids. Air-filled pores substantially increase resistivity; water filled pores substantially decrease it (Fallah-Safari et al., 2013). Because resistivity data are most sensitive to structure near the surface, mineralogy can strongly influence the potential measured by the array (Loke, 1999). To evaluate this effect, soil samples were taken from three of the 5 sinkholes mapped along the bedrock fracture interpreted by Parker and Hawman (2012; Figure 2.6). Figure 3.4 shows photographs of a sinkhole from which data was taken. The samples were

each bagged and labeled separately and then taken for further analysis. Data and results from the mineralogical analysis are summarized in Appendix B.

Modeling Program

Each series of resistance measurements taken for a given position along the profiles was converted to a mean value with the maximum and minimum values being treated as plus and minus two standard deviations from the mean value. The resistance data were inverted for 2D resistivity models of the subsurface using the program "R2" (Binley, 2013). R2 uses the damped-least squares method. The models were parameterized by a large number of cells. All of the lines were constructed using a 87x10 two-dimensional array of cells, except for Line Y, which used a 117x10 array. Each cell in the model was 2x2 m. The initial models were created with a homogenous subsurface with every cell initially having 100 ohm-m resistivity. The resistivity in each cell then was adjusted iteratively to optimize the fit to the data. Electrical potentials were computed over a finer mesh of nodes, where the node spacing was 0.5 m. The model cells were embedded in a larger background mesh to avoid edge effects.

Inversion Theory

The goal of an inversion is to find a model that shows responses similar to what is observed with actual measured values (Loke, 2001). This model is an "idealized mathematical representation" of the subsurface and has a set of parameters that are physical quantities estimated from observed data (Loke, 2001). The inverse problem can be thought of as the transformation of data directly into model parameters which is "inverse" to the forward problem which relates model parameters into data.

The forward problem used a finite difference technique to determine the electrical potential given a 2D model of the resistivity (Dey and Morrison, 1979). The finite difference model is created by creating artificial boundaries in the subsurface, in this case rectangular, as noted in the previous section, and assigning resistivity values for each cell (Dey and Morrison, 1979). These rectangular elements, each having four points one at each corner, can be written symbolically as:

$$\mathbf{C\phi = S} \tag{3}$$

where C is an MNxMN matrix called the capacitance matrix and "is a function of the geometry and the physical property distribution, i.e., conductivities, in the grid" (Dey and Morrison, 1979). ϕ is what is being solved for in the model and is a "vector corresponding to the electrical potential at all of the nodes" (Dey and Morrison, 1979). S is a vector that contains two non-zero elements, one positive and one negative, that is determined by the location of the current probes (Dey and Morrison, 1979). After the electrical potentials have been determined for each rectangular element, the apparent resistivities are calculated and compared to the field measurements.

The inverse problem is linearized and solved iteratively so that the difference between the model response and observed data is reduced as much as possible or within a set limit (Loke, 2001). Stein and Wysession (2003) describe a generalized inversion equation to measure how well an inverted model fits the data and reduces the misfit between the observed and predicted data. This measure of misfit is defined as:

$$\mathbf{x^2 = \sum_i (1/\sigma_i^2)(\Delta d_i - \Delta d_i^m)^2} \tag{4}$$

where d_i is observed data, d_i^m is data predicted by the model, and σ_i is the uncertainty of each datum d_i.

Table 3.1 - Lengths of each profile

Line	Line Lengths
Line A	170 m
Line B	100 m
Line C	120 m
Line D	90 m
Line E	85 m
Line F	90 m
Line G	90 m
Line Y	225 m
Line Z	155 m

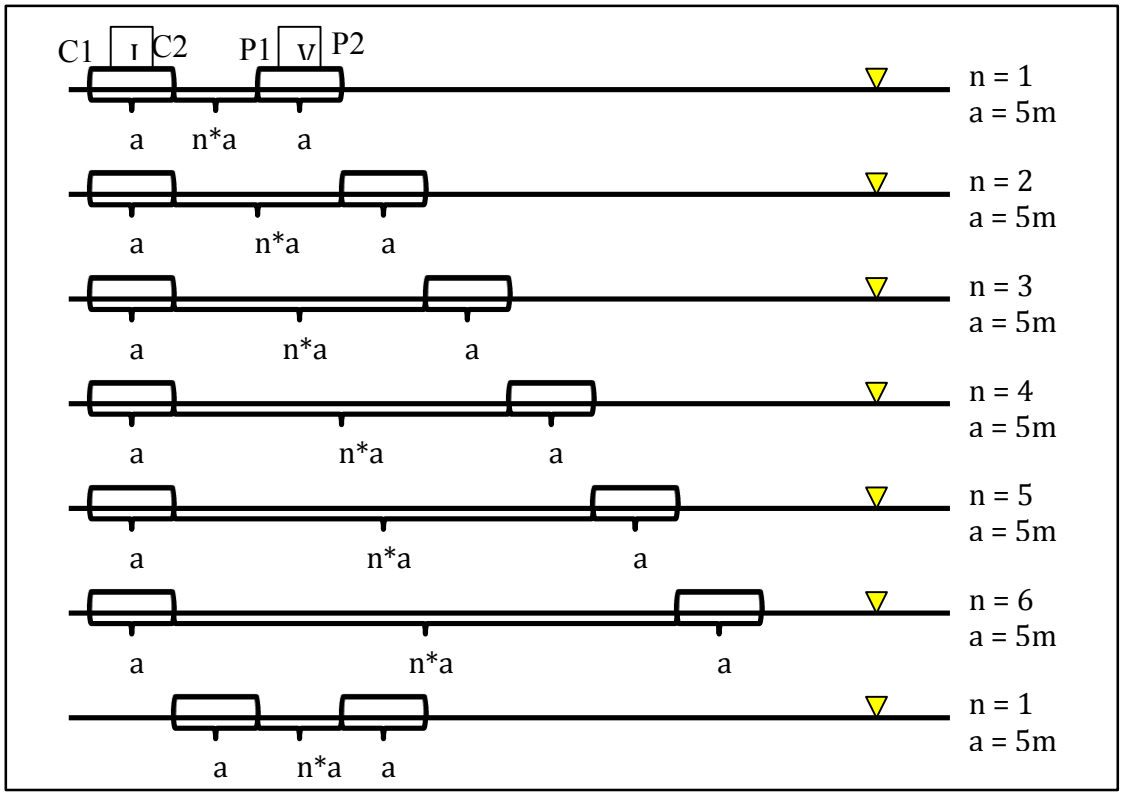

Figure 3.1 - Geometry of a dipole-dipole, “roll-along” profile (Wylie *et al.,* 2014). C1 and C2 are the two current electrodes and P1 and P2 are the two potential electrodes.

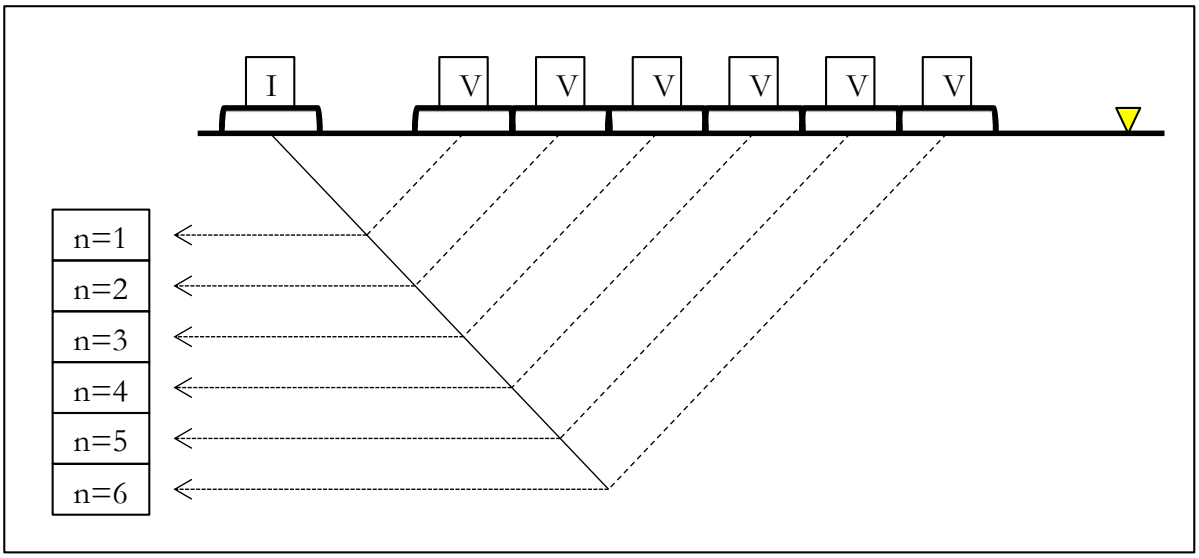

Figure 3.2 - “N” measurements along the profile and their corresponding approximate depths (Wylie *et al.,* 2014).

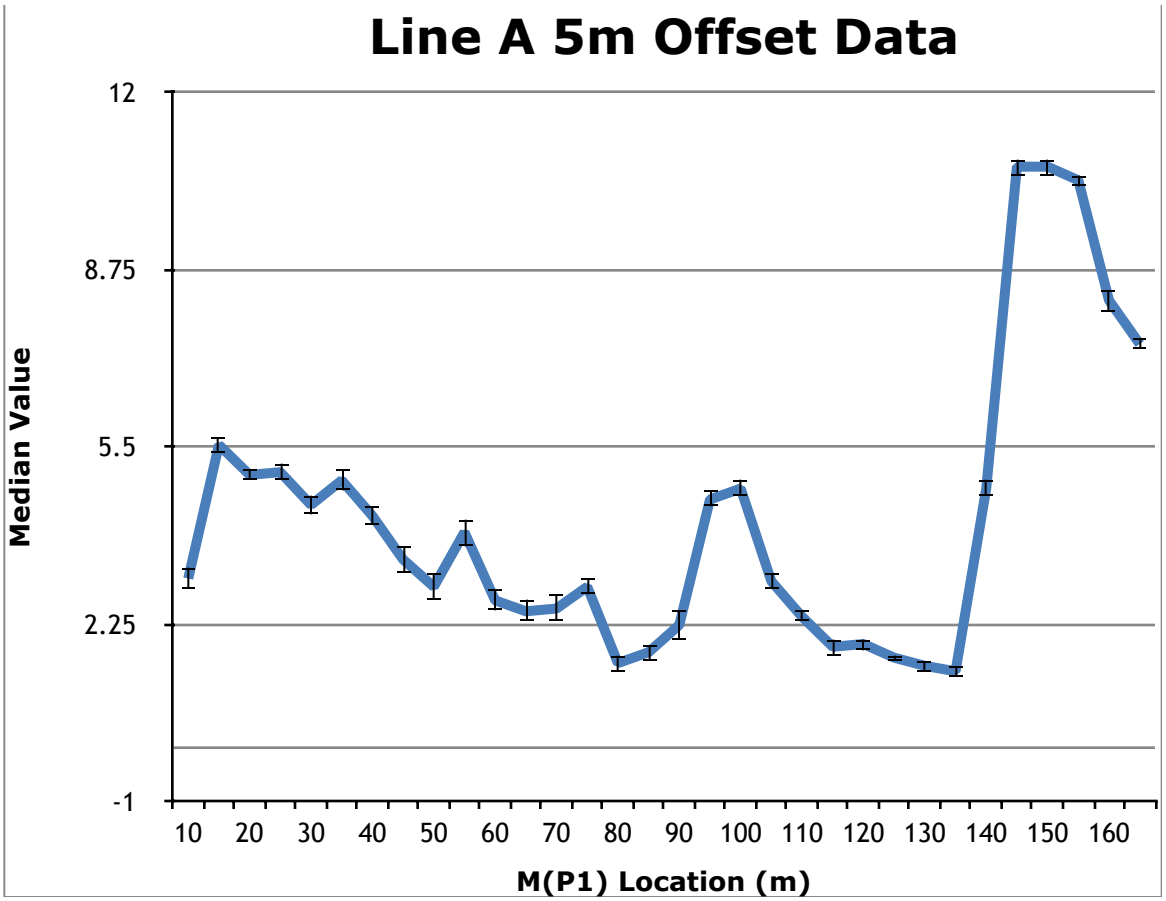

Figure 3.3 - Line A 5m offset plot with +/- 2σ scatter error bars. The vertical axis is the median values in ohms (multiplied by 10, the instrument gain setting).

A)

B)

Figure 3.4 - A) Side of a sinkhole B) Standing inside of the sinkhole ready to take samples.

This sinkhole is located along the interpreted fracture in Figure 2.6.

CHAPTER 4

RESULTS

Initial Inversion Tests

The electrical resistance data for each line were inverted for 2D models of resistivity structure. The models incorporate variations in elevation. Trial inversions with chi-squared (x^2) values of 1.0, 0.75, 0.50, 0.33, and 0.25 were generated for each line. Examples showing the differences in the log resistivity values for Lines A, Y, and Z are shown in Appendix D. The main objective of these tests was to determine the optimum value of x^2 to use for the inversions. Choosing a value too large results in a poor fit to the data and choosing a value too small results in overfitting the data, meaning some of the model details can't be resolved by the data. Very small values of x^2 can also result in model instability, e.g., extremely high values for bedrock resistivities that grow in magnitude as x^2 becomes smaller and smaller. These unstable values occur in the deeper parts of the model, where current penetration is insufficient to constrain resistivities. The goal was to find the largest value of x^2 that could resolve geologic structures. Decreasing x^2 from 1.0 to 0.5 brought the lateral continuity of structures, e.g. the bedrock surface, into better focus without generating instability. Table 4.1 shows the final iterations for each line, the x^2 value, and the average apparent resistivity (input data) for each line.

General Comments Regarding Plots

Figures 4.1-4.9 show the results of the inverse modeling for Lines A-G ,Y, and Z for x^2 =0.5. Each figure contains a 2D model of resistivity, log resistivity, and a sensitivity matrix. The

resistivity and log resistivity profiles are shown with contours and a blue-to-red color scale with blue representing lower resistivities and red representing higher resistivities. A scale bar is also included in each plot to indicate the resistivity values seen in each profile. Each profile is scaled separately to bring out as much detail as possible. Each model is plotted using 8 contours spaced evenly between the maximum and minimum resistivity values. The contours are used to show zones and variations in the subsurface more clearly throughout the profiles. Plots of log resistivity suppress the damping effects of extremely high and low resistivity. The sensitivity matrix shows the overall sensitivity of the data to different parts of the model. Portions of the model with low sensitivity are not well constrained by the data and are therefore not well resolved.

Resolution is best near the surface and decreases with depth and towards the edges of the model, where sampling by current flow lines become more sparse. This loss of sensitivity results in artifacts that are most pronounced in wedge-shaped regions at the ends of the models. In Figures 4.1-4.9 these regions are retained. In later figures, they are muted out. The following sections discuss the results for each line.

Comparisons of resistivity models and shear-wave velocity models are shown in Figures 4.10-4.18. The van-source velocity models provide a smoothed, more generalized image of the bedrock surface than the hammer-source velocity models. Therefore the van-source models were used to compare bedrock depth with the resistivity models. In the plots on the right, circles are used to highlight similar anomalies (high resistivity/high velocity or low resistivity/low velocity). Rectangles are used to highlight anomaly pairs of the opposite sense (high resistivity/low

velocity or low resistivity/high velocity). Black arrows indicate approximate depth to bedrock. Red arrows indicate sinkhole locations noted in the field by Parker and Hawman (2012).

Criteria for Identifying Bedrock

Resistivity values in the models range from 6-450 ohm-m. All profiles show a marked increase in resistivity at approximately 10m depth. This is interpreted as the transition from the sandy-clay overburden to limestone bedrock of the Ocala Formation. The range in resistivity for the top of the bedrock was based on the steepness of the resistivity gradient. This transition was constrained further using the known bedrock depth along Line A (9 meters based on borehole logs), and also the 350 m/s velocity contour in the van seismic profiles. Table 4.2 shows ranges of resistivity for the overburden, top of bedrock, and below the bedrock surface. On average, the bedrock surface, seen at approximately 10m depth, shows a resistivity range of 80-120 ohm-m with Line A being an outlier with resistivities of 156-250 ohm-m (Table 4.2). The bedrock depths seen in the resistivity and shear-wave velocity models differ from the borehole depths because the resistivity models and shear-wave velocity model values represent lateral and vertical averages associated with the sampling of current flow lines and the surface waves, while borehole depth gives an "exact" depth to bedrock at one particular location. The increases in resistivity are in close agreement with a steep velocity gradient marking the increase in shear-wave velocity to 350 m/s observed in the van-source seismic profiles and the bedrock depth observed for a nearby borehole. On average, the resistivity of the clay-rich overburden ranges from 6-100 ohm-m and the limestone bedrock and air-filled zones range from 100-352 ohm-m. These values are consistent with those found in previous studies (Telford *et al.,* 1990; Robinson and Coruh, 1988; Park *et al.*, 2009)

Discussion of Results

Line A

Line A (Figure 4.10) was 170 m long and crossed the line of sinkholes, noted in Parker and Hawman (2012), in the area west of 105 m. Figure 4.10 shows the results of the inversion. Bedrock depth is seen at 11m depth on the resistivity profile and van profile. Resistivities marking the top of the bedrock are 156-250 ohm-m. Along the resistivity profile there is a zone of low resistivity at approximately 78-86 m along the line from 0-4 m depth. This zone of low resistivity is matched by a low shear-wave velocity zone from 76-88 m from 0-4 m depth seen on the full-spread and half-spread hammer-source profiles. This anomaly correlates with the location of a mapped burn pit and is described in more detail below. On the resistivity profile, there is a zone of high resistivity from 136-168 m along the line at 0-7 m depth indicating dry material. Along that same area in the full-spread hammer-source data there is a slight increase in shear-wave velocity from 145-155 m where the profile ends, indicating a less porous material. Resistivities along Line A are higher than the rest of the lines. The differences in resistivity values across each line can be attributed to the competency of the bedrock in that given area. The less fractured and broken the bedrock is, the higher the resistivity.

In the vicinity of the burn pit noted above, Line A shows a zone of increased resistivity centered about 85m at depths of 6-11 m, overlain by a zone of decreased resistivity over depths of 0-5m. This roughly correlates with a low-velocity zone in the shear-wave velocity model (Figure 4.10). These results are consistent with a shallow zone of damp clay-rich soil overlying drier, highly porous organic material of the burn pit.

In Parker and Hawman (2012), the borehole logs and standard penetration tests at several positions along Line A indicated a more rigid clayey-sand layer from 2-5 m depth that overlies a weaker clay layer. This correlates with a higher-velocity layer overlying a low-velocity layer. In the resistivity inversions, there was occasionally a higher resistivity layer overlying a lower resistivity layer. This would correspond to the standard penetration tests and the shear-wave velocities indicating a stiff layer that is highly porous and dry overlying a more saturated, weaker clay layer.

Line B

On Line B (Figure 4.11), the interpreted depth to bedrock on the resistivity profile is 13 m while the van seismic data shows bedrock at 8m depth. There is a slight shallowing of the bedrock from east to west on the resistivity profile. There is a zone of low resistivity at 35-40 m at 0-2 m depth and on the half-spread hammer-source profile there is a zone of low shear-wave velocity from 35-40 m in the same depth range. Overall there is a relatively higher resistivity and shear-wave velocity in the upper 2-3 m over a zone of lower resistivity and shear-wave velocity from 3-8 m depth. This is seen across the whole line.

Line C

Line C (Figure 4.12) was 120 m long and also crosses the interpreted fracture seen in Parker and Hawman (2012). The seismic van-source data indicates a 9m depth to bedrock. The steep gradient in resistivity values marking the bedrock surface at 9 m depth lies between 73.4 and 84.4 ohm-m. A low-resistivity zone at 35-55 m at a depth of 2-11 m correlates with a low shear-wave velocity zone from 35-45 at 8-12 m depth. There also appears to be a bedrock ridge at 60 m along the line at 7 m depth on both the resistivity and velocity models. In the resistivity

model, there is a zone of very high resistivity from 90-116 m at 0-13 m depth that correlates with a zone of elevated shear-wave velocities. On the resistivity profile there is also high resistivity zone from 70-72 m along the line in the top meter, in contrast with the velocity model that shows lower shear-wave velocities.

A zone of high resistivity occurs at a distance 90-110 m and a depth of 3-8m, above the bedrock interface. Over the same zone, the seismic profiles show an area of relatively low shear-wave velocity (Figure 1.2). These results are consistent with a zone of high porosity but low fluid content.

Line D

Bedrock depth is seen at 9 m on the van-source seismic profile (Figure 4.13), in agreement with well data. In the full-spread hammer-source seismic profile, there is a zone of very low shear-wave velocity at 22 m, and on the half-spread hammer-source profile this low-shear-wave zone is at 15-25 m along the line at 2 m depth. This line was 3 m north of an electrical generator which added a significant amount of noise to the resistance data. In the resistivity model, there is a low-resistivity zone from 18-30 m from 0-3 m depth. The resistivity model for this line also shows very strong effects of the well platform that was located 3m south of the line and 25-35 m along the line. To minimize the effects of the platform, inversions were run again, first with obviously bad data points removed (Figure 4.19) and then with just the smallest-offset (5 m) readings (Figure 4.21). The new model (Figure 4.19) indicates that depth to bedrock beneath the western part of the profile is 12 meters marked by a resistivity range from 74.5-95.6 ohm-m. The 12 m depth could be inaccurate because the model still shows effects of the well platform.

Line E

Bedrock depth seen on the van-source velocity model is 9 m (Figure 4.14). Like Line D, this line was next to an electrical generator that produced a lot of noise. Moving away from the generator toward the west end of the line, the bedrock appears flat. There is a low-resistivity zone at 28-36 m from 0-4 m depth. In the model derived from the full-spread hammer-source data, this anomaly is a zone of high shear-wave velocity at 28-36 m at 0-5 m depth. There is also a low-resistivity zone from 65-74 m along the line at 4 m depth. This anomaly is seen on the half-spread hammer-source shear-wave velocity model as a zone of low shear-wave velocity at 65-75 m from 0-3 m depth. Line E also shows effects from the well platform that was located 7m north of the line and 25-35 m along the line. Again, the inversions were repeated with bad data points removed (Figure 4.20) and with only 5 m offset data (Figure 4.22). The alternative model shown in Figure 4.20 suggests a bedrock depth of 11 m marked by a resistivity range of 80.6-106 ohm-m beneath the western half of the profile.

Line F

Bedrock depth is seen at 10 m and shallows to 7 m depth going from east to west across the shear-wave velocity and resistivity models (Figure 4.15) The steep gradient in resistivity values marking the top of bedrock lies between 85.6-112 ohm-m. Seen throughout the resistivity profile is a band of higher values over lower values, the higher values occurring in the top 2 m. In the shear-wave velocity models, there is a similar trend of higher shear-wave velocities over lower shear-wave velocities. These higher velocities are in the top 3m of the profile. This high-over-low pattern is interpreted as drier material with higher porosity overlying the 3 m wet clay-rich layer noted by Parker and Hawman (2012). From 35-65 m there is a high-resistivity zone

from 8-15 m depth which correlates with a high-velocity zone in the full-spread seismic data from 45-78 m at 8-15 m depth (not circled). Throughout this profile there seems to be a sense of shift 5 m west when comparing the seismic to the resistivity profile.

Line G

Bedrock depth is seen at 11 m and shallows to 9 m from east to west. The steep gradient in resistivity values marking the bedrock surface covers a range between 93.3-112 ohm-m (Figure 4.16). At 20 m there is a low-resistivity zone from 0-2 m depth which overlies a zone of higher resistivity. This correlates with a high shear-wave velocity zone overlying a low-velocity zone at 25 m along the line on the half-spread hammer-source shear-wave velocity model. In the full-spread hammer-source shear-wave velocity model there is an overall trend of higher velocities from 0-4 m depth overlying lower velocities from 4-7 m depth.

Line Y

Bedrock depth marked by a steep gradient in resistivity values between 96.1 and 114 ohm-m is seen at roughly 10 m depth across the line and shallows to 7 m in the south (Figure 4.17). Resistivity along the profile increases towards the south as elevation increases and the higher resistive bedrock becomes shallower and follows the topography. This increase in resistivity towards the south is probably a result of drier overburden because of water movement downhill. In the upper 2m there is a zone of higher resistivity from 25-50 m. In the half-spread hammer-source seismic model there is a higher shear-wave velocity zone from 20-50 m in that same depth range. There is also an increase in shear-wave velocity seen in the van-source model from 140-190 m along the line from 0-3 m depth. There is a zone of higher resistivity interpreted as a bedrock ridge from 70-120 m at 11-15 m depth and this correlates with a zone of high shear-

wave velocity seen in the full-spread hammer-source data from 70-100 m at 8-15 m depth. Overall, in the resistivity model, the bedrock surface follows the topography as the elevation increases to the south.

Line Z

Bedrock depth is at 6 m depth from 0-75 m along the line and 10 m depth from 110-155 m along the line. The steep gradient in resistivity values marking the top of bedrock lies between 104 and 122 ohm-m (Figure 4.18). There are two bedrock ridges in the van-source model that center at 60 m and 117 m and these locations correlate to ridges seen in the resistivity model at those locations. Along the line from 0-35 m at 0-3 m depth there is a zone of high resistivity which correlates with a zone of higher shear-wave velocities seen in the full-spread hammer-source shear-wave velocity model. From 58-62 m this zone of low resistivity and shear-wave velocity (full-spread and half-spread hammer-source) directly corresponds to the location of a mapped burn pit. There is a zone of high-over-low resistivity from 80-140 m from 0-6 m depth that correlates to a high-over-low velocity zone in the same area (not circled). Over the whole profile, except for the area of the burn pit, a thin layer (3 m) of high resistivity at the surface overlies a zone of lower resistivity. This high-over-low pattern is also seen as a high shear-wave velocity layer over a low shear-wave velocity layer in the shear-wave velocity models, indicating the clay-rich layer is present along this profile. At 140 m there is a low-resistivity anomaly at 2-6 m depth and this is seen in the velocity models as a very low shear-wave velocity at the same depth.

Similar zones of high resistivity occur from 80-120 m and 130-140 m at 0-3 m depth (Figure 4.18). The resistivity model shows two areas of higher resistivity at the surface, centered

at 100 m and 135 m, that also seen as low velocity zones on the full-spread hammer-source shear-wave velocity models. These two separate zones are interpreted as potential sinkholes because the combination of low velocity with high resistivity indicates pore-spaces filled with air, suggesting that at some point support could be lost and the overburden would collapse. Bedrock depth from 0-80 m along the line is shallower in Line Z (6-7 m) than in Line Y (15-20 m).

High Resistivity Anomaly on Line D and Line E

As noted above, Line D (Figure 4.13) and Line E (Figure 4.14) both show a very high resistivity zone within the subsurface that is interpreted as an effect from the platform where the well and generator were housed. This generates a false high-resistivity zone in the subsurface because as the electrode spacings are increased, current flow lines avoid the high-resistivity material of the platform, resulting in a higher density of current flow lines in the adjacent soil that increases the measured potential difference (and therefore the apparent resistivity). The high resistivity zone on both Line D and Line E was from 15-50 m, at a depth of 4-20 m. This was expected as resistance values collected in the field near the well were either negative or clearly different from other values along the profile. To remove or at least minimize the effect of the platform, the inversions were re-run after removing bad data such as negative readings. The results are shown in Figures 4.19-4.20. For Line D, removing bad data improved the resolution of the bedrock surface from 45-80 m along the line and the high resistivity anomaly was decreased in size slightly. For Line E, resolution of the bedrock surface is also better from 45-80 m and the high resistivity anomaly was also decreased in size.

Next, to determine whether the platform affected all the field data or was restricted to recordings at larger distances, an inversion was run that included data from only the 5-m offset (Figure 4.21-4.22). The results for both Line D and Line E show no effect from the well platform. Line D shows zones of relatively higher resistivity (30-36 ohm-m) centered at 5, 50, and 75 m along the line and shows no real correlation to the half-spread hammer velocity model. Line E shows zones of relatively higher resistivity (31-39 ohm-m) centered at 8 m and from 35-60 m along the line. Again, no real correlation exists with the half-spread hammer velocity model because the resistivity models can not track changes in resistivities with depth because of the use of only one offset.

Composite Profiles of Resistivity Models

In Figure 4.23 and Figure 4.24, the seven east-west models are aligned to evaluate any trends across the entire field area. Figure 4.23 and Figure 4.24 show composite profiles in resistivity and log resistivity values for Lines A-G. These composite profiles show a bedrock ridge at approximately 55-60 m along each line except for updated models for Line D and E where the effect of the well platform is not completely removed. Figure 4.25 shows composite profiles in resistivity and log resistivity values for Line Y and Line Z. The resistivity in Line Y increases toward the south and the bedrock begins to follow the topography as the elevation increases. Resistivity values from Line Y to Line Z do not vary significantly like the shear-wave velocities do. In the shear-wave velocity models, Line Z shows lower shear-wave velocities at depths of 10-20 m than Line Y over the same depth range (Parker and Hawman, 2012).

Table 4.1 - Inversion Model Results

Line	Number of Iterations	RMS Value (RMS is the chi-squared measurement of misfit)	Avg. Apparent Resistivity (Avg. of input apparent resistivity values)
Line A	3	0.50	94.43
Line B	2	0.54	85.49
Line C	3	0.50	87.58
Line D	3	0.52	78.94
Line E	4	0.50	77.29
Line F	2	0.64	90.26
Line G	3	0.50	102.74
Line Y	3	0.50	83.53
Line z	3	0.77	79.47

Table 4.2 - Resistivities for overburden, bedrock, and transition zone

Line	Resistivity Range for Transition Zone (Ohm-m)	Resistivity Range of Overburden (Ohm-m)	Resistivity Range of Limestone Bedrock (Ohm-m)
A	156-250	7.38-155	251-401
B	89.7-103	23.4-89.6	104-129
C	73.4-84.4	16.7-73.2	84.4-107
D	74.5-95.6	11.2-74.4	95.6-159
E	80.6-106	5.67-80.5	107-180.5
F	85.6-112	19.7-85.5	113-125
G	93.3-112	20.4-93.2	113-166
Y	86-104	14.1-85	105-158
Z	96.1-114	7.13-96.0	115-149

A) **East** **West**

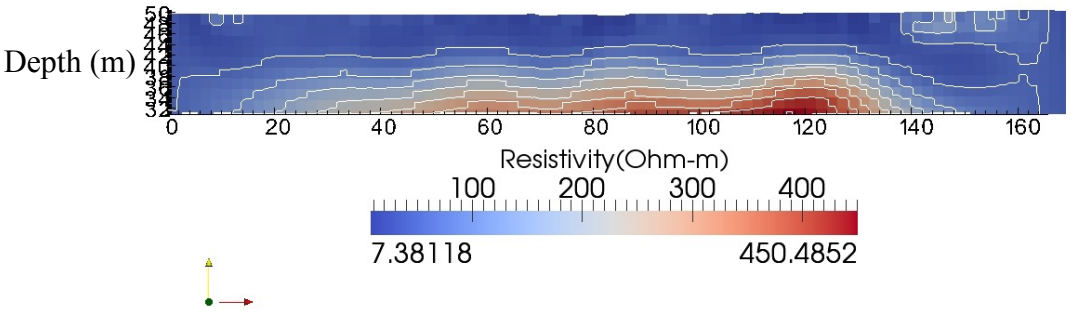

B)

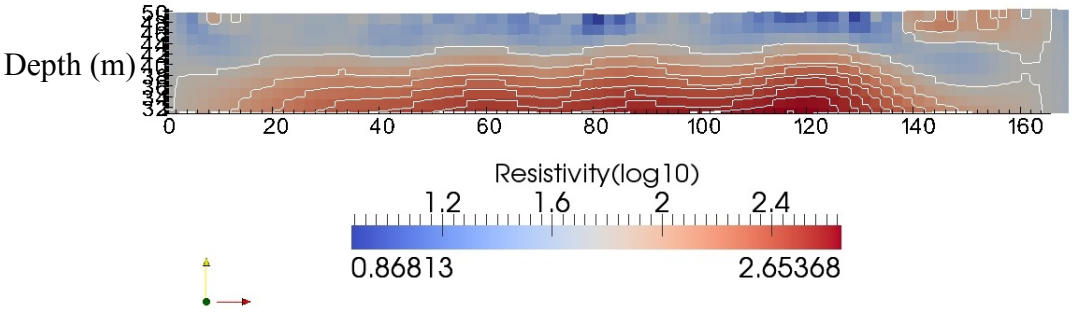

C)

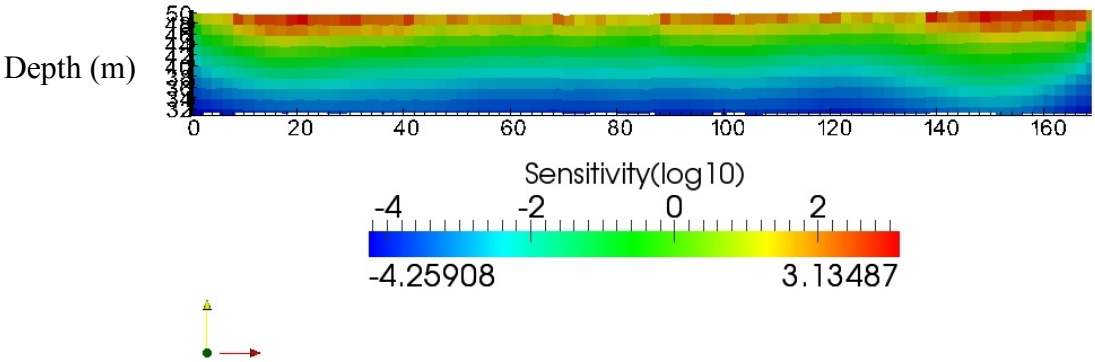

Figure 4.1 - Inversion results for Line A. A) Resistivity (ohm-m) B) Log Resistivity (ohm-m)

C) Sensitivity Matrix.

A) **East** **West**

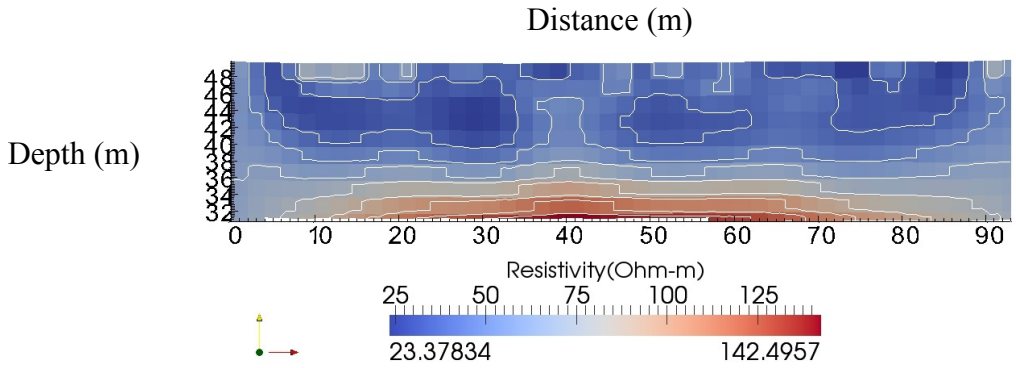

B)

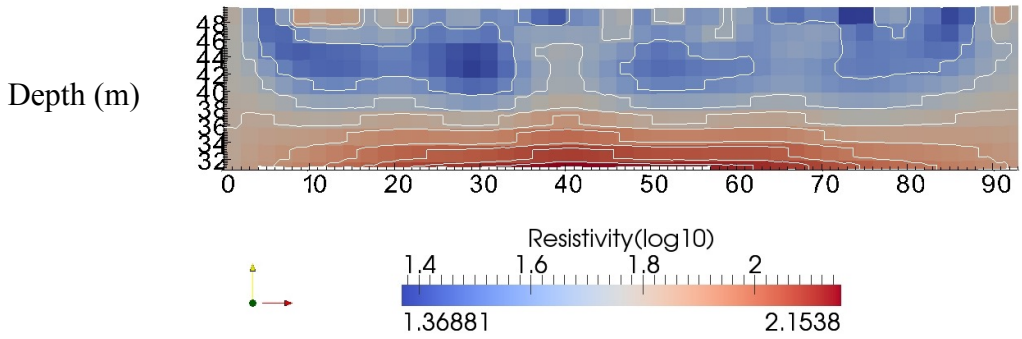

C)

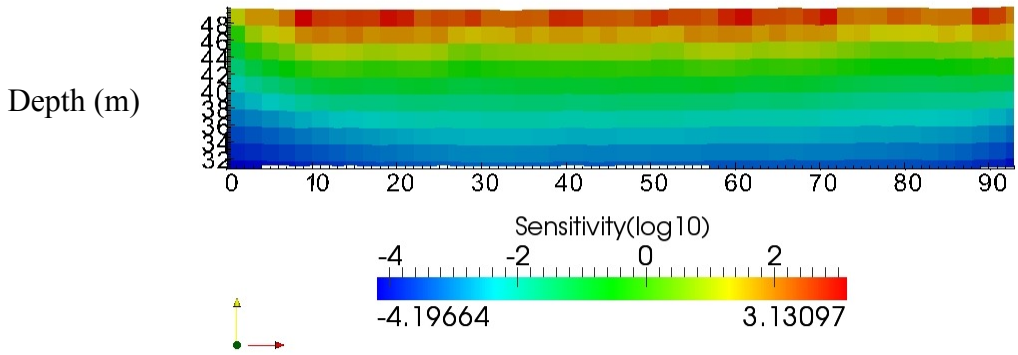

Figure 4.2 - Inversion results for Line B. A) Resistivity (ohm-m) B) Log Resistivity (ohm-m)

C) Sensitivity Matrix.

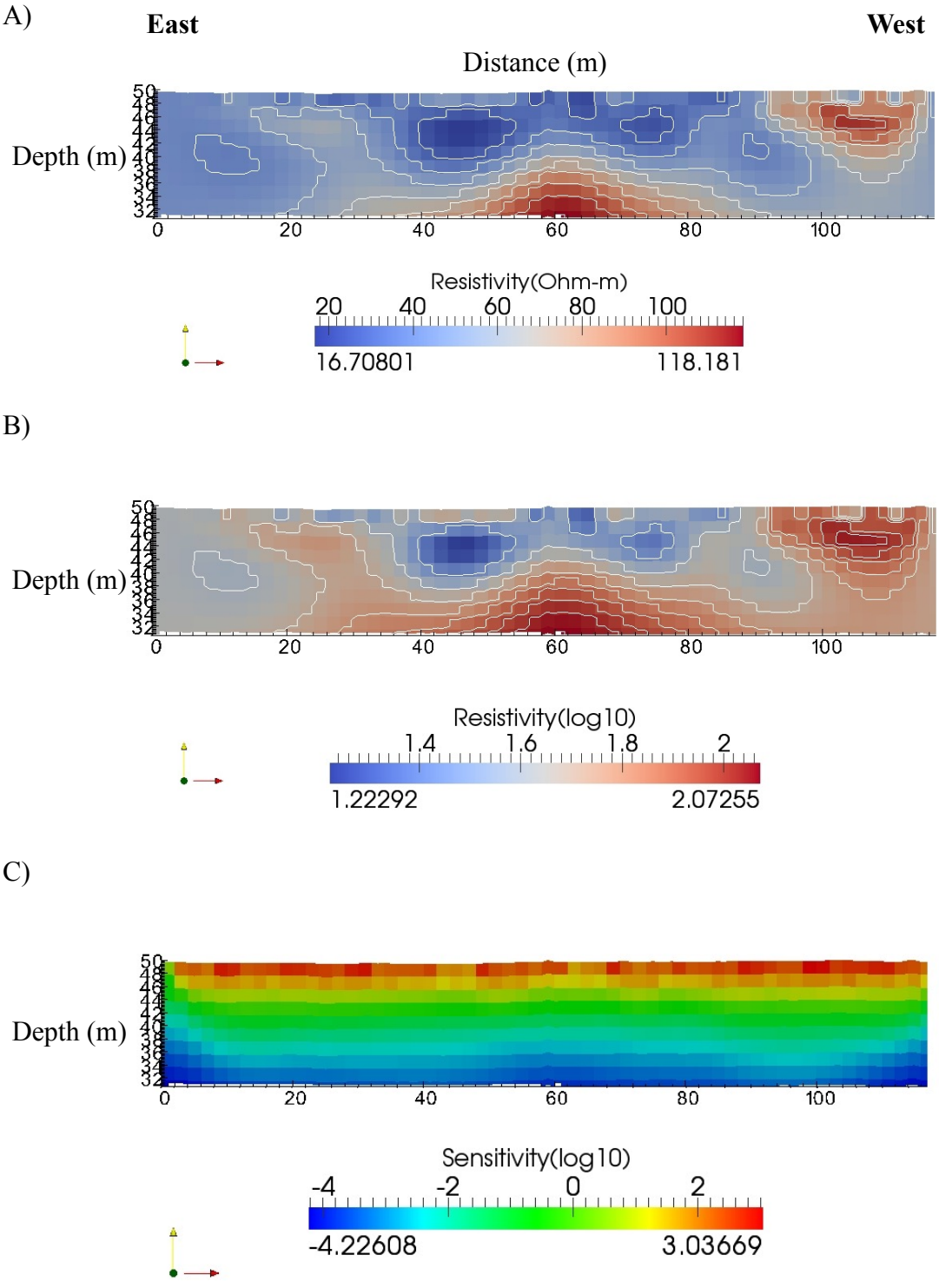

Figure 4.3 - Inversion results for Line C. A) Resistivity (ohm-m) B) Log Resistivity (ohm-m) C) Sensitivity Matrix.

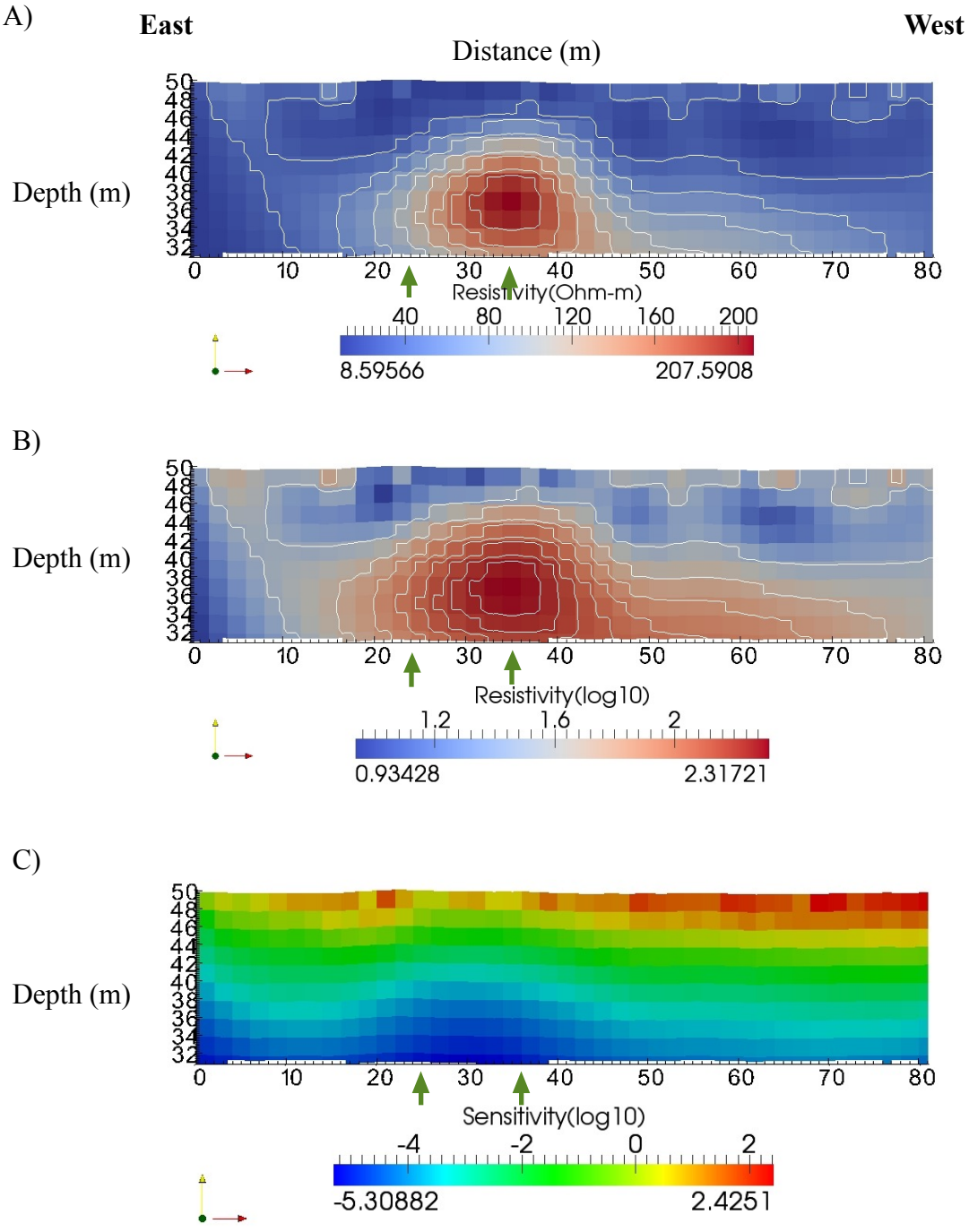

Figure 4.4 - Inversion results for Line D. A) Resistivity (ohm-m) B) Log Resistivity (ohm-m) C) Sensitivity Matrix. Green arrows indicate the edges of the well platform. The very high resistivity zone is the effect of the well platform.

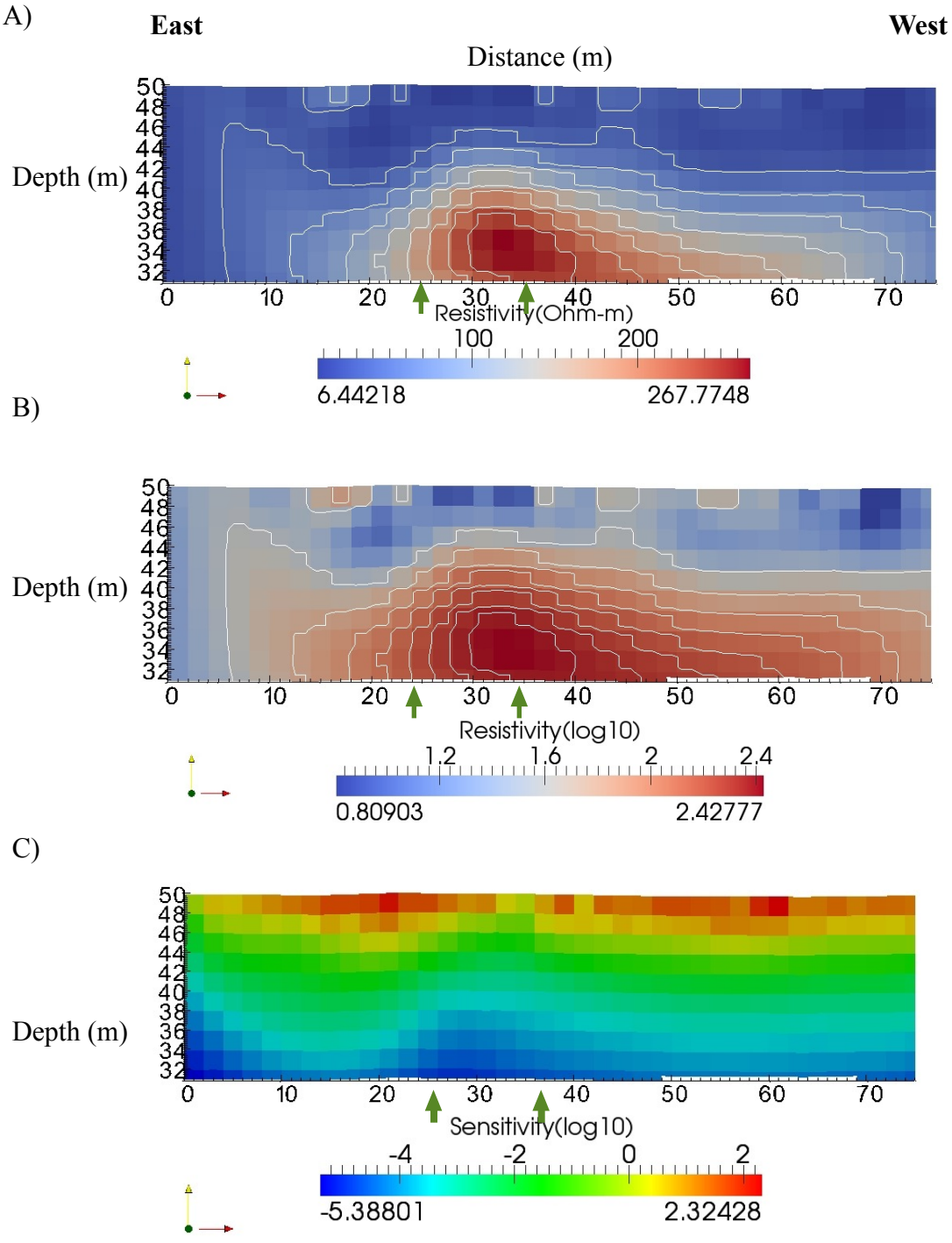

Figure 4.5 - Inversion results for Line E. A) Resistivity (ohm-m) B) Log Resistivity (ohm-m) C) Sensitivity Matrix. Green arrows indicate the edges of the well platform. The very high resistivity zone is the effect of the well platform.

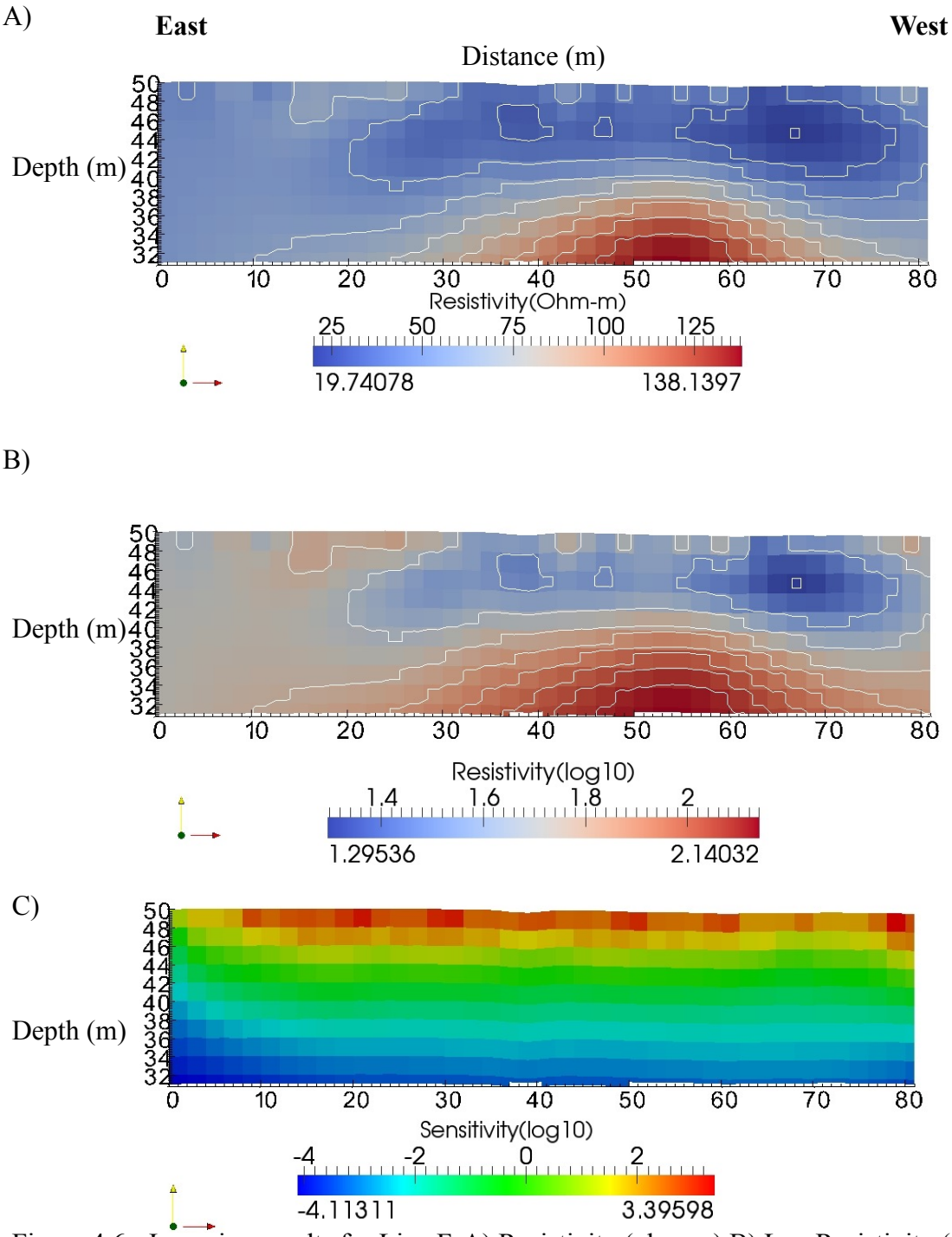

Figure 4.6 - Inversion results for Line F. A) Resistivity (ohm-m) B) Log Resistivity (ohm-m) C) Sensitivity Matrix.

A)

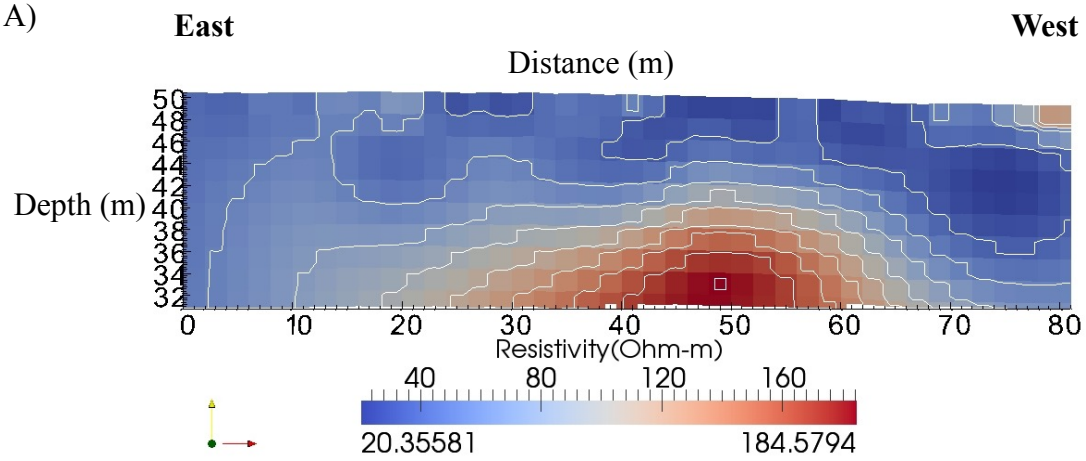

B)

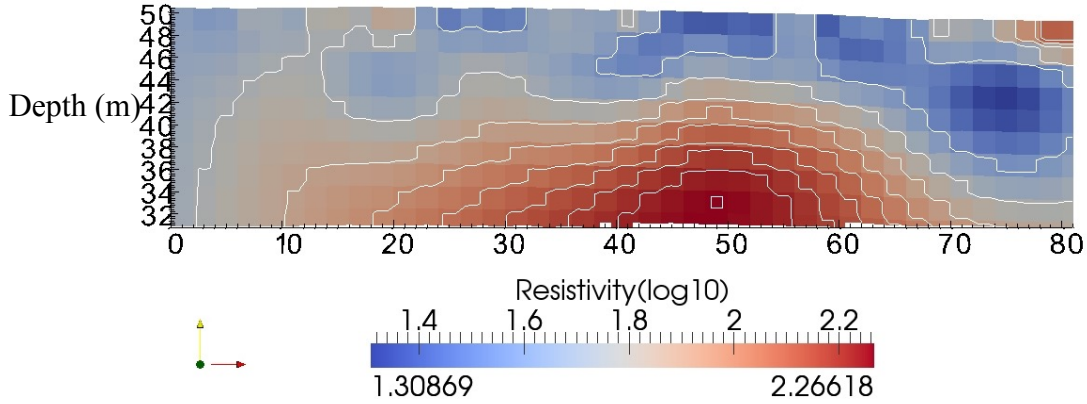

C)

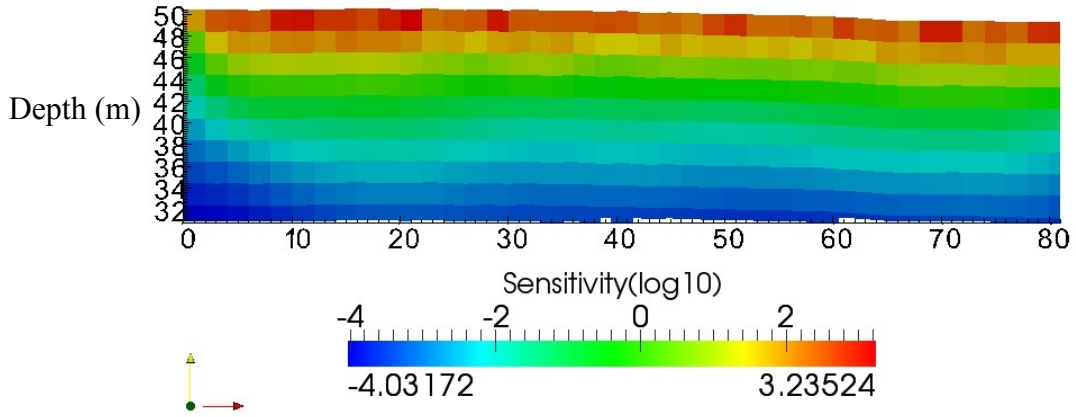

Figure 4.7 - Inversion results for Line G. A) Resistivity (ohm-m) B) Log Resistivity (ohm-m)

C) Sensitivity Matrix.

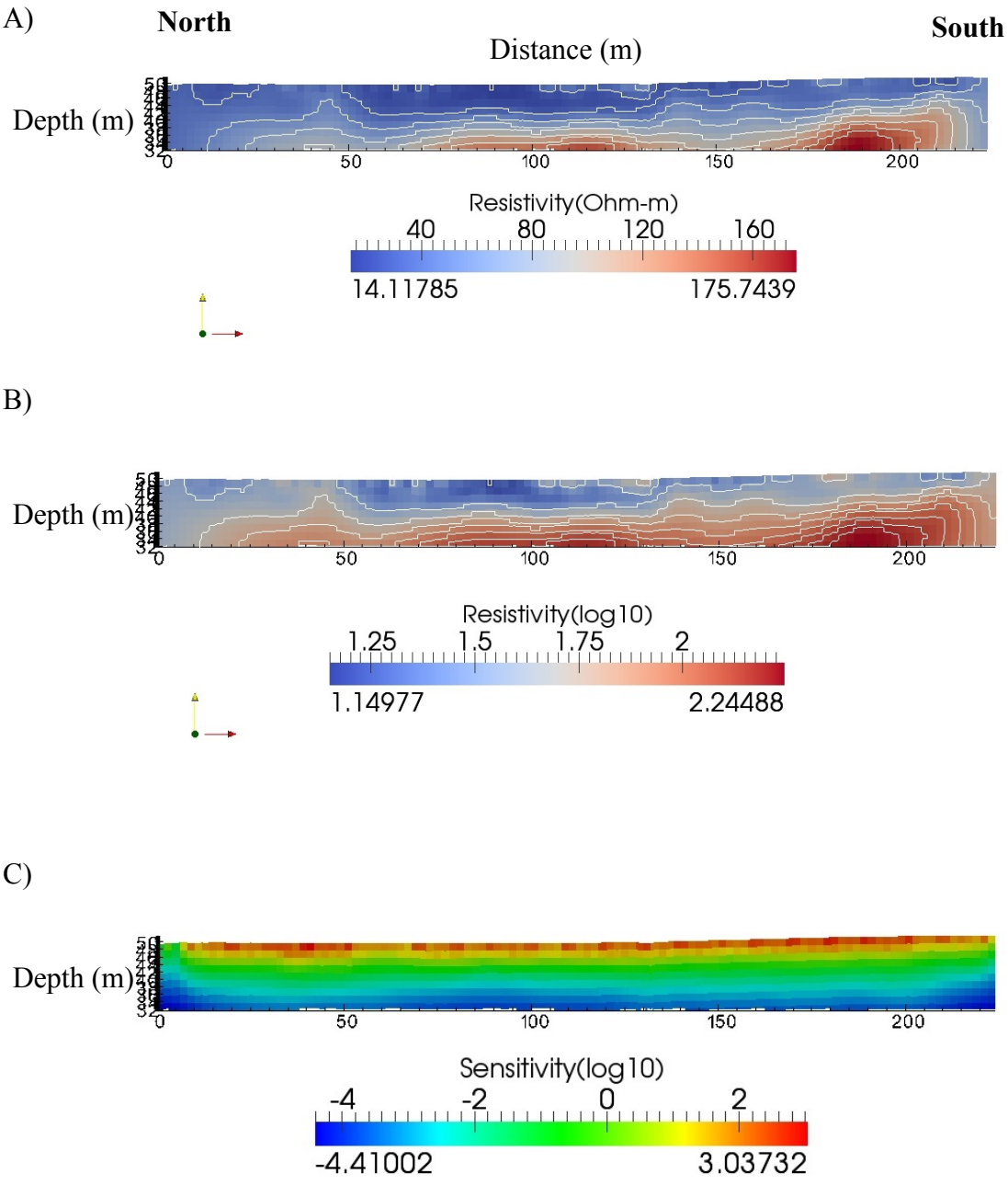

Figure 4.8 - Inversion results for Line Y. A) Resistivity (ohm-m) B) Log Resistivity (ohm-m) C) Sensitivity Matrix.

A)

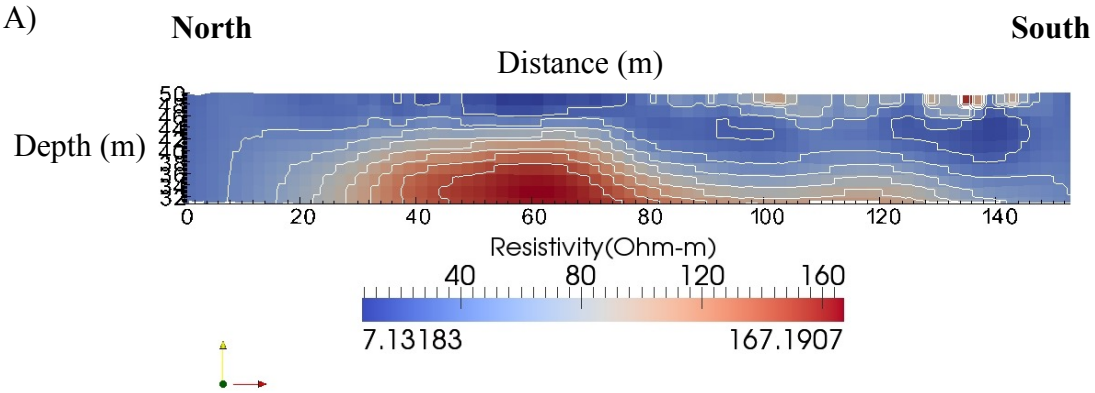

B)

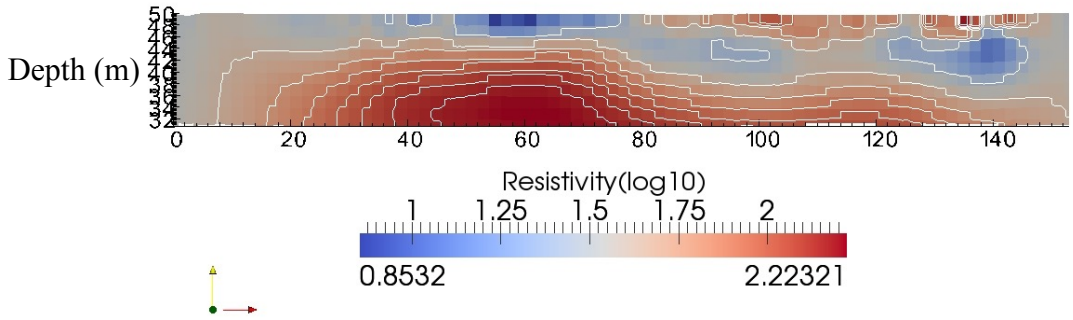

C)

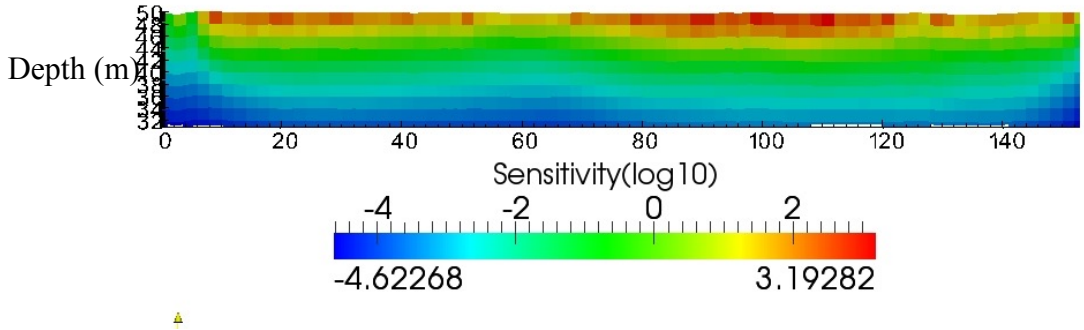

Figure 4.9 - Inversion results for Line Z. A) Resistivity (ohm-m) B) Log Resistivity (ohm-m) C) Sensitivity Matrix.

Figure 4.10 - Line A: comparison between resistivity inversion models and shear-wave velocity models derived from full-spread hammer, half-spread hammer, and van seismic data with artifact zones removed. Red arrows indicate sinkhole locations according to Park and Hawman (2012). Resistivity values marking the top of the bedrock for Line A are 156-250 ohm-m. All seismic profiles are scaled to the resistivity distances along the line.

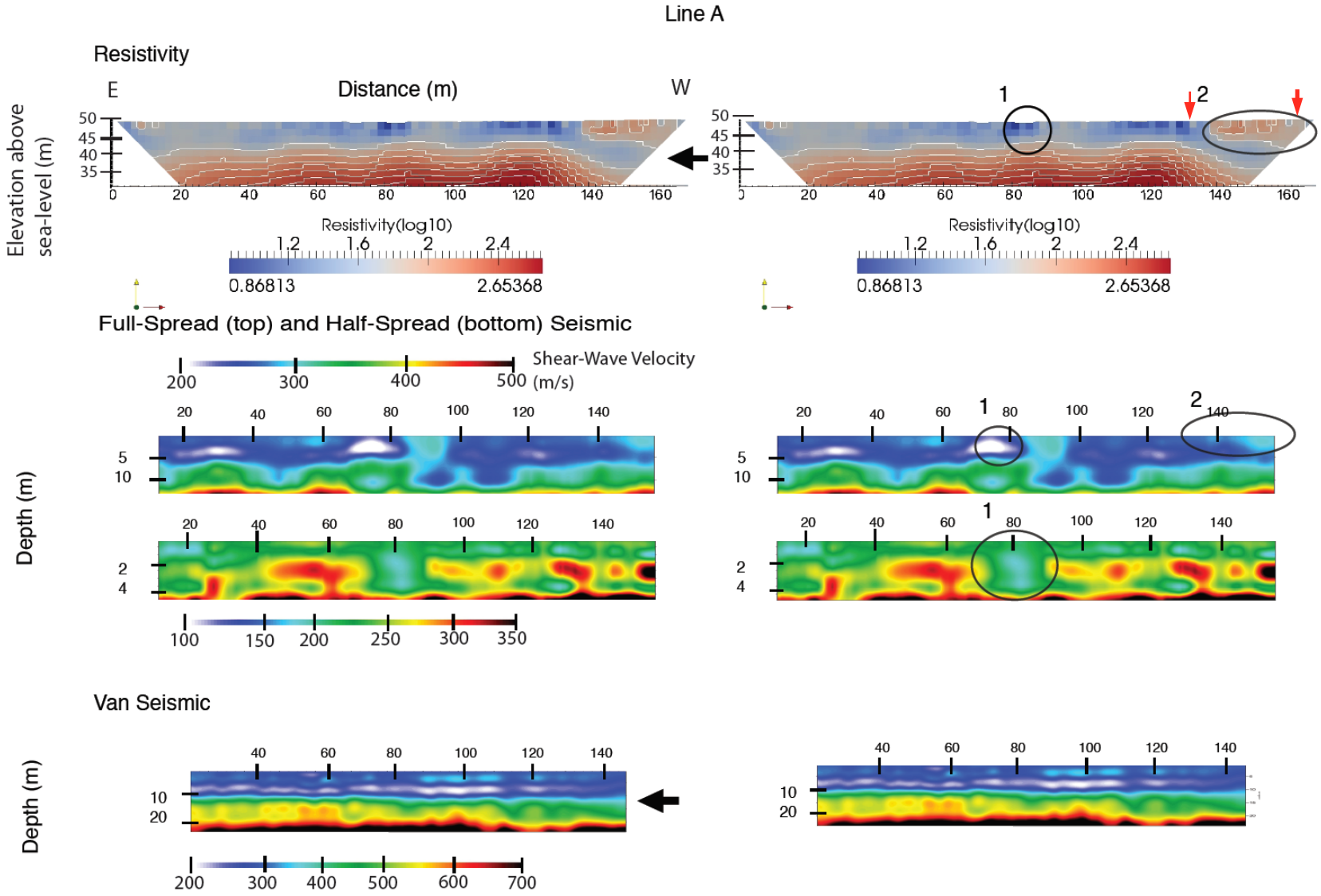
Line A
Resistivity
E
Distance (m)
W
Elevation above sea-level (m)
Resistivity(log10)
0.86813
2.65368
Full-Spread (top) and Half-Spread (bottom) Seismic
Shear-Wave Velocity (m/s)
Depth (m)
Van Seismic
1
2

Figure 4.11 - Line B: comparison between resistivity inversion models and shear-wave velocity models derived from full-spread hammer, half-spread hammer, and van seismic data with artifact zones removed. Resistivity values marking the top of the bedrock for Line B are 89.7-103 ohm-m. All seismic profiles are scaled to the resistivity distances along the line.

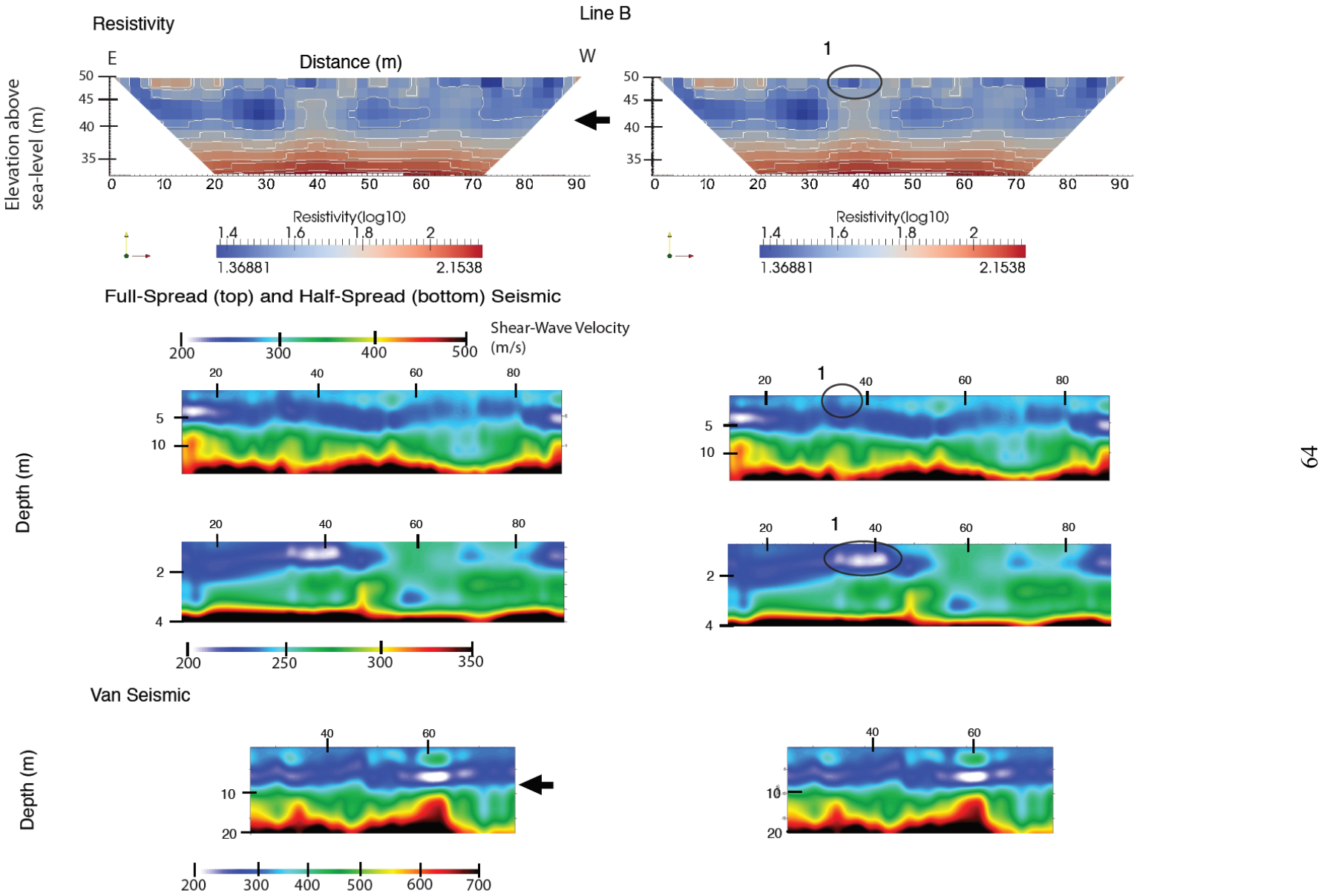
Line B
Resistivity
E
Distance (m)
W
1
Elevation above sea-level (m)
Resistivity(log10)
1.36881
2.1538
Full-Spread (top) and Half-Spread (bottom) Seismic
Shear-Wave Velocity (m/s)
Depth (m)
Van Seismic

Figure 4.12 - Line C: comparison between resistivity inversion models and shear-wave velocity models derived from full-spread hammer, half-spread hammer, and van seismic data with artifact zones removed. Resistivity values marking the top of the bedrock for Line C are 73.4-84.4 ohm-m. All seismic profiles are scaled to the resistivity distances along the line.

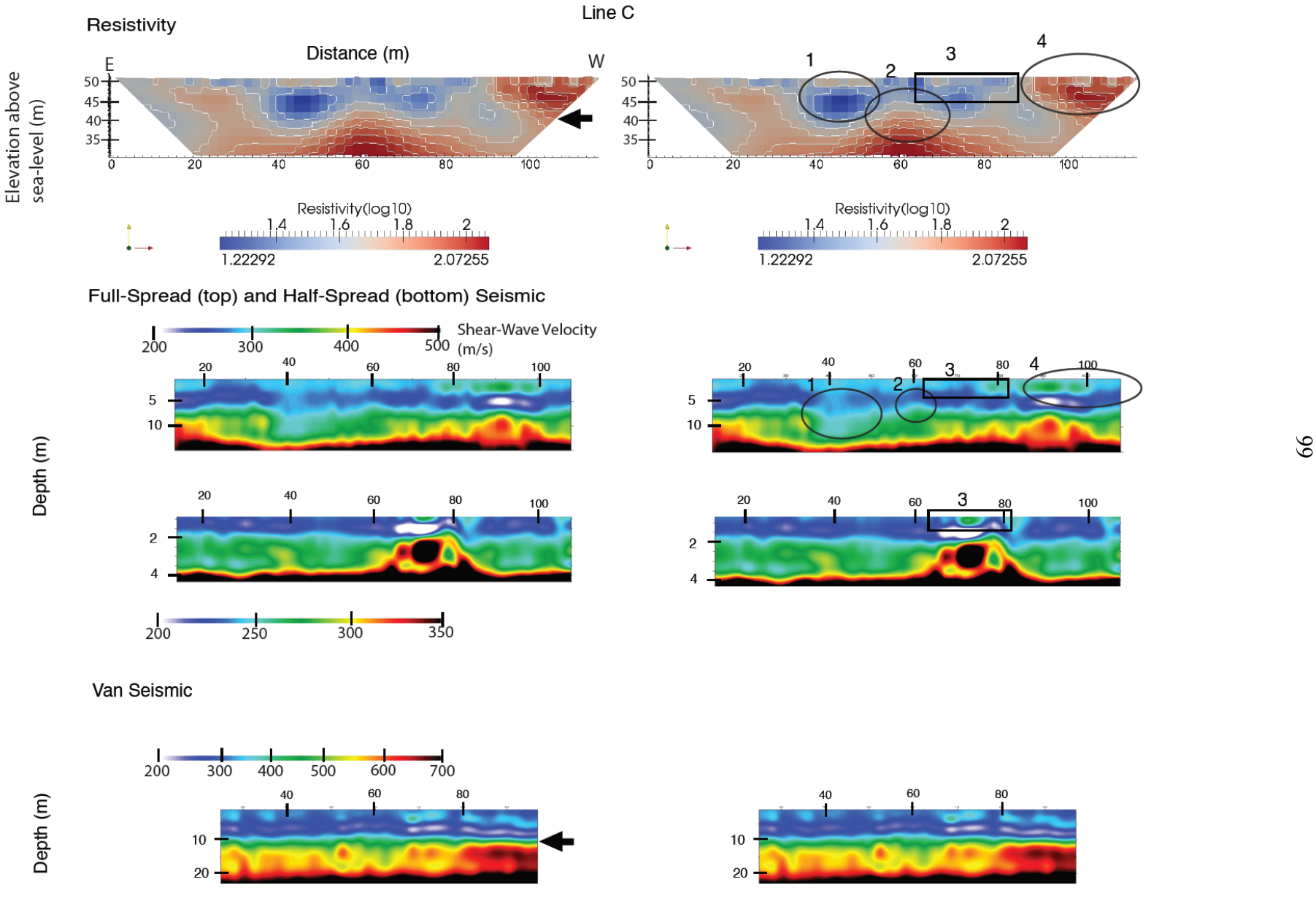
Line C
Resistivity
Distance (m)
E
W
Elevation above sea-level (m)
Resistivity(log10)
1.22292
2.07255
Full-Spread (top) and Half-Spread (bottom) Seismic
Shear-Wave Velocity (m/s)
Depth (m)
Van Seismic

Figure 4.13 - Line D: comparison between resistivity inversion models and shear-wave velocity models derived from full-spread hammer, half-spread hammer, and van seismic data with artifact zones removed. Green arrows indicate the edge of the well platform. The well platform effect in the inversion models results in a high resistivity zone because current avoids the high-resistivity platform creating a higher density of current flow lines in the adjacent subsurface which then increases the electrical potential difference and therefore the apparent resistivity. Resistivity values marking the top of the bedrock for the west side of the profile are 97.0-119 ohm-m. Corresponding values for the model in Figure 4.19 (with bad data removed) are 74.5-95.6 ohm-m. All seismic profiles are scaled to the resistivity distances along the line.

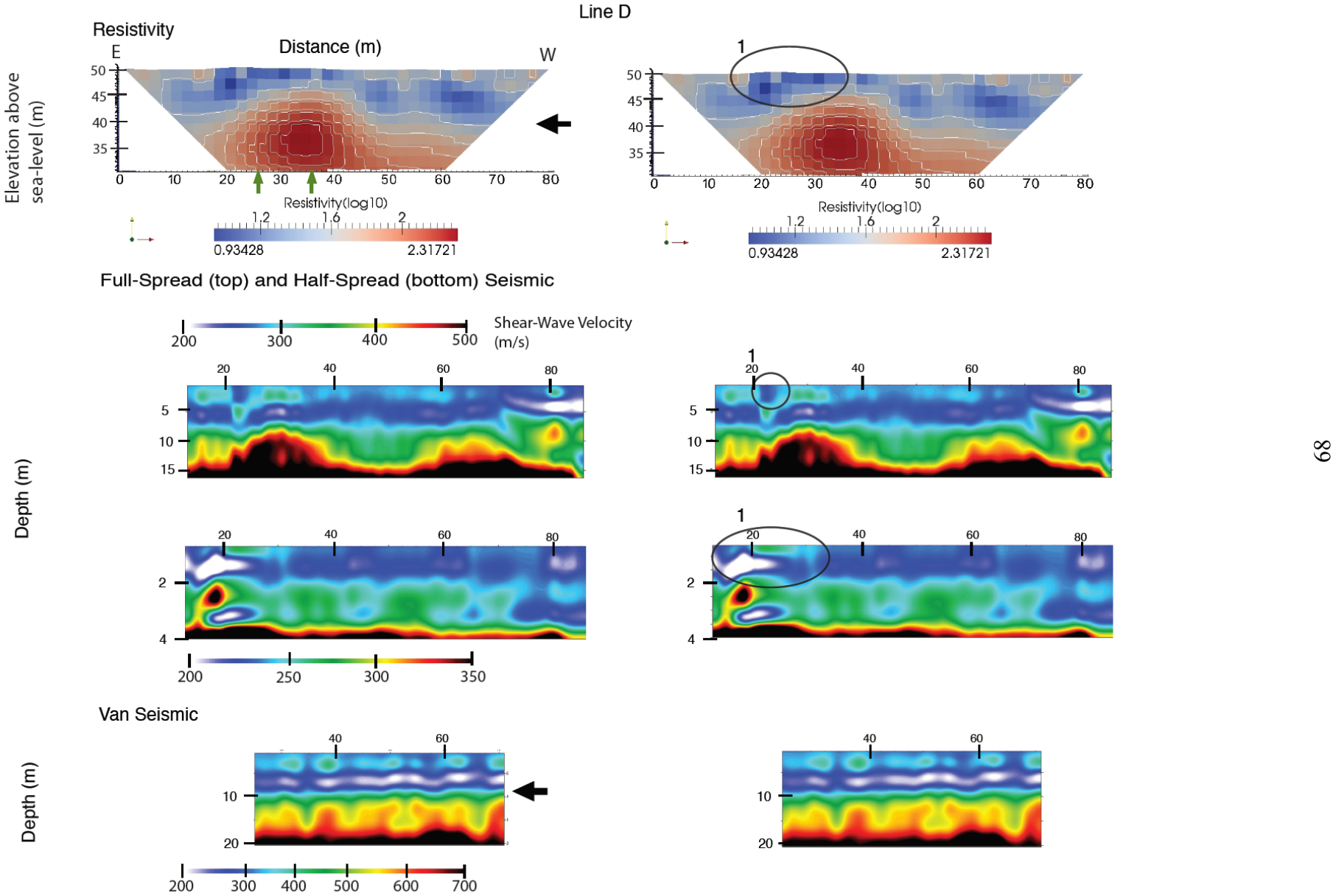
Line D
Resistivity
E
Distance (m)
W
Elevation above sea-level (m)
Resistivity(log10)
0.93428
2.31721
1
Full-Spread (top) and Half-Spread (bottom) Seismic
Shear-Wave Velocity (m/s)
Depth (m)
Van Seismic

Figure 4.14 - Line E: comparison between resistivity inversion models and shear-wave velocity models derived from full-spread hammer, half-spread hammer, and van seismic data with artifact zones removed. Green arrows indicate the edge of the well platform. The well platform effect in the inversion models results in a high resistivity zone because current avoids the high-resistivity platform creating a higher density of current flow lines in the adjacent subsurface which then increases the electrical potential difference and therefore the apparent resistivity. Resistivity values marking the top of the bedrock for the west side of the profile are 93.6-112 ohm-m. Corresponding values for the model in Figure 4.19 (with bad data removed) are 80.6-106 ohm-m. All seismic profiles are scaled to the resistivity distances along the line.

Line E

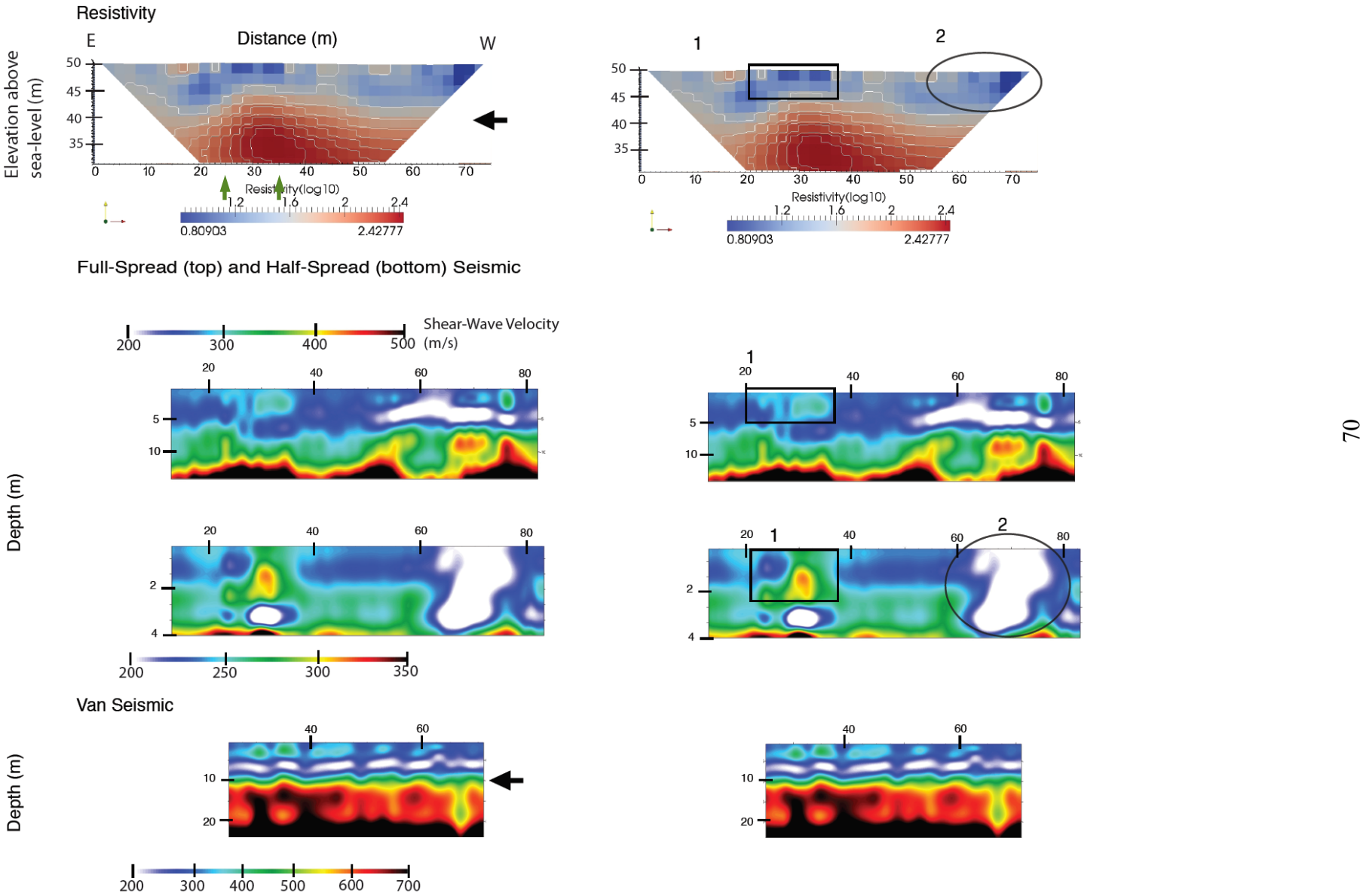
Resistivity
E
Distance (m)
W
Elevation above sea-level (m)
50
45
40
35
0
10
20
30
40
50
60
70
Resistivity(log10)
1.2
1.6
2
2.4
0.80903
2.42777
1
2
Full-Spread (top) and Half-Spread (bottom) Seismic
Shear-Wave Velocity (m/s)
200
300
400
500
Depth (m)
5
10
2
4
250
350
Van Seismic
600
700

Figure 4.15 - Line F: comparison between resistivity inversion models and shear-wave velocity models derived from full-spread hammer, half-spread hammer, and van seismic data with artifact zones removed. Resistivity values marking the top of the bedrock for Line F are 85.6-112 ohm-m. All seismic profiles are scaled to the resistivity distances along the line.

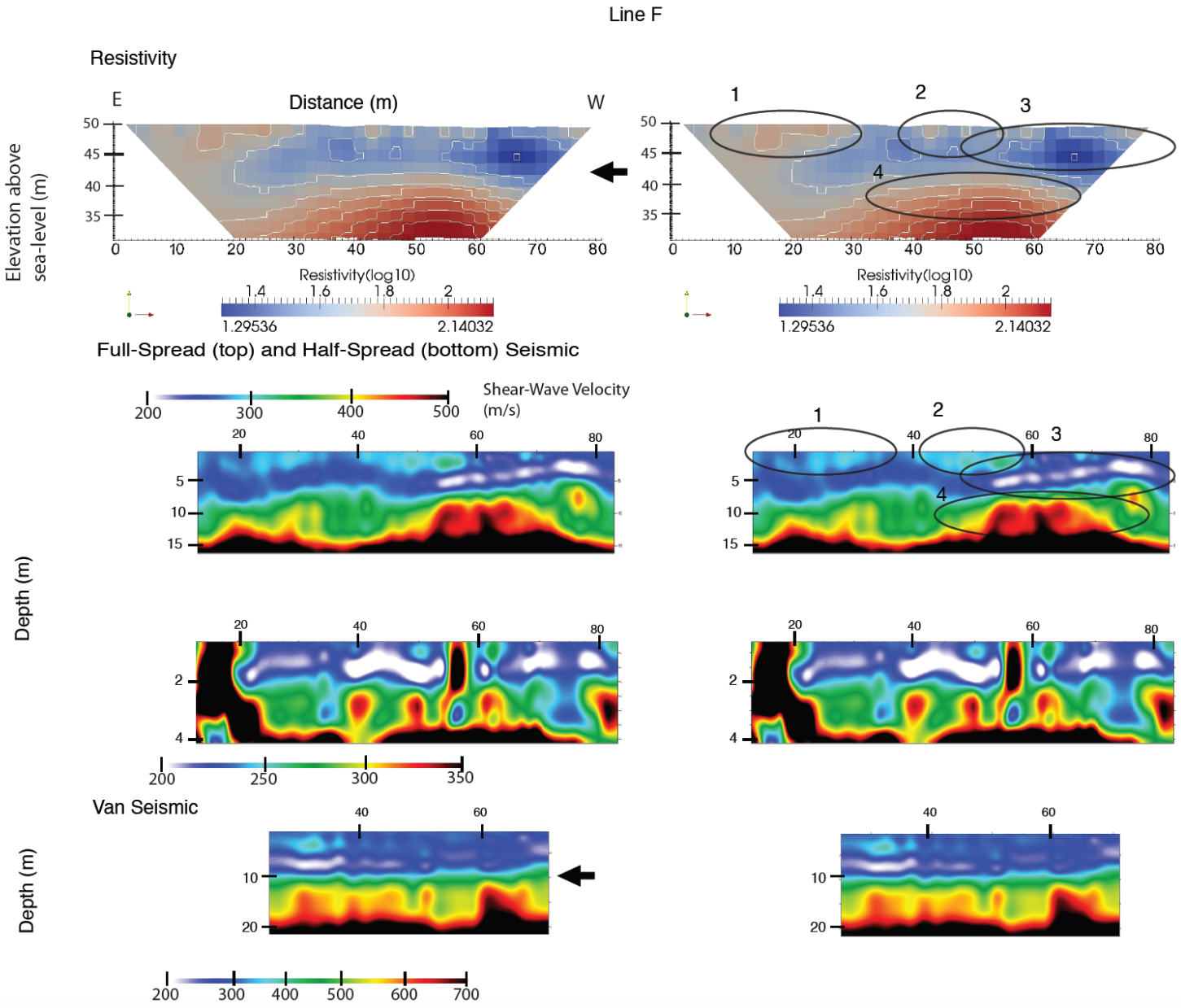
Line F
Resistivity
E
Distance (m)
W
Elevation above sea-level (m)
Resistivity(log10)
1.29536
2.14032
1
2
3
4
Full-Spread (top) and Half-Spread (bottom) Seismic
Shear-Wave Velocity (m/s)
Depth (m)
Van Seismic
Depth (m)

Figure 4.16 - Line G: comparison between resistivity inversion models and shear-wave velocity models derived from full-spread hammer, half-spread hammer, and van seismic data with artifact zones removed. Resistivity values marking the top of the bedrock for Line G are 93.3-112 ohm-m. All seismic profiles are scaled to the resistivity distances along the line.

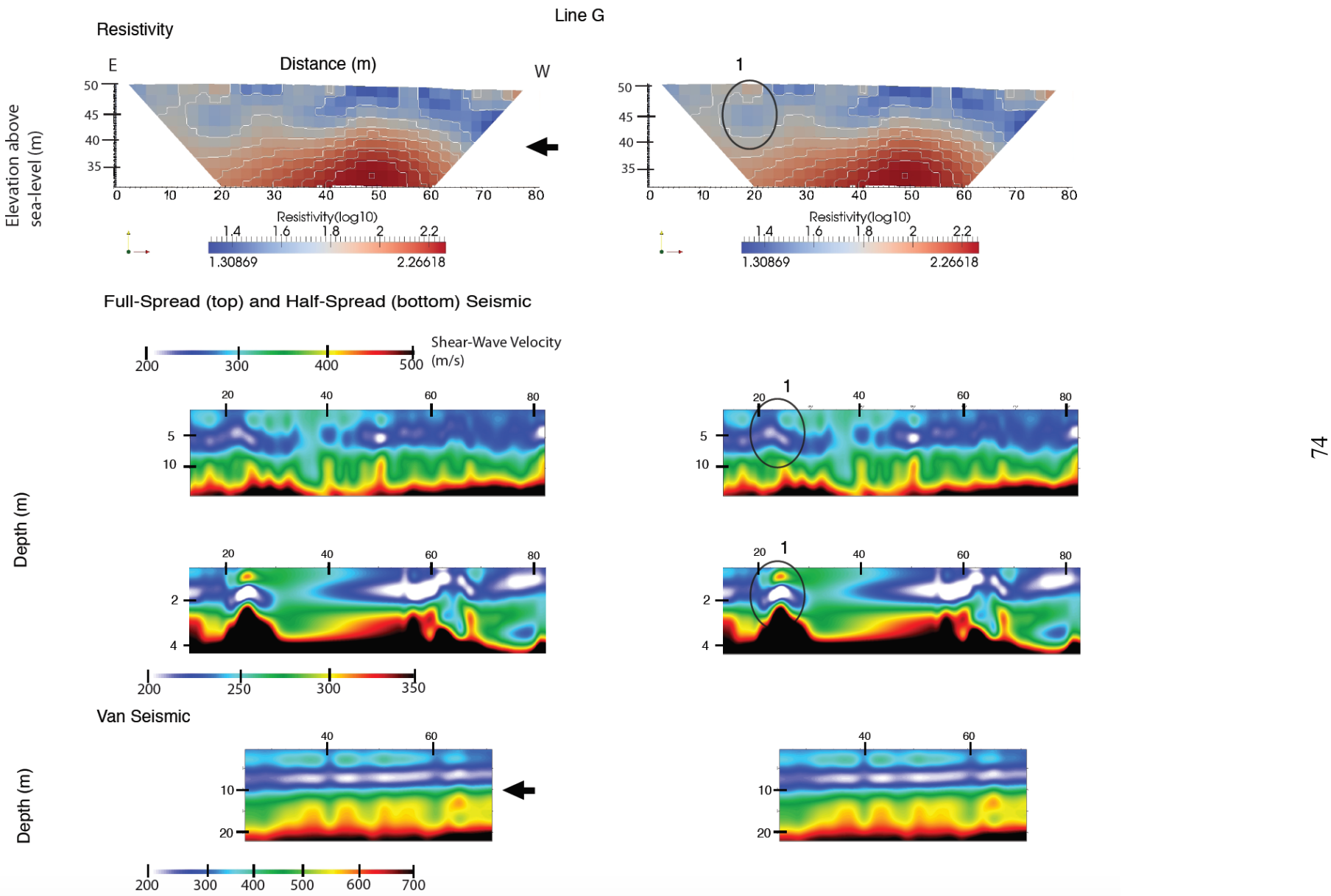
Line G
Resistivity
E
Distance (m)
W
Elevation above sea-level (m)
Resistivity(log10)
1.30869
2.26618
1
Full-Spread (top) and Half-Spread (bottom) Seismic
Shear-Wave Velocity (m/s)
Depth (m)
Van Seismic

Figure 4.17 - Line Y: comparison between resistivity inversion models and shear-wave velocity models derived from full-spread hammer, half-spread hammer, and van seismic data with artifact zones removed. Resistivity values marking the top of the bedrock for Line Y are 96.1-114 ohm-m. All seismic profiles are scaled to the resistivity distances along the line.

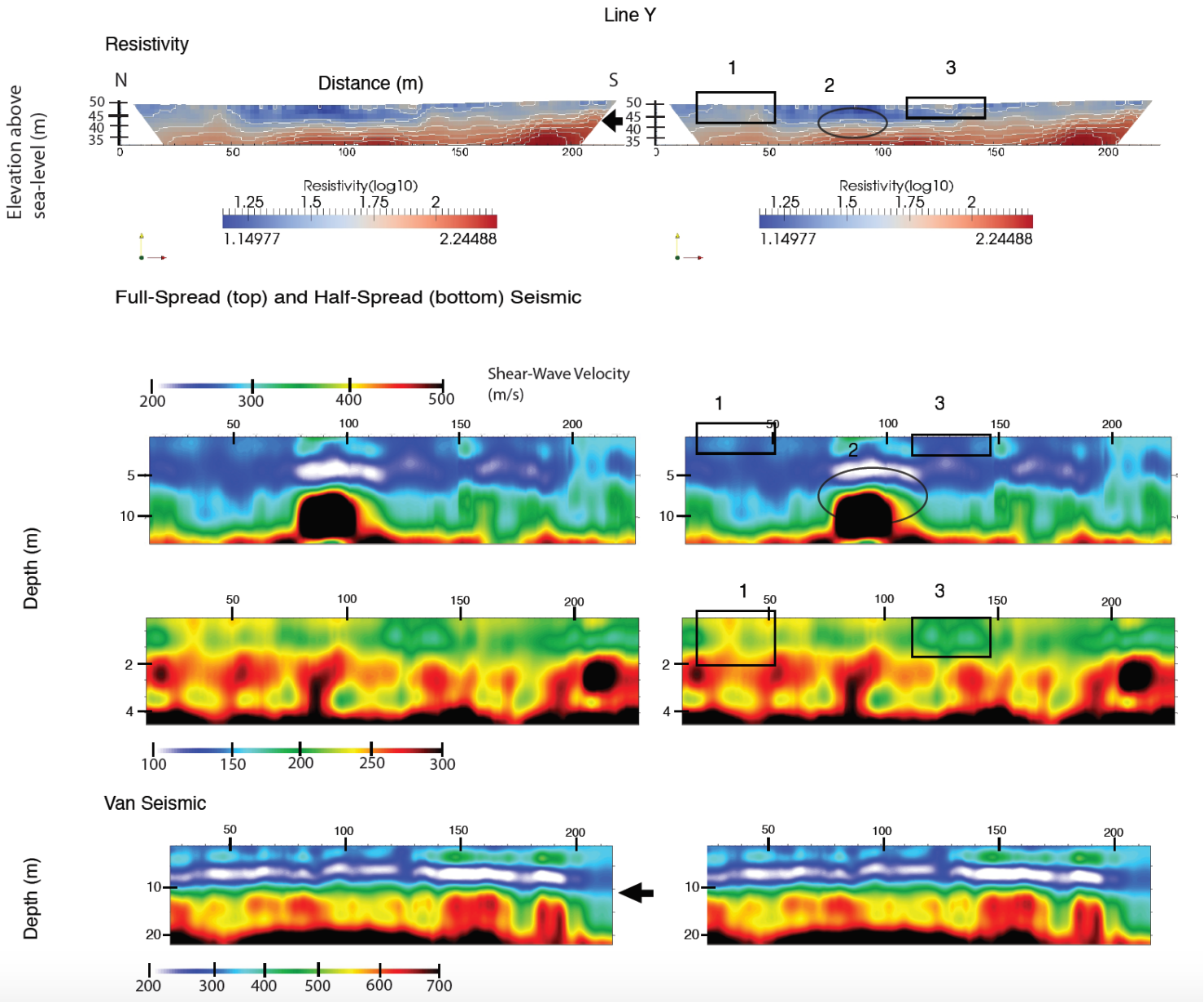
Line Y
Resistivity
N
Distance (m)
S
Elevation above sea-level (m)
Resistivity(log10)
1.14977
2.24488
Full-Spread (top) and Half-Spread (bottom) Seismic
Shear-Wave Velocity (m/s)
Depth (m)
Van Seismic

Figure 4.18 - Line Z: comparison between resistivity inversion models and shear-wave velocity models derived from full-spread hammer, half-spread hammer, and van seismic data with artifact zones removed. Red arrows indicate sinkhole locations according to Park and Hawman (2012). Resistivity values marking the top of the bedrock for Line Z are 104-122 ohm-m. All seismic profiles are scaled to the resistivity distances along the line.

Line Z

Resistivity

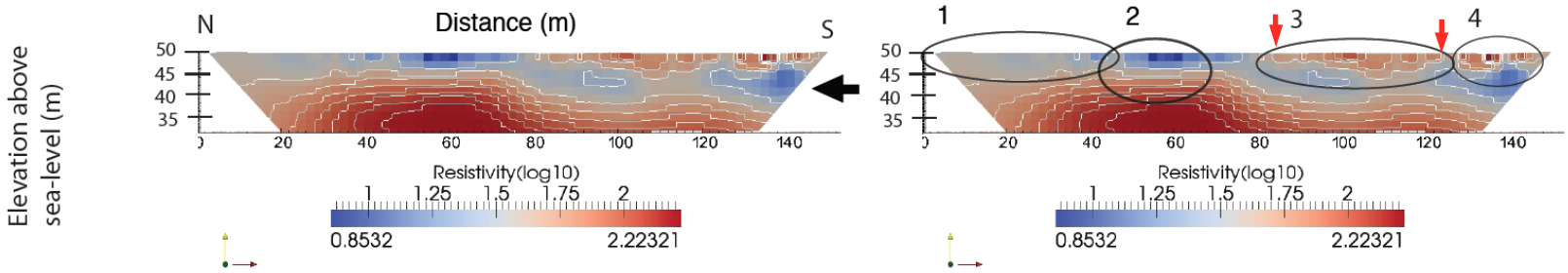

Full-Spread (top) and Half-Spread (bottom) Seismic

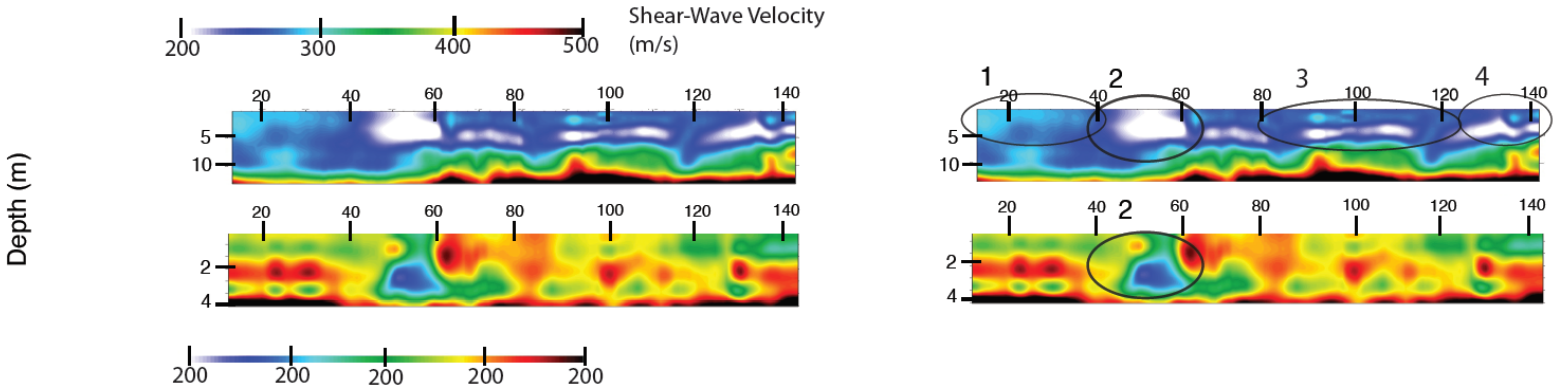

Van Seismic

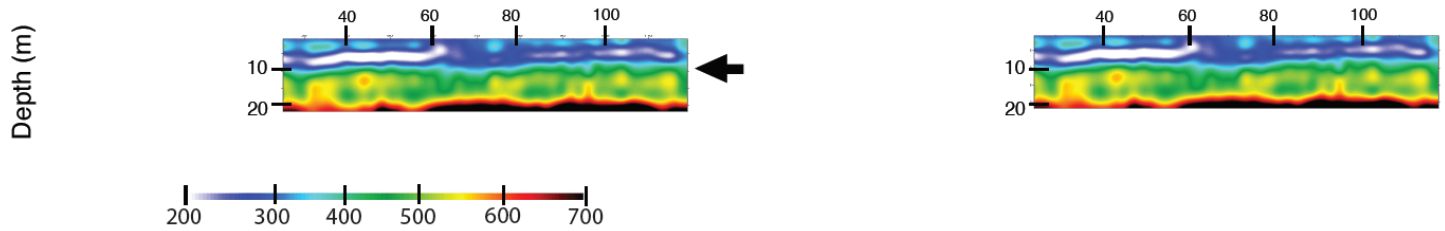

Figure 4.19 - Line D: comparison of original inversion models (left) with inversion models with bad data points (negative resistances) removed (right) for x^2=0.5. The top model is resistivity, the middle model is log resistivity, and the bottom model is the sensitivity matrix. Green arrows indicate the well platform boundaries. The high resistivity anomaly has become smaller and the bedrock surface from 45-80 m down the line is better resolved.

Line D

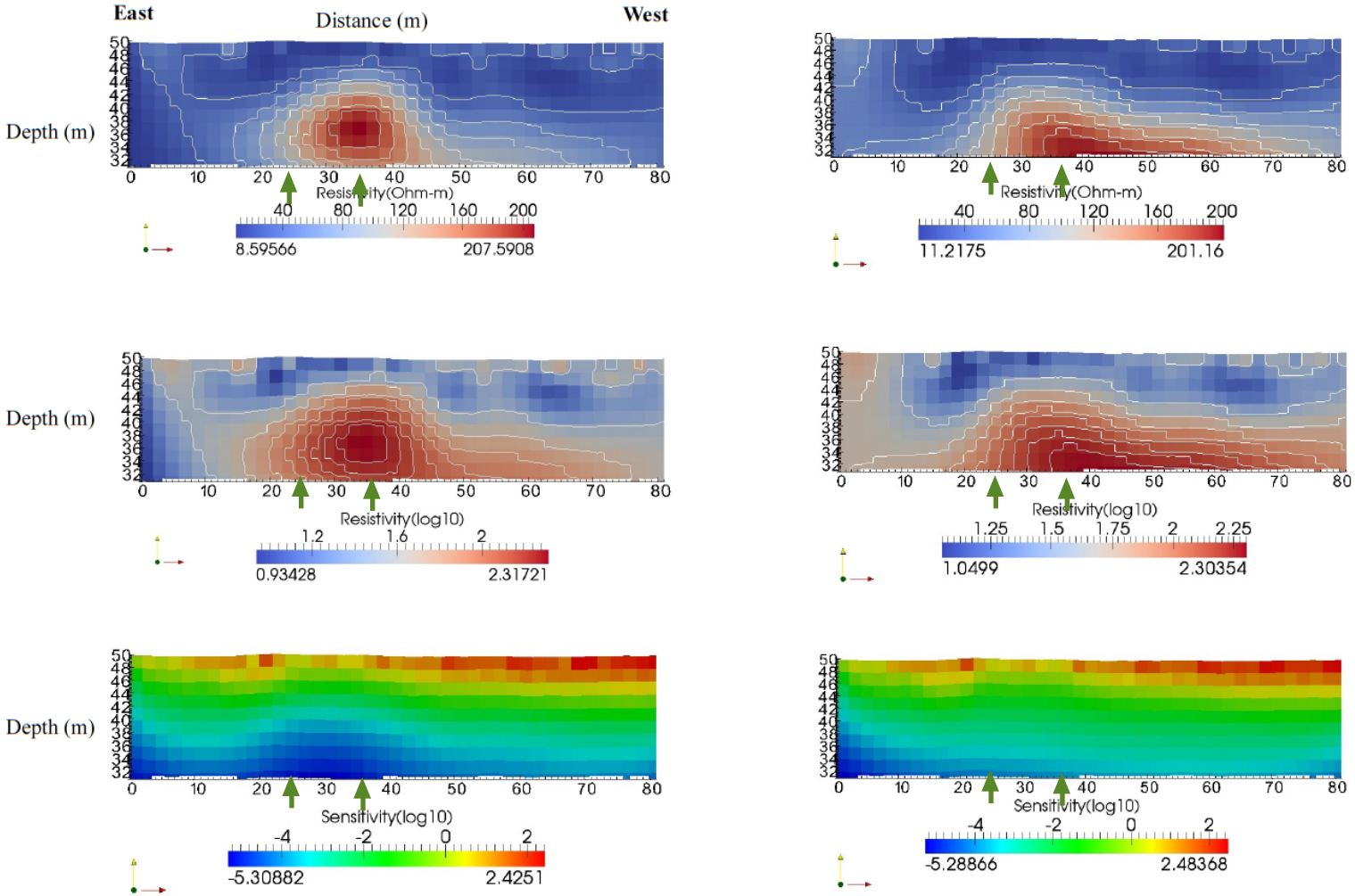
East
Distance (m)
West
Depth (m)
Resistivity(Ohm-m)
8.59566
207.5908
Resistivity(Ohm-m)
11.2175
201.16
Depth (m)
Resistivity(log10)
0.93428
2.31721
Resistivity(log10)
1.0499
2.30354
Depth (m)
Sensitivity(log10)
-5.30882
2.4251
Sensitivity(log10)
-5.28866
2.48368

Figure 4.20 - Line E: comparison of original inversion models (left) with inversion models with bad data points (negative resistances) removed (right) for x^2=0.5. The top model is resistivity, the middle model is log resistivity, and the bottom model is the sensitivity matrix. Green arrows indicate the well platform boundaries. The high resistivity anomaly has become smaller and the bedrock surface from 45-80 m down the line is better resolved.

Line E

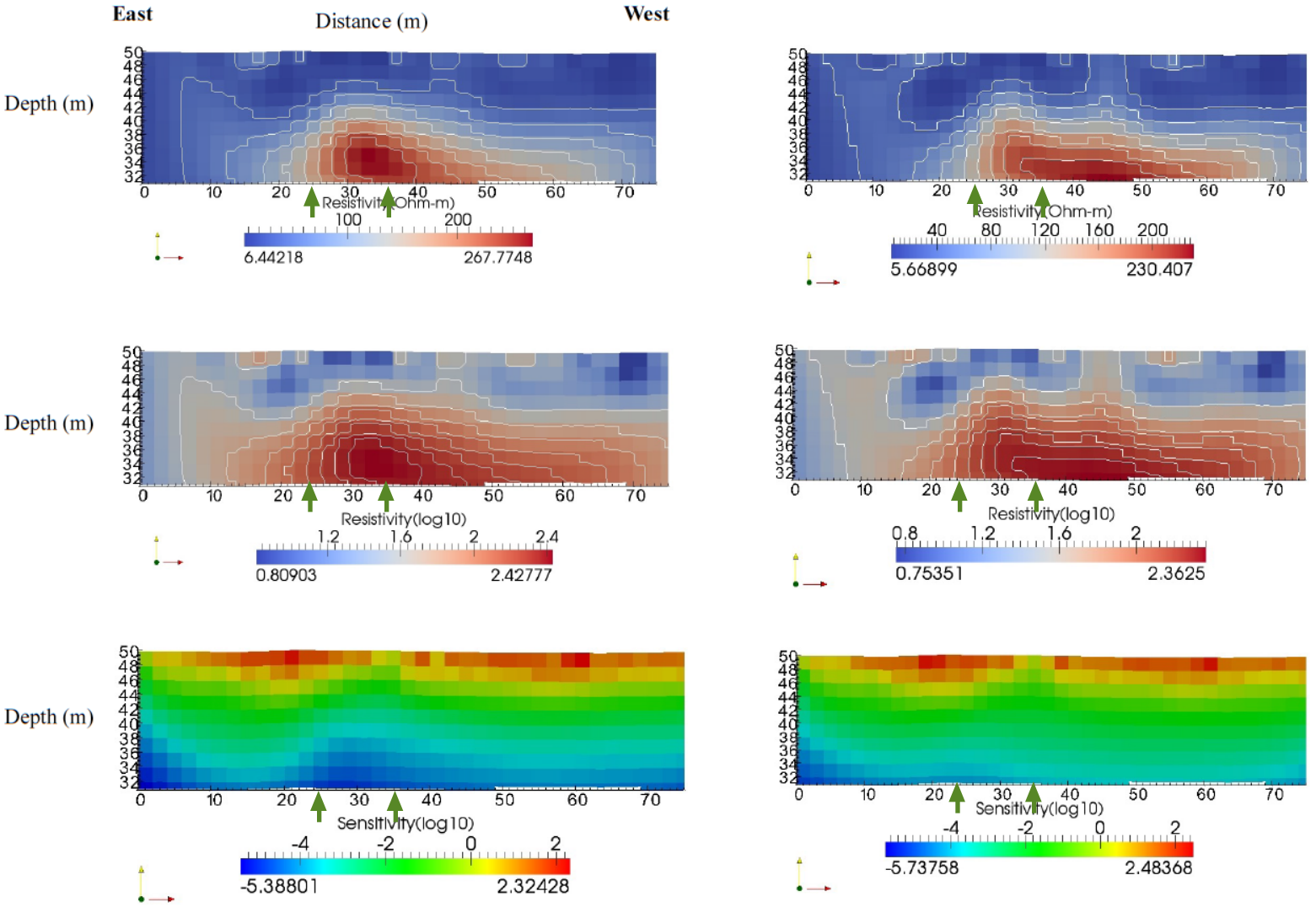
East
Distance (m)
West
Depth (m)
Resistivity (Ohm-m)
6.44218
267.7748
Resistivity (Ohm-m)
5.66899
230.407
Depth (m)
Resistivity(log10)
0.80903
2.42777
Resistivity(log10)
0.75351
2.3625
Depth (m)
Sensitivity(log10)
-5.38801
2.32428
Sensitivity(log10)
-5.73758
2.48368

Figure 4.21 - Line D: comparison of original inversion models for the uppermost 10 m (left) with inversion models derived using only 5 m offset data(right); x^2=0.5. The top model is resistivity, the middle model is log resistivity, and the bottom model is the sensitivity matrix. Green arrows indicate the well platform boundaries. The effect from the platform has been removed in the new inversion model.

Line D

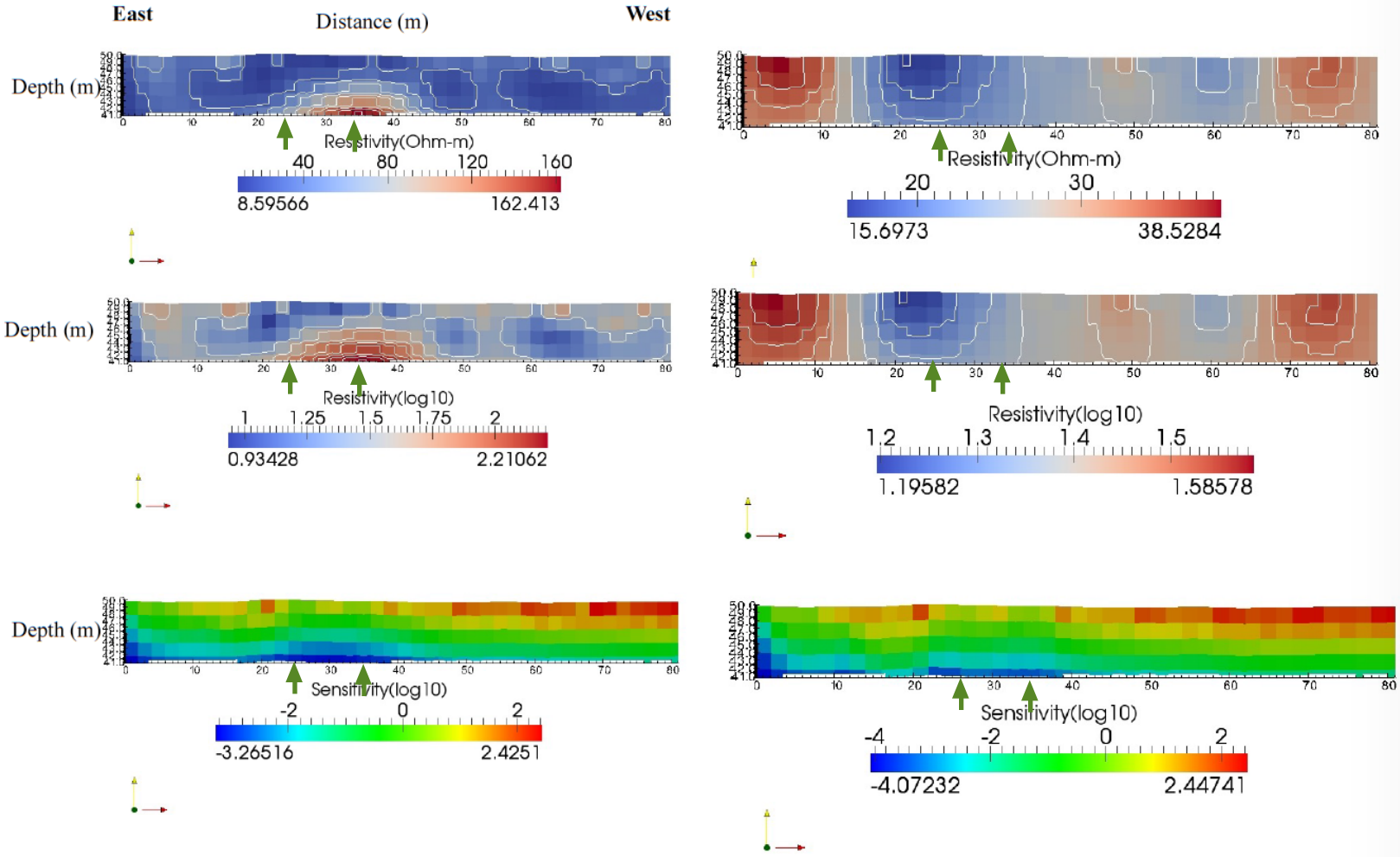
East
Distance (m)
West
Depth (m)
Resistivity(Ohm-m)
40
80
120
160
8.59566
162.413
Resistivity(Ohm-m)
20
30
15.6973
38.5284
Depth (m)
Resistivity(log10)
1
1.25
1.5
1.75
2
0.93428
2.21062
Resistivity(log10)
1.2
1.3
1.4
1.5
1.19582
1.58578
Depth (m)
Sensitivity(log10)
-2
0
2
-3.26516
2.4251
Sensitivity(log10)
-4
-2
0
2
-4.07232
2.44741

Figure 4.22 - Line E: comparison of original inversion models for the uppermost 10 m (left) with inversion models derived using only 5 m offset data(right); x^2=0.5. The top model is resistivity, the middle model is log resistivity, and the bottom model is the sensitivity matrix. Green arrows indicate the well platform boundaries. The effect from the platform has been removed in the new inversion model.

Line E

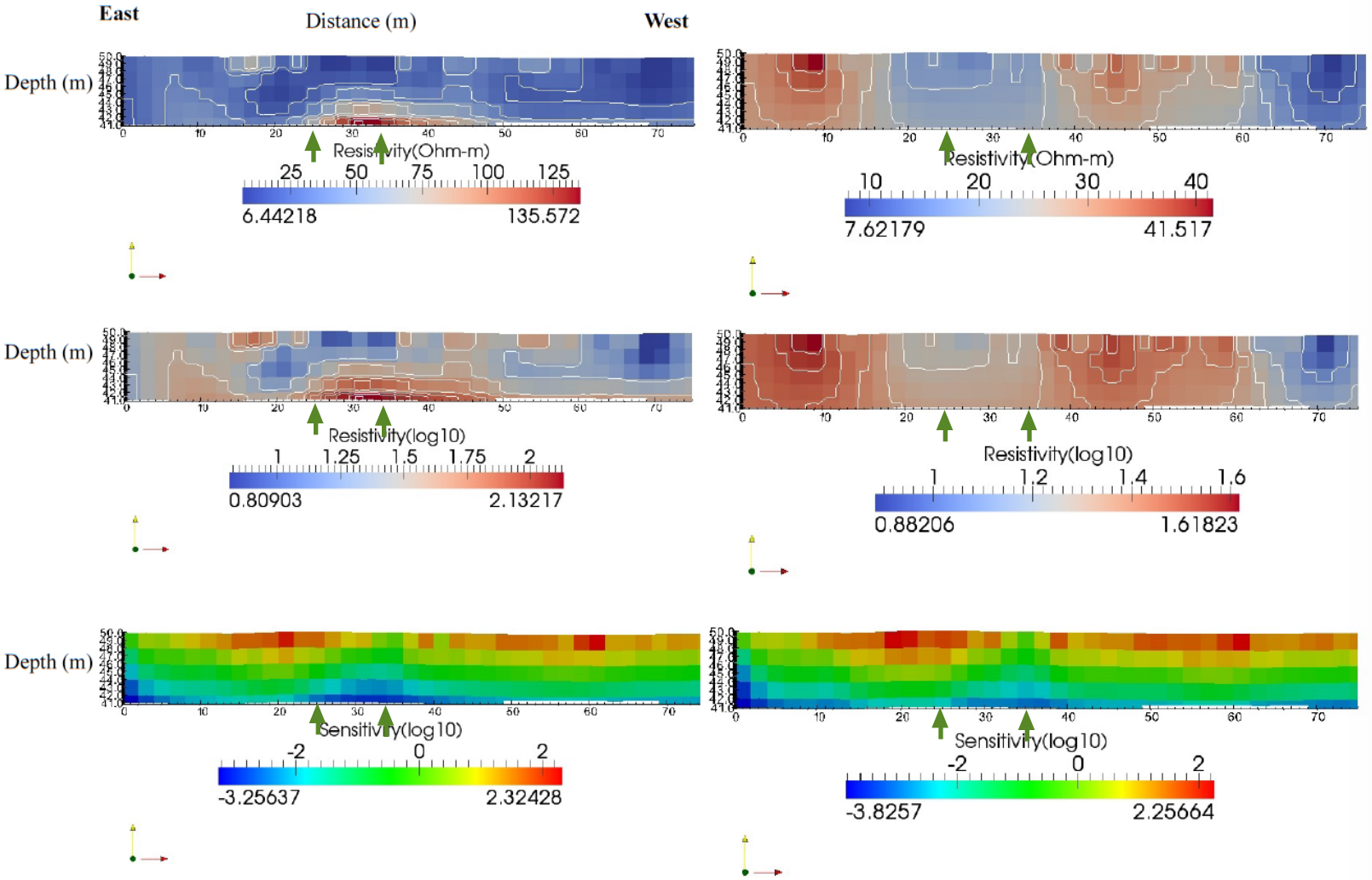
East
Distance (m)
West
Depth (m)
Resistivity(Ohm-m)
25 50 75 100 125
6.44218
135.572
Resistivity(Ohm-m)
10 20 30 40
7.62179
41.517
Depth (m)
Resistivity(log10)
1 1.25 1.5 1.75 2
0.80903
2.13217
Resistivity(log10)
1 1.2 1.4 1.6
0.88206
1.61823
Depth (m)
Sensitivity(log10)
-2 0 2
-3.25637
2.32428
Sensitivity(log10)
-2 0 2
-3.8257
2.25664

Figure 4.23 - Composite north-south view of all east-west lines in resistivity values. Depth is indicated on each plot's y-axis and distance is indicated on each plot's x-axis. The black arrow indicates a bedrock ridge. For Line D and Line E, models were derived from data sets with negative resistances removed (Figures 4.19 and 4.20). The well platform effect for these lines is still visible and affects the overall resistivity values surrounding the area. The green arrows show the platform boundaries in Line D and Line E.

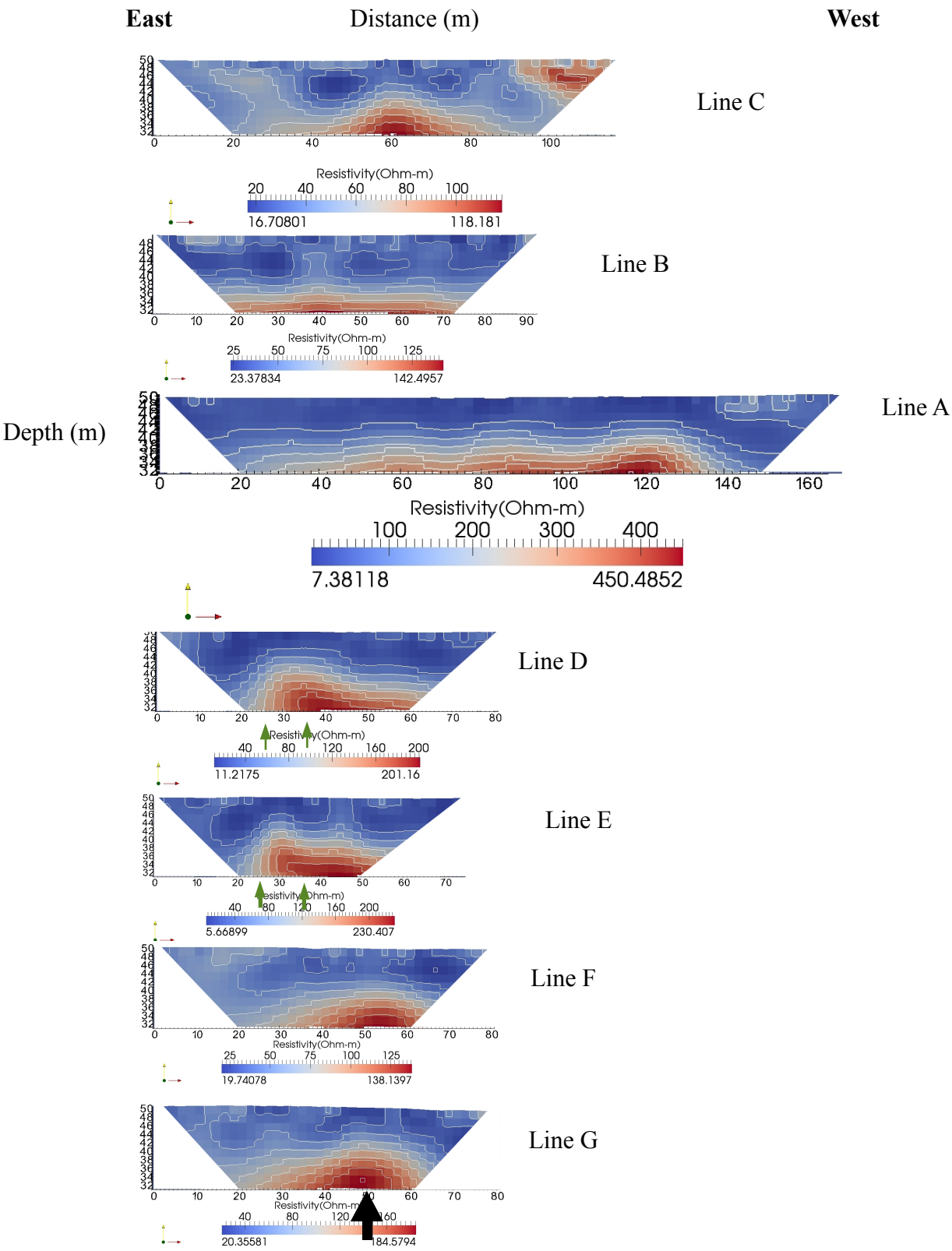
East
Distance (m)
West
Line C
Resistivity(Ohm-m)
20 40 60 80 100
16.70801 118.181
Line B
Resistivity(Ohm-m)
25 50 75 100 125
23.37834 142.4957
Depth (m)
Line A
Resistivity(Ohm-m)
100 200 300 400
7.38118 450.4852
Line D
11.2175 201.16
Line E
5.66899 230.407
Line F
19.74078 138.1397
Line G
20.35581 184.5794

Figure 4.24 - Composite north-south view of all east-west lines in log resistivity values. Depth is indicated on each plot's y-axis and distance is indicated on each plot's x-axis. The black arrow indicates a bedrock ridge. For Line D and Line E, models were derived from data sets with negative resistances removed (Figures 4.19 and 4.20). The well platform effect for these lines is still visible and affects the overall resistivity values surrounding the area. The green arrows show the platform boundaries in Line D and Line E.

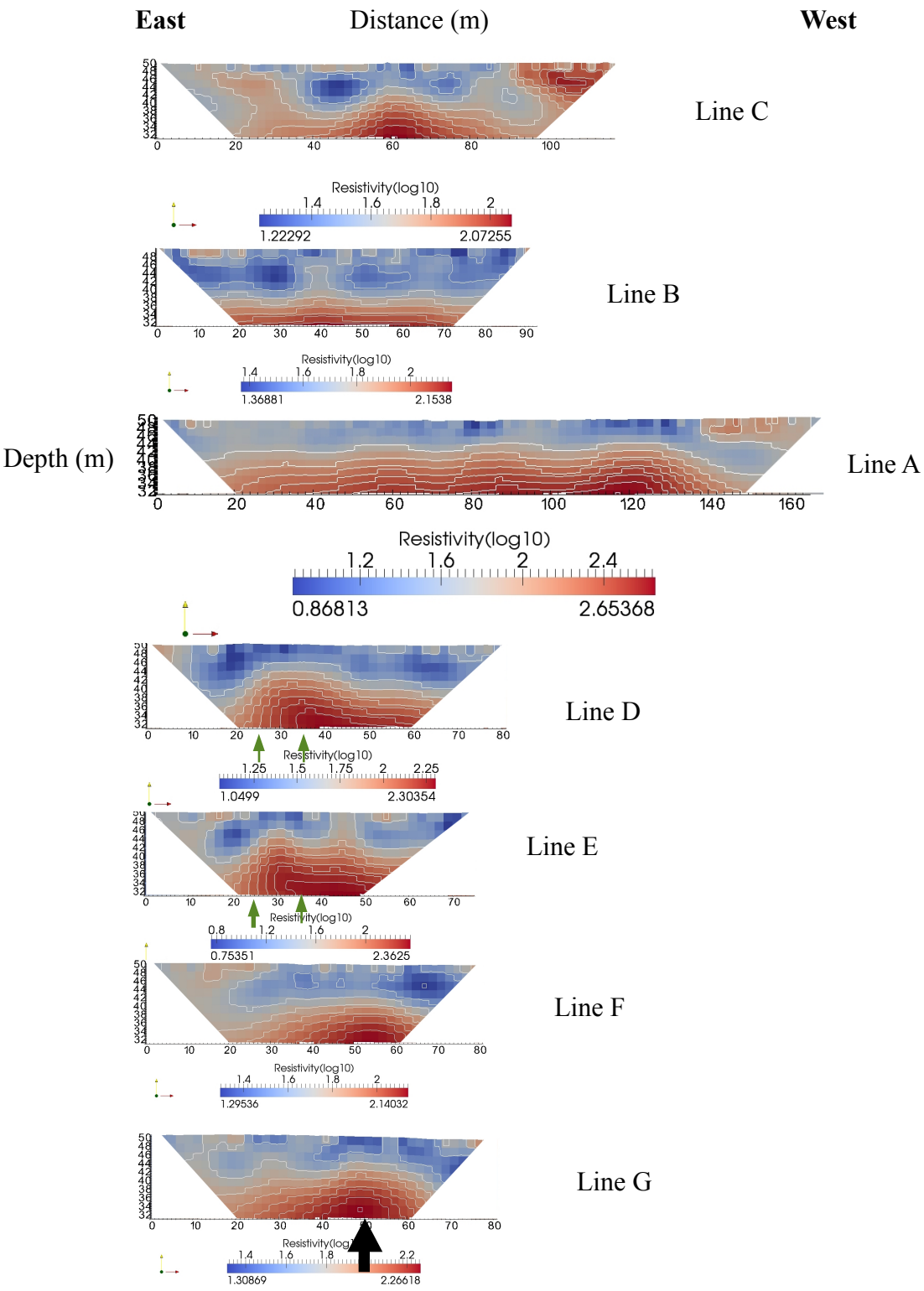
East
Distance (m)
West
Line C
Resistivity(log10)
1.4 1.6 1.8 2
1.22292 2.07255
Line B
Resistivity(log10)
1.4 1.6 1.8 2
1.36881 2.1538
Depth (m)
Line A
Resistivity(log10)
1.2 1.6 2 2.4
0.86813 2.65368
Line D
Resistivity(log10)
1.25 1.5 1.75 2 2.25
1.0499 2.30354
Line E
Resistivity(log10)
0.8 1.2 1.6 2
0.75351 2.3625
Line F
Resistivity(log10)
1.4 1.6 1.8 2
1.29536 2.14032
Line G
1.4 1.6 1.8 2.2
1.30869 2.26618

Figure 4.25 - Composite east-west view of both north-south lines in log resistivity values. Depth is indicated on each plot's y-axis and distance is indicated on each plot's x-axis. The top two models are Line Y and Line Z in resistivity values. The bottom two models are Line Y and Line Z in log resistivity values. Bedrock depth from 0-80 m along the line is shallower in Line Z (6-7 m) than in Line Y (15-20 m). Resistivity along the Line Y profile increases towards the south as elevation increases and the higher-resistivity bedrock becomes shallower and follows the topography. This increase in resistivity towards the south is probably a result of drier overburden because of water movement downhill. Resistivity values of the bedrock between Line Y and Line Z are similar. In contrast, for the shear-wave velocity models, Line Z shows lower shear-wave velocities at depths of 10-20 m than Line Y over the same depth range (Parker and Hawman, 2012).

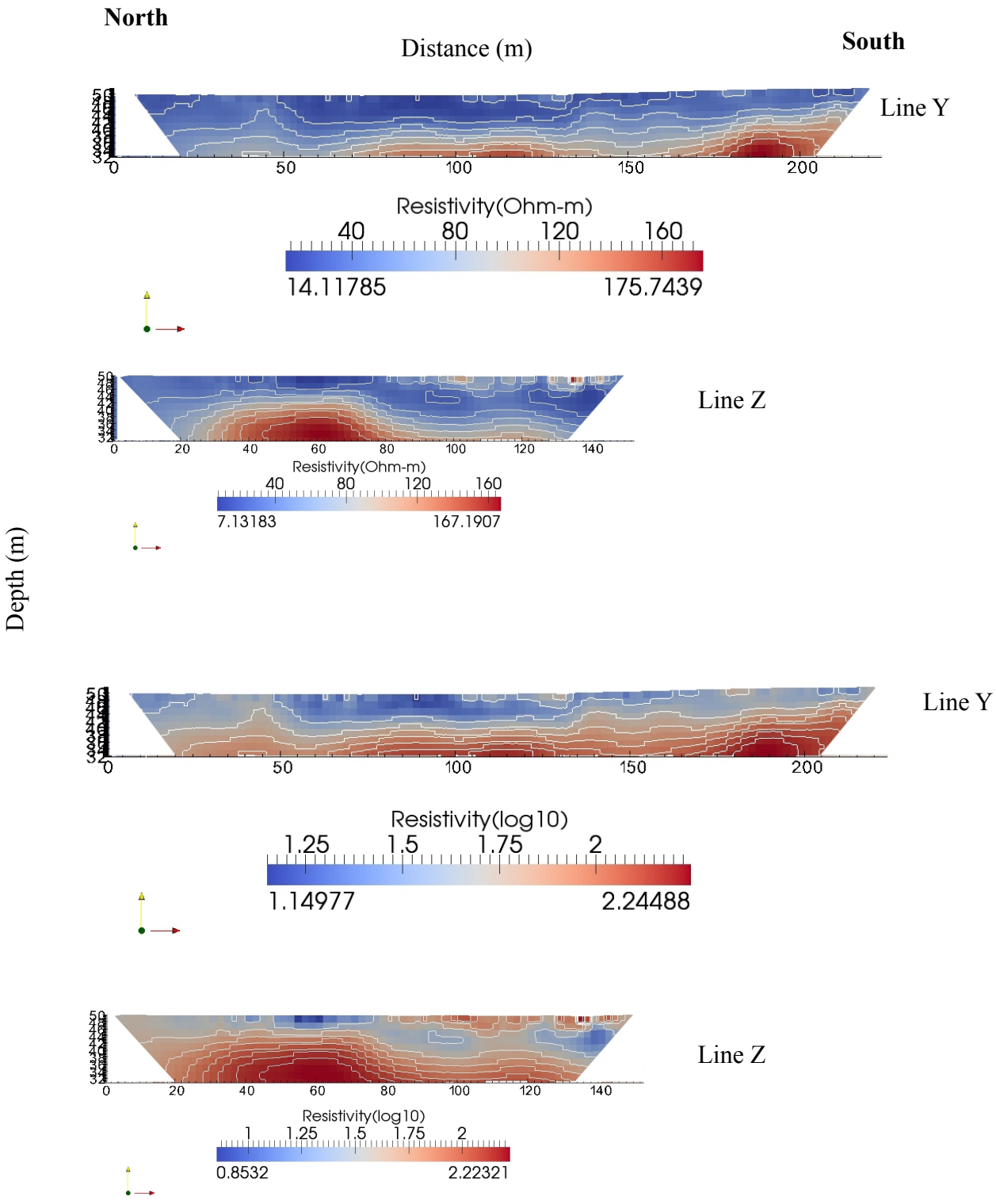
North
Distance (m)
South
Line Y
0
50
100
150
200
Resistivity(Ohm-m)
40
80
120
160
14.11785
175.7439
Line Z
0
20
40
60
80
100
120
140
Resistivity(Ohm-m)
40
80
120
160
7.13183
167.1907
Depth (m)
Line Y
Resistivity(log10)
1.25
1.5
1.75
2
1.14977
2.24488
Line Z
Resistivity(log10)
1
1.25
1.5
1.75
2
0.8532
2.22321

CHAPTER 5

CONCLUSIONS

Future Work

In the future, the gravity method and ground penetrating radar (GPR) could be a useful tool in this area. The gravity method would require a large density contrast between the material filling the sinkhole and the surrounding material (Schoor, 2002). This type of survey would therefore only likely produce results for sinkholes that were air-filled (Schoor, 2002). GPR can be used to help identify sinkhole locations but in the case of this field area, it is likely that the conductive clay-rich overburden would strongly attenuate radar signals and therefore would not allow proper depth penetration to image the sinkholes (Schoor, 2002).

A more rigorous comparison of resistivity and velocity models could be done by statistical analysis. This would help to establish the overall correlation between shear-wave velocity and resistivity in this karst setting.

Conclusions

The electrical resistivity method was used to map bedrock topography and to identify subsidence features. Using seven east-west lines and two north-south lines that directly overlapped previous seismic profiles allowed the direct comparison of resistivity and shear-wave velocity models. The most important results are summarized below:

1) The combination of resistivity and surface-wave analysis helped resolve ambiguities in the interpretation of anomalies. For example, high resistivities are consistent with dry materials

with high porosities, and combining this with low shear-wave velocities, potential zones of sinkhole development were identified. On the other hand, higher resistivity zones in combination with high shear-wave velocities are consistent with dry bedrock.

2) Resistivity values for the chalky limestone of the Ocala formation were determined to be in the range of 100-250 ohm-m. This was determined by calibrating the models with previous shear-wave velocity models and borehole data. This information will be helpful for future work in the area, especially for projects for which the principal goal is to map the bedrock surface, since resistivity data is much faster and cheaper to collect and analyze than seismic data.

3) Resistivities for materials in the overburden (sandy clay, clayey sands, and organic material) range from 6.44-73.4 ohm-m. The transition zone from overburden to bedrock is marked by a steep gradient in resistivities over a range of 73.5-123 ohm-m.

4) Both the van-source seismic and resistivity results suggest an average depth to bedrock of approximately 10 m. This is consistent with the bedrock depth found for a nearby well and test boreholes. Depth to bedrock is marked by steep gradients centered about 350 m/s in shear-wave velocity and 73-120 ohm-m in resistivity (except for Line A which had a range of 156-250 ohm-m).

5) Across all lines, in the uppermost 6 m, there is a general pattern of high-over-low resistivity and shear-wave velocity. This suggests a thin (3m), wet clay-rich layer under drier material with high porosity (Parker and Hawman, 2012).

6) A low-resistivity anomaly (56 ohm-m, 0-4 m depth) at the intersection of Line A and Line Z (A- 83 m and Z-55 m) occurs over a buried burn pit. This correlates with low shear-wave velocity anomalies.

7) Parker and Hawman (2012) interpreted a north-south alignment of five sinkholes as a result of karst processes along a prominent bedrock fracture that crosses Line A west of station 105 with an azimuth corresponding to a known preferred fracture orientation of N5°E. The study showed that void space, both open and infilled, contributes to low shear-wave velocities, in contrast with higher shear-wave velocities (500-650 m/s) seen for competent limestone bedrock. For all lines, shear-wave velocities ranging from 300-700 m/s are interpreted as variations in competency of the limestone bedrock (Parker, 2010). Fracture zones and more weathered limestone velocities occur at the lower end of the 300-700 m/s range (Parker, 2010). Zones of high resistivity/low shear-wave velocity at the west ends of Line A (156 ohm-m, 0-7 m depth) and Line C (100 ohm-m, 0-10 m depth) follow the trend of the interpreted north-south fracture zone. High-resistivity/low shear-wave velocity zones (140 ohm-m, 0-5 m depth) seen in the south end of Line Z are parallel to the north-south trending lineament that is seen in Line A and C. They are tentatively identified as incipient sinkholes.

8) Overall, it was shown that the combined analysis of resistivity and seismic surface wave data is a powerful tool for mapping shallow structures in karst environments. As noted above, given the resistivities determined for the Ocala Limestone in this study, it should be possible to use the resistivity method alone to map the bedrock surface in the Dougherty Plain region.

REFERENCES

Athanasiou, E.N., P.I. Tsourlos, C.B. Papazachos, and G.N. Tsokas, 2007, Combined weighted inversion of electrical resistivity data from different array types, *Journal of Applied Geophysics,* v. 62, 124-140

Binley, A., 2013, R2 v2.7a Users Manual: Institute of Environmental and Natural Sciences, Lancaster University. A.Binley@lancaster.ac.uk

Baechle, G.T., G.P. Eberli, R.J. Weger, and J.L. Massafero, 2009, Changes in dynamic shear moduli of carbonate rocks with fluid substitution: Geophysics, 74, E135-E147.

Brooks, G.A., and T.L. Allison, 1983, Fracture mapping and ground subsidence susceptibility modeling in covered karst terrain: Dougherty County, Georgia, *in*, P.H. Dougherty, ed., Environmental Karst: Geospeleo Publications, 595-606

Clark Jr., W. Z. and A.C. Zisa, Physiographic Map of Georgia, Georgia Department of Natural Resources, 1976.

Dey, A. and H. F. Morrison, 1979, Resistivity Modeling for Arbitrarily Shaped Two-Dimensional Structures, Geophysical Prospecting, v 27, pp 106-136.

Dobecki, T.L., and S.B. Upchurch, 2006. Geophysical Applications to Detect Sinkholes and Ground Subsidence, The Leading Edge, March 2006, 336-341

Environmental Protection Agency, 2011, "Resistivity Methods", 7 Nov. 2011. Web. 23 July 2014. <http://www.epa.gov/esd/cmb/GeophysicsWebsite/pages/reference/methods/Surface_Geophysical_Methods/Electrical_Methods/Resistivity_Methods.htm>

Fallah-Safari, M., M.K. Hafizi, A. Ghalandarzadeh, 2013, The relationship between clay geotechnical data and clay electrical resistivity, Bollettino di Geofisica Teorica ed Applicata, v. 54, p. 23-38

Ford, D. and P. Williams, 2007, Karst hydrogeology and geomorphology: John Wiley & Sons Ltd.

Geoscan Research. Resistance Meter RM85 Instruction Manual. October, 2012

Gordon, D.W., 2011. Hydrologic Factors Affecting Sinkhole Development in a Well Field in the Karst Dougherty Plain, Southwest of Albany, Georgia. Proceedings of the 2011 Georgia Water Resources Conference, held April 11-13, 2001, at the University of Georgia.

Hicks, D.W., G.E. Gill, and S.A. Longsworth, 1987, Hydrogeology, chemical quality, and availability of ground water in the Upper Floridan Aquifer, Albany area, Georgia: U.S. Geological Survey Water-Resources Investigations Report 87-4145

Hyatt, J.A., and P.M. Jacobs, 1996, Distribution and morphology of sinkholes triggered by flooding following Tropical Storm Alberto at Albany, Georgia, USA: Geomorphology, 17, 305-316.

Kitware, 2010, ParaView 3.6.2, < http://www.kitware.com/news/home/browse/Paraview?2010_01_04&ParaView+3.6.2+Now+Available>

Loke, M.H., 2001, Tutorial: 2-D and 3-D electrical imaging surveys. 1 Sept. 2001. Web. 8 August 2014. <https://pangea.stanford.edu/research/groups/sfmf/docs/DCResistivity_Notes.pdf>

Loke, M.H. . "Electrical imaging surveys for environmental and engineering studies." 1 Jan 1999. Web. 8 August 2014. <http://www.geo.mtu.edu/~ctyoung/LOKENOTE.PDF>.

Mojica A., I. Diaz, C.A. Ho, F. Ogden, R. Pinzon, J. Fabrega, D. Vega, J. Hendrickx, Study of Seasonal Rainfall Infiltration Via Time-Lapse Surface Electrical Resistivity Tomography: Case Study of Gamboa Area, Panama Canal Watershed. *Air, Soil and Water Research* 2013:6 131–139 doi:10.4137/ASWR.S12306.

Moore, D.M., and R.C. Reynolds Jr., X-ray Diffraction and the Identification and Analysis of Clay Minerals, New York: Oxford University Press, 1997. Print

Nyquist, J.E., J.S. Peake, M.J.S. Roth, 2007, Comparison of an optimized resistivity array with dipole-dipole soundings in karst terrain, *Geophysics*, v. 72, p. F139-F144

Odum, J.K., R.A. Williams, W.J. Stephenson, D.M. Worley, C. von Hillebrandt-Andrade, E. Asencio, H. Irizarry, and A. Cameron, 2007, Near-surface shear wave velocity versus depth profiles, Vs 30, and NEHRP classifications for 27 sites in Puerto Rico: USGS Open-File Report 2007-1174

Park, C.B., R.D. Miller, J. Xia, and J. Ivanov, 2007, Multichannel analysis of surface waves (MASW) - active and passive methods: The Leading Edge, 26, 60-64.

Park, S., C. Kim, J.S. Son, M.J. Yi, J.H. Kim, 2009, Detection of cavities in a karst area by means of a 3D electrical resistivity technique, *Exploration Geophysics,* v. 40, p. 27-32.

Parker Jr., E.H., 2010, Multi-channel Analysis of Surface Waves (MASW) in Karst Terrain, Southwest Georgia: Implications for detecting subsidence features and lineaments: M.S. thesis, University of Georgia, Athens, Georgia

Parker Jr., E.H. and R.B. Hawman, 2012. Multi-channel Analysis of Surface Waves (MASW) in Karst Terrain, Southwest Georgia: Implications for Detecting Anomalous Features and Fracture Zones, Journal of Environmental and Engineering Geophysics, 11006, 129-150.

Robinson, E.S., and C. Coruh, Basic Exploration Geophysics, John Wiley & Sons, Inc. 445-480, 1988. Print.

Schoor, M.V., 2002, Detection of sinkholes using 2D electrical resistivity imaging, *Journal of Applied Geophysics,* v. 50, p. 393-399

Stein, Seth, and Michael Wysession. " Inverse Problems." Chp. 7, pg. 9. An introduction to seismology, earthquakes, and earth structure. Malden, MA: Blackwell Pub., 2003. Print.

Stewart, L.M., D. Warner, and B.J. Dawson, 1999, Hydrogeology and water quality of the Upper Floridan Aquifer, western Albany area, Georgia: USGS Water-Resources Investigations Report 99-4140.

Stummer, P., H. Maurer, and A. G. Green, 2004, Experimental design: Electrical resistivity data sets that provide optimum subsurface information: Geophysics, 69, 120–139.

Telford, W.M., L.P. Geldhart, and R.E. Sheriff, Applied Geophysics Second Edition, Cambridge University Press, 283-335, 1990. Print

Wylie, B.; Jubran, R.; Carnes, C.; Hundley, B.; Gallagher, E.; Nguyen, T.; Khalifa, M.; Schroeder, P.; Dowd, J.; Hawman, R. Shallow Geophysical Studies of Natural Hazards and Groudwater Systems in the Southeastern US: Geological Society of America South Eastern Section Meeting Conference, Blacksburg, Virginia, April 9-10, 2014, poster forum.

Youssef, A.M., H. El-Kaliouby, Y.A. Zabramawi, 2012, Sinkhole detection using electrical resistivity tomography in Saudi Arabia, *Journal of Geophysics and Engineering*, v. 9, p. 655-663.

APPENDIX A

Data Offset Plots

In this appendix, common-offset plots of the raw resistance data for each line are displayed. The plots show mean values with error bars representing the scatter at that measurement. The vertical axis corresponds to the median values of resistance in ohms, times a factor of 10, the instrument gain.

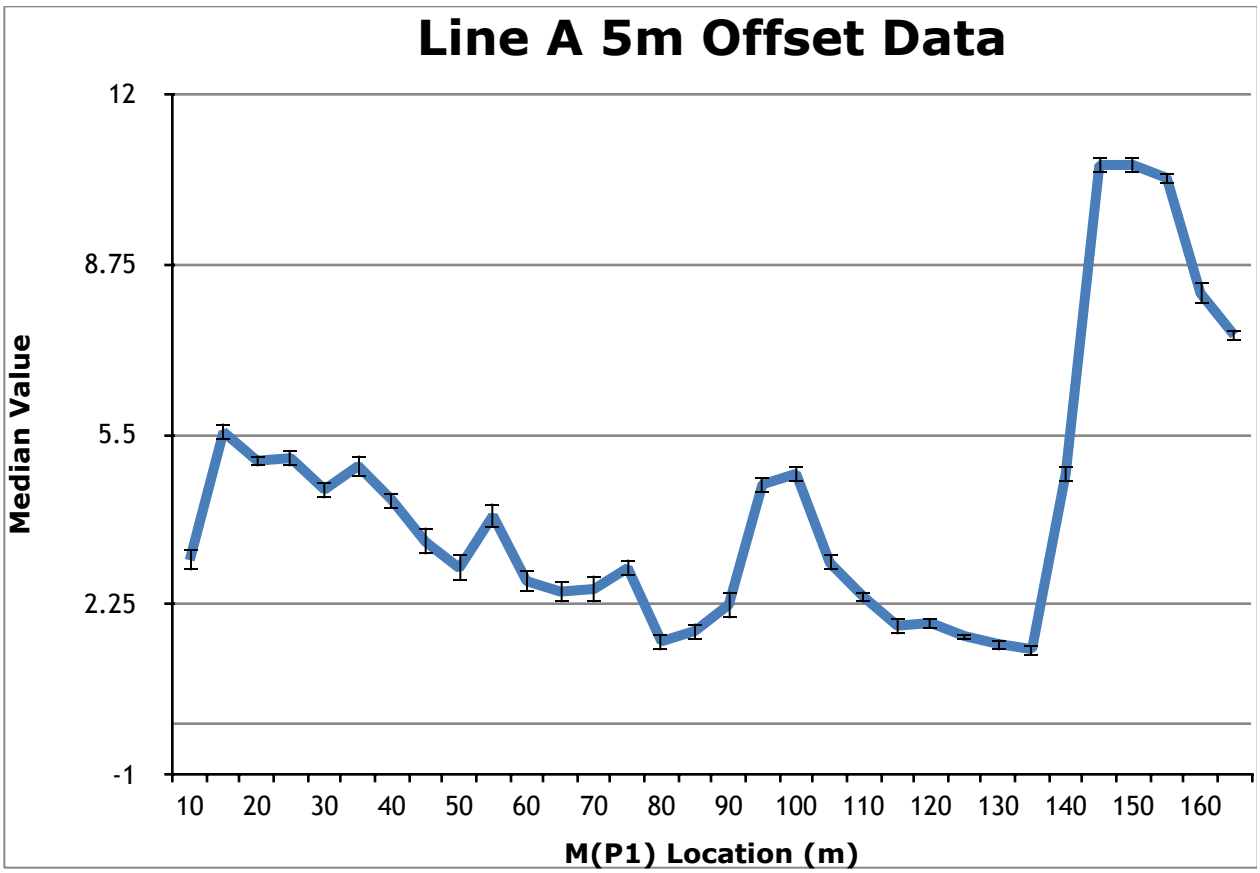
Line A 5m Offset Data
Median Value
12
8.75
5.5
2.25
-1
10
20
30
40
50
60
70
80
90
100
110
120
130
140
150
160
M(P1) Location (m)

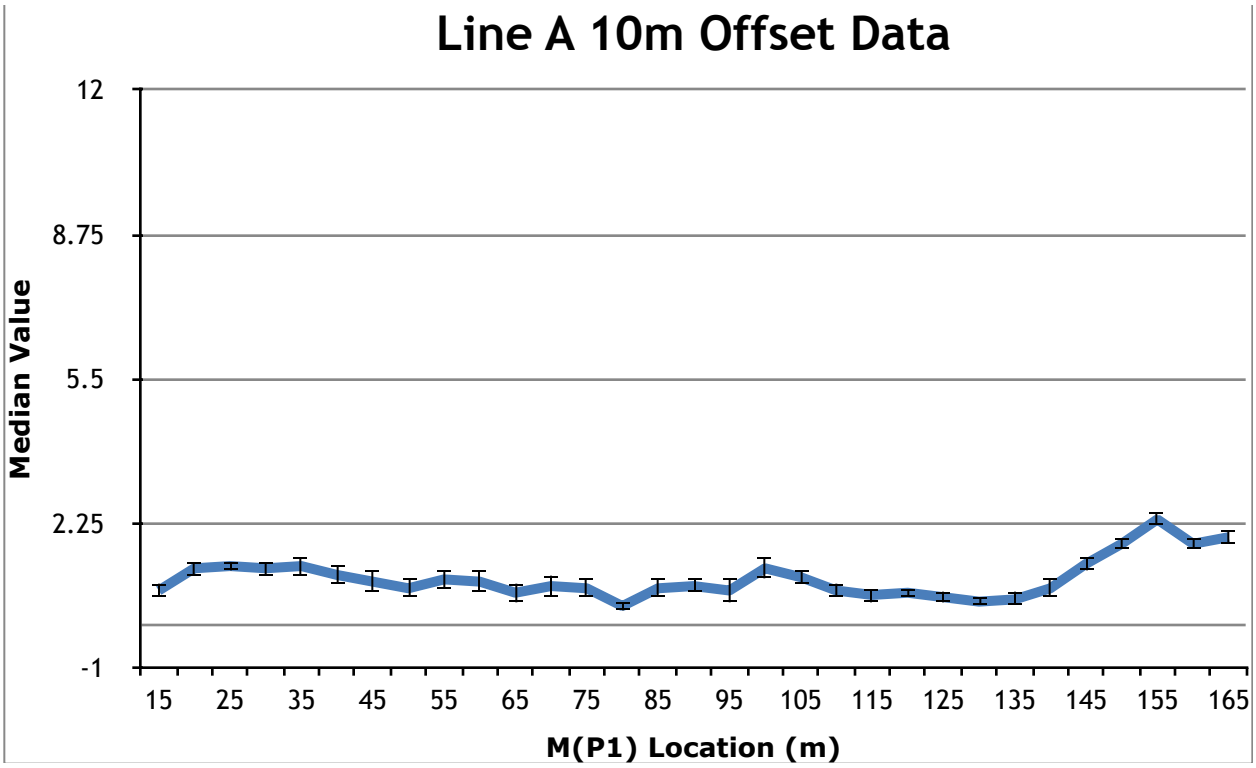
Line A 10m Offset Data
Median Value
12
8.75
5.5
2.25
-1
15
25
35
45
55
65
75
85
95
105
115
125
135
145
155
165
M(P1) Location (m)

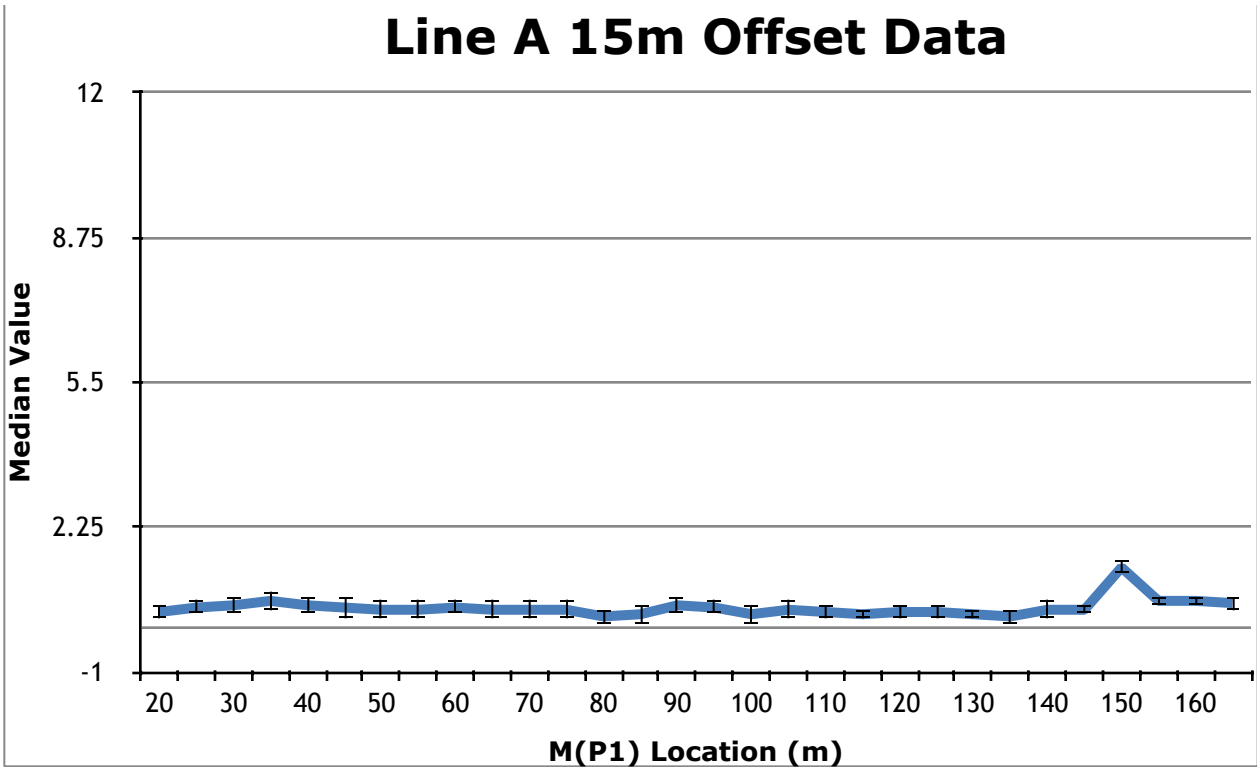
Line A 15m Offset Data
Median Value
12
8.75
5.5
2.25
-1
20
30
40
50
60
70
80
90
100
110
120
130
140
150
160
M(P1) Location (m)

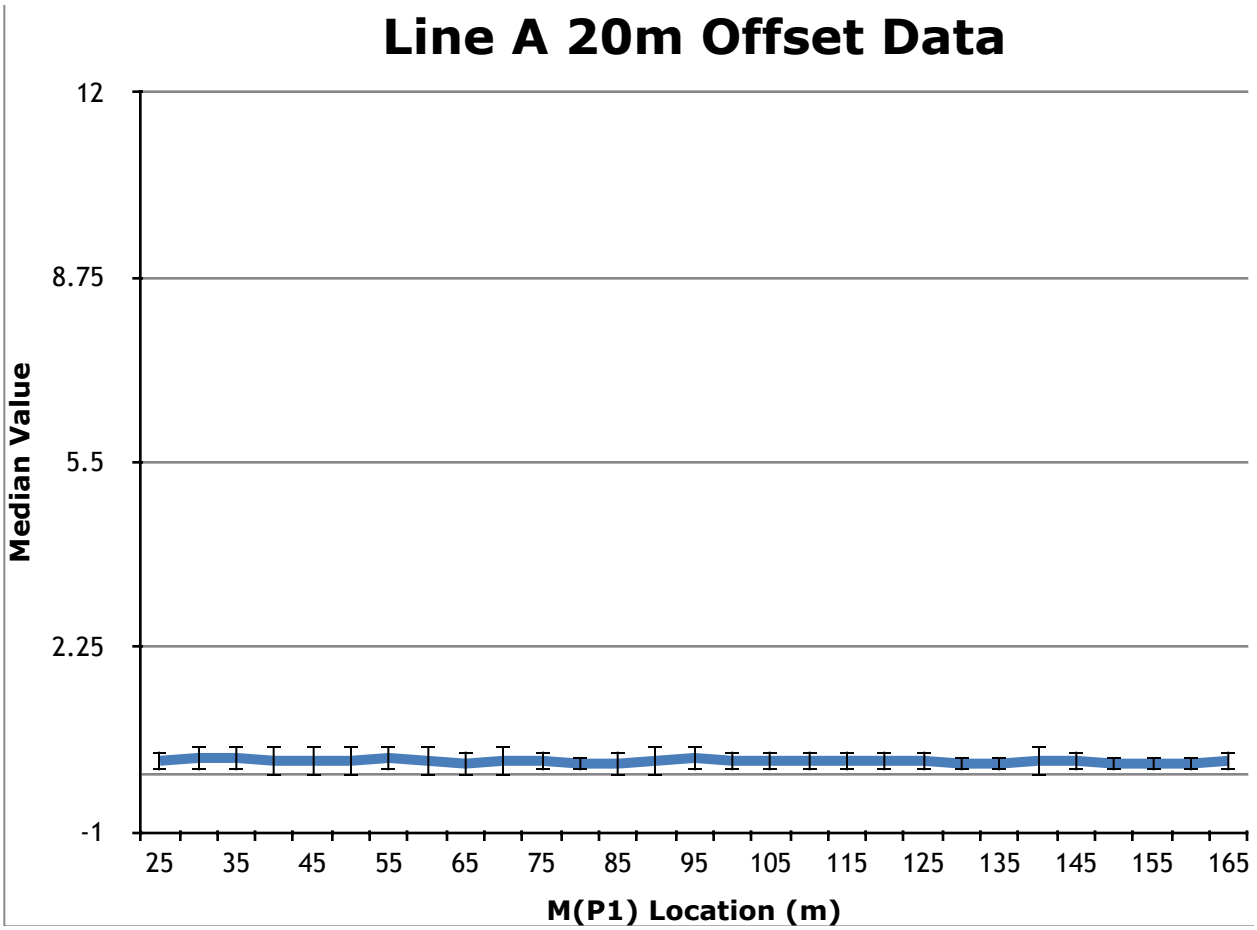
Line A 20m Offset Data
12
8.75
5.5
2.25
-1
Median Value
25
35
45
55
65
75
85
95
105
115
125
135
145
155
165
M(P1) Location (m)

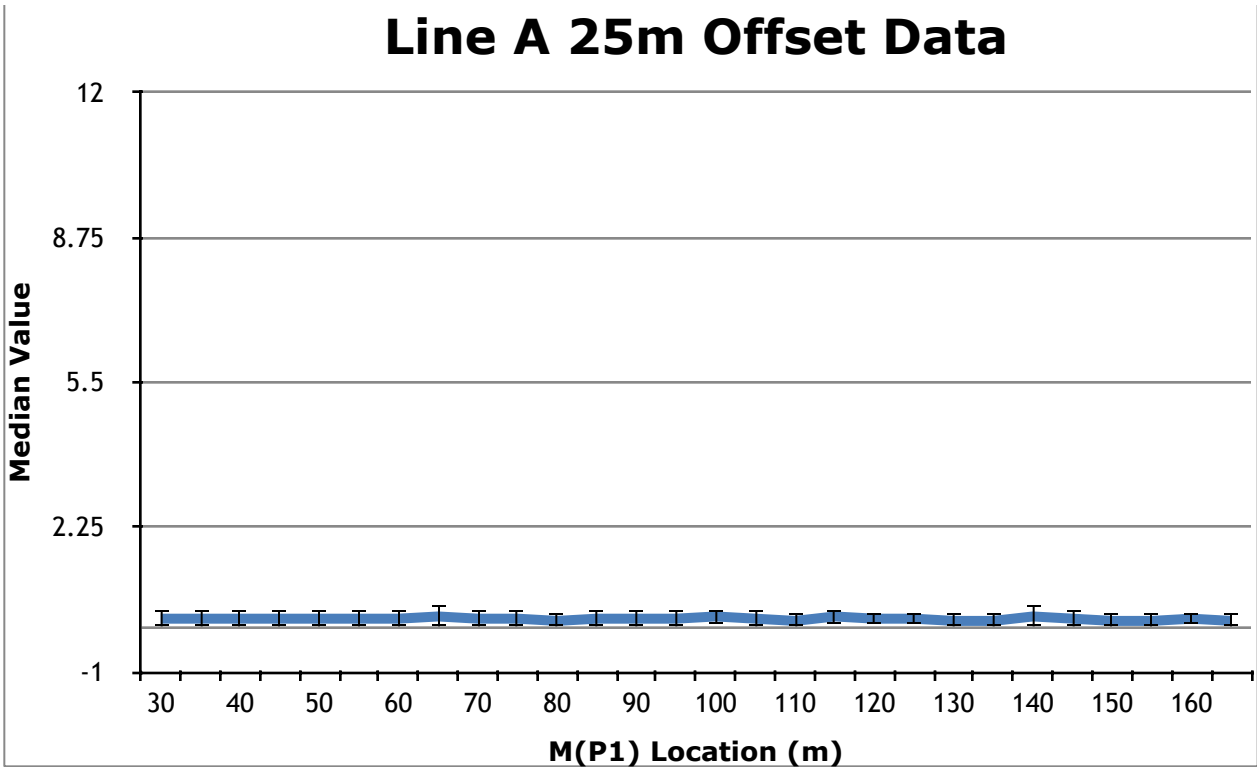
Line A 25m Offset Data
12
8.75
5.5
2.25
-1
Median Value
30
40
50
60
70
80
90
100
110
120
130
140
150
160
M(P1) Location (m)

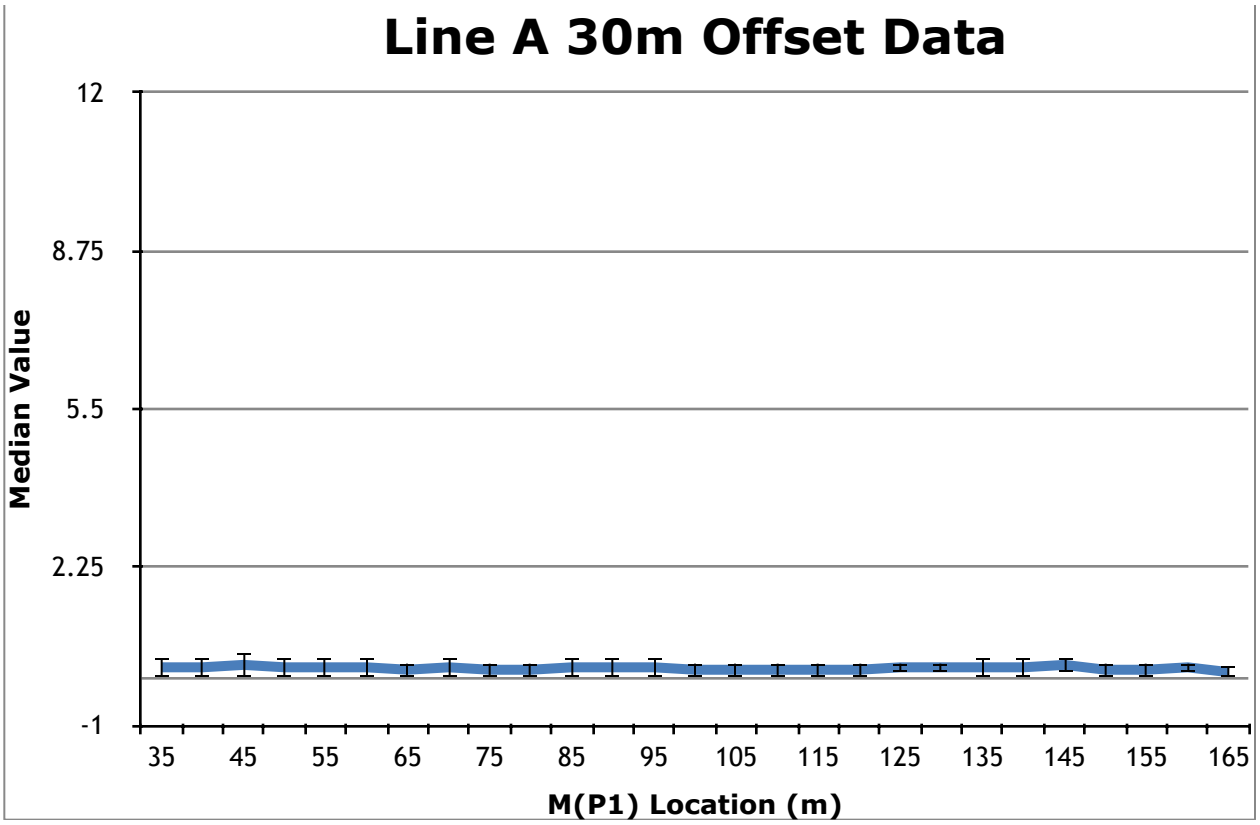
Line A 30m Offset Data
12
8.75
5.5
2.25
-1
Median Value
35
45
55
65
75
85
95
105
115
125
135
145
155
165
M(P1) Location (m)

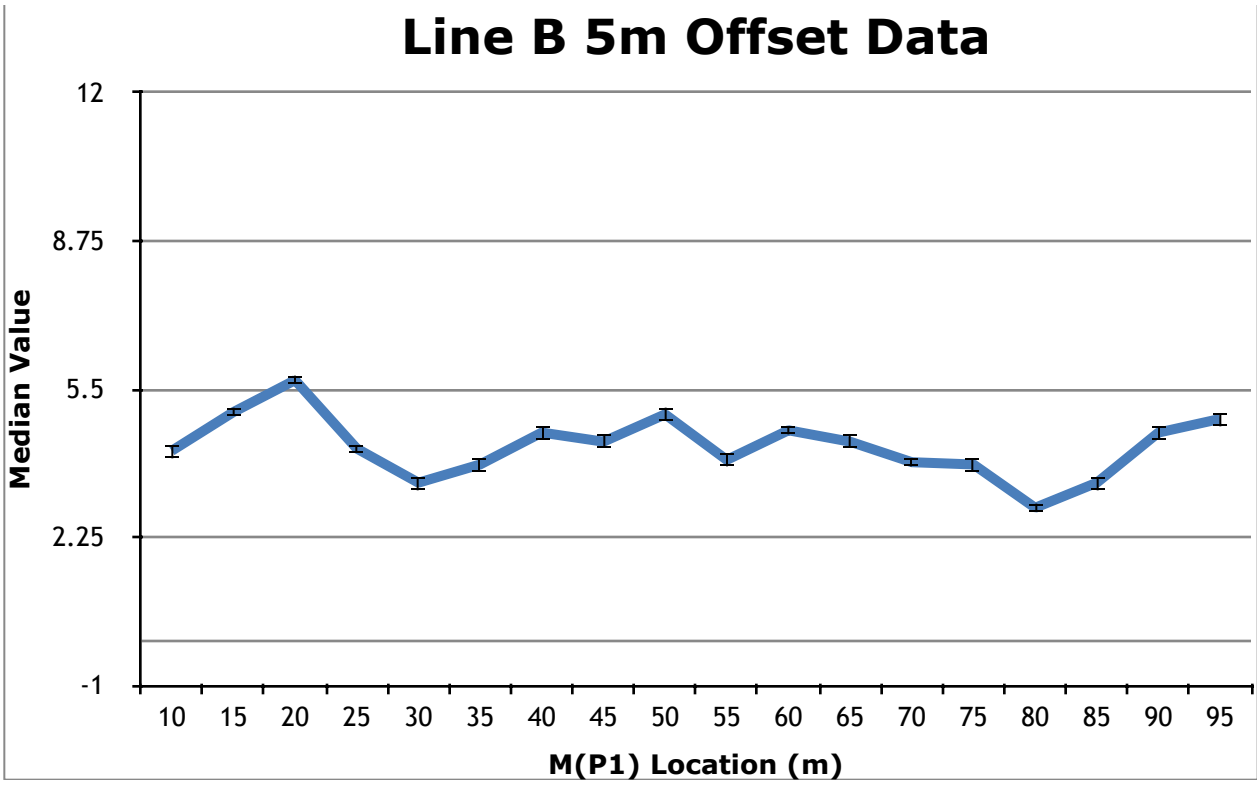
Line B 5m Offset Data
Median Value
12
8.75
5.5
2.25
-1
10 15 20 25 30 35 40 45 50 55 60 65 70 75 80 85 90 95
M(P1) Location (m)

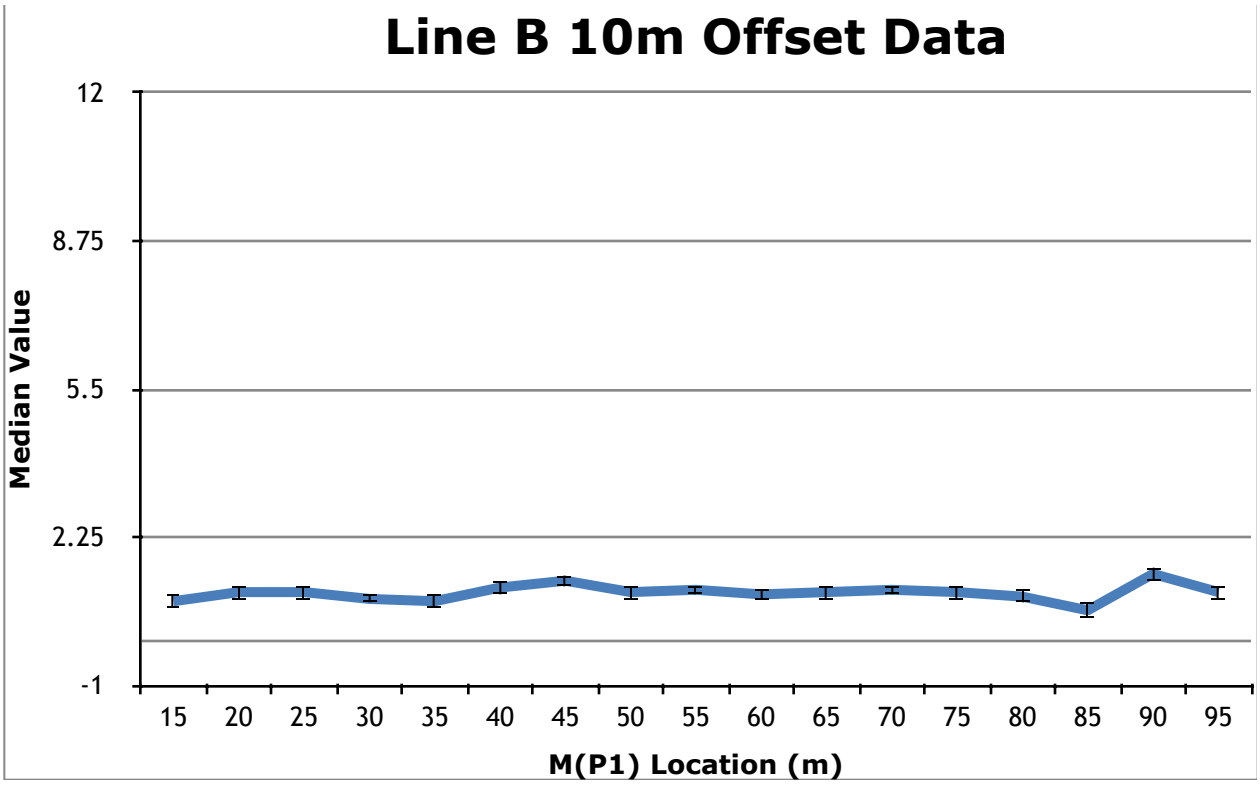
Line B 10m Offset Data
Median Value
12
8.75
5.5
2.25
-1
15
20
25
30
35
40
45
50
55
60
65
70
75
80
85
90
95
M(P1) Location (m)

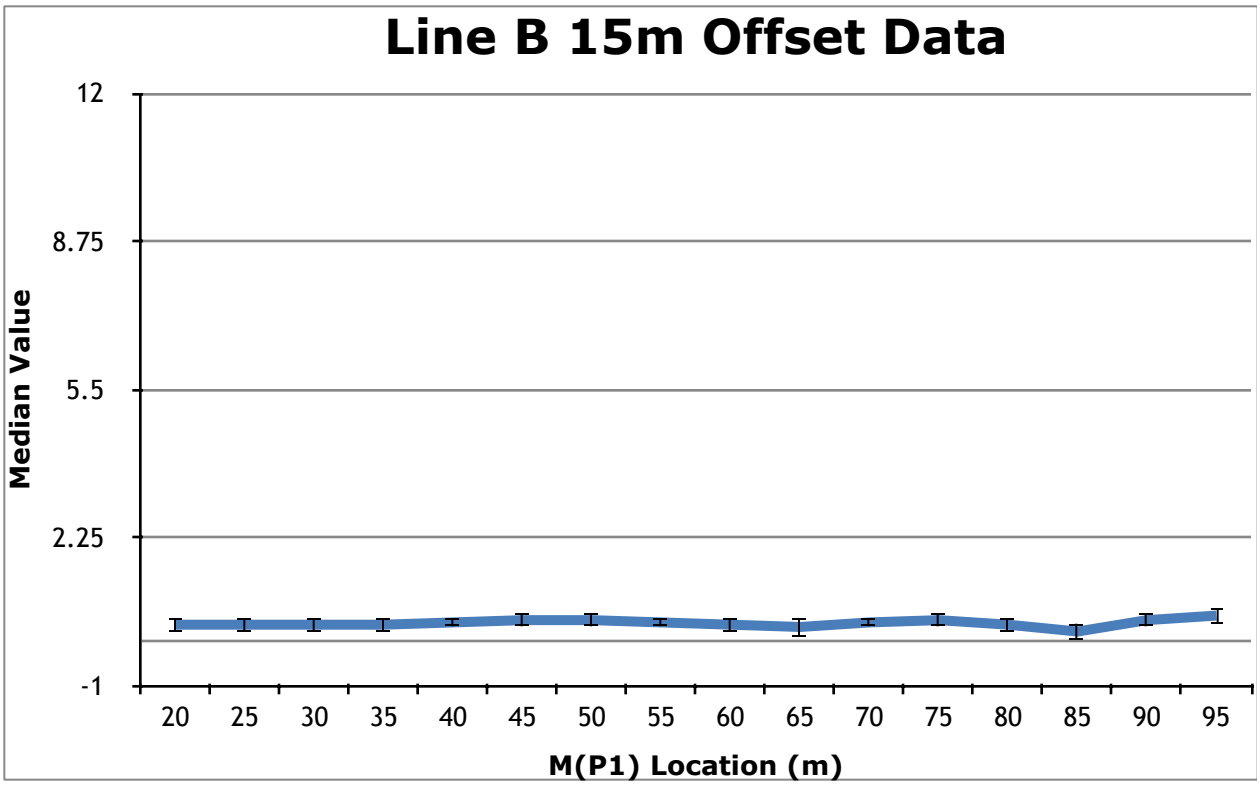
Line B 15m Offset Data
Median Value
12
8.75
5.5
2.25
-1
20
25
30
35
40
45
50
55
60
65
70
75
80
85
90
95
M(P1) Location (m)

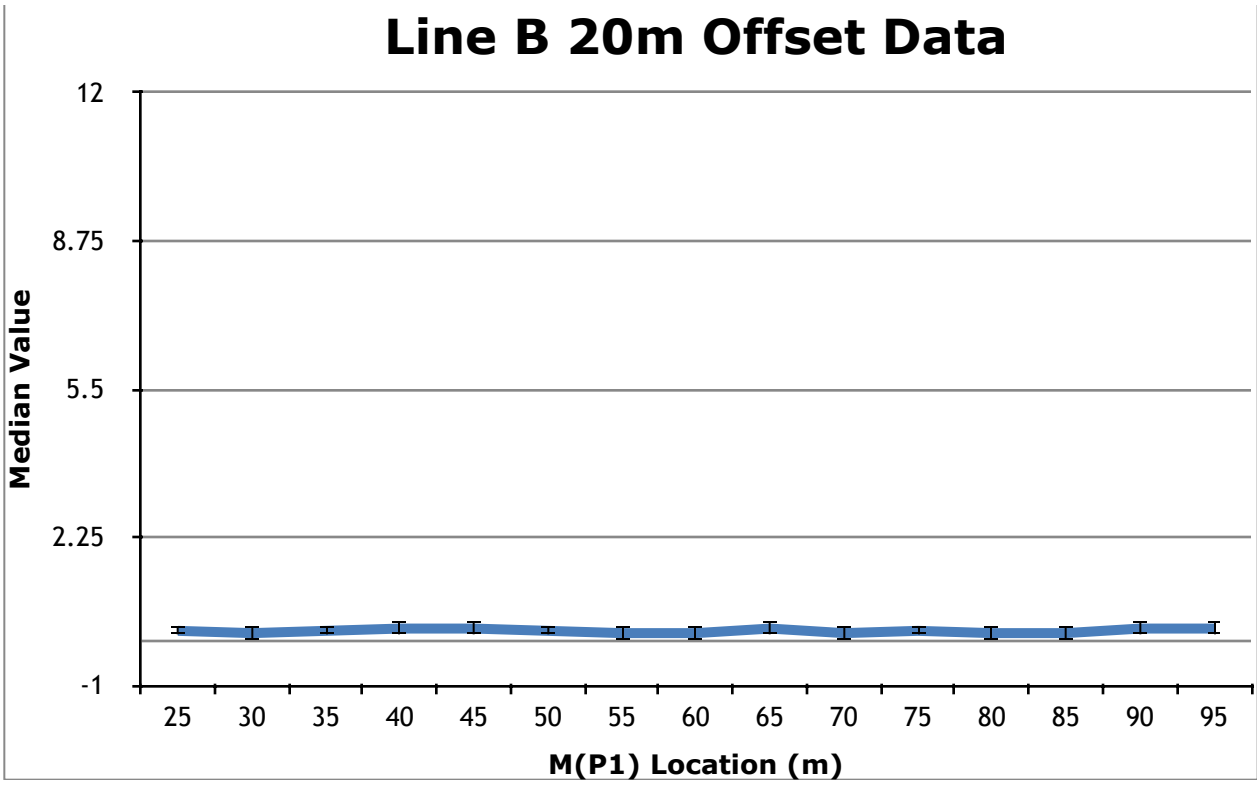
Line B 20m Offset Data
Median Value
12
8.75
5.5
2.25
-1
25
30
35
40
45
50
55
60
65
70
75
80
85
90
95
M(P1) Location (m)

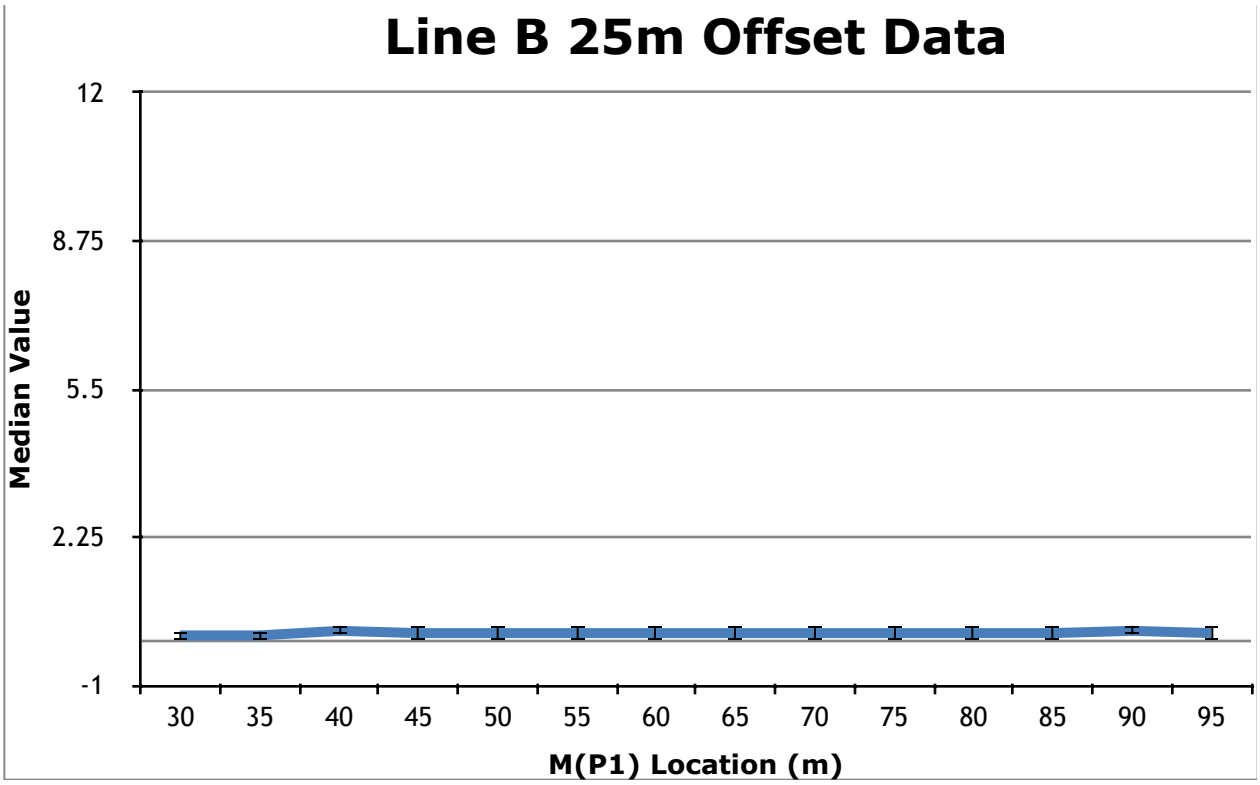
Line B 25m Offset Data
Median Value
12
8.75
5.5
2.25
-1
30
35
40
45
50
55
60
65
70
75
80
85
90
95
M(P1) Location (m)

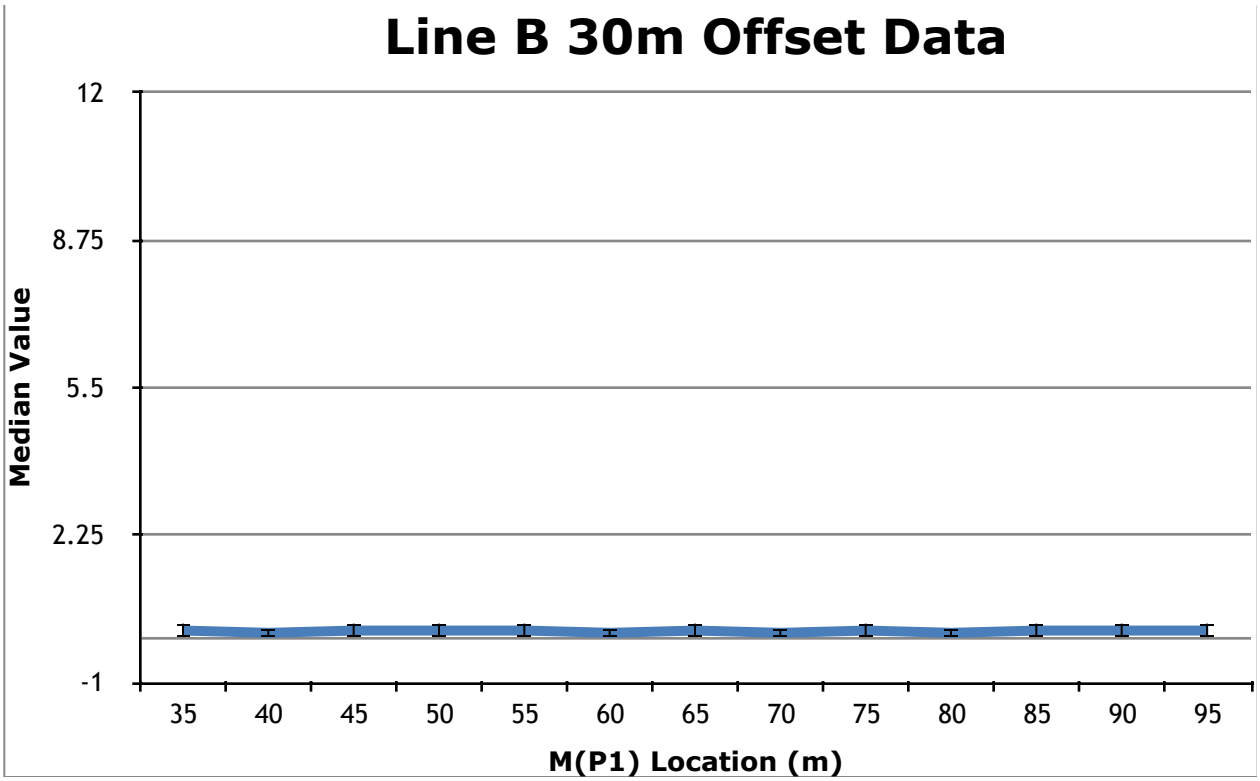
Line B 30m Offset Data
12
8.75
5.5
2.25
-1
Median Value
35
40
45
50
55
60
65
70
75
80
85
90
95
M(P1) Location (m)

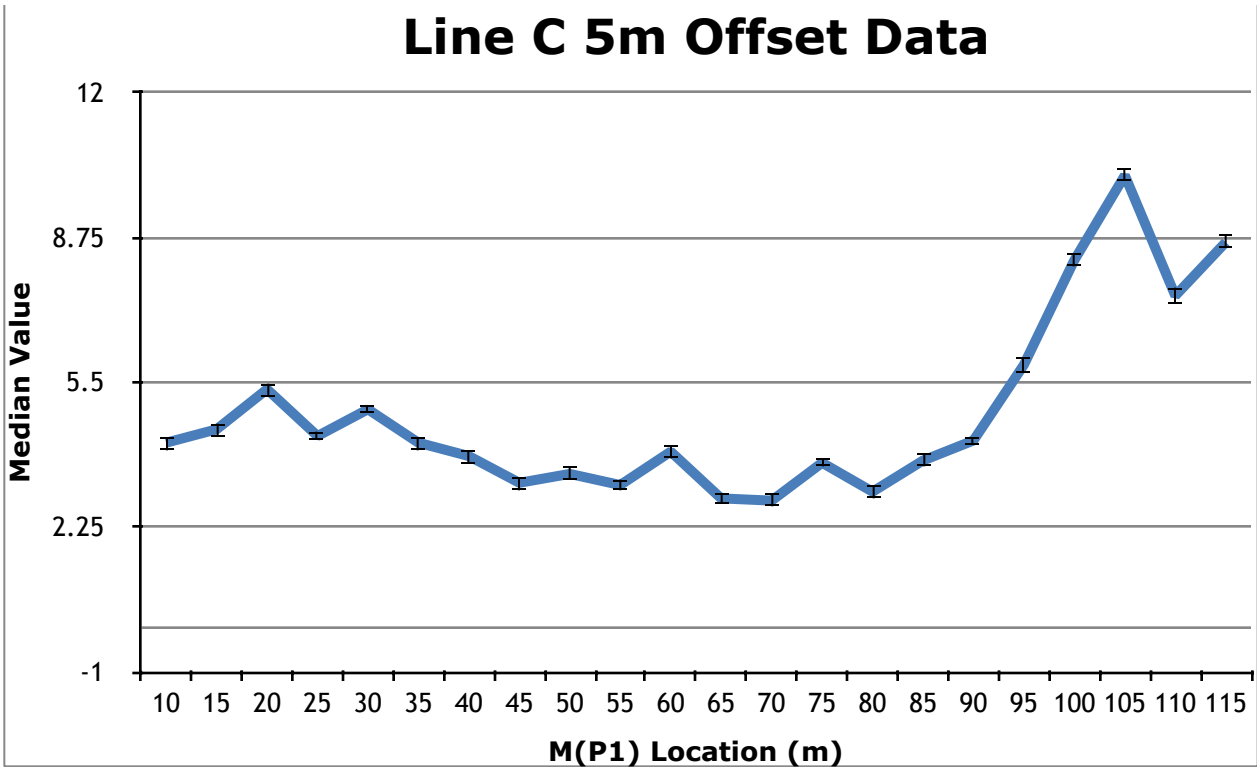
Line C 5m Offset Data
Median Value
12
8.75
5.5
2.25
-1
10 15 20 25 30 35 40 45 50 55 60 65 70 75 80 85 90 95 100 105 110 115
M(P1) Location (m)

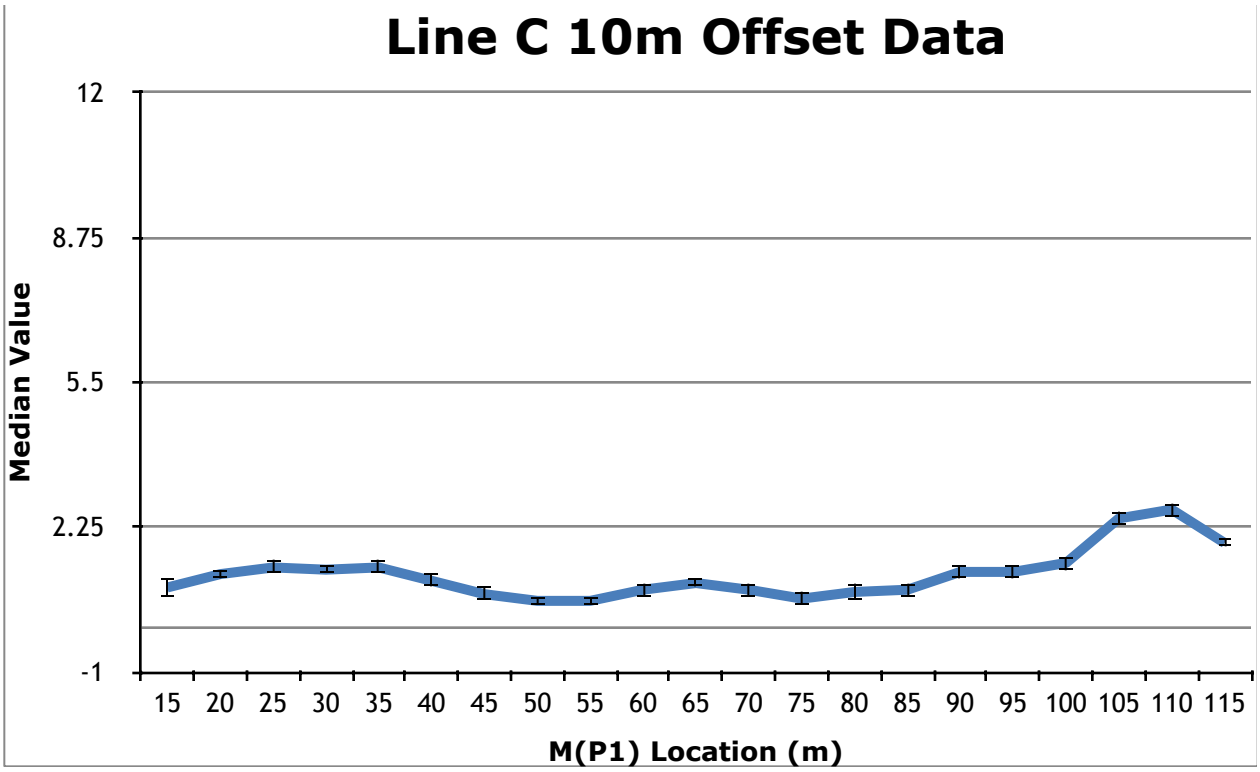
Line C 10m Offset Data
Median Value
12
8.75
5.5
2.25
-1
15 20 25 30 35 40 45 50 55 60 65 70 75 80 85 90 95 100 105 110 115
M(P1) Location (m)

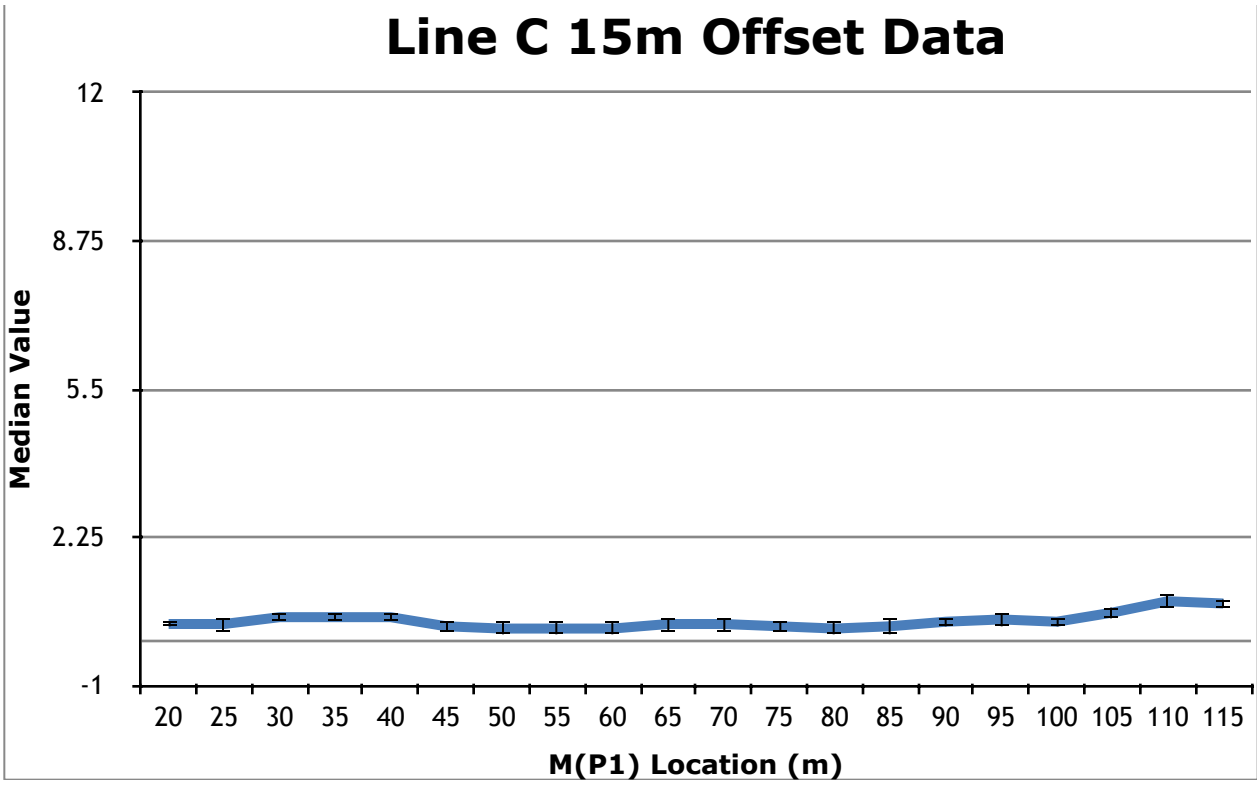
Line C 15m Offset Data
Median Value
12
8.75
5.5
2.25
-1
20 25 30 35 40 45 50 55 60 65 70 75 80 85 90 95 100 105 110 115
M(P1) Location (m)

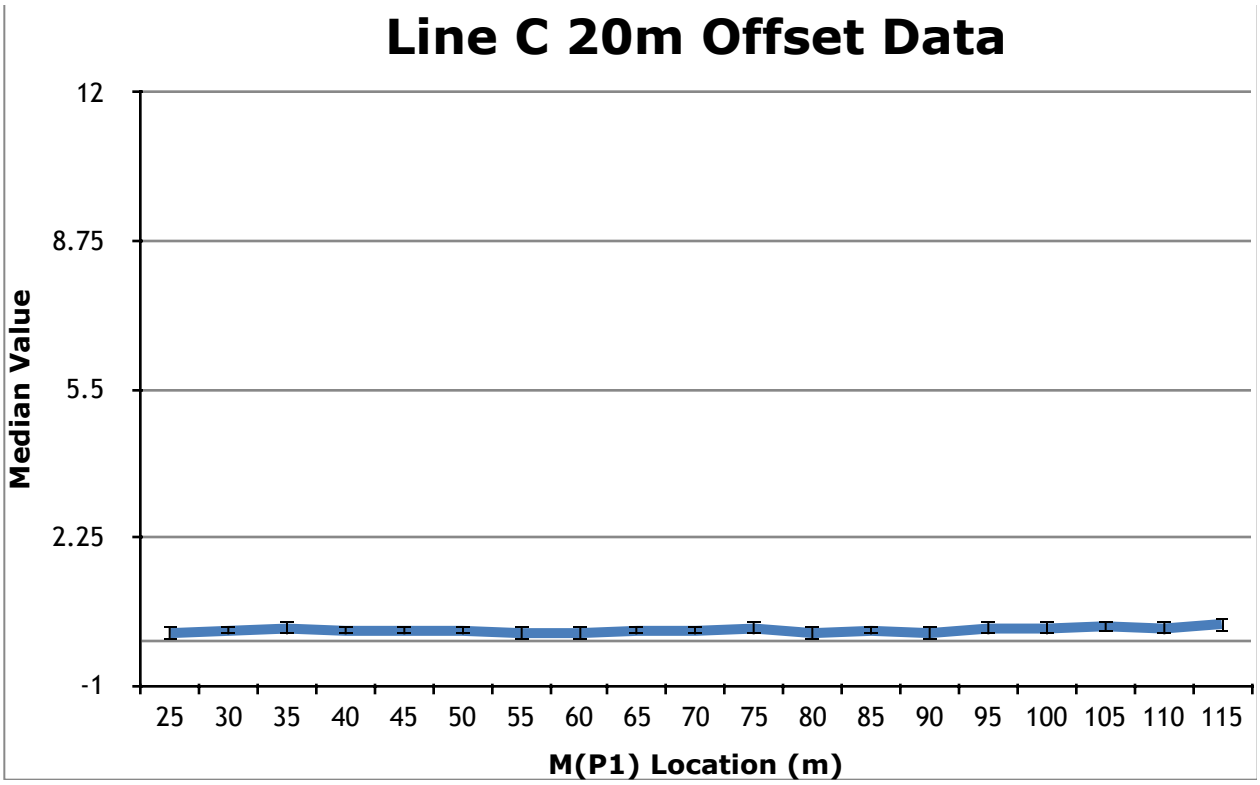
Line C 20m Offset Data
Median Value
12
8.75
5.5
2.25
-1
25 30 35 40 45 50 55 60 65 70 75 80 85 90 95 100 105 110 115
M(P1) Location (m)

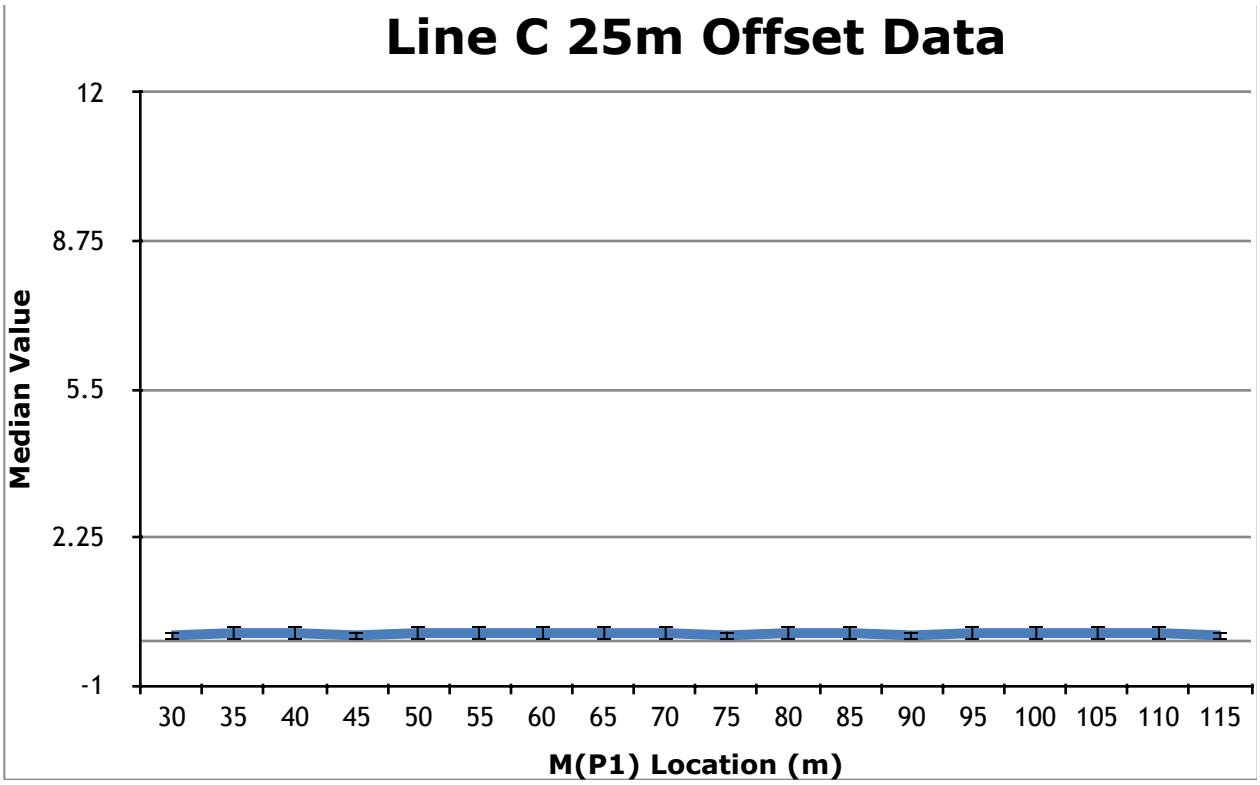
Line C 25m Offset Data
Median Value
12
8.75
5.5
2.25
-1
30
35
40
45
50
55
60
65
70
75
80
85
90
95
100
105
110
115
M(P1) Location (m)

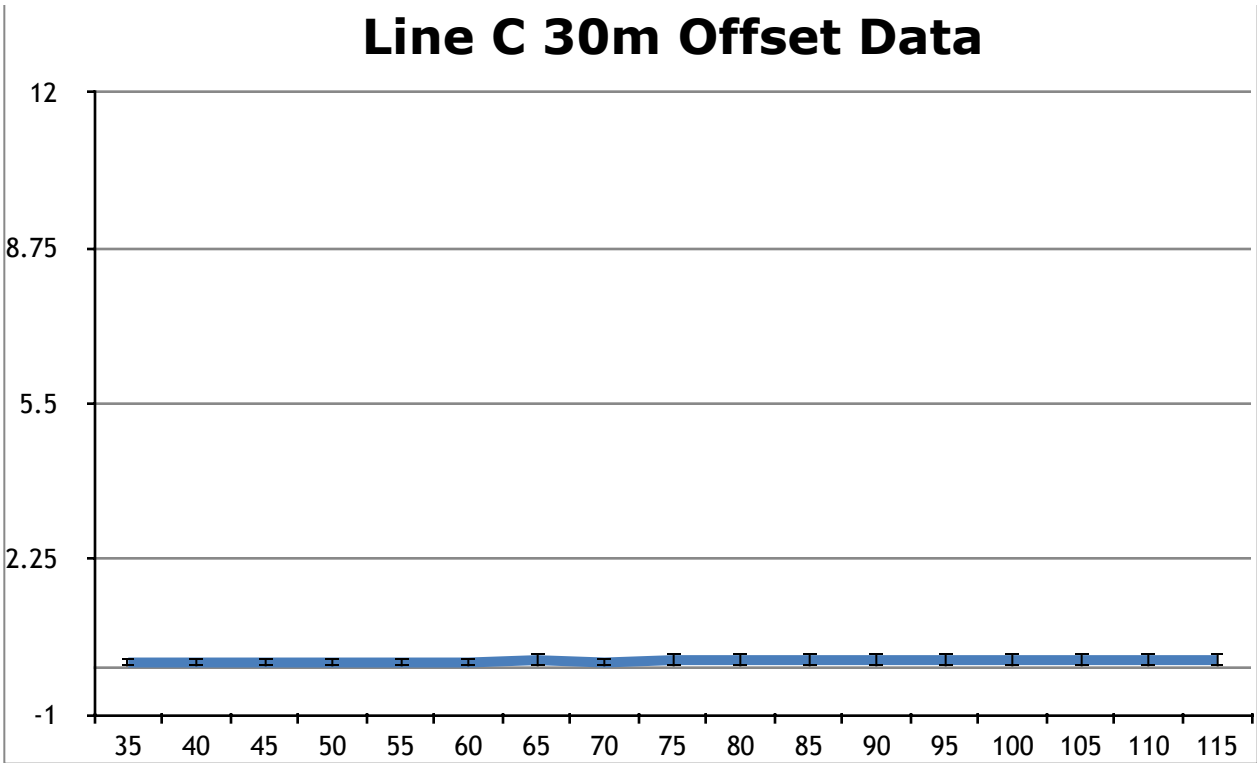
Line C 30m Offset Data
12
8.75
5.5
2.25
-1
35
40
45
50
55
60
65
70
75
80
85
90
95
100
105
110
115

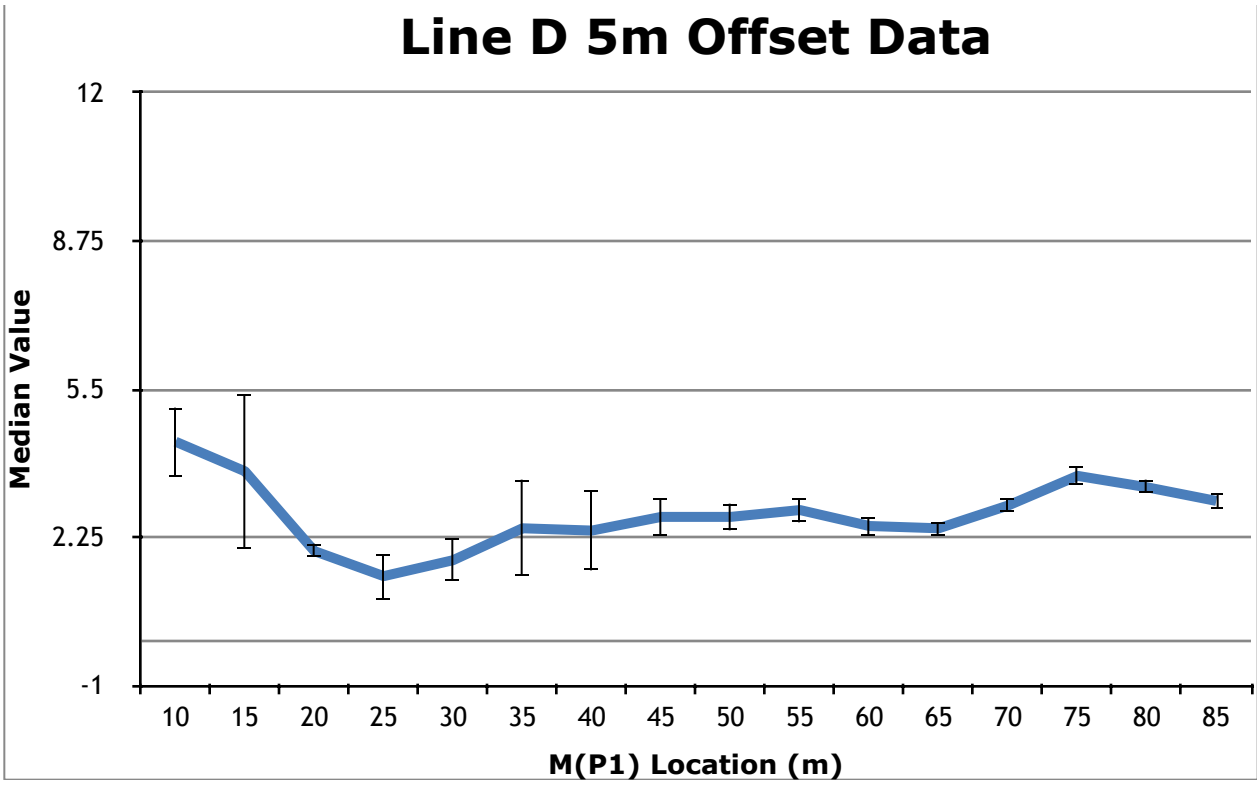
Line D 5m Offset Data
Median Value
12
8.75
5.5
2.25
-1
10
15
20
25
30
35
40
45
50
55
60
65
70
75
80
85
M(P1) Location (m)

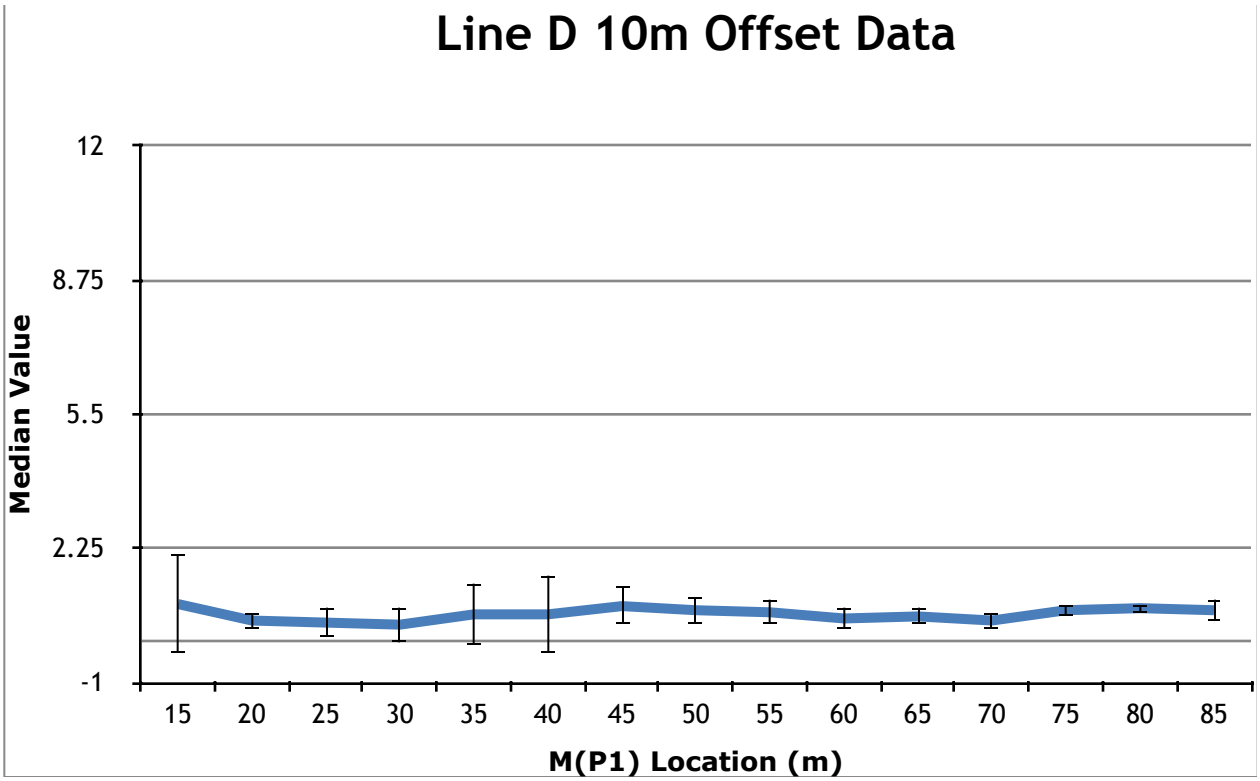
Line D 10m Offset Data
Median Value
12
8.75
5.5
2.25
-1
15
20
25
30
35
40
45
50
55
60
65
70
75
80
85
M(P1) Location (m)

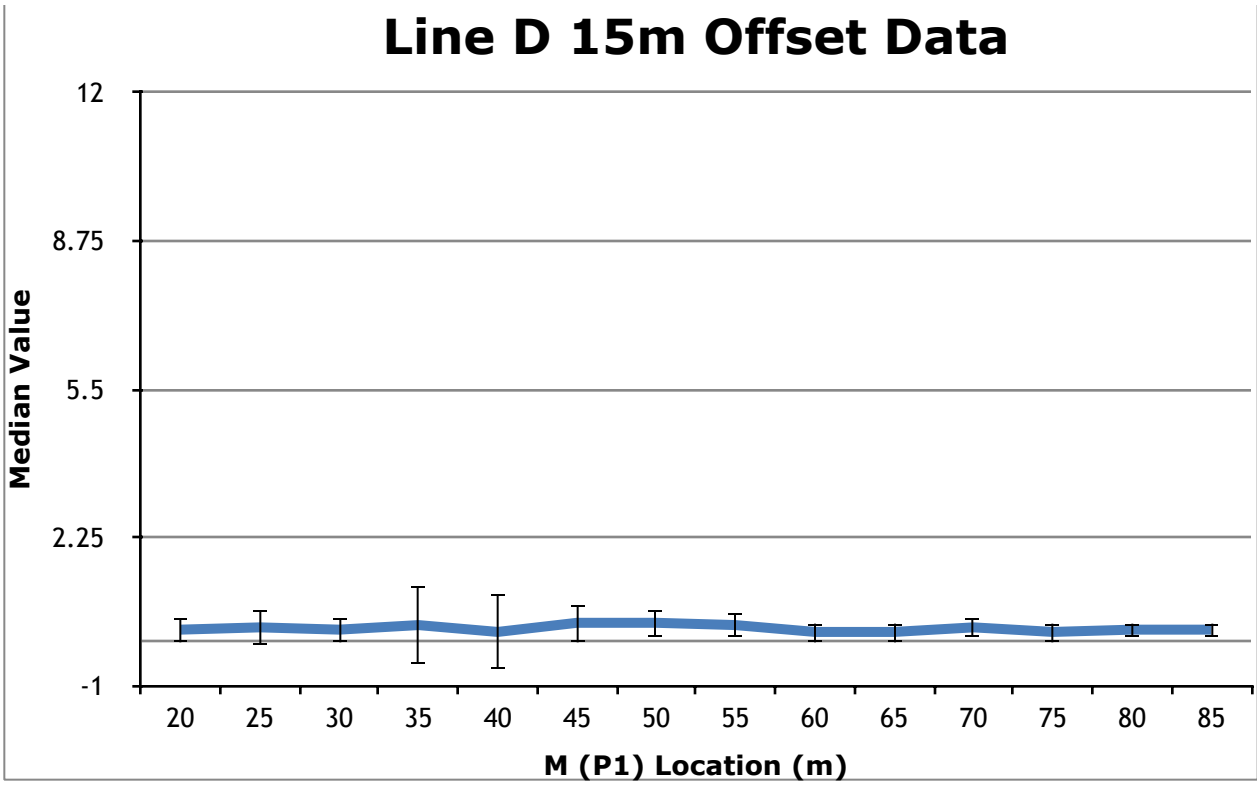
Line D 15m Offset Data
Median Value
12
8.75
5.5
2.25
-1
20
25
30
35
40
45
50
55
60
65
70
75
80
85
M (P1) Location (m)

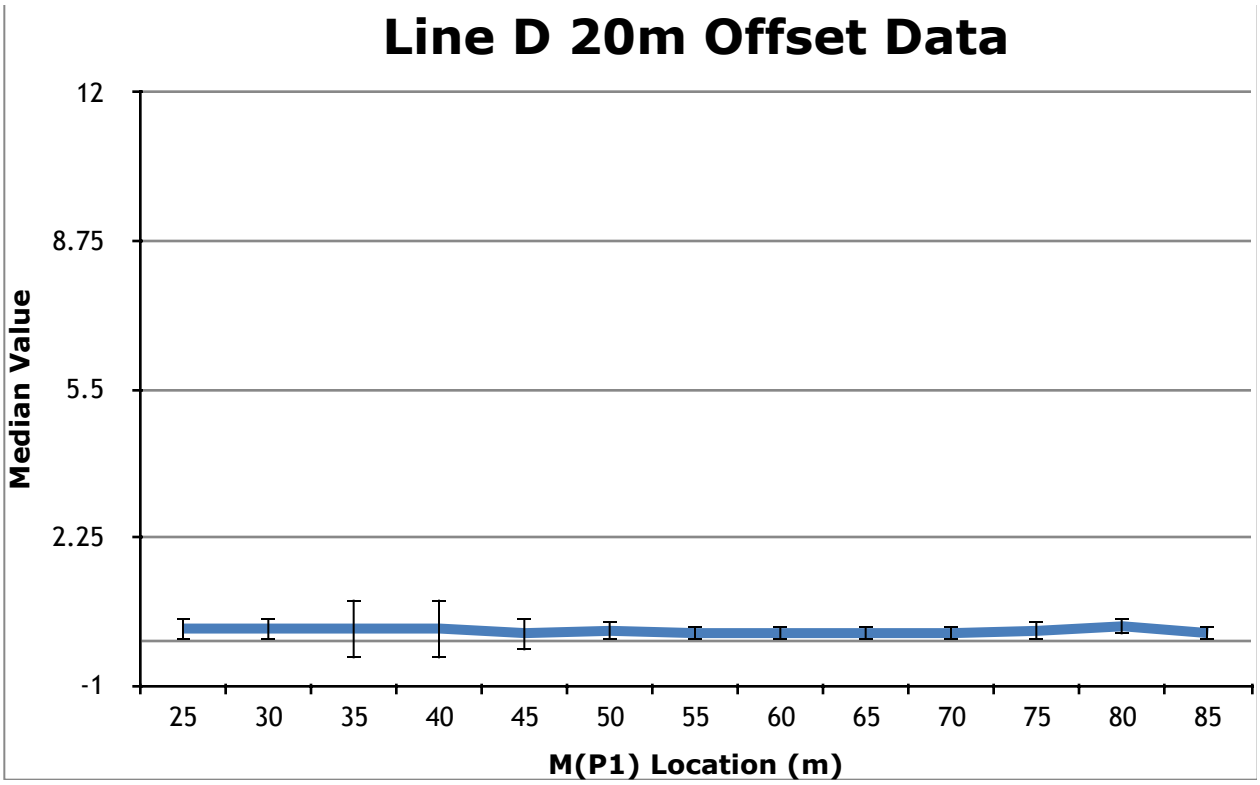
Line D 20m Offset Data
Median Value
12
8.75
5.5
2.25
-1
25
30
35
40
45
50
55
60
65
70
75
80
85
M(P1) Location (m)

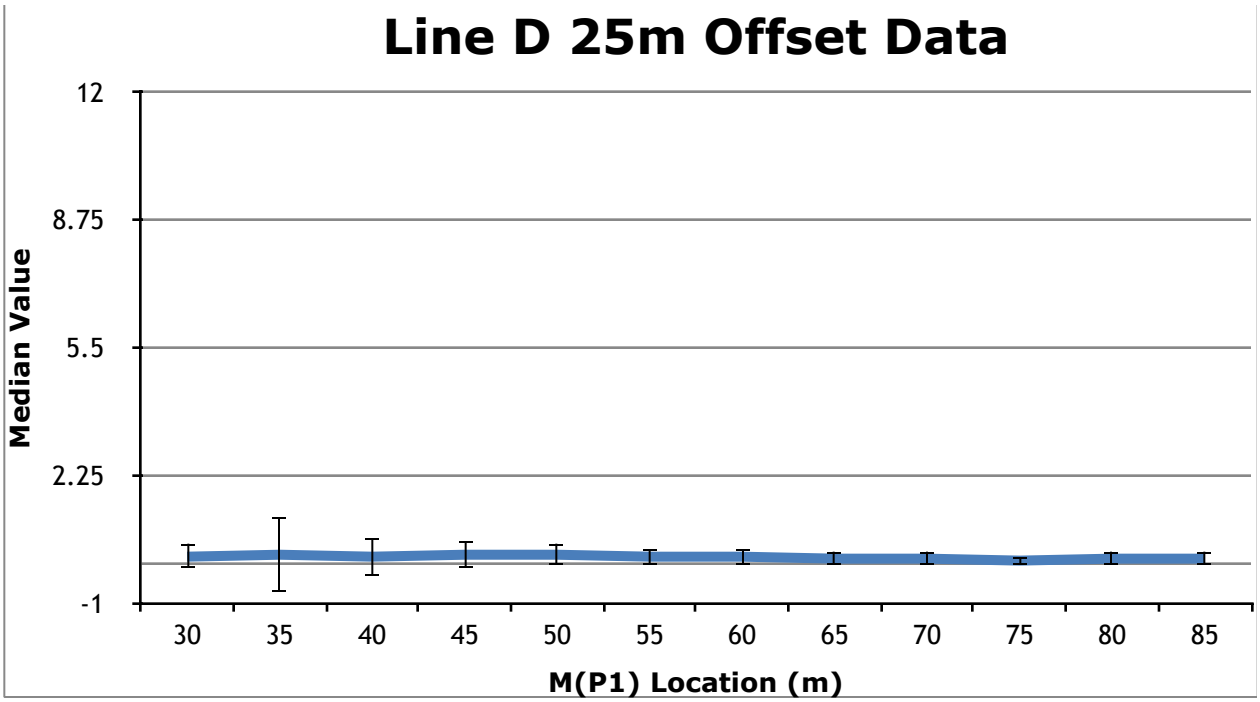
Line D 25m Offset Data
12
8.75
5.5
2.25
-1
Median Value
30
35
40
45
50
55
60
65
70
75
80
85
M(P1) Location (m)

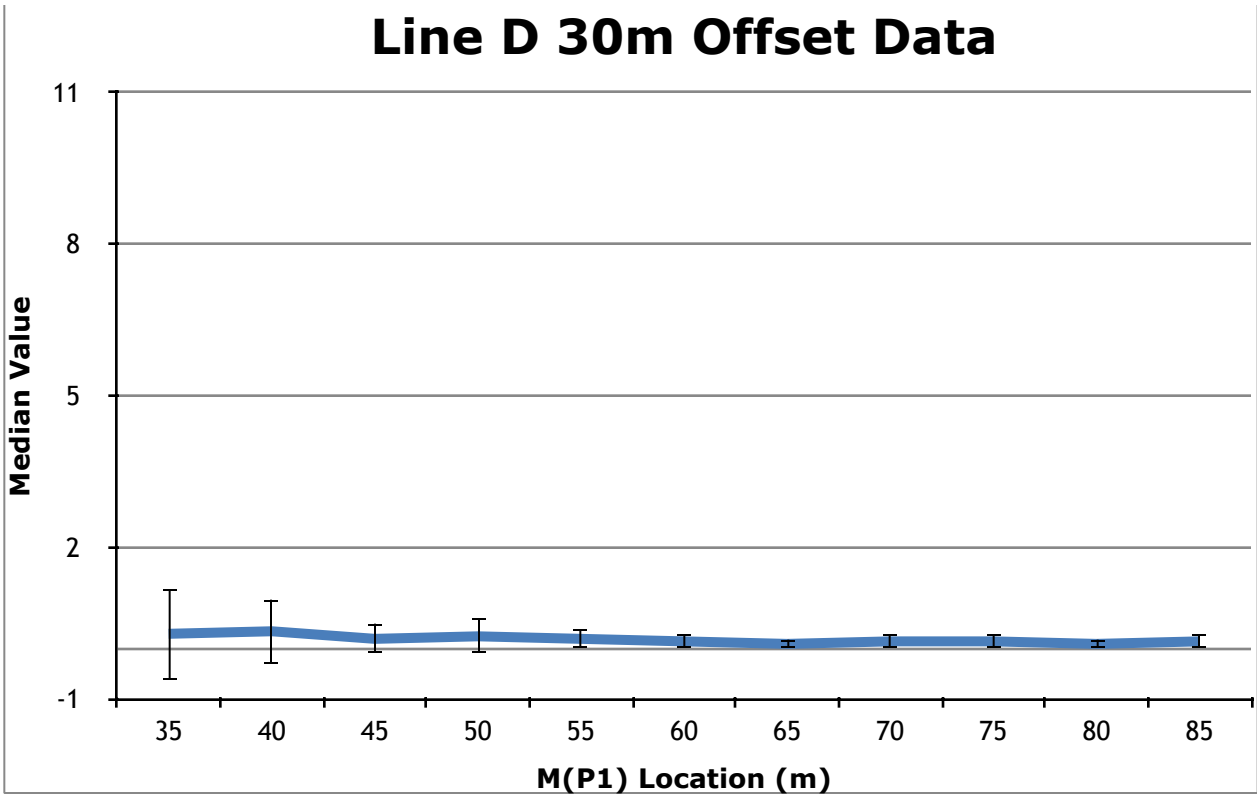
Line D 30m Offset Data
11
8
5
2
-1
Median Value
35
40
45
50
55
60
65
70
75
80
85
M(P1) Location (m)

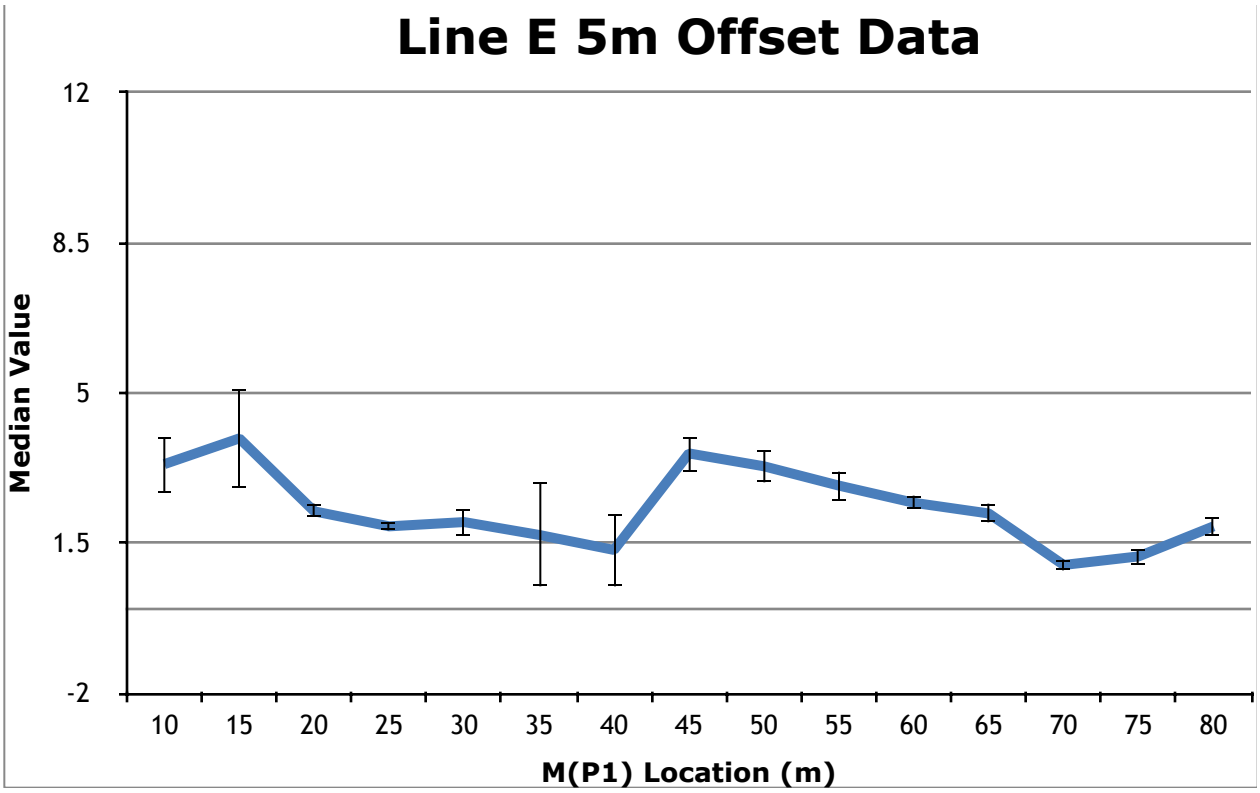
Line E 5m Offset Data
Median Value
12
8.5
5
1.5
-2
10
15
20
25
30
35
40
45
50
55
60
65
70
75
80
M(P1) Location (m)

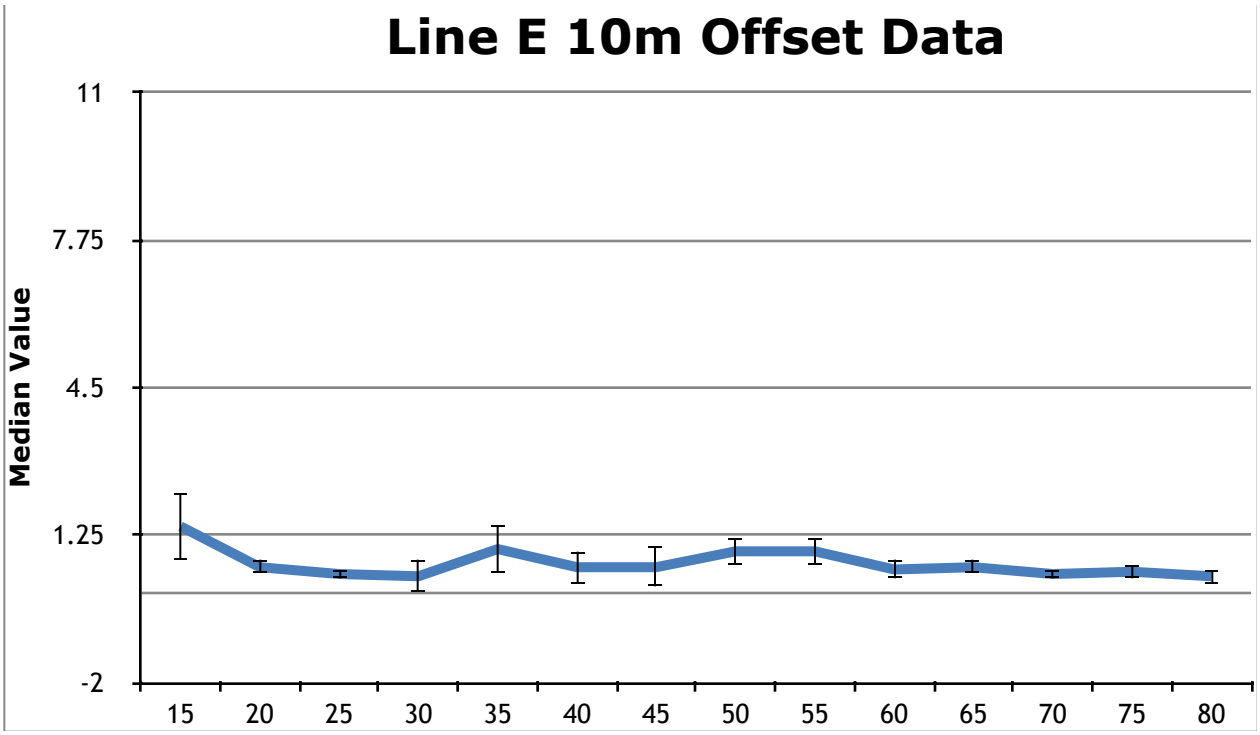
Line E 10m Offset Data
Median Value
11
7.75
4.5
1.25
-2
15
20
25
30
35
40
45
50
55
60
65
70
75
80

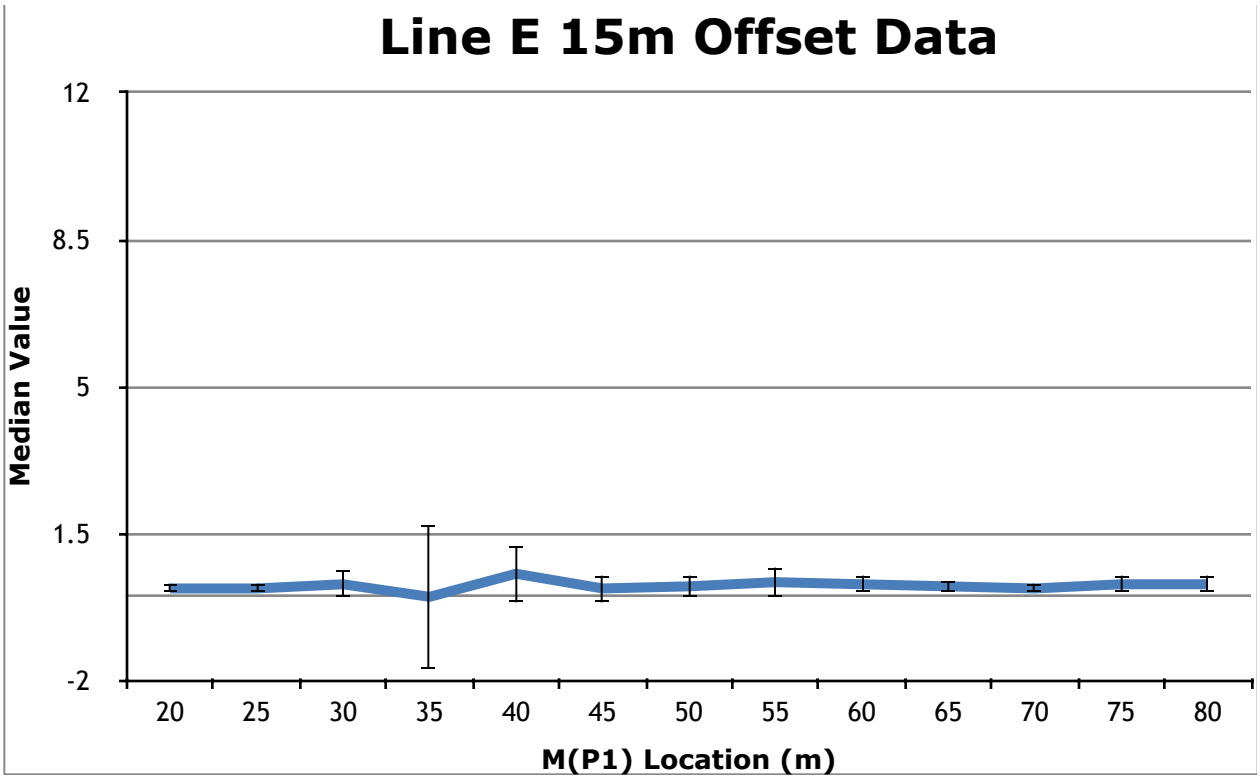
Line E 15m Offset Data
12
8.5
5
1.5
-2
Median Value
20
25
30
35
40
45
50
55
60
65
70
75
80
M(P1) Location (m)

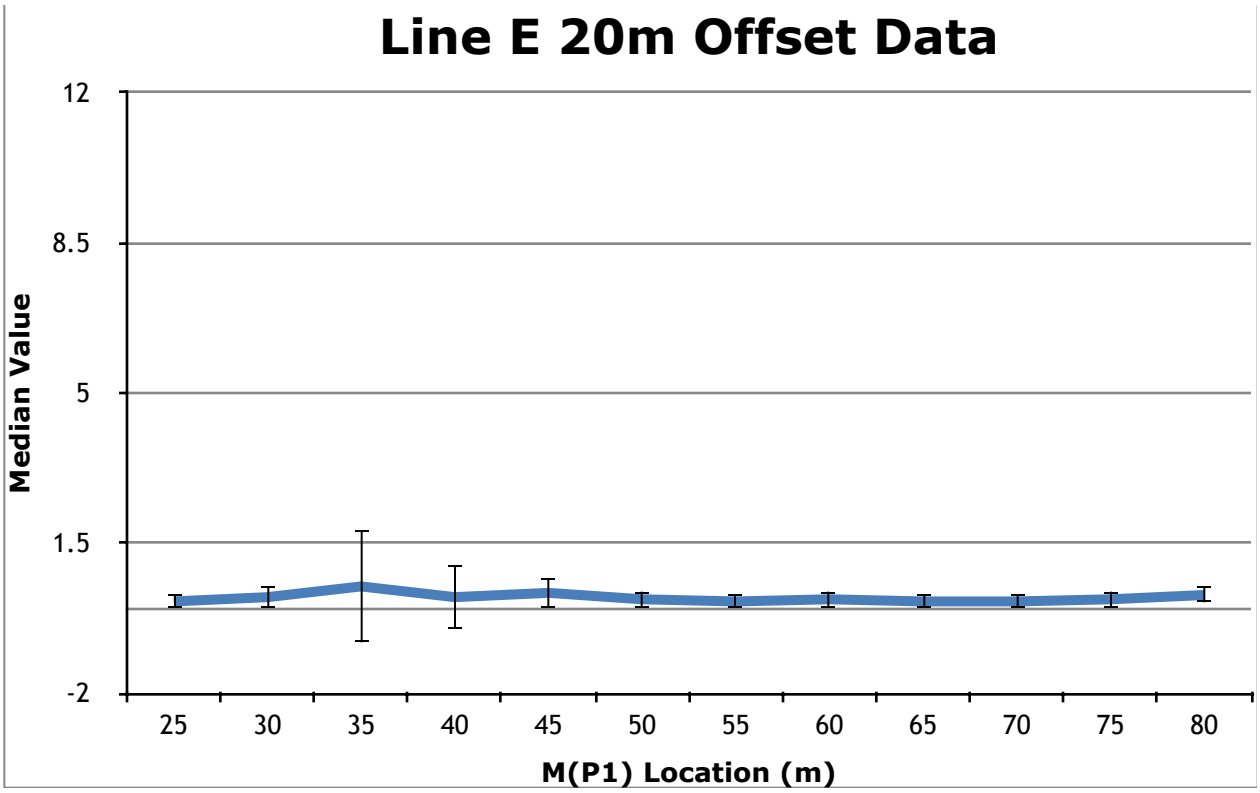
Line E 20m Offset Data
12
8.5
5
1.5
-2
Median Value
25
30
35
40
45
50
55
60
65
70
75
80
M(P1) Location (m)

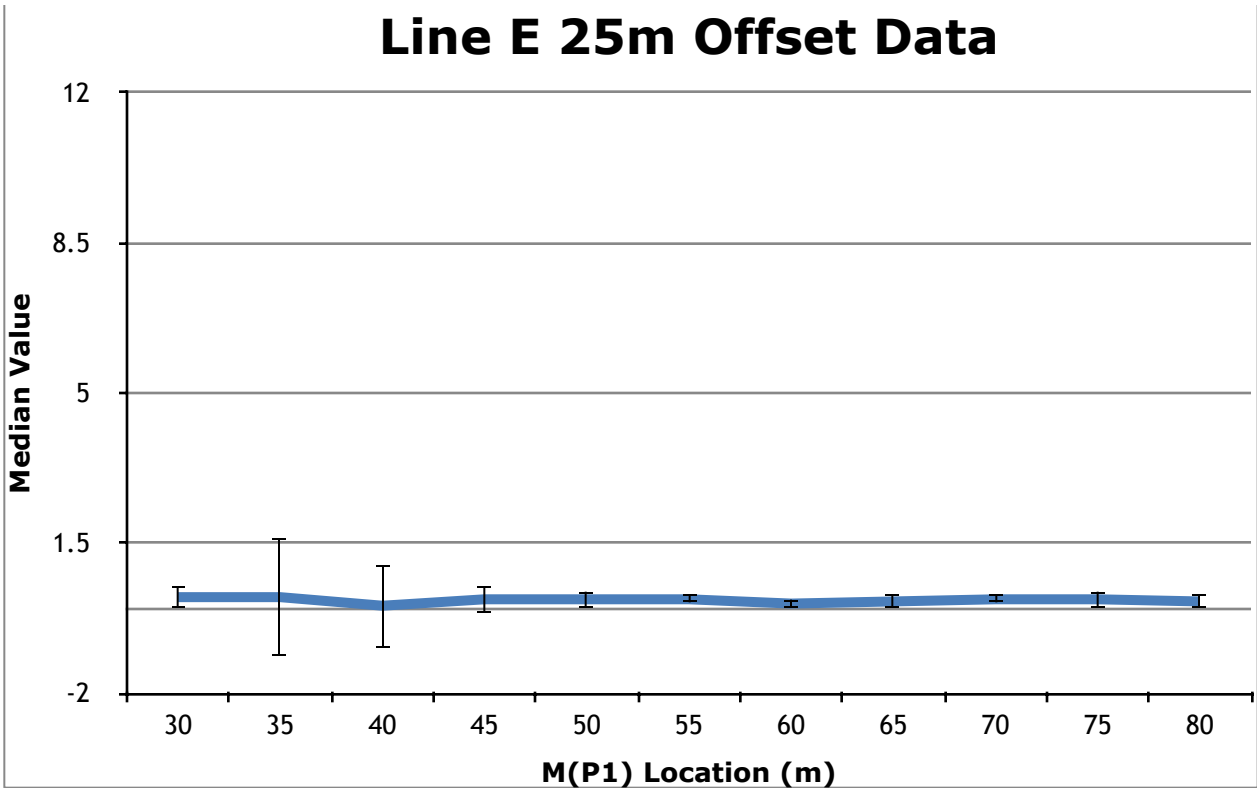
Line E 25m Offset Data
12
8.5
5
1.5
-2
Median Value
30
35
40
45
50
55
60
65
70
75
80
M(P1) Location (m)

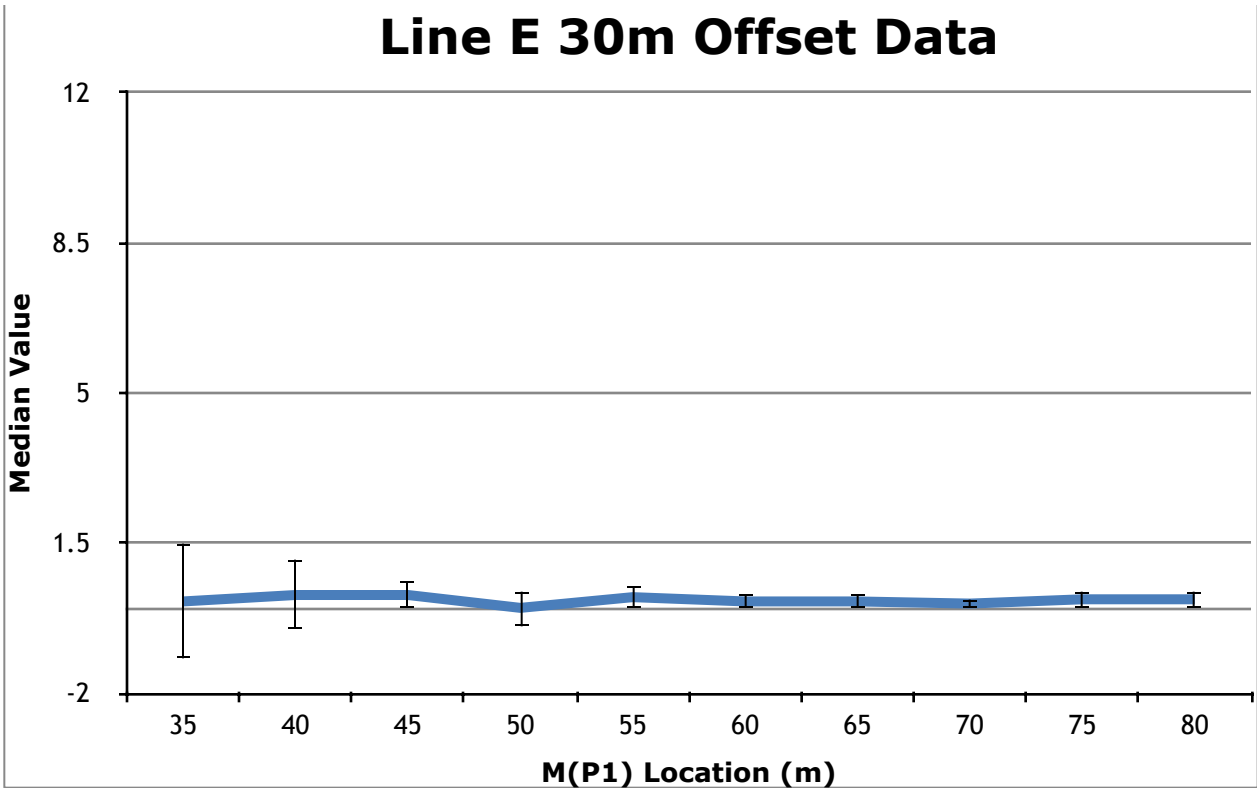
Line E 30m Offset Data
12
8.5
5
1.5
-2
Median Value
35
40
45
50
55
60
65
70
75
80
M(P1) Location (m)

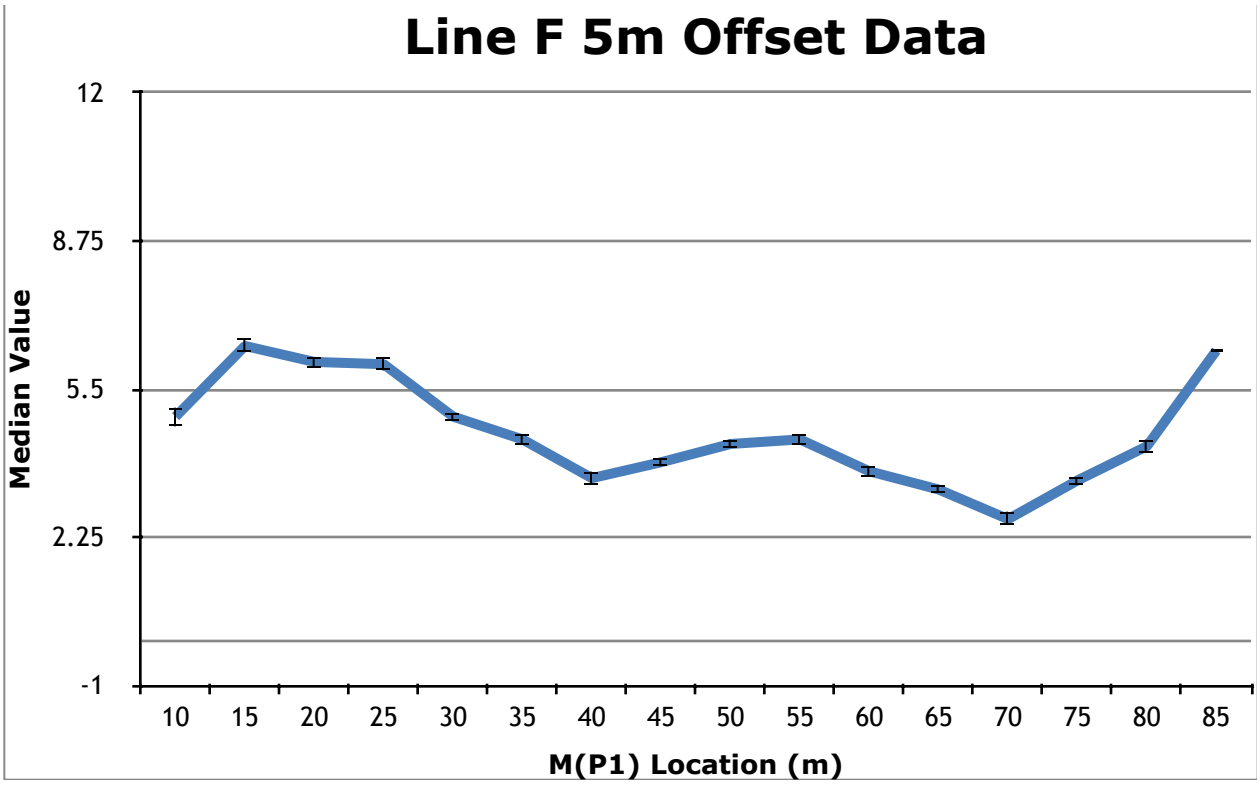
Line F 5m Offset Data
Median Value
12
8.75
5.5
2.25
-1
10
15
20
25
30
35
40
45
50
55
60
65
70
75
80
85
M(P1) Location (m)

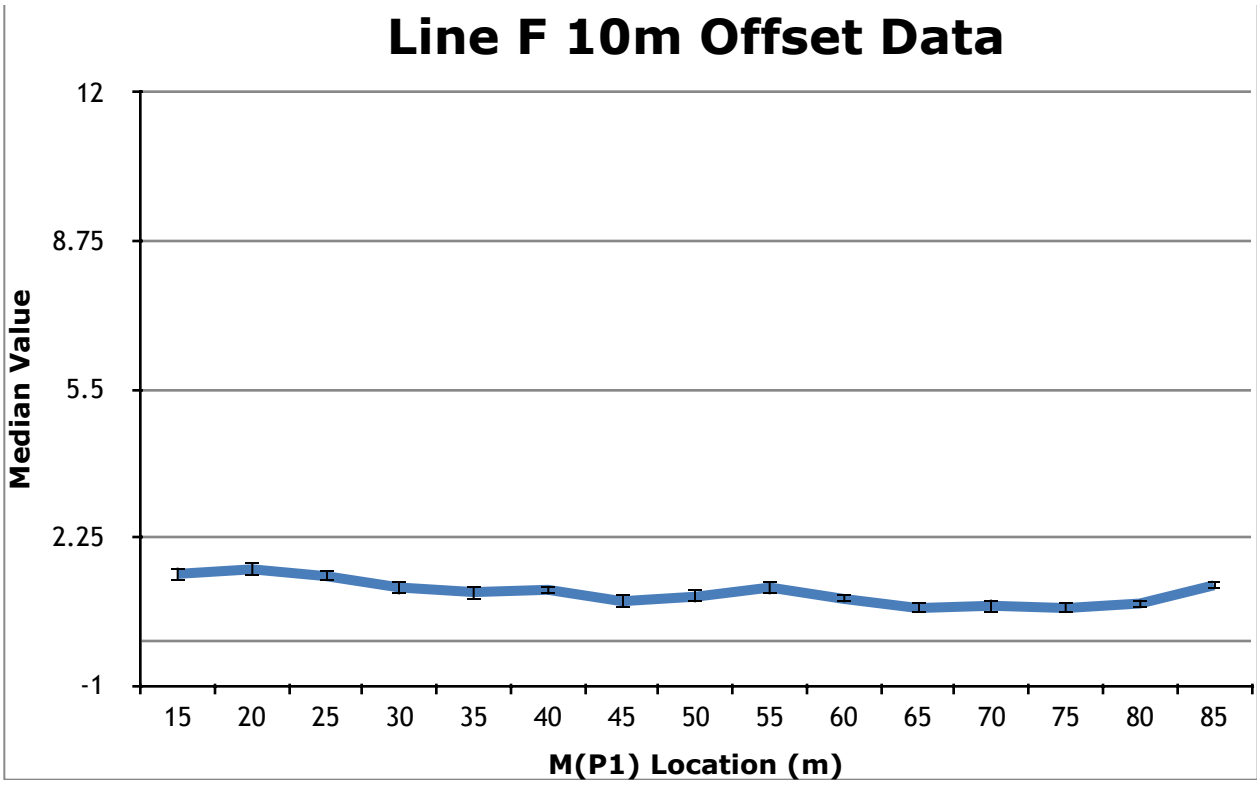
Line F 10m Offset Data
Median Value
12
8.75
5.5
2.25
-1
15
20
25
30
35
40
45
50
55
60
65
70
75
80
85
M(P1) Location (m)

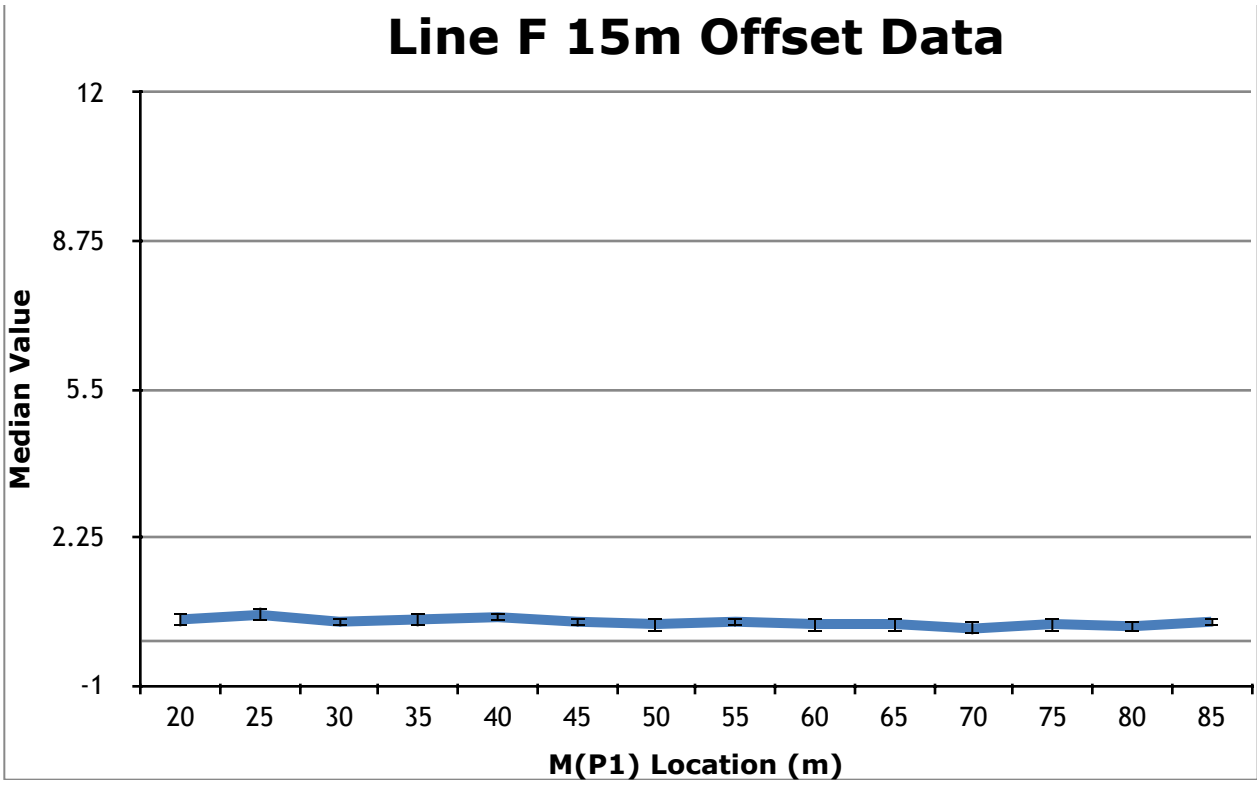
Line F 15m Offset Data
Median Value
12
8.75
5.5
2.25
-1
20
25
30
35
40
45
50
55
60
65
70
75
80
85
M(P1) Location (m)

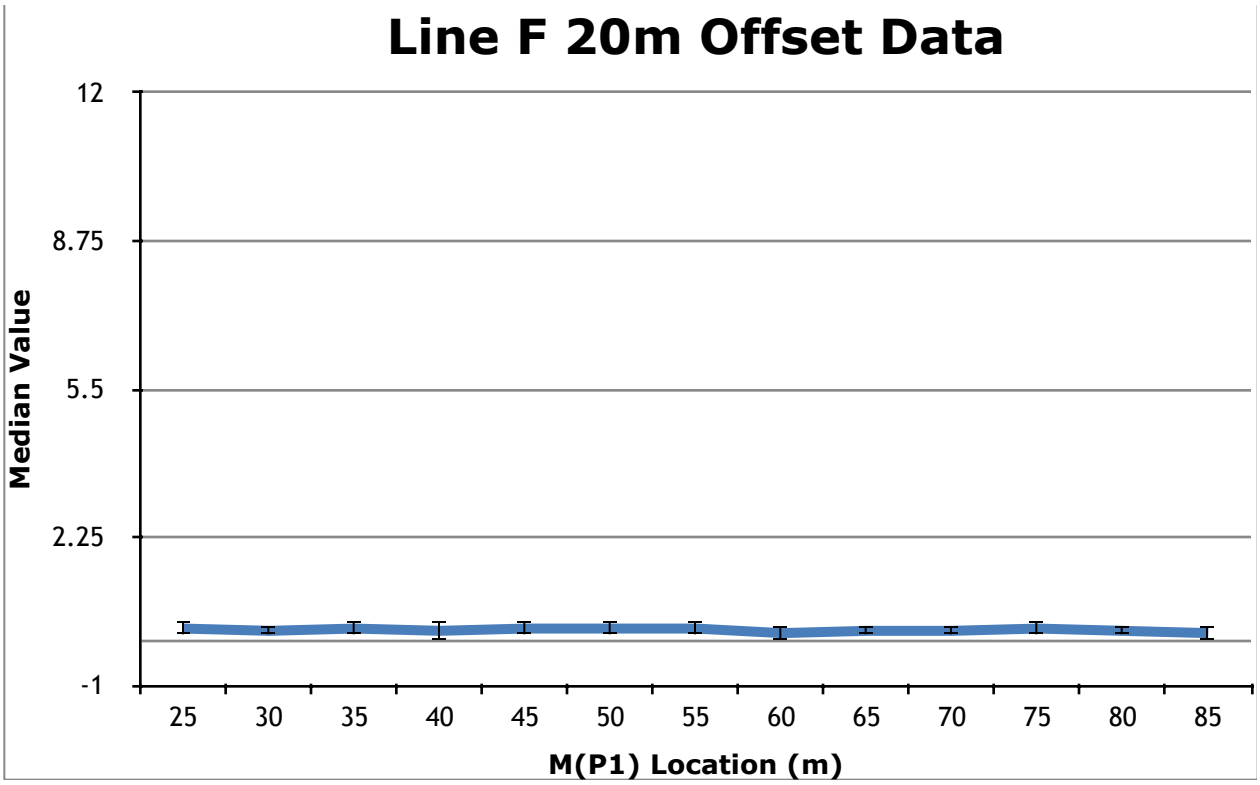
Line F 20m Offset Data
12
8.75
5.5
2.25
-1
Median Value
25
30
35
40
45
50
55
60
65
70
75
80
85
M(P1) Location (m)

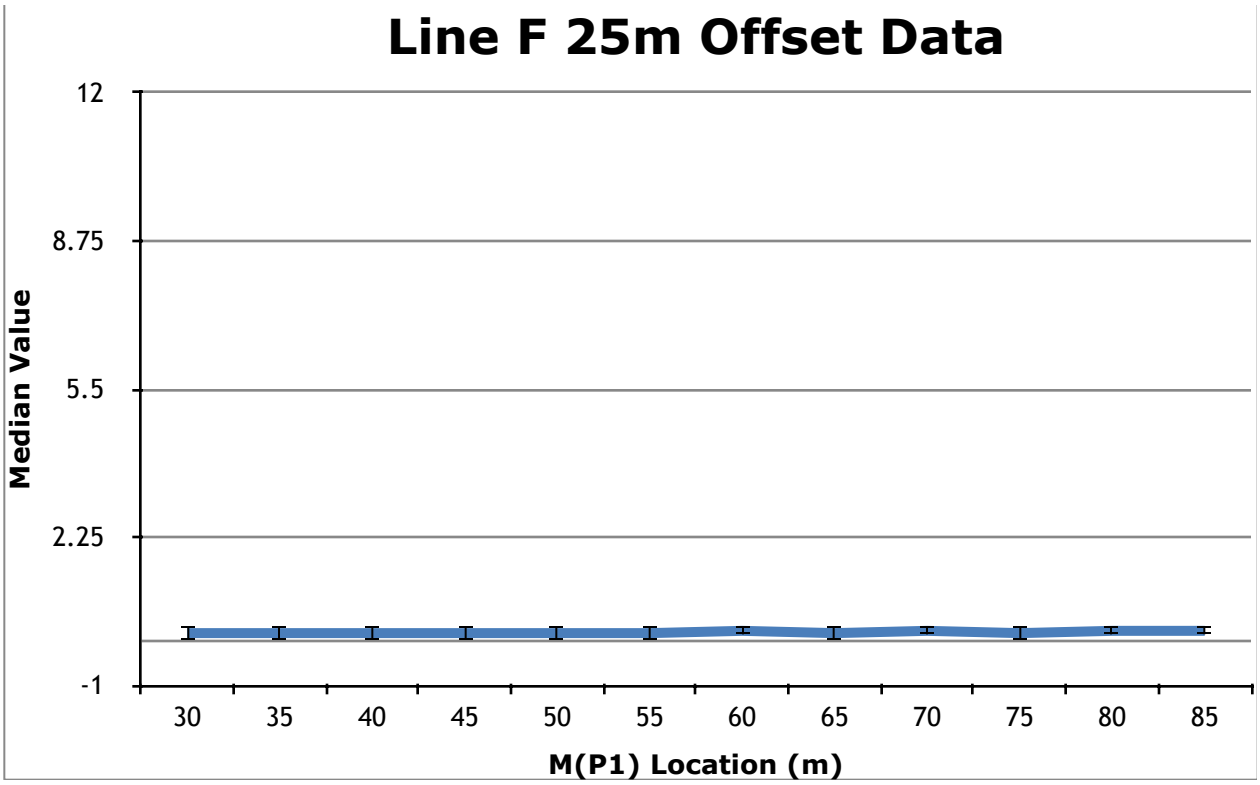
Line F 25m Offset Data
Median Value
12
8.75
5.5
2.25
-1
30
35
40
45
50
55
60
65
70
75
80
85
M(P1) Location (m)

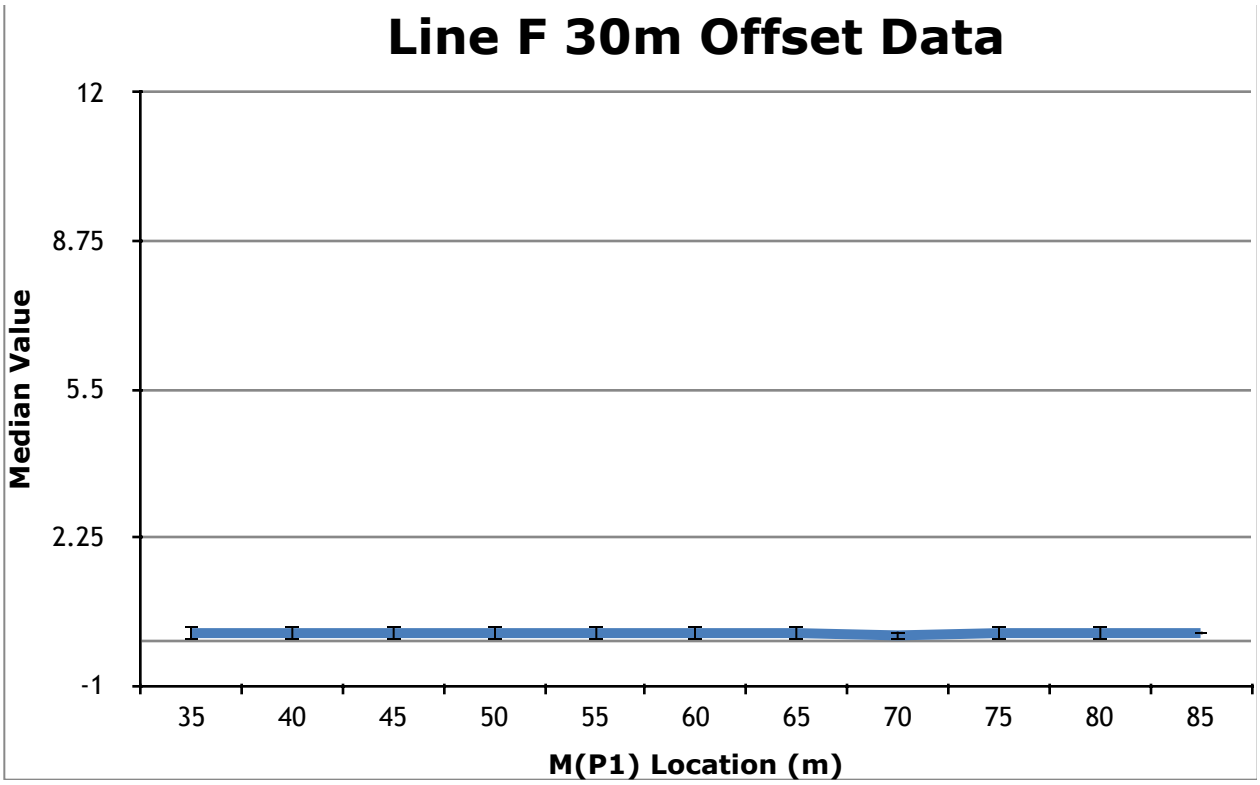
Line F 30m Offset Data
Median Value
12
8.75
5.5
2.25
-1
35
40
45
50
55
60
65
70
75
80
85
M(P1) Location (m)

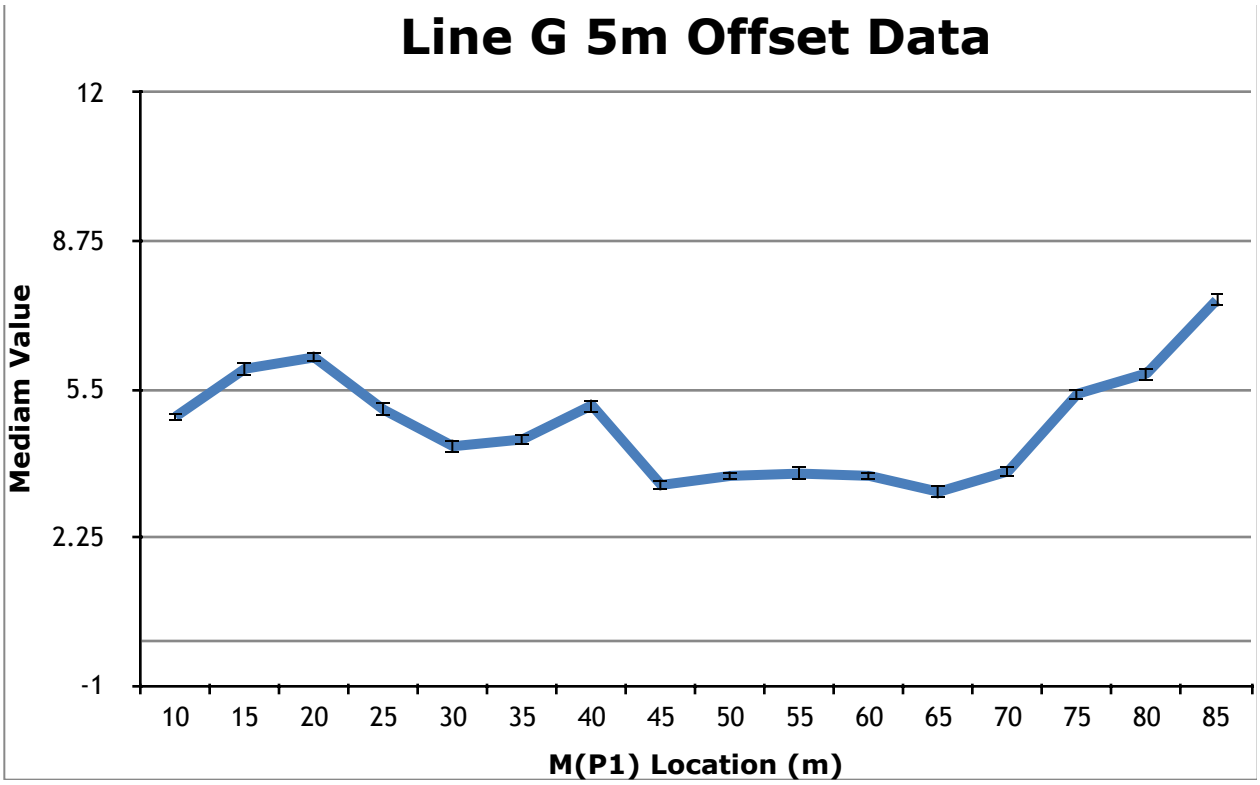
Line G 5m Offset Data
Mediam Value
12
8.75
5.5
2.25
-1
10
15
20
25
30
35
40
45
50
55
60
65
70
75
80
85
M(P1) Location (m)

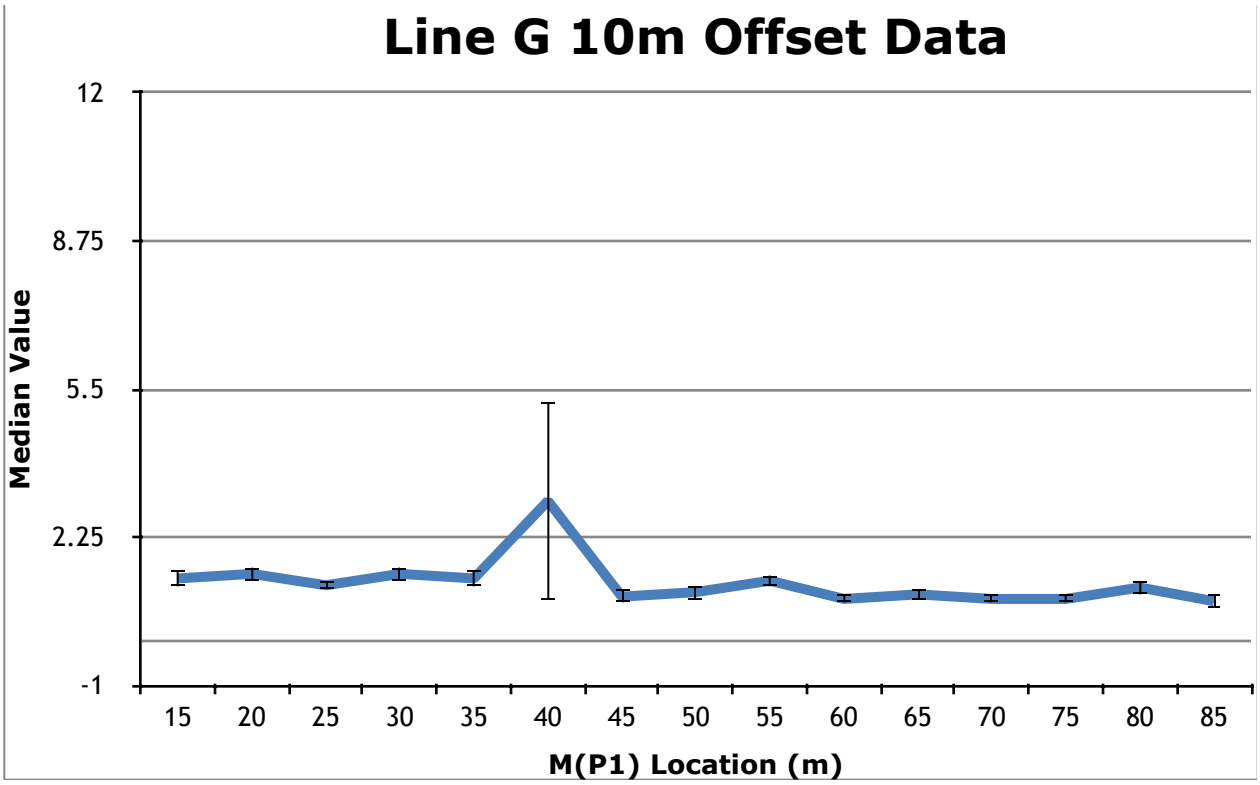
Line G 10m Offset Data
Median Value
12
8.75
5.5
2.25
-1
15
20
25
30
35
40
45
50
55
60
65
70
75
80
85
M(P1) Location (m)

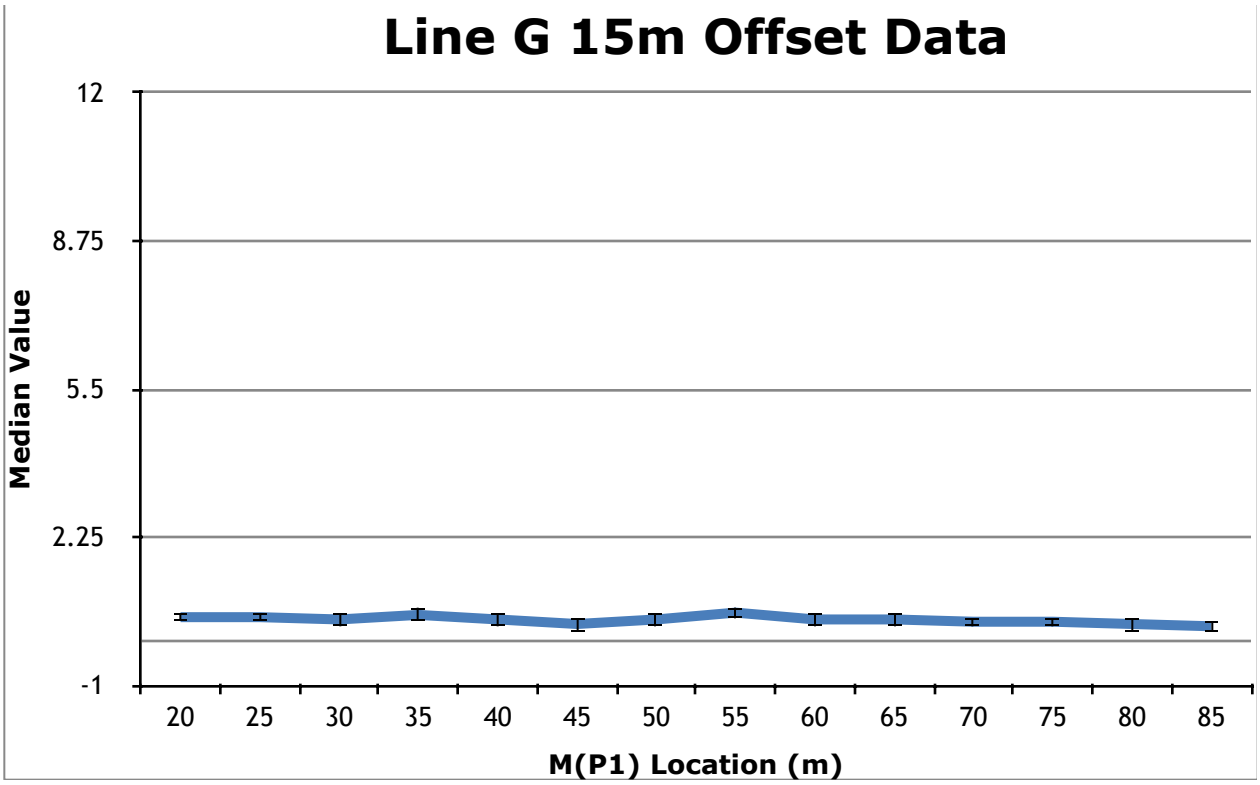
Line G 15m Offset Data
Median Value
12
8.75
5.5
2.25
-1
20
25
30
35
40
45
50
55
60
65
70
75
80
85
M(P1) Location (m)

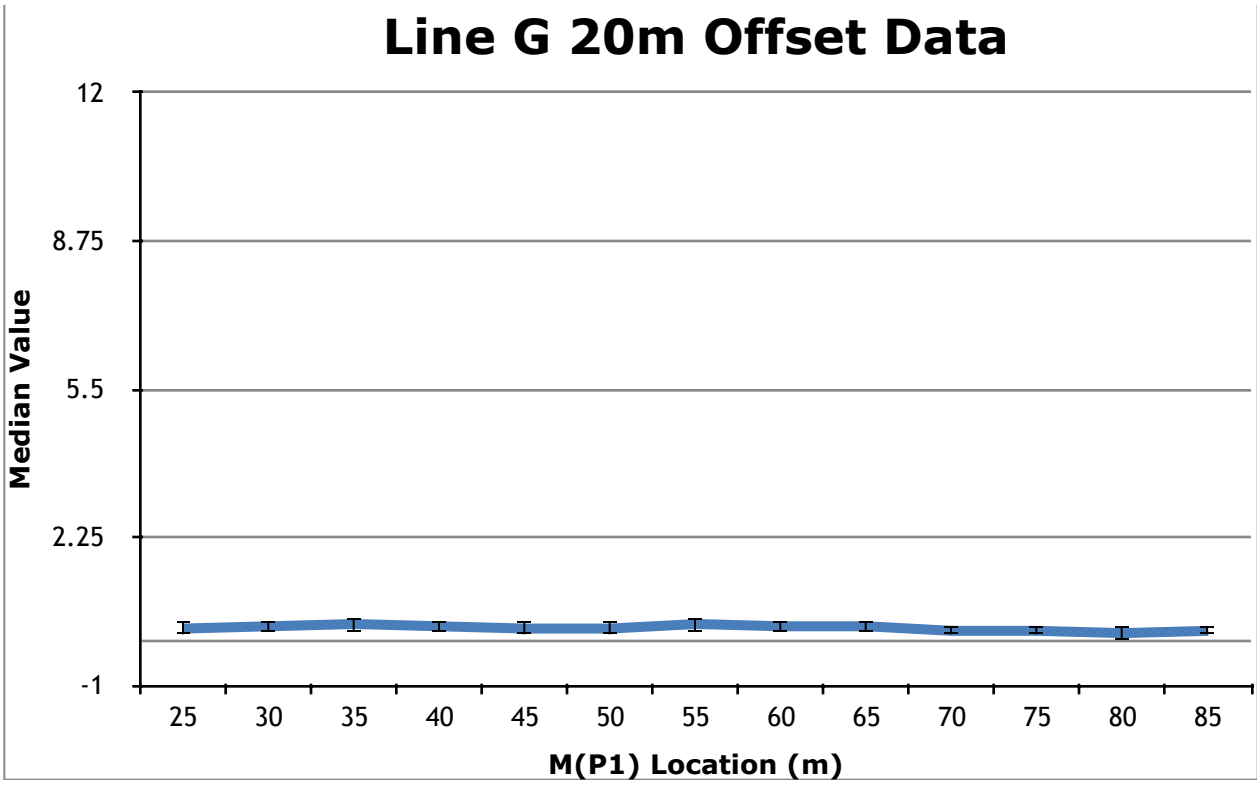
Line G 20m Offset Data
Median Value
12
8.75
5.5
2.25
-1
25
30
35
40
45
50
55
60
65
70
75
80
85
M(P1) Location (m)

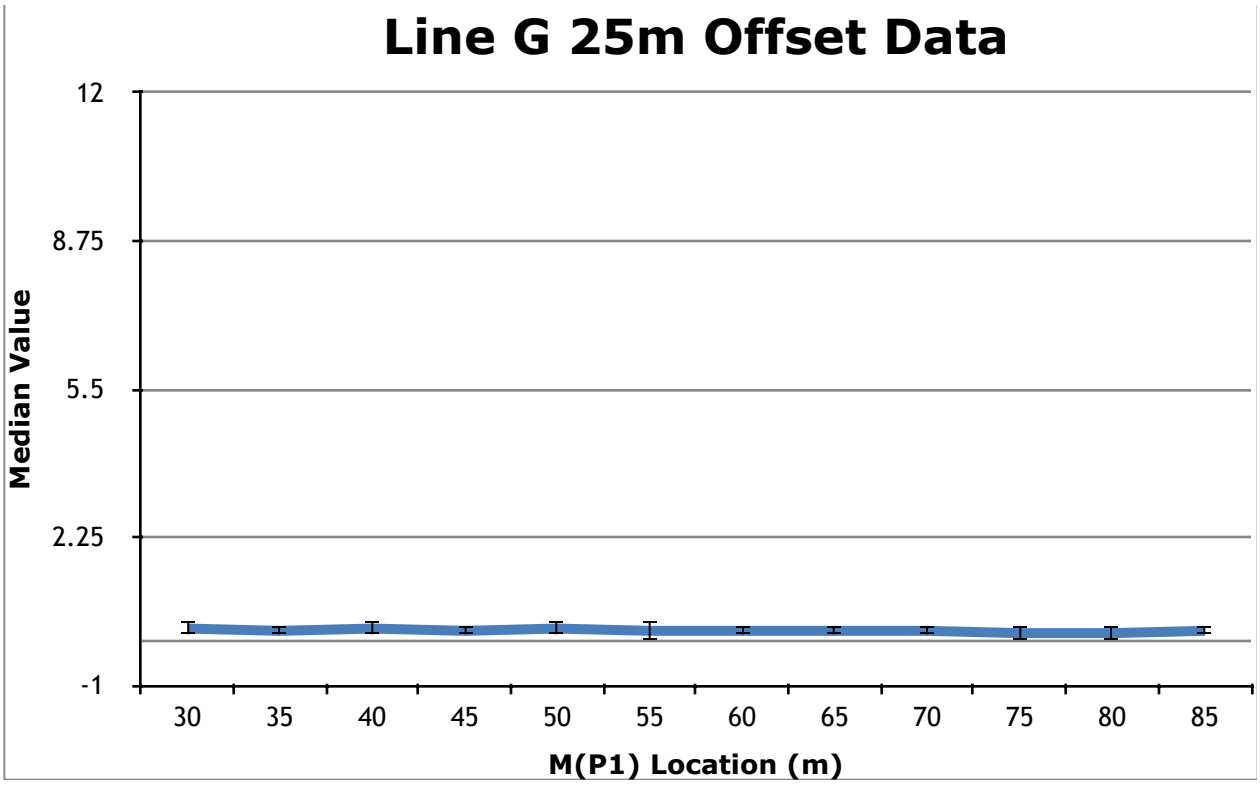
Line G 25m Offset Data
Median Value
12
8.75
5.5
2.25
-1
30
35
40
45
50
55
60
65
70
75
80
85
M(P1) Location (m)

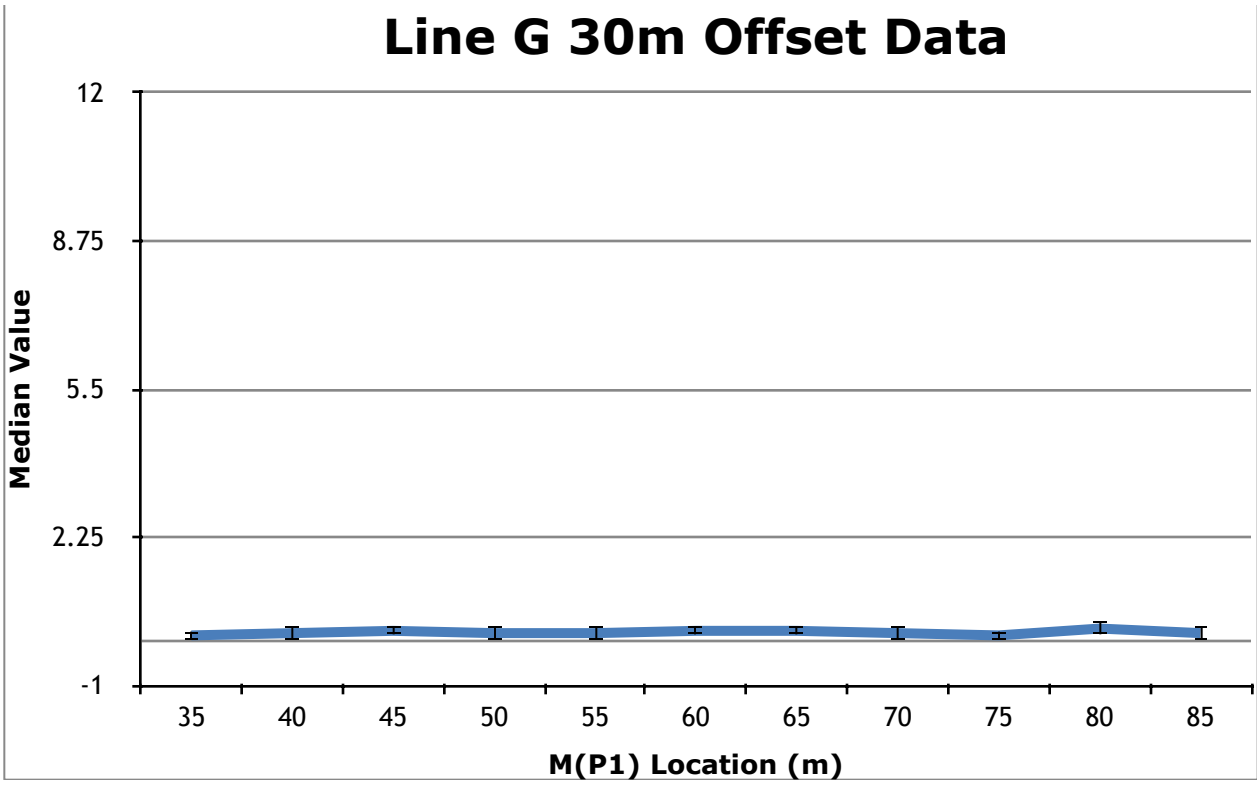
Line G 30m Offset Data
Median Value
12
8.75
5.5
2.25
-1
35
40
45
50
55
60
65
70
75
80
85
M(P1) Location (m)

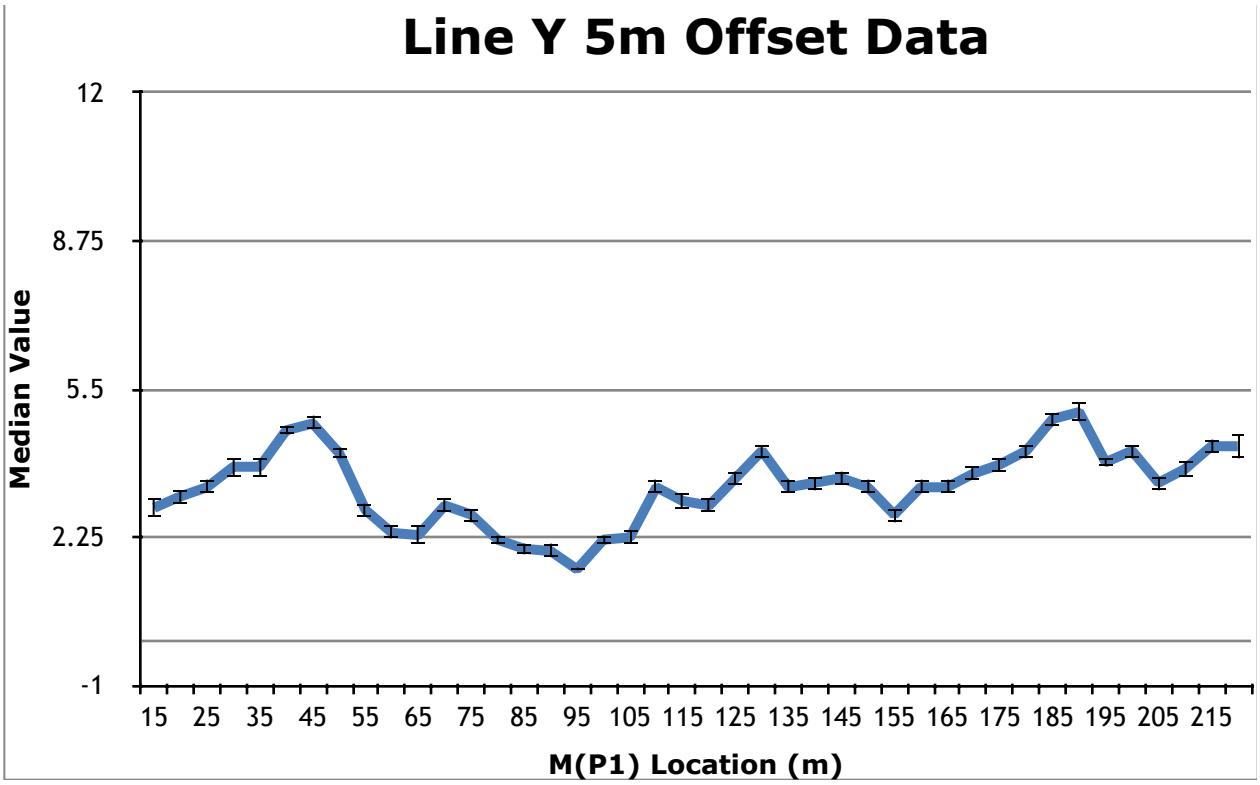
Line Y 5m Offset Data
Median Value
12
8.75
5.5
2.25
-1
15 25 35 45 55 65 75 85 95 105 115 125 135 145 155 165 175 185 195 205 215
M(P1) Location (m)

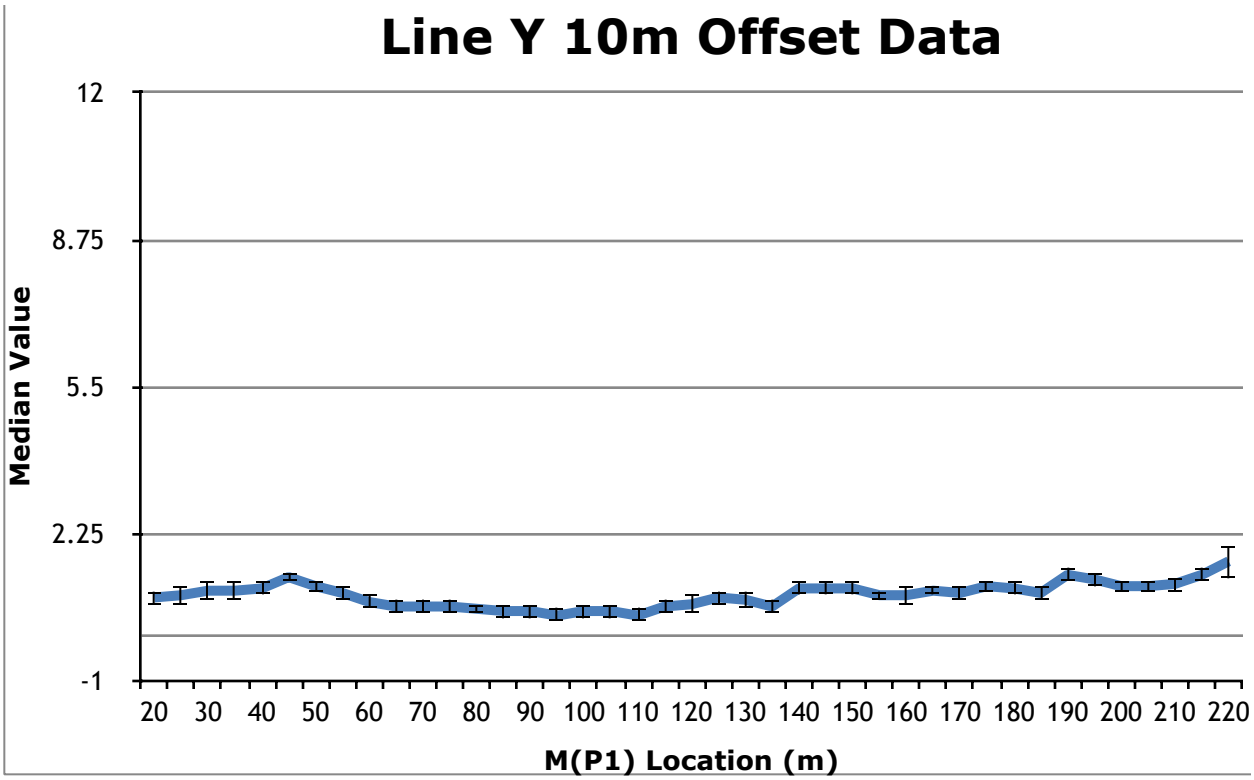
Line Y 10m Offset Data
Median Value
12
8.75
5.5
2.25
-1
20 30 40 50 60 70 80 90 100 110 120 130 140 150 160 170 180 190 200 210 220
M(P1) Location (m)

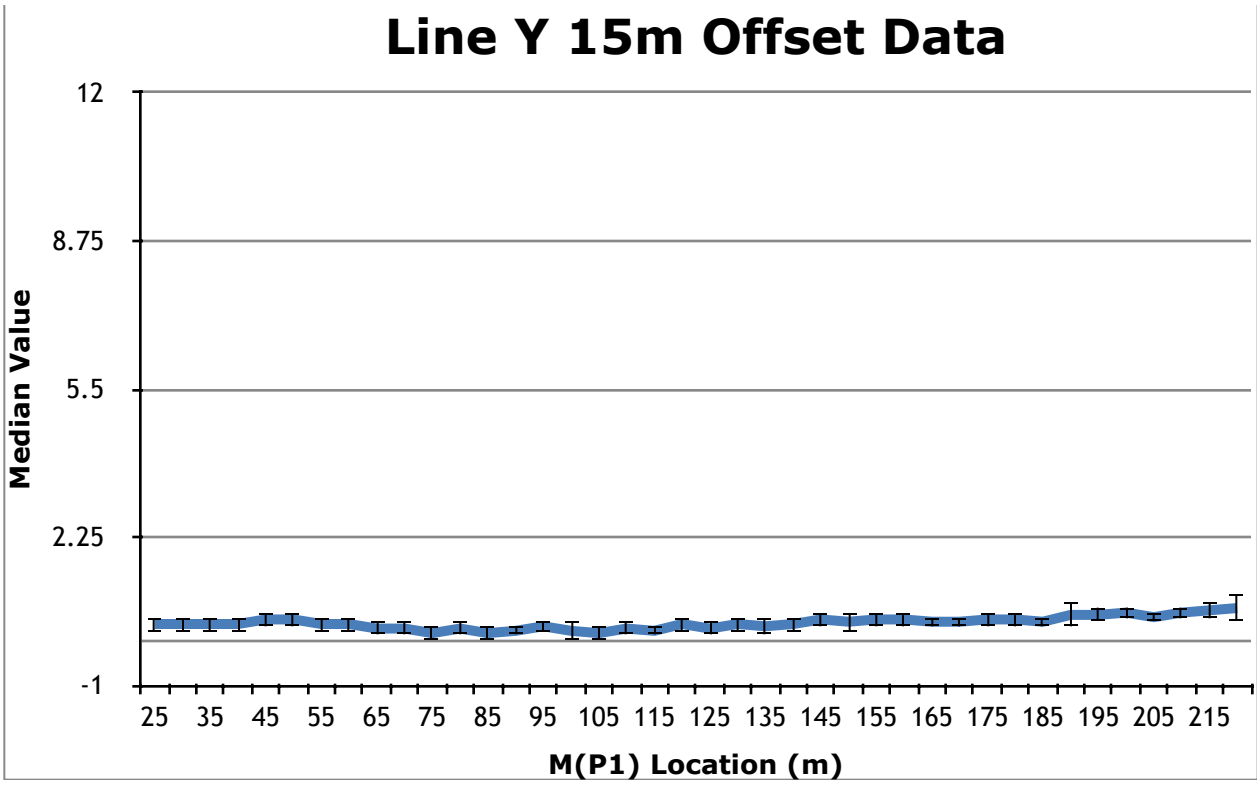
Line Y 15m Offset Data
Median Value
12
8.75
5.5
2.25
-1
25 35 45 55 65 75 85 95 105 115 125 135 145 155 165 175 185 195 205 215
M(P1) Location (m)

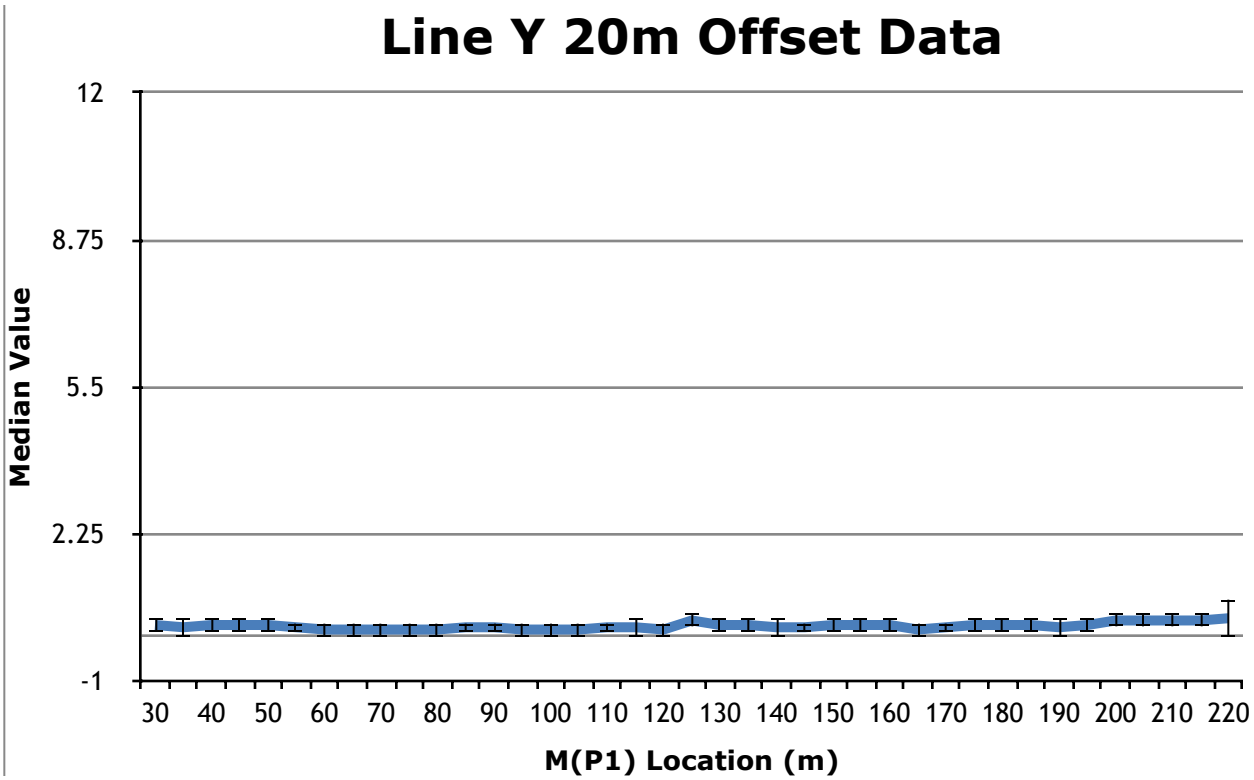
Line Y 20m Offset Data
Median Value
12
8.75
5.5
2.25
-1
30 40 50 60 70 80 90 100 110 120 130 140 150 160 170 180 190 200 210 220
M(P1) Location (m)

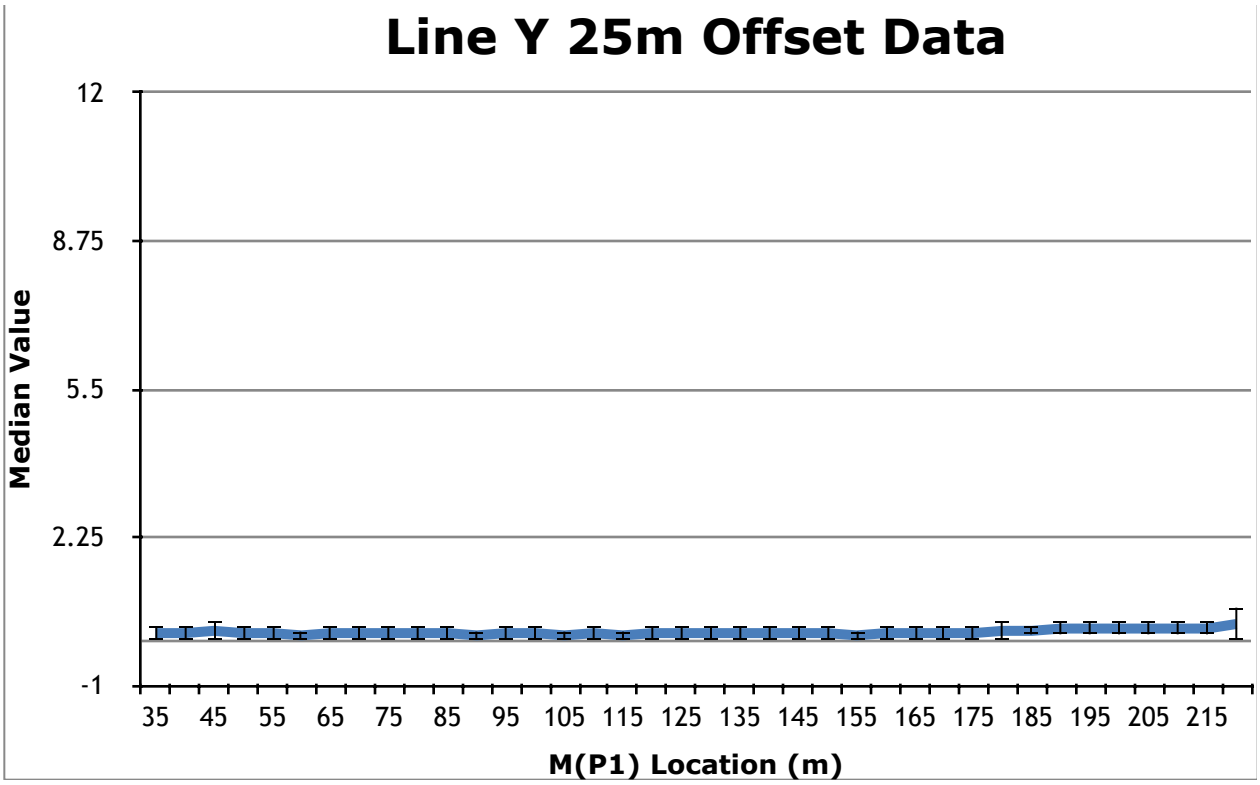
Line Y 25m Offset Data
Median Value
12
8.75
5.5
2.25
-1
35
45
55
65
75
85
95
105
115
125
135
145
155
165
175
185
195
205
215
M(P1) Location (m)

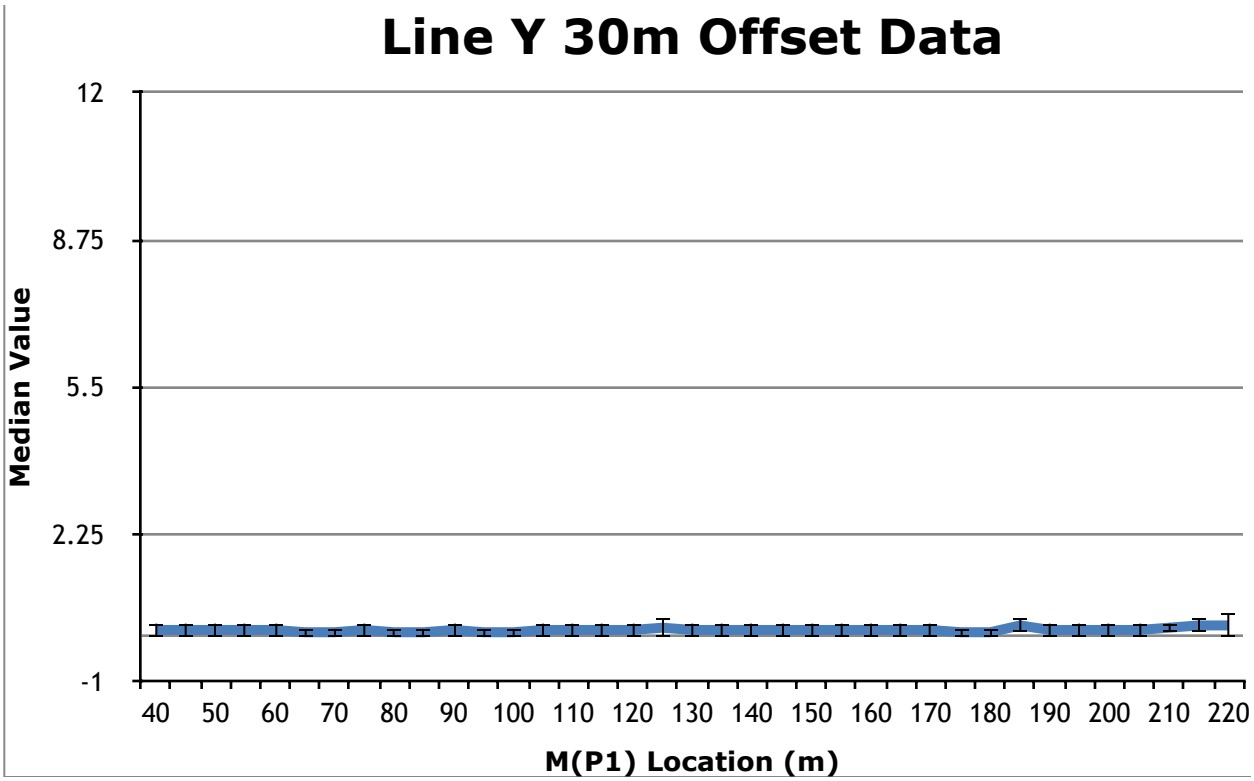
Line Y 30m Offset Data
Median Value
12
8.75
5.5
2.25
-1
40 50 60 70 80 90 100 110 120 130 140 150 160 170 180 190 200 210 220
M(P1) Location (m)

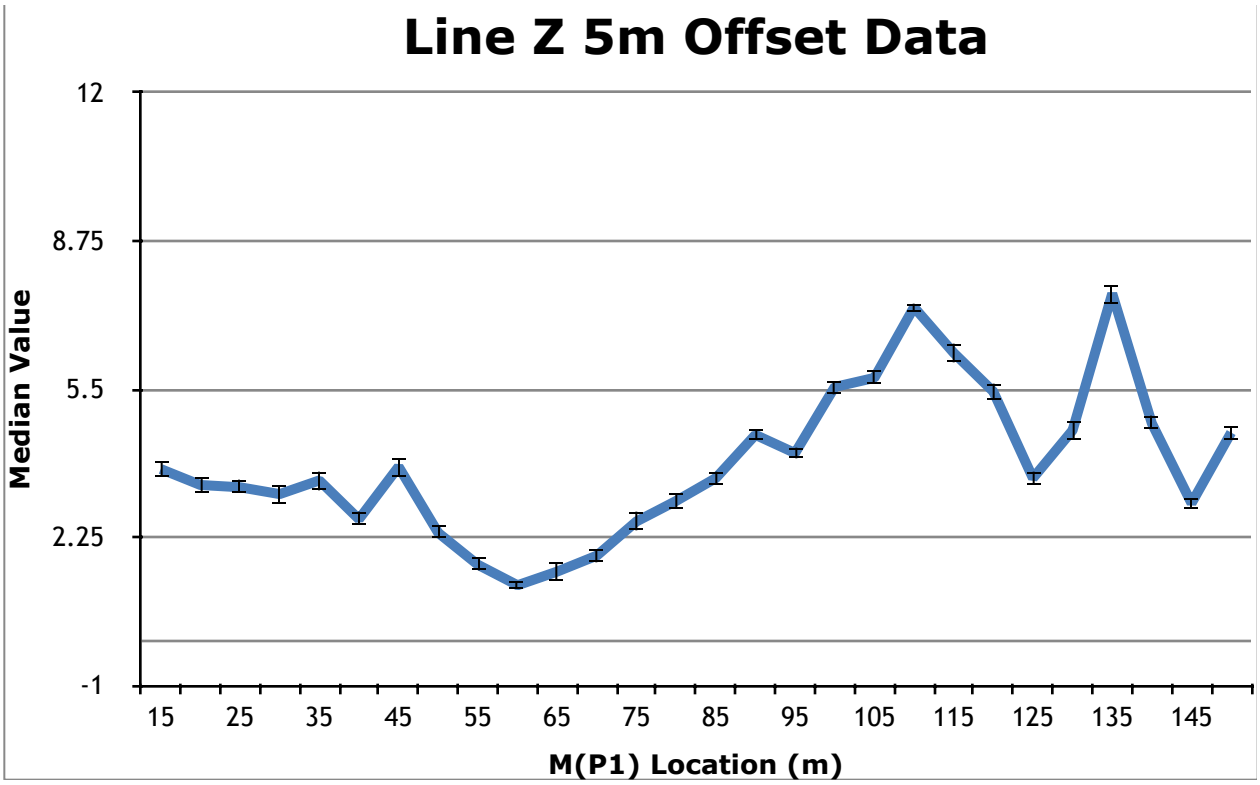
Line Z 5m Offset Data
Median Value
12
8.75
5.5
2.25
-1
15
25
35
45
55
65
75
85
95
105
115
125
135
145
M(P1) Location (m)

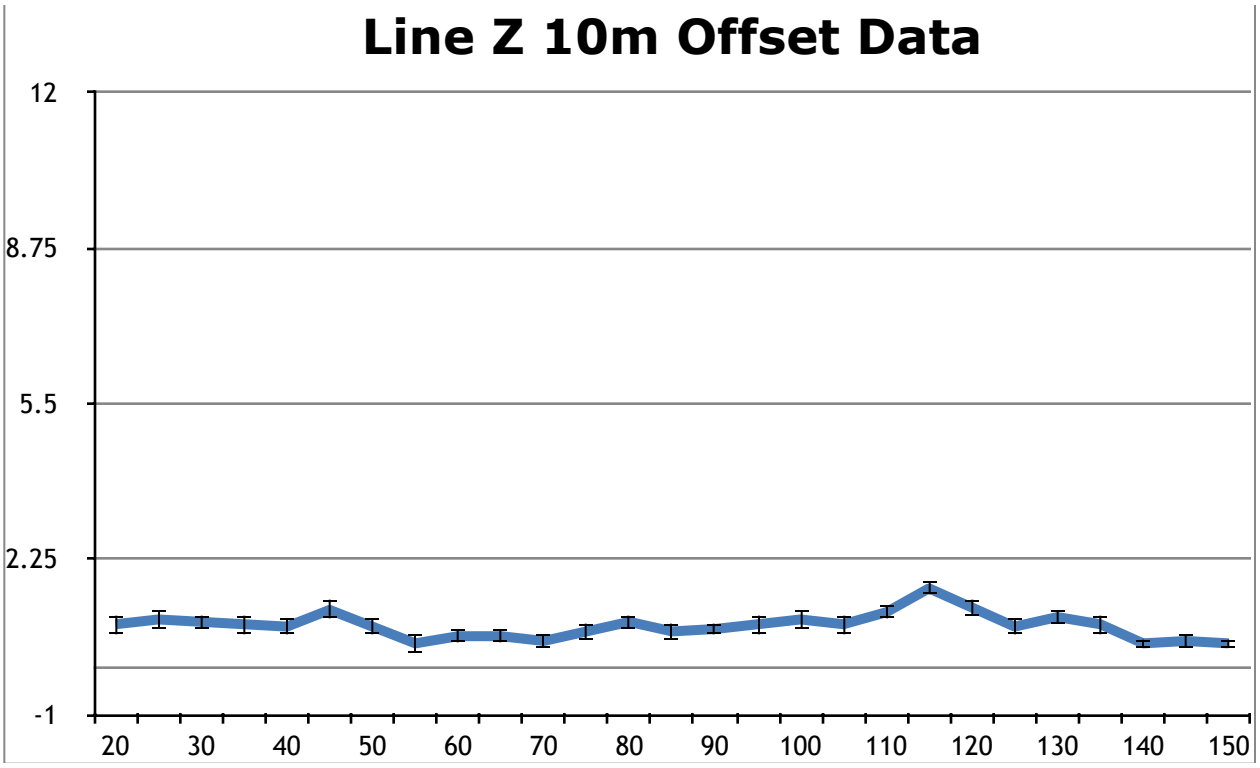
Line Z 10m Offset Data
12
8.75
5.5
2.25
-1
20
30
40
50
60
70
80
90
100
110
120
130
140
150

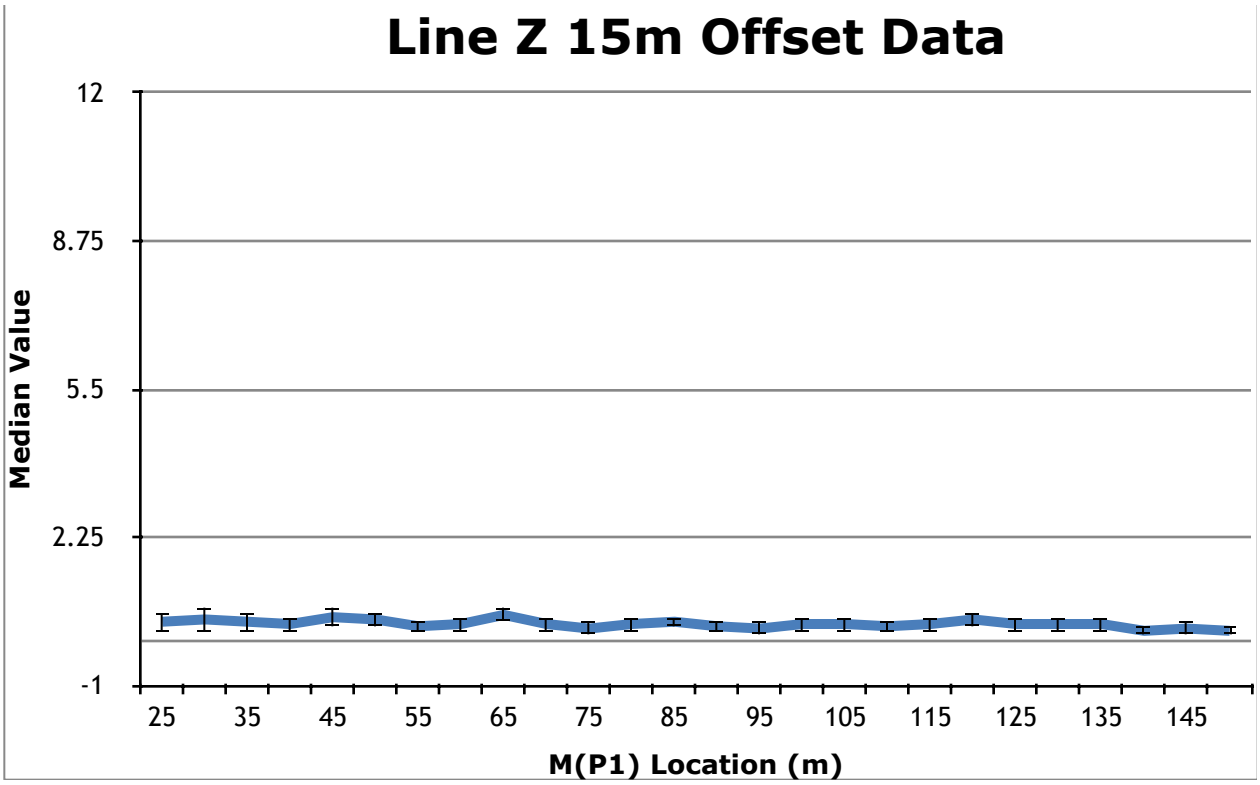
Line Z 15m Offset Data
12
8.75
5.5
2.25
-1
Median Value
25
35
45
55
65
75
85
95
105
115
125
135
145
M(P1) Location (m)

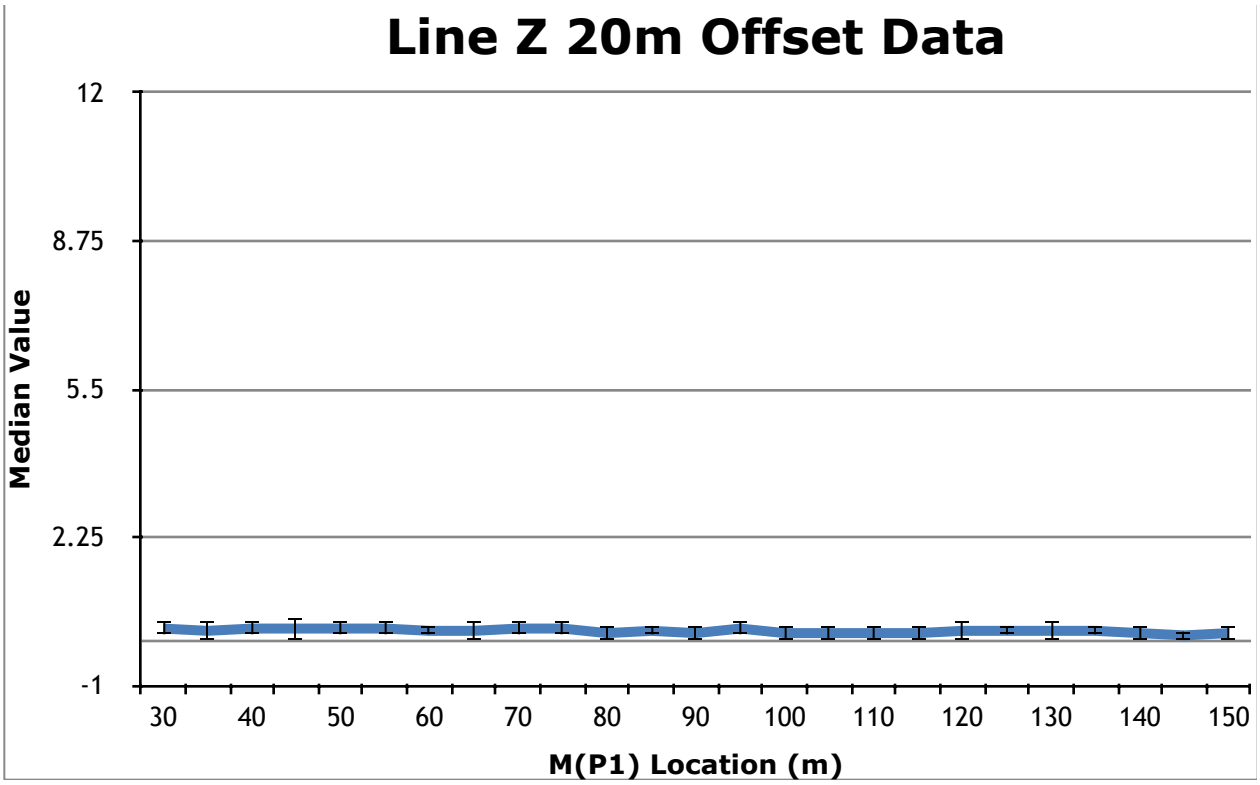
Line Z 20m Offset Data
Median Value
12
8.75
5.5
2.25
-1
30
40
50
60
70
80
90
100
110
120
130
140
150
M(P1) Location (m)

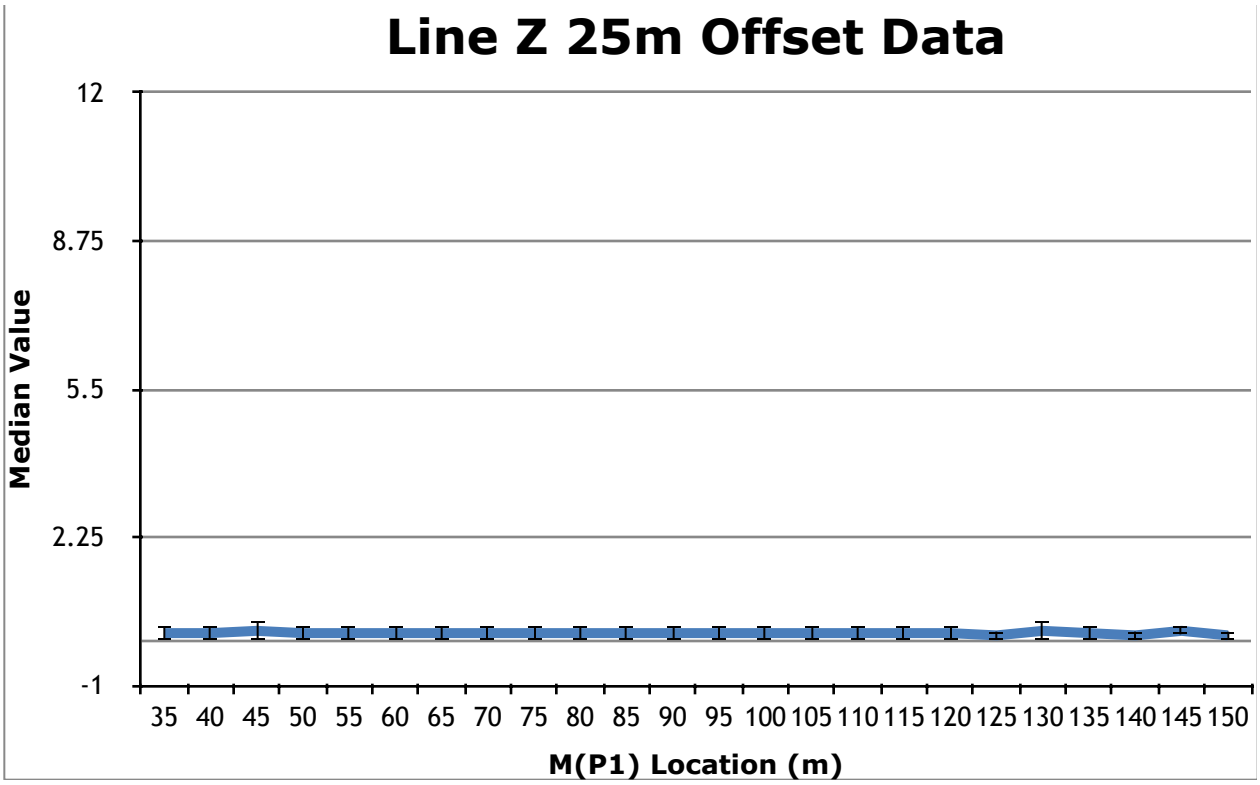
Line Z 25m Offset Data
Median Value
12
8.75
5.5
2.25
-1
35 40 45 50 55 60 65 70 75 80 85 90 95 100 105 110 115 120 125 130 135 140 145 150
M(P1) Location (m)

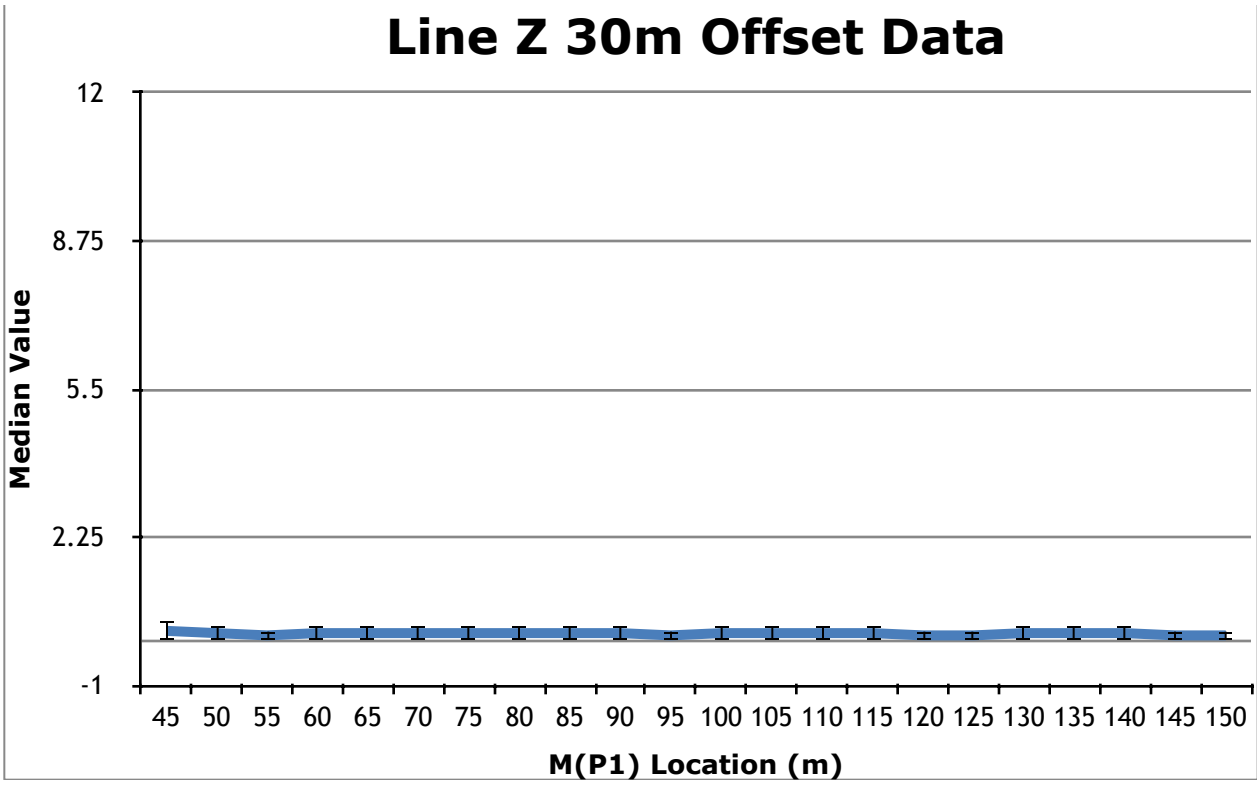
Line Z 30m Offset Data
Median Value
12
8.75
5.5
2.25
-1
45 50 55 60 65 70 75 80 85 90 95 100 105 110 115 120 125 130 135 140 145 150
M(P1) Location (m)

APPENDIX B

Clay Mineralogy Analysis

X-ray diffraction analysis of soil samples collected from the walls of three mature sinkholes in the area was carried out to determine the mineralogy of the overburden. The mineralogy of an area can have an impact on the water content of the soils, and therefore have an impact on the resistivity readings.

In dipole-dipole electrical resistivity arrays, the resistivity inversions are more sensitive to changes to resistivity at the surface simply because there is more data at the surface. Because different clays and materials can have an impact on the resistivity measurements, it was important to know exactly what minerals were being encountered in the subsurface. X-ray diffraction analysis is a relatively simple way to determine the make-up of the material, and by knowing the minerals in the soils, resistivity values can be explained.

"The primary method for identifying and analyzing clay minerals is X-ray diffraction" (Moore and Reynolds, 1997). X-rays are scattered by electrons surrounding the nucleus of the atoms that make up the sample and the X-rays are "modified in three ways: 1) by the way in which the electrons of a particular atom are distributed within the field of influence of that atom 2) by the thermal vibrations that tend to blur the atoms as scattering centers as temperature increases 3) by the way atoms are arranged within the unit cell" (Moore and Reynolds, 1997). Atoms, unit cells, or crystallites, can be treated as scattering centers and each scattering center gives off a diffracted beam that can be represented as a vector; summing all of

these vectors a resultant diffracted beam with specific amplitude and phase can be used to calculate intensity of the beam (Moore and Reynolds, 1997). When using a diffractometer it is rare to observe scattered X-rays through the crystal, so Bragg's Law is used to describe the relationship of X-rays going into the crystal and its reflection off of a crystal surface (Moore and Reynolds, 1997). The angle of reflection and the intensity of the beam can be diagnostic for the minerals inside of the sample.

Samples from the side of the inside of each mature sinkhole were taken at depths where there was a clear change in color of the overburden or what seemed to be a change in composition. This resulted in samples taken at 1.8, 2.1, 3.0 m depth, but since each sinkhole wasn't the same approximate depth, some sinkholes didn't provide samples from the greater depths. Samples 1, 4, and 5 were taken from the 1.8 m deep, Sample 2 and 6 from 2.1 m deep, and Sample 6 from 3.0 m deep. This data is summed up in Table A.1.

X-ray diffraction analysis was performed on each soil sample taken. The diffractometer uses CuKα radiation, a divergent slit size of 0.3 which controls the area of the sample exposed to X-rays, a scan range of 3-90°, a step of 0.02°. A diffraction pattern for each sample was created to graph the counts on the y-scale and the °2$\boldsymbol{\theta}$ on the x-scale. Each diffraction pattern was Kα-stripped and background corrected.

Two different preparation techniques were used in X-ray diffraction analysis of the soil samples. The first was a bulk-mount method where the sample was prepared by removing any visible organics, then using a mortar and pestle to grind down any larger grains to ensure uniform grain size. Then the samples were tamped down in a sample holder without adding so much pressure that orientation was introduced or that the sample bulged as to not allow a flat surface.

The second technique used was making oriented slides as described by Moore and Reynolds (1997). The objective of an oriented slide is to use the clay fraction of the sample and orient the individual crystals. To achieve this, samples were first mortal and pestled to get the grains to a uniform size. Then, the sample was mixed with a dispersant and ionized water, ultra sonicated, and placed into a centrifuge at 2000 rpm for two minutes. The suspension was then decanted into a beaker with the material that was decanted being the clay fraction. Then the clay fraction was placed in the centrifuge two more times before being decanted to get the appropriate sizes of the crystals for the oriented slides.

The resulting sample was then mixed with ethylene glycol to create a solution and this solution was then dripped onto a glass slide creating a flat thin film of clay. The problem was that when the sample dried, it peeled, and "some materials, no matter how they are treated, shrink on drying with the result that the sample curls, breaks up, and separates from the substrate" (Moore and Reynolds 1997). This can be caused by angular grains, flocculation of clay minerals during sample preparation, a large particle-size range, and the presence of gelatinous, hydrated colloidal material (Moore and Reynolds, 1997). To remedy this, the Millipore filter transfer method was used. This method uses a vacuum filter apparatus to collect the oriented clay minerals by pouring the suspension that was created over the filter while vacuuming the liquid through the filter and into a flask. The clay minerals are then transferred from the paper onto a glass slide. Several steps were then taken to treat the oriented sample before it was placed in the diffractometer. First, the sample was air-dried and placed in the diffractometer. Then, the sample was heated to 375° C and analyzed. After that, the sample was heated to 500° C and analyzed. Another oriented slide was then prepared and allowed to dry in a glycol saturated container and then scanned. A scan for

the bulk mounted sample and the different oriented sample types were completed for each sample taken from the three sinkholes.

The results from the clay mineralogy analysis are shown in Table A.2 and the diffraction patterns underneath. Because the results were consistent from sinkhole to sinkhole, one single sample was plotted on the diffraction plots so that there wasn't too much clutter in the plot. The random powder mounts from Sample 1, 4, and 5 resulted in extremely consistent mineralogy across the three sinkholes with this layer containing quartz, kaolinite, and vermiculite. Results from Sample 2 and 6 yielded consistent mineralogy and contained quartz, kaolinite, mica, hematite, and vermiculite . Based on the counts in the XRD analysis, there was a lesser amount of quartz in these samples than from Sample 1, 4, and 5. Sample 3 was comprised of quartz, kaolinite, hematite, mica, and vermiculite. This sample was comprised with the least amount of quartz. The bulk mount XRD analysis and the oriented slide XRD analysis were both very consistent across samples and the relative amounts of minerals in each sample were compared. The deeper into the ground the sample was taken, the more clay content that was in the samples.

Table A.1 - Sample Depths

Sample	Depth of Sample (m)
1	1.8
2	2.1
3	3
4	1.8
5	1.8
6	2.1

Table A.2 - Sample Mineralogy

Sample	Mineralogy
1	quartz, kaolinite, and vermiculite
2	quartz, kaolinite, vermiculite, mica, hematite/ less quartz overall
3	quartz, kaolinite, vermiculite, mica, hematite/ least amount of quartz overall
4	quartz, kaolinite, and vermiculite
5	quartz, kaolinite, and vermiculite
6	quartz, kaolinite, vermiculite, mica, hematite/ less quartz overall

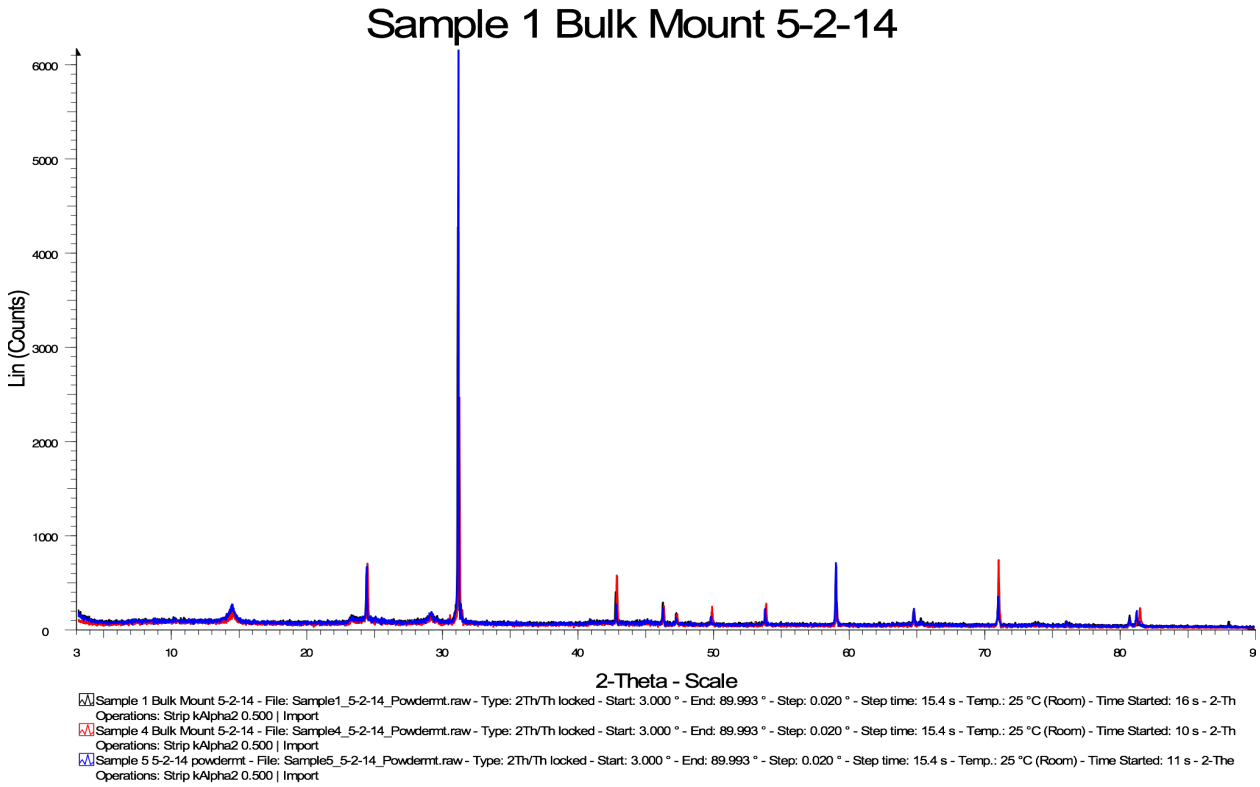

Sample 1, 4, and 5 bulk mount diffraction pattern. Sample 1 is in black, Sample 4 in red, and Sample 5 in blue.

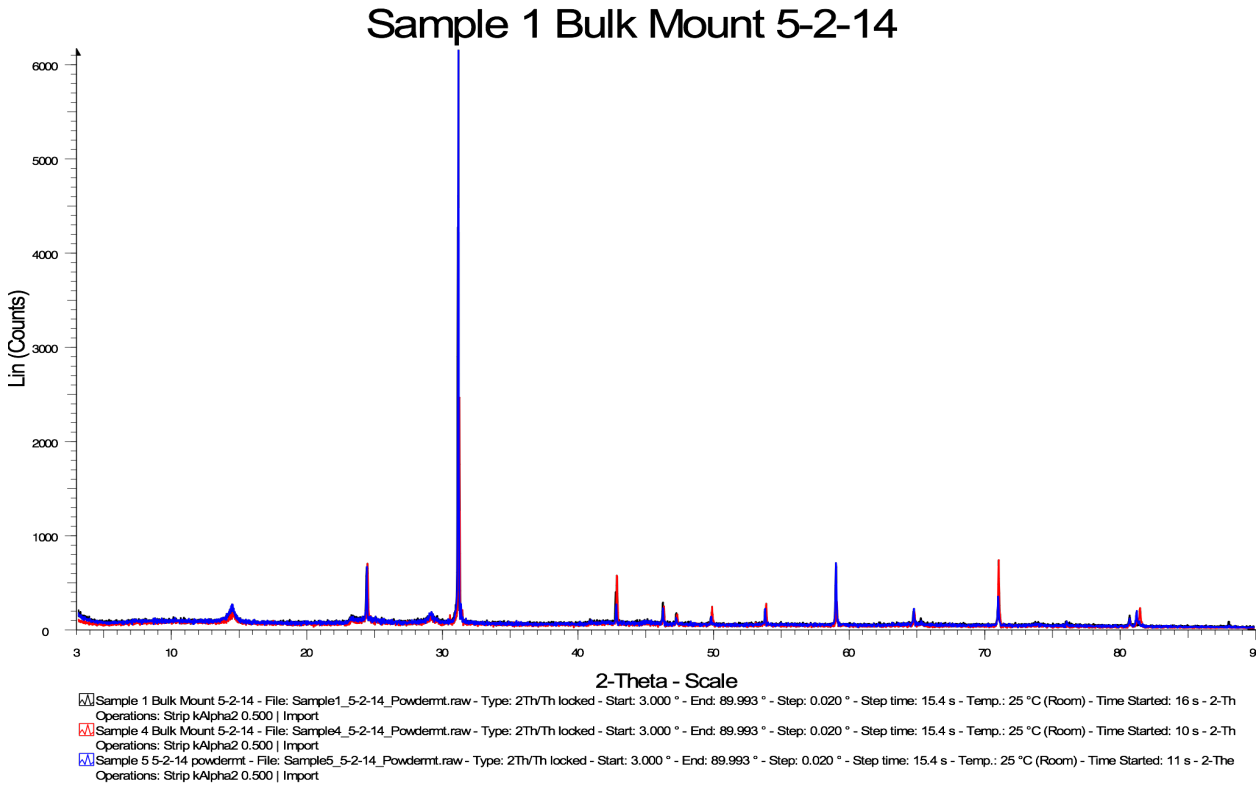

Sample 1, 4, and 5 bulk mount diffraction pattern. Sample 1 is in black, Sample 4 in red, and Sample 5 in blue.

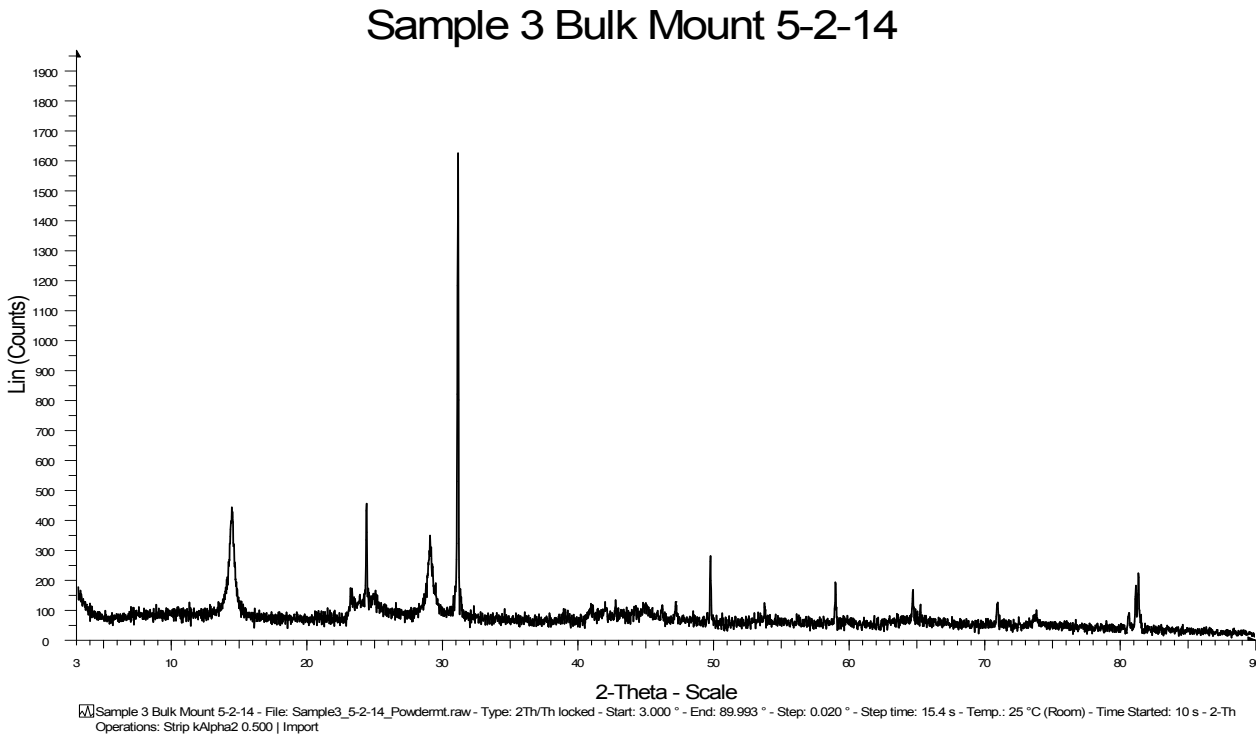

Sample 3 bulk mount diffraction pattern

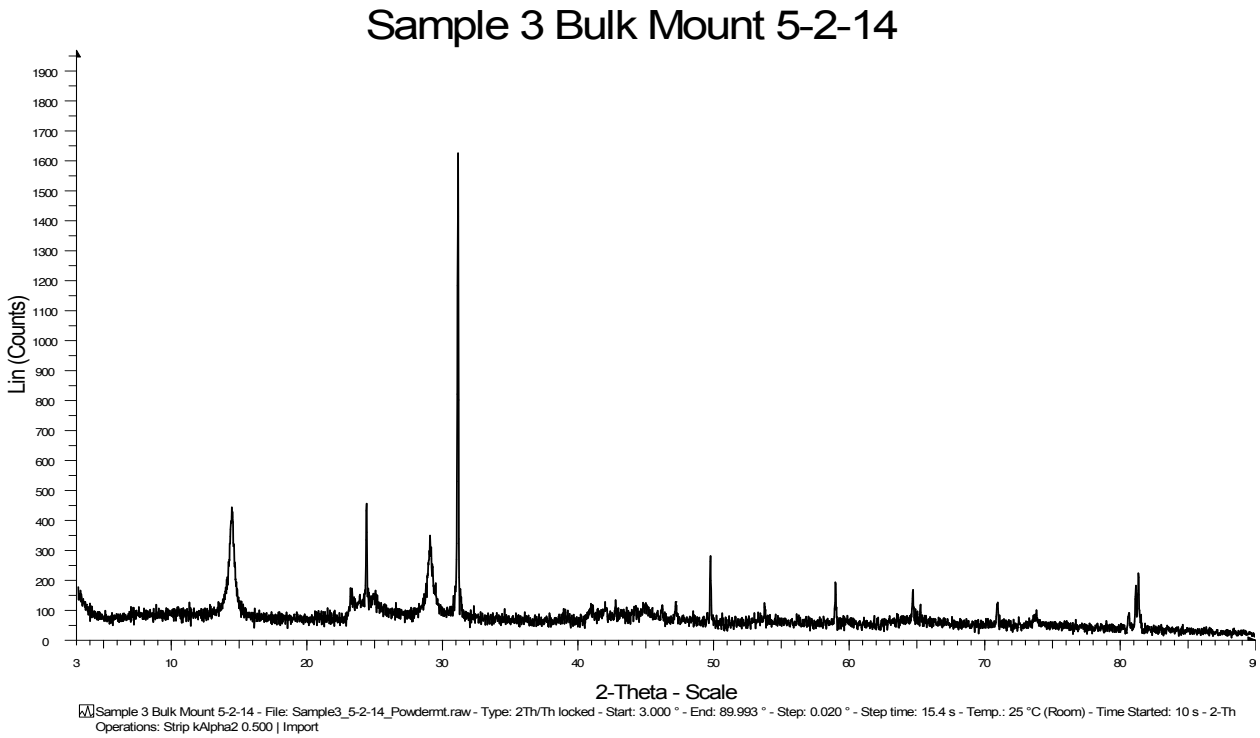

Sample 3 bulk mount diffraction pattern

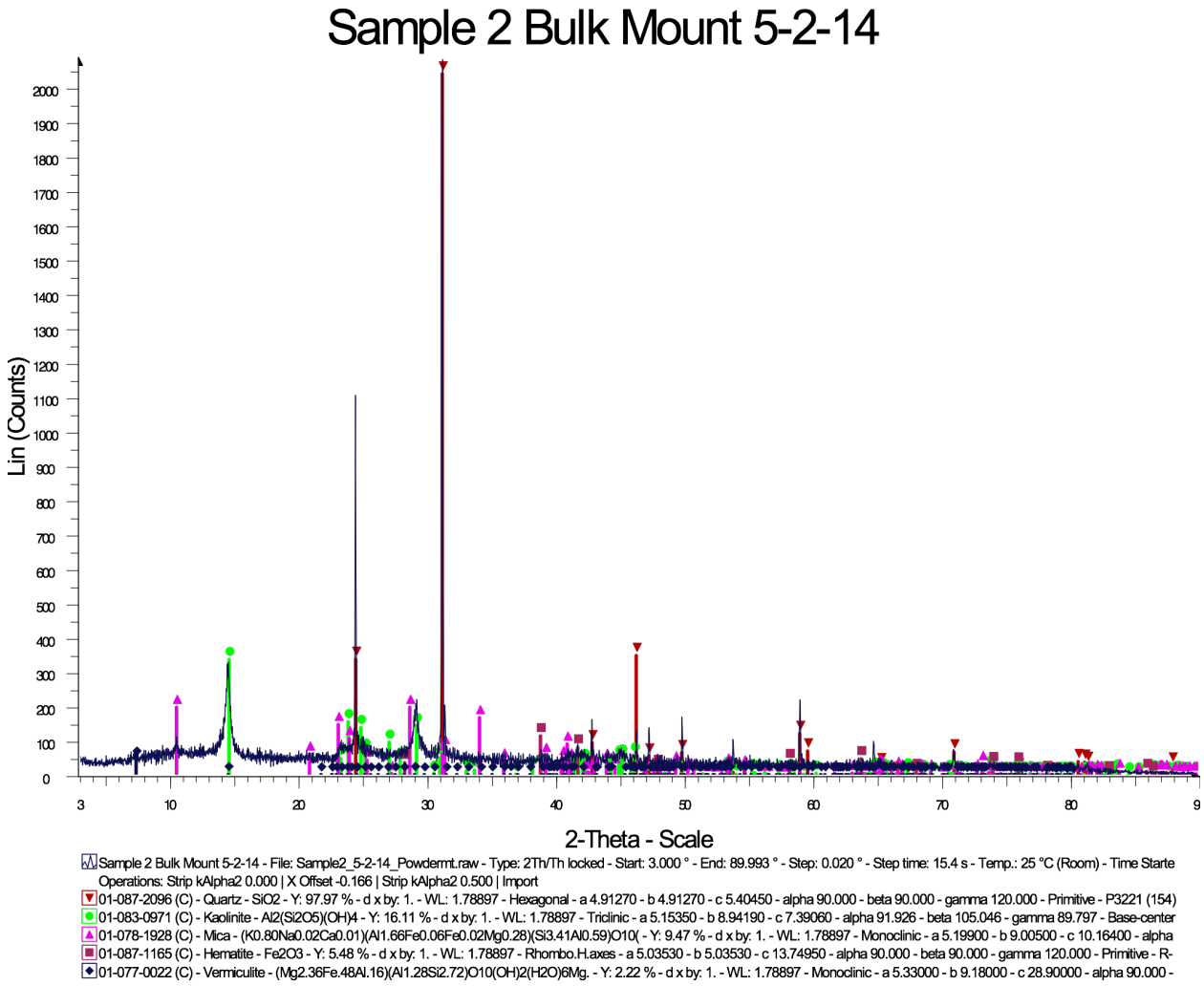

Sample 2 bulk mount mineralogy. Quartz peaks are in red, kaolinite peaks in green, mica peaks in pink, hematite peaks in brown, and vermiculite in blue

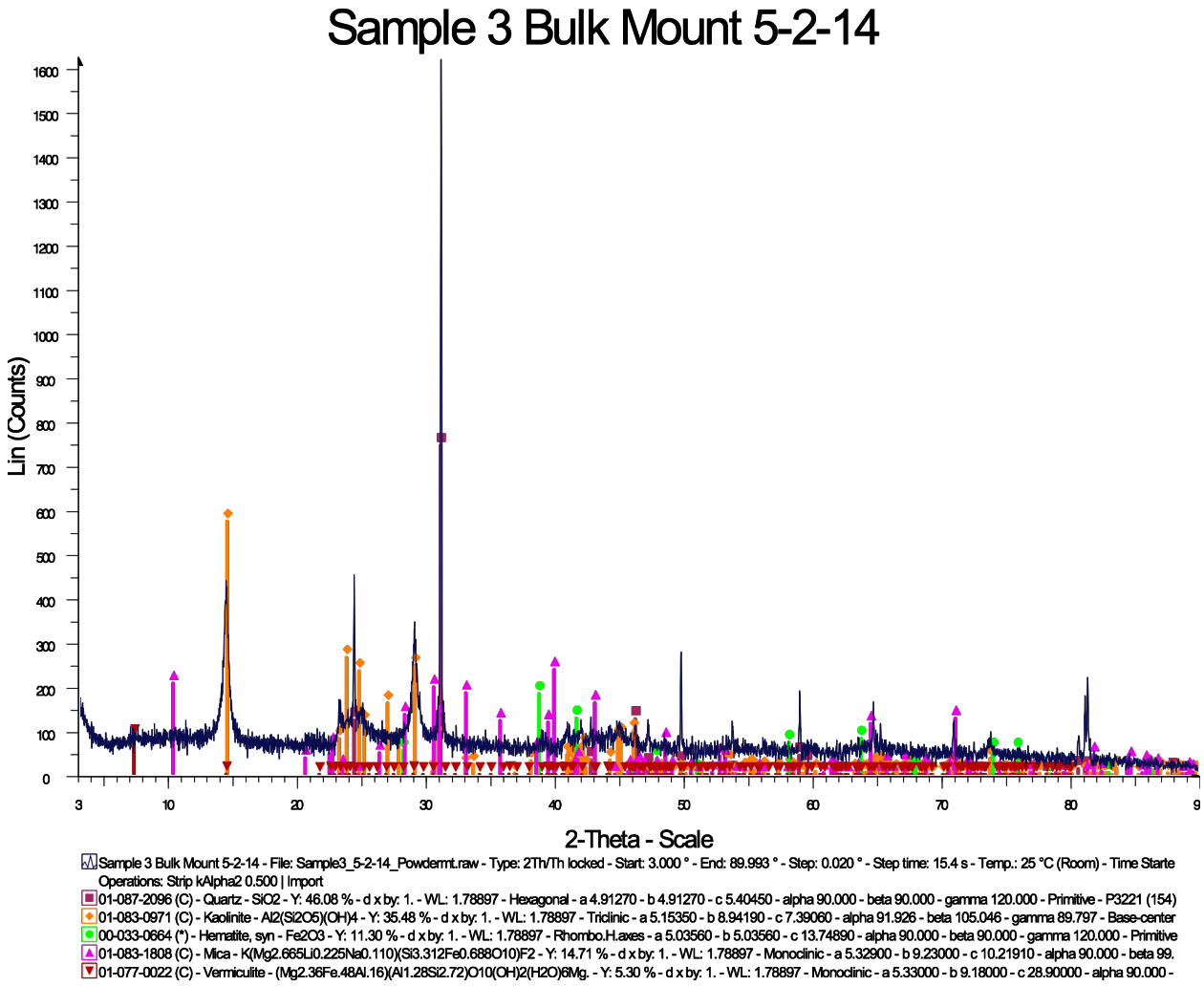

Sample 3 bulk mount mineralogy. Quartz peaks are in red, kaolinite peaks in orange, hematite peaks in brown, mica peaks in pink, and vermiculite peaks in brown.

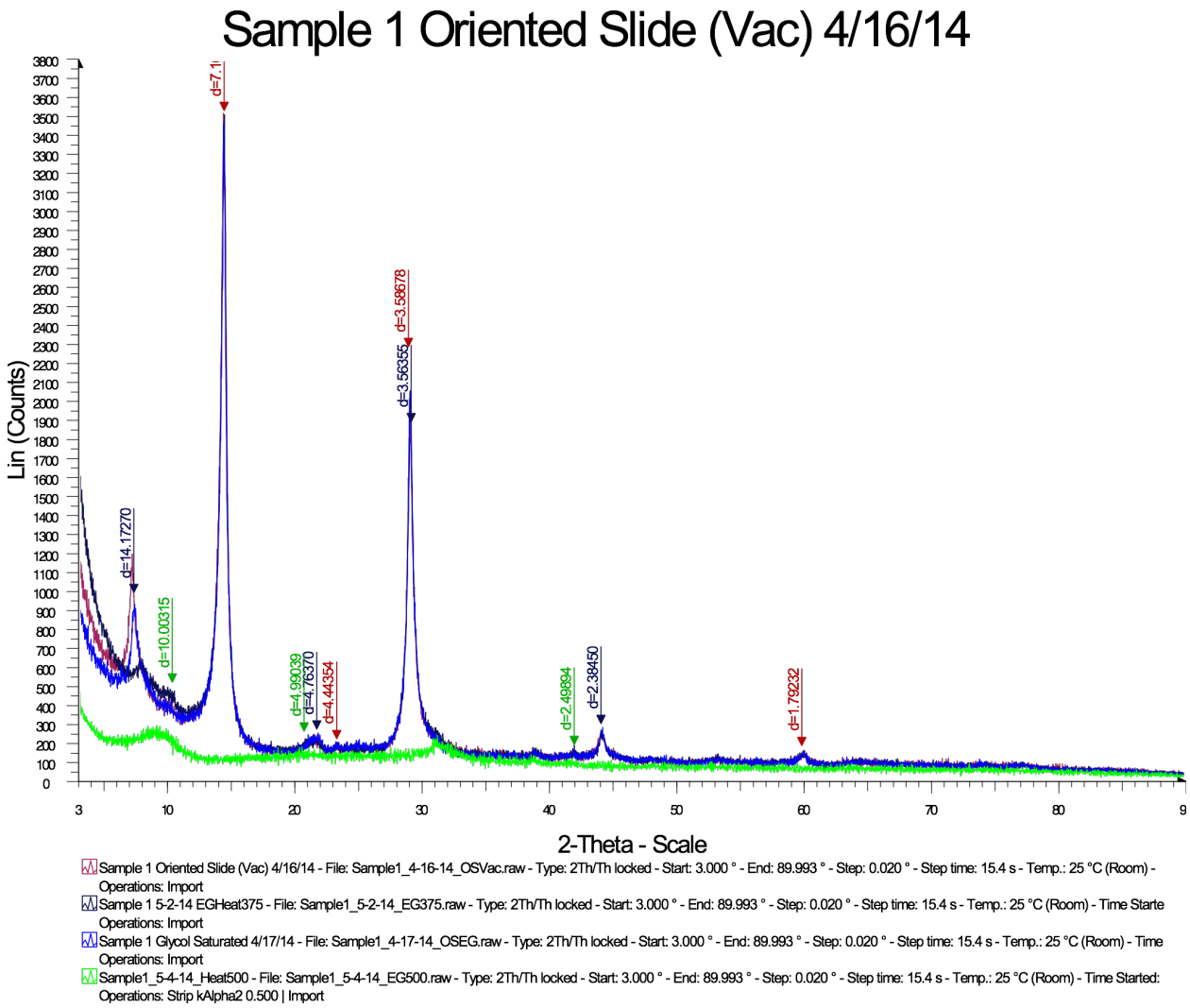

Sample 1 oriented slide diffraction plot. The air dried plot is shown in pink, heated to 375°C in black, glycol saturated in blue, and heated to 500°C in green.

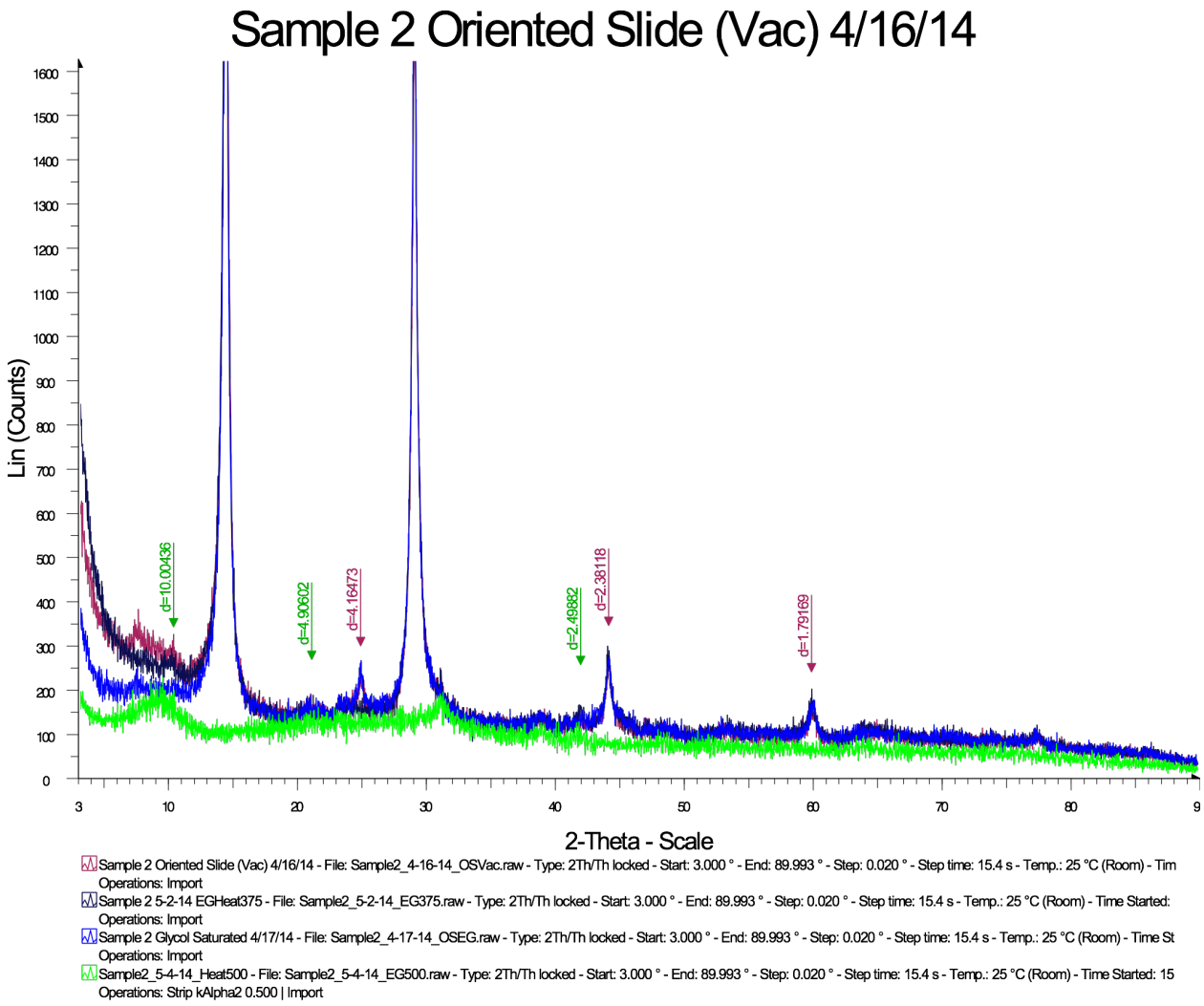

Sample 2 oriented slide diffraction plot. The air dried plot is shown in pink, heated to 375°C in black, glycol saturated in blue, and heated to 500°C in green.

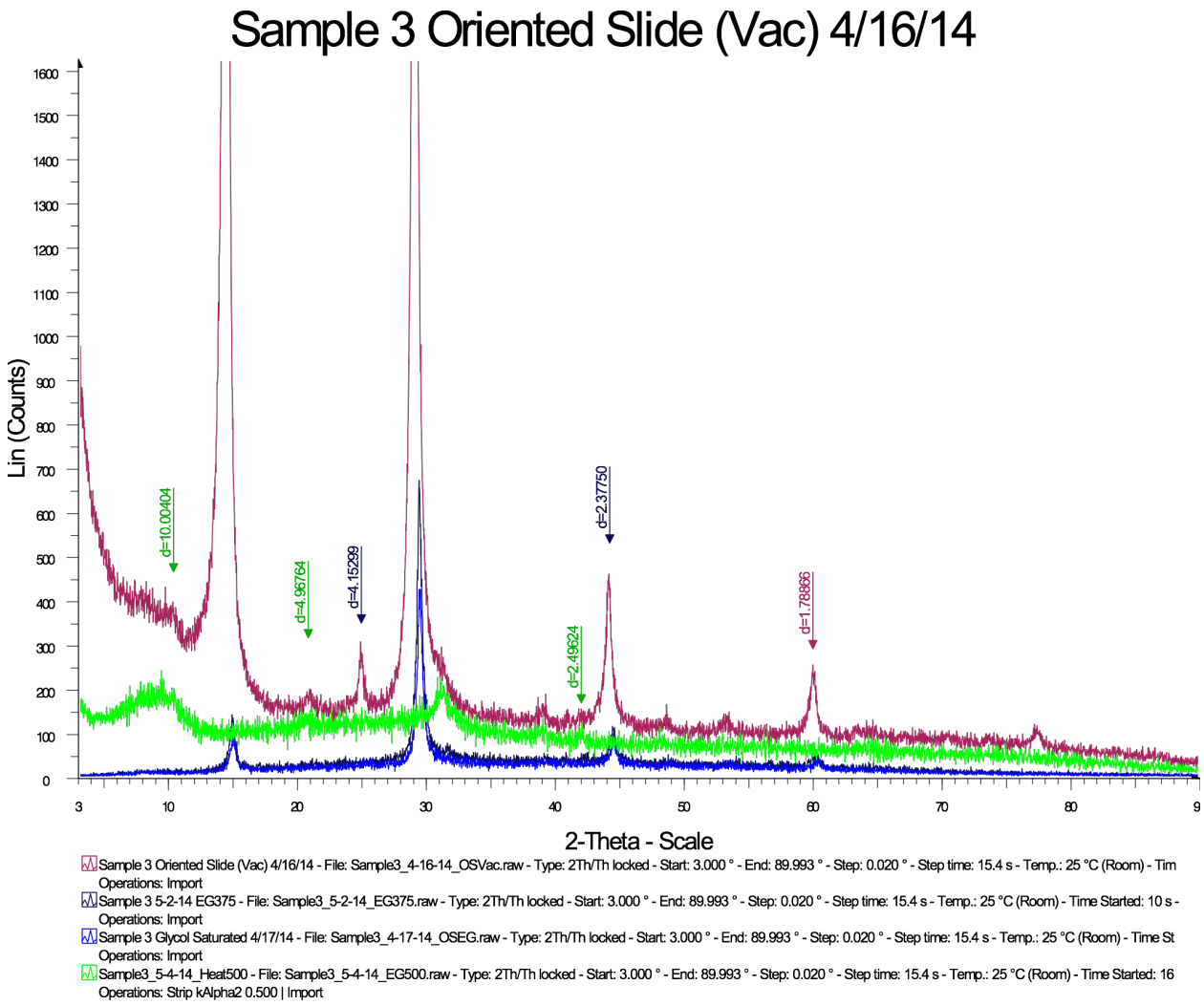

Figure 4.28 - Sample 3 oriented slide diffraction plot. The air dried plot is shown in pink, heated to 375°C in black, glycol saturated in blue, and heated to 500°C in green.

APPENDIX C

Resistivity Inversion Model Input Files

This appendix gives examples of the R2.in and protocol.dat files that were mentioned in the text. The file protocol.dat contains the measurements taken in the field. As described by Binley (2013), the program outputs several different files. The file f001_res.vtk is the output file that is used to plot the inversion results using a program called ParaView (Kitware, 2010). ParaView was chosen because it is compatible with R2 and is relatively easy to use. Paraview takes the .vtk file and will display the results in a cross-sectional view. Users are able to change the color scale and plot resistively values, log resistivity, and sensitivity values.

The following is an example of the R2.in file for the inversion model for Line A:

Inverse model for dp-dp survey; adapted from Fig 5.7 of Binley & Kemna(2005)

1 4 3.0 0 1

373 49 << numnp_x, numnp_y

-190.5 -90.5 -40.5 -20.5 -10.5 -5.5 -3.5 -2.5 -2.0 -1.5 -1.0 -0.5

0.0 0.5 1.0 1.5 2.0 2.5 3.0 3.5 4.0 4.5

5.0 5.5 6.0 6.5 7.0 7.5 8.0 8.5 9.0 9.5

10.0 10.5 11.0 11.5 12.0 12.5 13.0 13.5 14.0 14.5

15.0 15.5 16.0 16.5 17.0 17.5 18.0 18.5 19.0 19.5

20.0 20.5 21.0 21.5 22.0 22.5 23.0 23.5 24.0 24.5

25.0 25.5 26.0 26.5 27.0 27.5 28.0 28.5 29.0 29.5

30.0 30.5 31.0 31.5 32.0 32.5 33.0 33.5 34.0 34.5

35.0 35.5 36.0 36.5 37.0 37.5 38.0 38.5 39.0 39.5

40.0 40.5 41.0 41.5 42.0 42.5 43.0 43.5 44.0 44.5

45.0 45.5 46.0 46.5 47.0 47.5 48.0 48.5 49.0 49.5

50.0 50.5 51.0 51.5 52.0 52.5 53.0 53.5 54.0 54.5

55.0 55.5 56.0 56.5 57.0 57.5 58.0 58.5 59.0 59.5

60.0 60.5 61.0 61.5 62.0 62.5 63.0 63.5 64.0 64.5

65.0 65.5 66.0 66.5 67.0 67.5 68.0 68.5 69.0 69.5

70.0 70.5 71.0 71.5 72.0 72.5 73.0 73.5 74.0 74.5

75.0 75.5 76.0 76.5 77.0 77.5 78.0 78.5 79.0 79.5

80.0 80.5 81.0 81.5 82.0 82.5 83.0 83.5 84.0 84.5

85.0 85.5 86.0 86.5 87.0 87.5 88.0 88.5 89.0 89.5

90.0 90.5 91.0 91.5 92.0 92.5 93.0 93.5 94.0 94.5

95.0 95.5 96.0 96.5 97.0 97.5 98.0 98.5 99.0 99.5

100.0 100.5 101.0 101.5 102.0 102.5 103.0 103.5 104.0 104.5

105.0 105.5 106.0 106.5 107.0 107.5 108.0 108.5 109.0 109.5

110.0 110.5 111.0 111.5 112.0 112.5 113.0 113.5 114.0 114.5

115.0 115.5 116.0 116.5 117.0 117.5 118.0 118.5 119.0 119.5

120.0 120.5 121.0 121.5 122.0 122.5 123.0 123.5 124.0 124.5

125.0 125.5 126.0 126.5 127.0 127.5 128.0 128.5 129.0 129.5

130.0 130.5 131.0 131.5 132.0 132.5 133.0 133.5 134.0 134.5

135.0 135.5 136.0 136.5 137.0 137.5 138.0 138.5 139.0 139.5

140.0 140.5 141.0 141.5 142.0 142.5 143.0 143.5 144.0 144.5

145.0 145.5 146.0 146.5 147.0 147.5 148.0 148.5 149.0 149.5

150.0 150.5 151.0 151.5 152.0 152.5 153.0 153.5 154.0 154.5

155.0 155.5 156.0 156.5 157.0 157.5 158.0 158.5 159.0 159.5

160.0 160.5 161.0 161.5 162.0 162.5 163.0 163.5 164.0 164.5

165.0 165.5 166.0 166.5 167.0 167.5 168.0 168.5 169.0 169.5

170.0 170.5 171.0 171.5 172.0 172.5 173.0 173.5 174.0 174.5

175.0 176.0 178.0 185.0 195.0 215.0 240.0 290.0 340.0 390.0

450.0 << xx

49.85 49.85 49.85 49.85 49.85 49.85 49.85 49.85 49.85 49.85 49.85 49.85

49.85 49.83 49.81 49.79 49.77 49.75 49.73 49.73 49.73 49.73

49.73 49.75 49.77 49.76 49.75 49.76 49.77 49.75 49.72 49.71

49.70 49.69 49.68 49.66 49.64 49.61 49.57 49.61 49.64 49.64

49.63 49.61 49.59 49.58 49.57 49.56 49.56 49.57 49.59 49.61

49.62 49.62 49.62 49.61 49.59 49.59 49.59 49.61 49.62 49.61

49.59 49.57 49.56 49.55 49.54 49.56 49.57 49.56 49.56 49.57

49.59 49.59 49.59 49.59 49.59 49.60 49.61 49.64 49.67 49.64

49.62 49.59 49.56 49.57 49.58 49.61 49.63 49.61 49.58 49.58

49.58 49.58 49.58 49.61 49.63 49.63 49.62 49.59 49.57 49.57

49.57 49.57 49.57 49.58 49.59 49.60 49.61 49.61 49.62 49.63

49.64 49.64 49.64 49.66 49.67 49.68 49.70 49.70 49.70 49.68

49.67 49.67 49.67 49.68 49.68 49.69 49.70 49.70 49.70 49.70

49.70 49.69 49.68 49.68 49.67 49.66 49.66 49.66 49.66 49.66

49.66 49.66 49.67 49.69 49.71 49.71 49.72 49.73 49.75 49.63

49.50 49.50 49.50 49.51 49.52 49.52 49.53 49.54 49.54 49.56

49.57 49.57 49.58 49.59 49.59 49.59 49.59 49.59 49.59 49.58

49.57 49.55 49.53 49.52 49.52 49.52 49.52 49.52 49.52 49.52

49.52 49.51 49.50 49.64 49.78 49.77 49.76 49.77 49.78 49.78

49.78 49.78 49.78 49.78 49.77 49.78 49.78 49.78 49.78 49.79

49.80 49.80 49.80 49.78 49.77 49.76 49.75 49.74 49.73 49.75

49.76 49.75 49.73 49.71 49.70 49.71 49.72 49.73 49.75 49.76

49.77 49.79 49.81 49.83 49.85 49.86 49.87 49.88 49.89 49.89

49.89 49.88 49.87 49.89 49.90 49.89 49.89 49.89 49.89 49.89

49.89 49.88 49.87 49.87 49.87 49.87 49.87 49.87 49.86 49.89

49.91 49.94 49.96 49.99 50.01 50.01 50.00 49.99 49.99 49.99

49.99 50.01 50.03 50.01 50.00 50.01 50.03 50.03 50.03 50.01

50.00 50.00 50.00 50.00 50.00 50.00 50.00 49.99 49.97 49.99

50.00 49.99 49.97 49.99 50.00 50.03 50.05 50.06 50.08 50.11

50.15 50.13 50.10 50.11 50.13 50.13 50.13 50.15 50.18 50.19

50.20 50.22 50.23 50.23 50.23 50.23 50.23 50.22 50.20 50.22

50.23 50.24 50.25 50.25 50.25 50.27 50.28 50.29 50.30 50.30

50.30 50.33 50.36 50.37 50.38 50.41 50.43 50.44 50.46 50.46

50.46 50.46 50.46 50.44 50.43 50.44 50.46 50.43 50.41 50.43

50.46 50.44 50.43 50.42 50.41 50.41 50.41 50.41 50.41 50.41

50.41 50.41 50.41 50.41 50.41 50.41 50.41 50.41 50.41 50.41

50.41 50.41 50.41 50.41 50.41 50.41 50.41 50.41 50.41 50.41

50.41 << topog

0.0 0.5 1.0 1.5 2.0 2.5 3.0 3.5 4.0 4.5

5.0 5.5 6.0 6.5 7.0 7.5 8.0 8.5 9.0 9.5

10.0 10.5 11.0 11.5 12.0 12.5 13.0 13.5 14.0 14.5

15.0 15.5 16.0 16.5 17.0 17.5 18.0 18.5 19.0 19.5

20.0 20.5 21.0 25.0 30.0 50.0 100.0 350.0 500.0 << yy

1 << num_regions

1 17856 100.000 << elem_1,elem_2,value

4 4 << no. patches in x, no. patches in z

1 << inverse_type

1 0 << data type (0=normal;1=log), regularization type

0.50 10 2 1.0 << tolerance, max_iterations, error_mod, alpha_aniso

0.00000 0.00000 -5000.0 5000.0 << a_wgt, b_wgt, rho_min, rho_max

5 << num_poly

0.0 -51

169.0 -51

169.0 -31

0.0 -31

0.0 -51

35 << num_electrodes

1 13 1 << elec, column, row

2 23 1

3 33 1

4 43 1

5 53 1

6 63 1

7 73 1

8 83 1

9 93 1

10 103 1

11 113 1

12 123 1

13 133 1

14 143 1

15 153 1

16 163 1

17 173 1

18 183 1

19 193 1

20 203 1

21 213 1

22 223 1

23 233 1

24 243 1

25 253 1

26 263 1

27 273 1

28 283 1

29 293 1

30 303 1

31 313 1

32 323 1

33 333 1

34 343 1

35 353 1

The following is the protocol.dat file for the inversion model for Line A : The first row is the total number of measurements recorded. The first column is the measurement count, column 2-5 is the electrode placement, column 6 is the negative of the observed resistance, and column 7 is the one sigma uncertainty of the resistance.

177

1 3 4 1 2 -0.31 0.01

2 4 5 1 2 -0.075 0.0075

3 5 6 1 2 -0.035 0.0075

4 6 7 1 2 -0.025 0.0075

5 7 8 1 2 -0.02 0.01

6 8 9 1 2 -0.02 0.01

7 4 5 2 3 -0.555 0.0075

8 5 6 2 3 -0.125 0.0075

9 6 7 2 3 -0.045 0.0075

10 7 8 2 3 -0.03 0.01

11 8 9 2 3 -0.02 0.01

12 9 10 2 3 -0.02 0.01

13 5 6 3 4 -0.5 0.005

14 6 7 3 4 -0.13 0.005

15 7 8 3 4 -0.05 0.01

16 8 9 3 4 -0.03 0.01

17 9 10 3 4 -0.02 0.01

18 10 11 3 4 -0.025 0.0125

19 6 7 4 5 -0.505 0.0075

20 7 8 4 5 -0.125 0.0075

21 8 9 4 5 -0.06 0.01

22 9 10 4 5 -0.025 0.0125

23 10 11 4 5 -0.02 0.01

24 11 12 4 5 -0.02 0.01

25 7 8 5 6 -0.445 0.0075

26 8 9 5 6 -0.13 0.01

27 9 10 5 6 -0.05 0.01

28 10 11 5 6 -0.025 0.0125

29 11 12 5 6 -0.02 0.01

30 12 13 5 6 -0.02 0.01

31 8 9 6 7 -0.49 0.01

32 9 10 6 7 -0.11 0.01

33 10 11 6 7 -0.045 0.0125

34 11 12 6 7 -0.025 0.0125

35 12 13 6 7 -0.02 0.01

36 13 14 6 7 -0.02 0.01

37 9 10 7 8 -0.425 0.0075

38 10 11 7 8 -0.095 0.0125

39 11 12 7 8 -0.04 0.01

40 12 13 7 8 -0.03 0.01

41 13 14 7 8 -0.02 0.01

42 14 15 7 8 -0.015 0.0075

43 10 11 8 9 -0.345 0.0125

44 11 12 8 9 -0.08 0.01

45 12 13 8 9 -0.04 0.01

46 13 14 8 9 -0.025 0.0125

47 14 15 8 9 -0.025 0.0125

48 15 16 8 9 -0.02 0.01

49 11 12 9 10 -0.295 0.0125

50 12 13 9 10 -0.1 0.01

51 13 14 9 10 -0.045 0.0075

52 14 15 9 10 -0.02 0.01

53 15 16 9 10 -0.02 0.01

54 16 17 9 10 -0.015 0.0075

55 12 13 10 11 -0.395 0.0125

56 13 14 10 11 -0.095 0.0125

57 14 15 10 11 -0.04 0.01

58 15 16 10 11 -0.025 0.0125

59 16 17 10 11 -0.02 0.01

60 17 18 10 11 -0.015 0.0075

61 13 14 11 12 -0.27 0.01

62 14 15 11 12 -0.07 0.01

63 15 16 11 12 -0.04 0.01

64 16 17 11 12 -0.025 0.0075

65 17 18 11 12 -0.015 0.0075

66 18 19 11 12 -0.02 0.01

67 14 15 12 13 -0.25 0.01

68 15 16 12 13 -0.085 0.0125

69 16 17 12 13 -0.04 0.01

70 17 18 12 13 -0.02 0.005

71 18 19 12 13 -0.02 0.01

72 19 20 12 13 -0.02 0.01

73 15 16 13 14 -0.255 0.0125

74 16 17 13 14 -0.08 0.01

75 17 18 13 14 -0.025 0.0075

76 18 19 13 14 -0.02 0.01

77 19 20 13 14 -0.02 0.01

78 20 21 13 14 -0.02 0.01

79 16 17 14 15 -0.295 0.0075

80 17 18 14 15 -0.04 0.005

81 18 19 14 15 -0.03 0.01

82 19 20 14 15 -0.025 0.0125

83 20 21 14 15 -0.02 0.01

84 21 22 14 15 -0.015 0.0075

85 17 18 15 16 -0.155 0.0075

86 18 19 15 16 -0.08 0.01

87 19 20 15 16 -0.05 0.01

88 20 21 15 16 -0.03 0.01

89 21 22 15 16 -0.025 0.0075

90 22 23 15 16 -0.015 0.0075

91 18 19 16 17 -0.175 0.0075

92 19 20 16 17 -0.085 0.0075

93 20 21 16 17 -0.045 0.0075

94 21 22 16 17 -0.025 0.0075

95 22 23 16 17 -0.02 0.01

96 23 24 16 17 -0.015 0.0075

97 19 20 17 18 -0.225 0.0125

98 20 21 17 18 -0.075 0.0125

99 21 22 17 18 -0.03 0.01

100 22 23 17 18 -0.025 0.0075

101 23 24 17 18 -0.015 0.0075

102 24 25 17 18 -0.015 0.0075

103 20 21 18 19 -0.455 0.0075

104 21 22 18 19 -0.125 0.0125

105 22 23 18 19 -0.04 0.01

106 23 24 18 19 -0.025 0.0075

107 24 25 18 19 -0.025 0.0075

108 25 26 18 19 -0.015 0.0075

109 21 22 19 20 -0.475 0.0075

110 22 23 19 20 -0.105 0.0075

111 23 24 19 20 -0.035 0.0075

112 24 25 19 20 -0.025 0.0075

113 25 26 19 20 -0.02 0.005

114 26 27 19 20 -0.02 0.005

115 22 23 20 21 -0.305 0.0075

116 23 24 20 21 -0.075 0.0075

117 24 25 20 21 -0.03 0.005

118 25 26 20 21 -0.025 0.0075

119 26 27 20 21 -0.02 0.005

120 27 28 20 21 -0.02 0.005

121 23 24 21 22 -0.24 0.005

122 24 25 21 22 -0.065 0.0075

123 25 26 21 22 -0.035 0.0075

124 26 27 21 22 -0.025 0.0075

125 27 28 21 22 -0.015 0.0075

126 28 29 21 22 -0.02 0.01

127 24 25 22 23 -0.185 0.0075

128 25 26 22 23 -0.07 0.005

129 26 27 22 23 -0.035 0.0075

130 27 28 22 23 -0.02 0.005

131 28 29 22 23 -0.015 0.0075

132 29 30 22 23 -0.02 0.01

133 25 26 23 24 -0.19 0.005

134 26 27 23 24 -0.06 0.005

135 27 28 23 24 -0.03 0.005

136 28 29 23 24 -0.02 0.005

137 29 30 23 24 -0.025 0.0125

138 30 31 23 24 -0.025 0.0075

139 26 27 24 25 -0.165 0.0025

140 27 28 24 25 -0.05 0.005

141 28 29 24 25 -0.025 0.0075

142 29 30 24 25 -0.025 0.0125

143 30 31 24 25 -0.02 0.01

144 31 32 24 25 -0.015 0.0075

145 27 28 25 26 -0.15 0.005

146 28 29 25 26 -0.055 0.0075

147 29 30 25 26 -0.04 0.01

148 30 31 25 26 -0.025 0.0075

149 31 32 25 26 -0.015 0.0075

150 32 33 25 26 -0.015 0.0075

151 28 29 26 27 -0.14 0.005

152 29 30 26 27 -0.08 0.01

153 30 31 26 27 -0.04 0.005

154 31 32 26 27 -0.02 0.005

155 32 33 26 27 -0.015 0.0075

156 33 34 26 27 -0.02 0.005

157 29 30 27 28 -0.475 0.0075

158 30 31 27 28 -0.135 0.0075

159 31 32 27 28 -0.040 0.0050

160 32 33 27 28 -0.02 0.005

161 33 34 27 28 -0.02 0.005

162 34 35 27 28 -0.01 0.005

163 30 31 28 29 -1.065 0.0075

164 31 32 28 29 -0.18 0.005

165 32 33 28 29 -0.06 0.005

166 33 34 28 29 -0.02 0.005

167 34 35 28 29 -0.015 0.0075

168 31 32 29 30 -1.065 0.0075

169 32 33 29 30 -0.235 0.0075

170 33 34 29 30 -0.06 0.005

171 34 35 29 30 -0.025 0.0075

172 32 33 30 31 -1.04 0.005

173 33 34 30 31 -0.18 0.005

174 34 35 30 31 -0.055 0.0075

175 33 34 31 32 -0.82 0.01

176 34 35 31 32 -0.195 0.0075

177 34 35 32 33 -0.74 0.005

The following is an example of an output file after the inversion was completed:

```
>> R 2  Resistivity Inversion v2.7 <<

 >> Date: 15 - 11 - 2014
 >> Inverse model for dp-dp survey; adapted from Fig 5.7 of Binley & Kemna(2005)
 >> Inverse Solution Selected <<
 >> Regularised Type <<
 >>  Linear Filter  <<
 >> Log-Data Inversion <<
 >> Normal Regularisation <<
 >> Data weights will be modified <<
 WARNING: it is recommended that the tolerance is set to 1
 >> Data weight to be read from data file <<



 Processing dataset   1



 Measurements read:   177     Measurements rejected:     0
  Geometric mean of apparent resistivities:  0.94439E+02
```

Iteration 1

Initial RMS Misfit: 21.65 Number of data ignored: 0

WARNING: managed to achieve CG tolerance of: 0.756E-03

Alpha: 5919.822 RMS Misfit: 16.38

Alpha: 2747.738 RMS Misfit: 15.99

Alpha: 1275.387 RMS Misfit: 15.29

Alpha: 591.982 RMS Misfit: 14.19

Alpha: 274.774 RMS Misfit: 12.73

Alpha: 127.539 RMS Misfit: 11.03

Alpha: 59.198 RMS Misfit: 9.15

Alpha: 27.477 RMS Misfit: 7.25

Alpha: 12.754 RMS Misfit: 5.57

Alpha: 5.920 RMS Misfit: 4.30

Step length set to 1.00000

Final RMS Misfit: 4.30

Updated data weights

Iteration 2

Initial RMS Misfit: 2.64 Number of data ignored: 0

Alpha: 3.500 RMS Misfit: 3.10

Alpha: 1.625 RMS Misfit: 2.58

Alpha: 0.754 RMS Misfit: 2.22

Alpha: 0.350 RMS Misfit: 1.93

Alpha: 0.162 RMS Misfit: 1.66

Alpha: 0.075 RMS Misfit: 1.40

Alpha: 0.035 RMS Misfit: 1.20

Alpha: 0.016 RMS Misfit: 1.08

Alpha: 0.008 RMS Misfit: 1.04

Alpha: 0.004 RMS Misfit: 1.09

Step length set to 1.00000

Final RMS Misfit: 1.04

Updated data weights

Iteration 3

Initial RMS Misfit: 0.79 Number of data ignored: 0

Alpha: 0.004 RMS Misfit: 0.60

Alpha: 0.002 RMS Misfit: 0.52

Alpha: 0.001 RMS Misfit: 0.47

Step length set to 1.00000

Final RMS Misfit: 0.47

Step length set to 0.77931

Final RMS Misfit: 0.50

Solution converged - Outputing results to file

Calculating sensitivity map

Processing dataset 2

End of data: Terminating

Timing Summary

==========

Total time taken: 178. s

Percent time taken forming element equations: 17.4 %

Percent time taken solving forward equations: 64.2 %

Percent time taken forming Jacobian: 1.3 %

Percent time taken solving inverse equations: 19.1 %

Percent time taken calculating res. matrix: 0.0 %

Timing Details

==========

Number of calls to form element equations: 252

Average time taken in call: 0.1 s

Number of calls to solve forward equations: 8820

Average time taken in call: 0.0 s

Number of calls to form Jacobian: 3

Average time taken in call: 0.8 s

Number of calls to solve inverse equations: 23

Average time taken in call: 1.5 s

Number of calls to calculate res. matrix: 0

Average time taken in call: 0.0 s

APPENDIX D

Examples of Elevation Inversion Files with Different Chi-Squared Values

This appendix includes Lines A, Y, and Z and shows the difference between inversions with different chi-squared values. Each inversion shows the log resistivity and has elevation data included. The main objective of these tests was to determine the optimum value of x^2 to use for the inversions. Choosing a value too large results in a poor fit to the data and choosing a value too small results in overfitting the data, meaning some of the model details can't be resolved by the data. Very small values of x^2 can also result in model instability, e.g., extremely high values for bedrock resistivities that grow in magnitude as x^2 becomes smaller and smaller. These unstable values occur in the deeper parts of the model, where current penetration is insufficient to constrain resistivities. The goal was to find the largest value of x^2 that could resolve geologic structures.

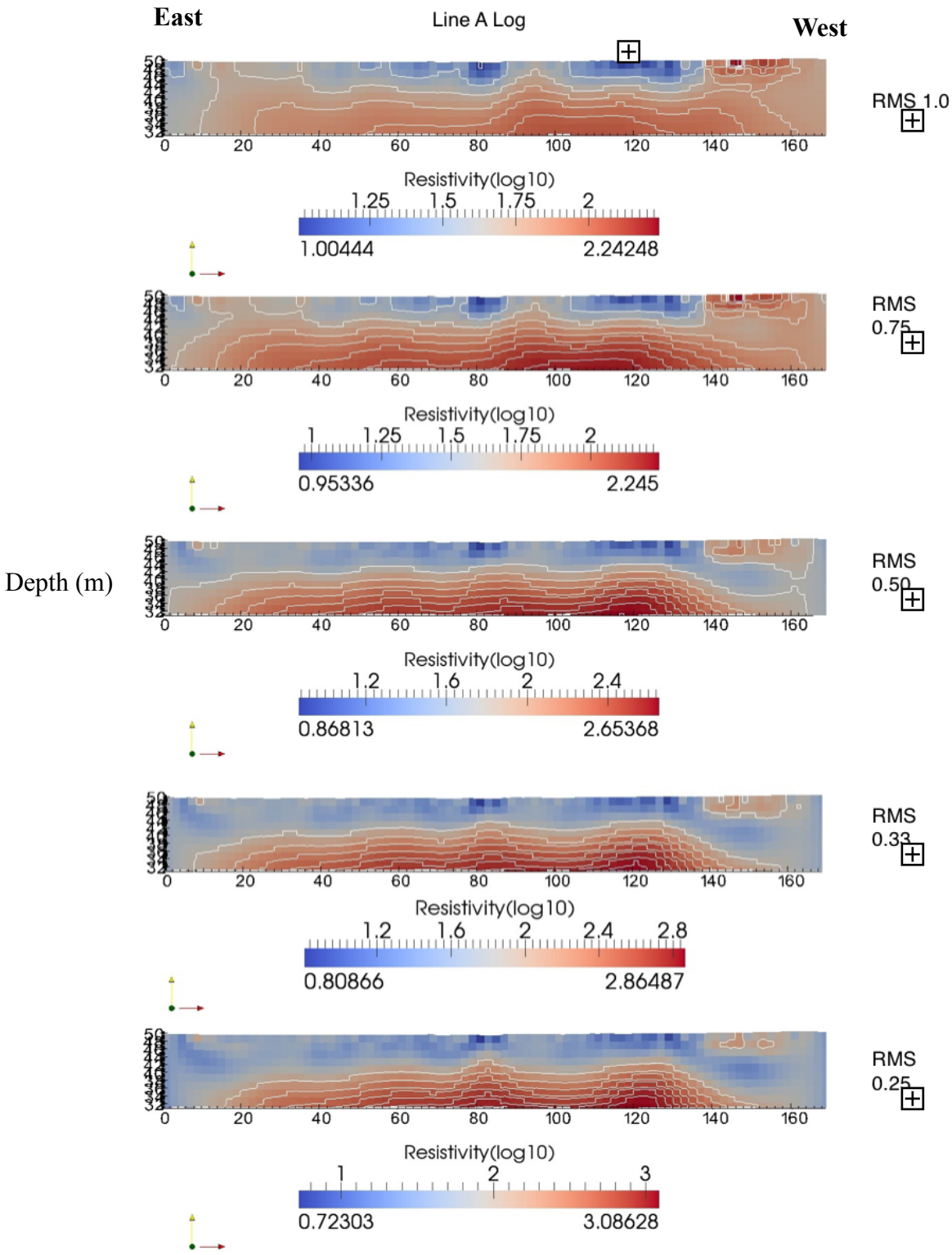
East
Line A Log
West
RMS 1.0
Resistivity(log10)
1.25 1.5 1.75 2
1.00444 2.24248
RMS 0.75
Resistivity(log10)
1 1.25 1.5 1.75 2
0.95336 2.245
RMS 0.50
Resistivity(log10)
1.2 1.6 2 2.4
0.86813 2.65368
RMS 0.33
Resistivity(log10)
1.2 1.6 2 2.4 2.8
0.80866 2.86487
RMS 0.25
Resistivity(log10)
1 2 3
0.72303 3.08628
0 20 40 60 80 100 120 140 160
Depth (m)
Distance (m)

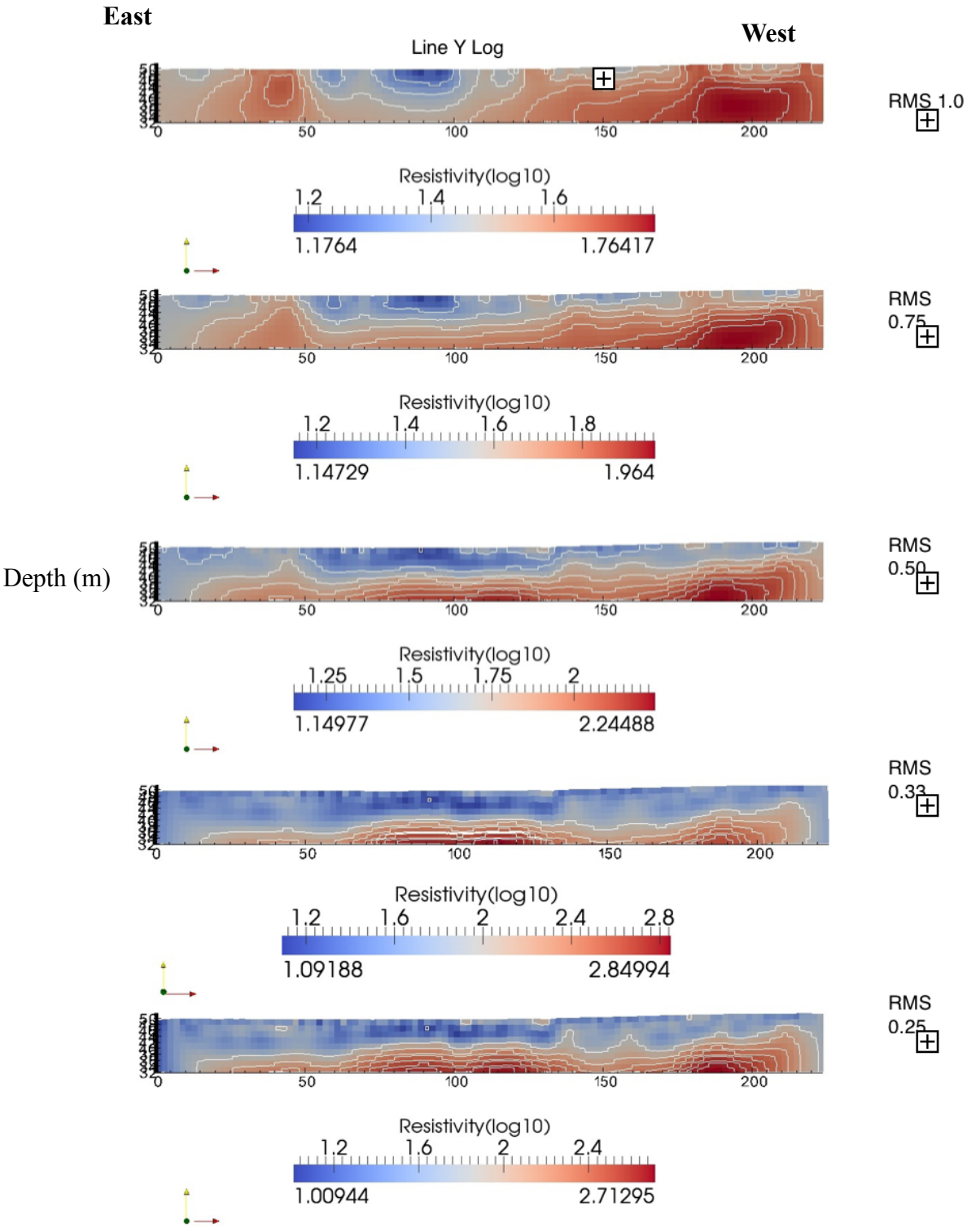
East
West
Line Y Log
RMS 1.0
Resistivity(log10)
1.2
1.4
1.6
1.1764
1.76417
RMS
0.75
Resistivity(log10)
1.2
1.4
1.6
1.8
1.14729
1.964
RMS
0.50
Resistivity(log10)
1.25
1.5
1.75
2
1.14977
2.24488
RMS
0.33
Resistivity(log10)
1.2
1.6
2
2.4
2.8
1.09188
2.84994
RMS
0.25
Resistivity(log10)
1.2
1.6
2
2.4
1.00944
2.71295
0
50
100
150
200
Depth (m)
Distance (m)

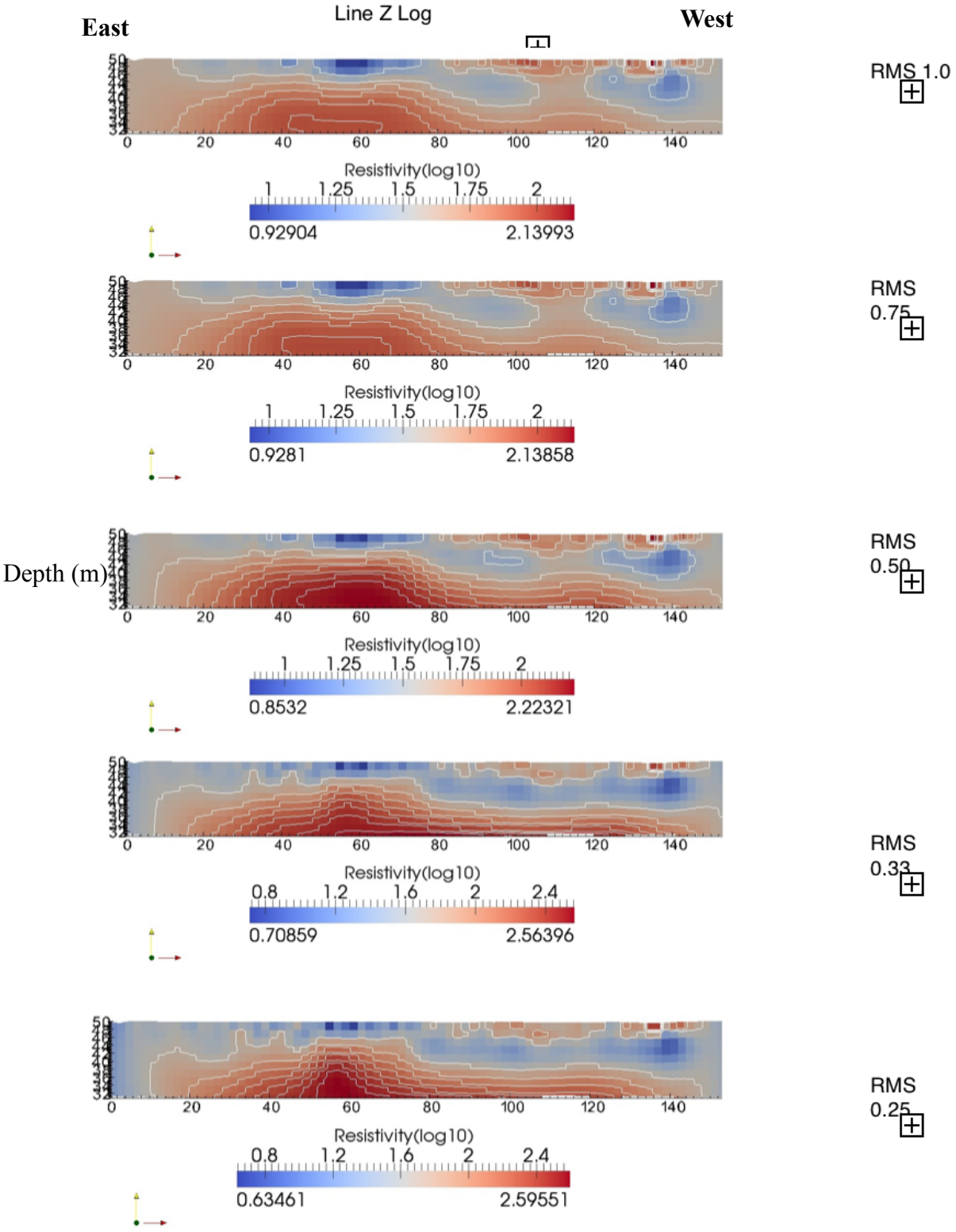
Line Z Log
East
West
RMS 1.0
RMS 0.75
RMS 0.50
RMS 0.33
RMS 0.25
Depth (m)
Distance (m)
Resistivity(log10)
1 1.25 1.5 1.75 2
0.92904 2.13993
0.9281 2.13858
0.8532 2.22321
0.8 1.2 1.6 2 2.4
0.70859 2.56396
0.63461 2.59551
0 20 40 60 80 100 120 140